VIBRATIONAL ENERGY HARVESTING USING PIEZOELECTRIC CERAMICS AND FREE-STANDING THICK-FILM STRUCTURES

by

YANG BAI

A thesis submitted to the University of Birmingham
for the degree of
DOCTOR OF PHILOSOPHY

School of Metallurgy and Materials
College of Engineering and Physical Science
University of Birmingham
January 2015

SYNOPSIS

This thesis presents a series of broad but systematic and consecutive investigations on the topic of piezoelectric energy harvesting. These include material fabrication and characterisation, harvester fabrication and material parameter selection, electric output and dynamic behaviour tests of energy harvesters, and the feasibility of utilising lead-free piezoelectric materials for energy harvesting. Three lead-based and one lead-free perovskite solid-solutions compositions (commercial soft PZT, 3 mol% La-doped $0.25Pb(Zn_{1/3}Nb_{2/3})O_3$-$0.75Pb(Zr_{0.55}Ti_{0.45})O_3$ (PZnN-P3LZT), 5 mol% La-doped $0.25Pb(Zn_{1/3}Nb_{2/3})O_3$-$0.75Pb(Zr_{0.53}Ti_{0.47})O_3$ (PZnN-P5LZT) and $(Ba_{0.85}Ca_{0.15})(Zr_{0.1}Ti_{0.9})O_3$ (50BCZT)) have been researched individually and compared to each other. In the form of bulk ceramics the lead-free composition is considered capable of replacing the lead-based compositions for vibrational energy harvesting at room temperature, despite the 50BCZT requiring a much higher sintering temperature (>1400 °C) and having a much lower Curie temperature (<90 °C). Typical properties of $\varepsilon_r \approx 4700$, $P_r \approx 9\ \mu C/cm^2$, $d_{33} \approx 630\ pC/N$, $k_p \approx 0.56$ and $\varepsilon_r \approx 2300$, $P_r \approx 9\ \mu C/cm^2$, $d_{33} \approx 500\ pC/N$, $k_p \approx 0.51$ have been achieved for the 50BCZT and PZT compositions respectively. Bulk ceramics of all the compositions and free-standing single-layer thick-films of two of the lead-based compositions with a low-temperature sintering additive have also been investigated. Vibrational energy harvesting based on a novel structure of piezoelectric/silver multi-layer free-standing thick-film unimorph and bimorph cantilevers have been investigated using two of the lead-based compositions. A planar shrinkage difference of 3-6% between the silver and piezoelectric layers is suggested in order to ensure successful fabrication. When tested under harmonic vibration conditions, a comparison of unimorph individual harvesters suggests that higher piezoelectric voltage and electromechanical coupling coefficients may be preferred when selecting materials. Further optimisations involving bimorph devices with tip

proof mass have demonstrated maximum harvester outputs (root mean square) of about 9 μW and 2.8 V with approximately 14% bandwidth under resonant vibrations (100-150 Hz, 0.5-1.0g). In addition, the cantilevers have utilised to harvest wind energy with a modified spinning configuration, exhibiting 3.4 V average open-circuit output voltage in optimum wind conditions.

ACKNOWLEDGEMENTS

First of all, I would like to thank my supervisor, Prof. Tim W. Button, for offering me the opportunity to do the research work, for providing advanced and satisfied research environment, and for his encouraging guidance and excellent supervision.

Also, I must acknowledge the School of Metallurgy and Materials of the University of Birmingham for the provision of other experimental facilities.

I would like to express my gratitude to Mr. Carl Meggs for his professional training on the laboratory equipment and practical advice on the experimental design.

My thanks also go to Dr. Hana Hughes, Dr. Yun Jiang and Dr. Pavel Tofel for their useful suggestions and help of solving technical problems and obtaining data.

Finally, my special acknowledgements belong to Mr. Ma Hongshen and Mrs. Yang Xiaoying, my parents Mr. Li Shiguo and Mrs. Li Jihong, as well as my wife Mrs. Ma Yangshuangshuang, for their financial support, their love and understanding throughout my study.

CONTENTS

INDEX OF FIGURES

INDEX OF TABLES

Nomenclature

Abbreviations

EH	energy harvesting
EHer	energy harvester
EEHer	electrostatic energy harvester
EMEHer	electromagnetic energy harvester
PEHer	piezoelectric energy harvester
ESEHer	electrostrictive energy harvester
MEMS	micro-electromechanical systems
DC	direct current
AC	alternating current
EM	electromagnetic
RF	radio frequency
MPB	morphotropic phase boundary
BT	$BaTiO_3$, Barium Titanate
PZT	$Pb(Zr_xTi_{1-x})O_3$, Lead Zirconate Titanate
PZnN	$Pb(Zn_{1/3}Nb_{2/3})O_3$, Lead Zinc Niobate
PMN-PT	$Pb(Mg_xNb_{1-x})O_3$-$PbTiO_3$
KNN	$(K,Na)NbO_3$, Sodium Potassium Niobate
KN	$KNbO_3$
NN	$NaNbO_3$
BNT	$Bi_{1/2}Na_{1/2}TiO_3$, Bismuth Sodium Titanate
BKT	$Bi_{1/2}K_{1/2}TiO_3$, Bismuth Potassium Titanate
BZT	Barium Zirconate Titanate

BCT	Barium Calcium Titanate
BCZT	Barium Calcium Zirconate Titanate
PVDF	polyvinylidene floride
SOI	silicon on insulator
FWHM	full width at half maximum
IDE	interdititated electrode
PPE	parallel plate electrode
SEM	scanning electron microscope
DSC	differential scanning calorimetry
TGA	thermal gravimetric analysis
XRD	X-ray diffraction or X-ray diffractometer
SE	secondary electron
BSE	back scatter electron

Parameters (physical)

T	temperature
T_c	Curie temperature
T_d	depoling temperature
$tol.$	tolerance factor
s	compliance constant
c	stiffness constant
Y	Young’s modulus
$\varLambda$	Poisson’s ratio
G	shear modulus

D	charge displacement
σ	stress
E	electric field
S	strain
C	capacitance
f_0	fundamental resonant frequency
f	overall natural resonant frequency
λ_0	function of fundamental resonant boundary condition
ρ	density
L, l	length
w	width
H, t	thickness
r	radius
ΔL	displacement deflection
U_{in}	applied voltage or input voltage
U_{out}	output voltage
U	open-circuit output voltage
F	applied force
q	charge sensitivity
m	mass
m_{pul}	mass per unit length
ξ	damping constant
γ	spring constant
I	moment of inertia

y	distance
δz	tip displacement

Parameters (dielectric, ferroelectric and piezoelectric)

ε	permittivity
ε_r	relative permittivity or dielectric constant
ε_0	vacuum permittivity of free space
δ	phase difference
$tan\delta$	dissipation factor or dielectric loss factor
β	inverse of ε
d	piezoelectric charge coefficient
g	piezoelectric voltage coefficient
e, h	other piezoelectric coefficients
k	electromechanical coupling coefficients
Q	total quality factor
Q_M	mechanical quality factor
f_r	resonant frequency (piezoelectric)
f_a	anti-resonant frequency (piezoelectric)
N	frequency constant
J_0, J_1	Bessel functions
A	ageing effect constant
η	energy conversion efficiency

CHAPTER 1. INTRODUCTION

Piezoelectric materials have a long history of being widely used in sensors and actuators. Energy harvesting technology has also been studied for several decades: environmental energy is converted into useful electricity, thus solving the problems of frequently replacing/recharging batteries, providing autonomous power supplies, and making wireless sensor networks self-powered and real 'wireless'. However, the use of piezoelectricity to harvest mechanical energy, especially vibrational energy, was only formally proposed about 10 years ago. Although piezoelectric energy harvesters tend to be advantageous over other vibrational energy harvesters at the micro-scale and meso-scale, they are not fully understood in terms of material selection, dynamic behaviour and feasibility in real applications. Also, replacing currently used lead-rich materials with new lead-free materials to avoid toxicity, whilst maintaining the necessary functionality, has become an urgent issue in the piezoelectric research field.

This project was inspired by the above description, and is the pioneering work on the topic of piezoelectric energy harvesting in the Functional Materials Group of University of Birmingham. It covers broad but systematic and consecutive studies, including material fabrication and characterisation, harvester fabrication and parameter selection, electric output and dynamic behaviour testing of energy harvesters, and demonstrates the feasibility of using lead-free piezoelectric materials for energy harvesting. Thus, it provides a general view of piezoelectric energy harvesting as well as creating relevant background and an initial data base in the group.

This thesis is presented in a logical structure. Chapters 2 to 4 offer comprehensive reviews of relevant backgrounds, consisting of general energy harvesting technology (Chapter 2), principles and fabrication of piezoelectric materials (Chapter 3), as well as specific theories of piezoelectric and vibrational energy harvesting (Chapter 4). Chapter 5 summarises the aims and objectives of the project, and Chapter 6 gives the details of the implemented experiments. Chapter 7 and 8 detail the main results and discussions. Chapter 7 gathers all of the information about compositional investigations, including the fabrication and characterisation of lead-based and lead-free materials, and an exploration of routes to lower sintering temperature, though the experiments of lead-free materials were carried out after most of the work reported in Chapter 8 had been completed. Chapter 8 discusses the fabrication, modelling, optimisation and testing of piezoelectric energy harvesters, which is based on a novel structure of multi-layer free-standing thick-films. Finally, Chapter 9 concludes the entire project and gives suggestions to potential further studies.

CHAPTER 2. ENERGY HARVESTING

2.1 General Introduction

Energy, in the forms of light, heat, fluid or motion, has been serving the world since the first creature came into life. However it had never made human beings so powerful and dominant until electricity, a remarkable form of energy converted from natural resources, was discovered, controlled and effectively utilised by people[1]. Conventionally, electricity has been generated using steam-driven electromechanical generators[2] fueled by the combustion of fossil fuels, e.g. coal, oil, natural gas, etc., which had been derived by the physical and chemical transformation of dead and decayed plants and animals and stored within the earth. The formation of such resources took millions of years, however, they are being consumed so rapidly that the predicted time until fossil fuels are totally consumed is negligible compared to that of their being re-generated by nature. In another words, methods of harvesting energy more efficiently from renewable resources must be investigated to prepare for the future fossil fuel shortage. Also, the combustion of fossil fuels emits greenhouse gases which may cause a global warming problem, and sulphur/nitrogen-based oxides and particles which are able to severely pollute the atmosphere, e.g. the situation in 20th century London and New York, and today in China.

Since human beings realised the challenges of future energy shortages as well as environmental issues, various green, clean and sustainable natural sources have been considered as potential next generation energies, of which solar and wind (or fluid) are the most popular[3]. Such energy sources are promising to complete the mission of converting and generating kW to MW level power for industrial or domestic use. However, the research fields of harvesting ambient micro-energies (μW to mW), such as structural/machinery vibration, droplet/micro-fluid, radio-frequency wave, etc., which are enough for low-power consumption microelectronics, were not investigated until an experiment of using a device to harvest micro-kinetic energy was firstly implemented about 30 years ago[4], and the concept of energy harvesting (EH) was systematically proposed and reviewed in 2000's[5,6]. Undoubtedly, human life is becoming smarter, with the help of emerging sensors and micro-scale electronics. It would be preferable for wireless microelectronic devices to be able to power themselves using ambient energies existing in their working environments, rather than extract energy from mains power stations (or via the frequent replacement of batteries), in order to avoid redundant wiring or integration and improve portability, independence and durability. Although small-sized batteries have been commonly used as power supplies of microelectronic devices, the development of EH technology is still urgently required because of limited lifespan[5], relatively low power density and corresponding cumbersome size[7,8] , the risk of causing explosion or fire[9], as well as issues of costly recharging/replacing[6,8], recycling, post-processing and contamination, of current chemical batteries.

Energy harvesting, power harvesting or energy/power scavenging has been defined as a special concept of the process that environmental energy, including but not limited to heat, light, fluid, wave and kinetic energy, which otherwise will be dissipated and wasted, is harvested and converted into usable low-level electricity (μW-mW) to power wireless sensor networks[6,10,11]. The component used for harvesting and converting energy is called an energy harvester (EHer). Unlike macro-scale industrial or domestic energy generation, where electricity is usually produced in an energy-rich place then transported to end users in another place by cables or grids, devices with EH technology are normally required to obtain energy within their working environments. Thus EH systems are cable-less and battery-less with respect to their energy requirements, although sometimes energy storage media (capacitors, super-capacitors or fast charging/discharging batteries) are allowed to be used only for short-term intermediate electricity storage[8,12-14]. In another words, an ideal EH system works in a totally self-sustainable manner with unlimited lifespan, and does not need regular maintenance.

The idea of EH was initially encouraged by redundant wiring or tedious and expensive battery recharging/replacing on wireless electronic devices[6,8], such as sensors for structural/machinery health monitoring[15], medical implants[16] and other devices embedded in remote/harsh environments which are difficult and/or impossible to service or which need to work continuously for more than 10 years[5]. With the development of microelectronic hardware, the power consumption of discrete devices and systems has been decreasing to sub-watt, sub-milli-watt or even lower levels[8,17,18]. This makes the ambition of creating autonomous electronic systems powered by ambient energy practical. Conventionally, such devices have been powered by small-sized batteries with capacities of hundreds or thousands of mAh. However, batteries are not the perfect power supplies for the systems outlined above, mainly because of their power densities over long periods of time[5]. Firstly, as the stored electricity within a fully charged battery is finite, the length of time it could keep powering a device is also finite, following which its capability to provide electrical energy would be zero. However, in principle, an EHer is able to provide infinite electricity since it obtains energy from the environment whose capacity and stored energy could be treated as unlimited. For example, comparing thermal energy, vibration energy and lithium batteries, the power densities for a one year lifetimes have been predicted as 15, 250 and 45 μW/cm^3, respectively[5]. In this situation, the battery performance is acceptable, at least much better than thermal energy. However, if the lifespan was required to be 10 years, the power densities of the environmental sources, thermal energy and vibration energy, can be considered constant, while that of lithium battery has been predicted to drop to only 3.5 μW/cm^3, much lower than the others[5]. In this scenario, to provide 1 mW power to a device, a vibration EHer would only need a volume of 4 cm^3, however a lithium battery would have to be 286 cm^3. Such a size would definitely make a microelectronic device cumbersome. Secondly, even a rechargeable battery is not able to make a device really 'wireless', because recharging needs connection to mains power with cables and/or some form of manual operation. If a device was implanted in a human or animal body, battery recharging or replacing would need additional surgery, which would cause discomfort to the patient and be very expensive; if a sensor was embedded in the structure of a bridge/building/vehicle/aircraft, regular and expensive maintenance would need to be done if it was powered by batteries; and if a monitoring system was mounted underground or in the wild and would not be touched for more than 10 years, it would be impossible for batteries to last for such a long time and still be able to power up the host. Besides, batteries would sometimes die without warning[6], or would cause explosion or fire[9], which would affect the performance or even destroy a device. However, EH technology is promising to solve all of the above issues.

2.2 Micro-energy Harvesting

2.2.1 Solar Energy and Photovoltaics

Photovoltaic technology is able to directly convert solar energy into electricity by the photovoltaic effect of semicondoctor materials[19]. It has been rapidly developed and commercialised during recent decades. The advantages of this technology involve large power density (>10 mW/cm^3) under sufficient outdoor sunlight[5,14], easy integration with host structures[20], and steady working status without noise or emmisions[20]. However, certain limitations still remain: (1) the variation of light intensity (e.g. in indoor evironment or murky weather) is likely to significantly reduce its efficiency; (2) the requirement of a large surface area may limit its application in micro-electromechanical systems (MEMS), as sizes at the micro-scale mean surfaces are extremely small[9]. In general, photovoltaic technology has undoubtedly become one of the dominant electricity generation methods for mains power stations (about 1 % of global electricity production) or large energy consumption devices.

2.2.2 Wind Energy and Wind Turbines

Wind turbines are able to convert wind energy into electricity, where the wind causes a rotor to rotate, thus driving an electrical generator[21]. Wind is also an attractive green and renewable resource. Similar to solar energy, wind energy is also ubiquitous. In the current state of the art, a wind farm, which properly combines a certain number of wind turbines, is able to provide kW to MW power levels, depending on the size[22]. However, what hinders this technology to be the top-ranking energy generation method may be the principle limit of energy conversion efficiency, about 59%, which is known as 'Betz limit'[23]. Considering further energy loss caused by mechanical friction and generator dissipation, the overall energy conversion efficiency of a wind turbine tends to be as low as 39 % (20 % when taking into account wind velocity)[24]. Although the efficiency of a photovoltaic panel could be up to 39 % (46 % with solar concentrator)[25], which is slightly better than that of a wind turbine, solar energy is considered more steady and reliable than wind. Also, for the application of powering MEMS devices where the space is limited, conventional wind turbines may suffer mechanical design difficulties[26]. This is likely to keep deteriorating the efficiency. In order to overcome such difficulties, other configurations such as piezoelectric energy harvesters could be introduced and combined with wind-driven configurations such as free-spinning fans[26]. Further details on this concept will be given in Chapter 4. In spite of the disadvantages, wind turbines are still promising to form supplementary power stations, especially for areas which experience windy conditions throughout the year.

2.2.3 Thermal Energy Harvesting

Thermal energy exists in heat flow (or temperature gradient), e.g. geothermal energy[27], machine/vehicle waste heat[28], temperature difference between human body/skin and atmosphere[29], etc. Unlike solar and wind energy, which mainly rely on single energy conversion principles, thermal energy could be harvested and converted through several effects, such as thermoelectric[30], pyroelectric[31], thermo-electrochemical[32], ferromagnetic[33], piezoelectric[34], etc., by properly designing EHer configurations.

The thermoelectric effect, or 'Seebeck effect'[35], has been a typical way to generate electricity from thermal energy during the past decades[36]. Thermoelectric materials usually hold charge carriers (electrons or holes), and such carriers are able to diffuse from hot parts to cold parts of the material to create an internal electric potential[36]. Conventionally, a thermoelectric EH cell consists of a pair of n-type and p-type semiconductors connected in series and placed between hot surface and cold surface[37], working reliably with little noise and emissions[20]. However, this design has been judged as inefficient because of the low Seebeck coefficients of current thermoelectric materials, especially in small temperature gradients (<10 °C) and small-scale devices (<1 cm^3)[20,38]. As a result, recent research has put more efforts into nano-structured bulk[39] or thin-film[40] thermoelectric materials. These novel forms of materials are promising to significantly enhance the performance of thermoelectric conversion[28,40].

Other than thermoelectric generators, researchers have also been seeking other possible thermal energy conversion methods. Thermo-electrochemical cell (or thermocell)[32] is another way to provide direct thermal-to-electric conversion, by creating redox ions and a resulting electric potential within a material between hot and cold sides[32]. Similar to thermoelectric converters, thermocells have also been struggling with low efficiency as well as costly electrode materials[27]. To cope with this issue, carbon-nanotube-based thermocells have been investigated to explore the possibility of improved efficiency and cost-effective structures[27].

The pyroelectric effect, which has been widely used in sensors[41-43] but rarely used as EHers, is also possible to convert thermal energy. The pyroelectric effect can be exhibited by piezoelectric materials when experiencing temperature variations[44]. More electric charges can be accumulated with larger temperature difference[31]. As harvester designs using pyroelectric materials, or combining ferromagnetic materials, are related to the integration of piezoelectric materials, which is the main topic of this thesis, more details will be presented in Chapter 4 together with piezoelectric EHers. Other novel designs include configurations which actually transfer thermal energy into mechanical motional energy firstly (e.g. by large temperature-induced deforming metals[45]), then convert mechanical energy into electricity by a mechanical EHers.

2.2.4 Kinetic (vibration/motion) Energy Harvesting

In principle, kinetic energy is everywhere since not only do the internal chemical or physical activities of the earth vibrate any macro-objects sitting on it, but even the microstructures (molecules, atoms and electrons) of objects keep vibrating. However, usable kinetic energy (or mechanical energy), which could be effectively harvested and converted into micro-scale electricity, usually exists together with a host, e.g. building/construction vibrating at eigenfrequency (natural resonant frequency)[46], machinery in motion[15], or the human body in daily activities or sports[47], etc.

Human or other biological activities have been considered attractive energy sources for wearable smart devices[48]. Such activities are able to generate much more energy than previously thought, enough to power some electronics if efficiently harvested[49]. The first publication regarding scavenging biological motion energy may be the integration of an EH system with the ribs of an animal[4], which generated 17 μW peak power. Although such power was not able to be practically utilised at that time[6], the idea has encouraged huge amount of research to investigate the possibility and feasibility of using biological motion energy, especially human motion, to power future wearable or implantable devices. Representative proposals or developments to date include shoe-mounted generators in the heel or sole[50-52], medical implants powered by blood pressure/heartbeats[16,53,54], knee replacement unit with self-powered sensors[55,56], wearable EHer harvesting wrist and arm motion during walking[57,58], EHer embedded in backpack shoulder straps[59,60] and other wearable or implantable designs[48,61].

Compared to human motion, the emphasis in harvesting vibrational energy on vehicles, machines or constructions, as well as its harvester itself, has been delayed nearly 20 years in terms of potential applications[5]. One of the reasons that such energy and harvester have drawn much attention recently may be that a large number of buildings and machines have been being constructed and manufactured, and people have become more dependent on them. Thus their working conditions should be fully monitored in case of any hidden or potential damage that could put residents or users at risk[62]. However, power supplies would be a large expense for these monitoring systems because of the reasons presented above. Harvesting vibration energy dissipated from the host structure of a machine or construction could not only solve the issue of tedious/expensive battery recharging/replacing, but also help to reduce energy waste and improve the main energy usage efficiency of the host. In the current state of the art, many novel EHers for powering certain monitoring systems have been reported, including those for asphalt pavement[63], oil pump[15], vehicle suspension[64], bridge[62], vehicle tyre[65], railway and train[66,67], aircraft and spacecraft[68], and others related to traffic and structures[69-71].

In order to harvest and convert kinetic energy, both conventional and novel EHers have been investigated, among which electrostatic-, electromagnetic-, piezoelectric-, and electrostrictive type EHers have been considered most suitable and promising, and thus their research have dominated the EH field[5,72,73]. All of these harvesters could be classified as inertial generators with functional parts attached to fixed bases[72]. The fixed bases transmit vibrations to suspended inertial masses mounted with the functional parts, inducing relative displacements[72]. This configuration could be generally modelled or simply treated as a spring-mass system[74], where the spring is vertically fixed on a vibrating platform whilst the mass is attached to the top of the spring. However, the working principles of the functional parts of different types of harvesters are based on different electromechanical conversion effects. For electrostatic EHer (EEHer), two electrodes (positive and negative) of a charged capacitor move relatively under vibration thus the capacitance varies and produce a charge flow[5,72]. Electromagnetic EHer (EMEHer) is a conventional technology being used in dynamos for macro-scale electricity generation, where a magnetic flux gradient (normally produced by a permanent magnet) and a conductor (normally a set of coils) move relatively to induce current flow in the conductor[5,72]. Piezoelectric EHer (PEHer) employs several pieces of functional/active piezoelectric materials, and deformations of such materials are able to generate electric potentials or charge flows[5,72]. Electrostrictive EHer (ESEHer) combines a dielectric material (could be polymer or ceramic according to published reports to date) and a bias DC electric field which induces polarizations within the dielectric material, working as a pseudo-PEHer[75,76].

In general, the capacitive gaps of EEHers could be at sub-micron level, and hence they could be easily fabricated into micro-scale and integrated with micro-systems[77], providing nW to µW power[72]. However, external voltage sources would be necessary to maintain the status of capacitors[5], which is likely to increase the complexity of the system. EMEHers and PEHers do not need any external source thus they are completely self-sustainable. According to the data of a large number of publications[20,72,78,79], these two kinds of harvesters have similar levels of energy conversion ability, although some reports describe PEHers as having higher power density[8] while others report EMEHers as having better maximum power generation ability[80]. However, EMEHers are more suitable for larger-scale EH where devices and power supplies could be large[80,81], generating mW or larger power[72]; PEHers suit all physical size levels ranging from electrostatic-level to electromagnetic-level[80] corresponding to nW to mW power generation levels, can be structurally simpler[72], and can generate higher voltage[81] than EMEHers. Compared to the above three kinds of harvesters which can be treated as 'relatively conventional' kinetic EHers, ESEHers based on polymer dielectrics have begun to receive industrial and research attention in recent years[73], due to high productivity and processability[73], as well as high flexibility which overcomes the disadvantages of ceramic-based PEHers or ESEHers[75]. However, similar to EEHers, an external bias electric field is needed, which is likely to affect the sustainability because of the lifespan of electric field provider. Further details about PEHers including fundamentals and advantages/disadvantages will be given in Chapter 4.

2.2.5 Electromagnetic Wave Energy Harvesting and Others

Nowadays people are exposed in pervasive electromagnetic (EM) waves including radio-frequency (RF) waves emitted by wireless communication devices (GHz level)[82], broadcast waves, power line dissipated waves[83] and other environmental electromagnetic waves (MHz level). Such kind of energy has also provided an opportunity to power micro-scale electronics. Harvesting and converting EM waves requires antenna or rectenna[82] with various dimensions in order to match different wave-lengths[83]. In addition, EM wave EH may benefit where other kinds of energy sources are unavailable. However, only nW-level power can be generated[14] and the efficiency depends on input energy and stays at an average low level[84].

Radioactive materials are another potential energy source for EH because of their extremely high energy density[14]. Although the half-lifes of some such materials can be centuries, their usage causes safety concerns and is a barrier for public acceptance[24]. Converting this energy needs the help of combination with piezoelectric or betavoltaic components[14], of which the combination with piezoelectric component will be introduced in Chapter 4.

Finally, some other potential micro-energy sources could also be considered, e.g. energy within marine sediments which could be harvested by miro-organisms[85], energy that could be extracted from biologic battery in inner ears[86], acoustic energy[87], etc., though they either have been rarely investigated or are too far away from real applications.

2.3 Summary

This chapter has given a broad and general review of the topic of energy harvesting. The importance of energy harvesting in low power devices has attracted a lot of attention over the last two decades, however research has been spread over a wide range of harvesting technologies and application environments. Certain environments may need several energy harvesting technologies to be fitted, in order to efficiently utilise various available environmental energy sources. Whereas, certain energy harvesting technologies are able to convert different energy sources, and can therefore be used in different environments. In this project, piezoelectric energy harvesting was selected for further investigation due to its good compatibility with various energy sources. The following chapters will review piezoelectricity, piezoelectric materials and their applications for energy harvesting.

References

1 Jones, D. A. Electrical engineering - the backbone of society. *IEEE Proceedings-A-Science Measurement and Technology* **138**, 1-10 (1991).

2 McLaren, P. G. Elementary electric power and machines. *Ellis Horwood: England*, pp. 182-183 (1984).

3 Carrasco, J. M., Franquelo, L. G., Bialasiewicz, J. T. *et al.* Power-electronic systems for the grid integration of renewable energy sources: A survey. *IEEE Transactions on Industrial Electronics* **53**, 1002-1016 (2006).

4 Hausler, E., Stein, L. and Harbauer, G. Implantable physiological power supply with PVDF film. *Ferroelectrics* **60**, 277-282 (1984).

5 Roundy, S., Wright, P. K. and Rabaey, J. A study of low level vibrations as a power source for wireless sensor nodes. *Computer Communications* **26**, 1131-1144 (2003).

6 Sodano, H. A., Inman, D. J. and Park, G. A review of power harvesting from vibration using piezoelectric materials. *Shock and Vibration Digest* **36**, 197-205 (2004).

7 Minazara, E., Vasic, D., Costa, F. and Poulin, G. Piezoelectric diaphragm for vibration energy harvesting. *Ultrasonics* **44**, E699-E703 (2006).

8 Priya, S. Advances in energy harvesting using low profile piezoelectric transducers. *Journal of Electroceramics* **19**, 167-184 (2007).

9 Zhang, L., Williams, K. A. and Xie, Z. C. Development and Validation of an Enhanced Coupled-Field Model for PZT Cantilever Bimorph Energy Harvester. *Mathematical Problems in Engineering* **2013**, 980161 (2013).

10 Anton, S. R. and Sodano, H. A. A review of power harvesting using piezoelectric materials (2003-2006). *Smart Materials & Structures* **16**, R1-R21 (2007).

11 Edler, F. and Lenz, E. Metrology for energy harvesting. *9th European Conference on Thermoelectrics, AIP Conference Proceedings* (eds K. M. Paraskevopoulos and E. Hatzikraniotis) **1449**, 369-372 (2012).

12 Ayers, J. P., Greve, D. W. and Oppenheim, I. J. Energy scavenging for sensor applications using structural strains. *Smart Structures and Materials 2003: Smart Systems and Nondestructive Evaluation for Civil Infrastructures, Proceedings of the Society of Photo-Optical Instrumentation Engineers (Spie)* (ed S. C. Liu) **5057**, 364-375 (2003).

13 Guan, M. J. and Liao, W. H. Characteristics of energy storage devices in piezoelectric energy harvesting systems. *Journal of Intelligent Material Systems and Structures* **19**, 671-680 (2008).

14 Penella, M. T., and Gasulla, M. A review of commercial energy harvestings for autonomous sensors. *IEEE Instrumentation & Measurement Technology Conference, Proceedings* **1-5**, 1807-1811 (2007).

15 du Plessis, A. J., Huigsloot, M. J. and Discenzo, F. D. Resonant packaged piezoelectric power harvester for machinery health monitoring. *Smart Structures and Materials 2005: Industrial and Commercial Applications of Smart Structures Technologies*, *Proceedings of the Society of Photo-Optical Instrumentation Engineers (Spie)* (ed E. V. White) **5762**, 224-235 (2005).

16 Sohn, J. W., Choi, S. B. and Lee, D. Y. An investigation on piezoelectric energy harvesting for MEMS power sources. *Proceedings of the Institution of Mechanical Engineers Part C-Journal of Mechanical Engineering Science* **219**, 429-436 (2005).

17 Chandrakasan, A., Amirtharajah, R., Goodman, J. and Rabiner, W. Trends in low power digital signal processing. *Proceedings of the 1998 International Symposium on Circuits and Systems* **1-6**, C604-C607 (1998).

18 Davis, W. R., Zhang, N., Camera, K. *et al.* A design environment for high throughput, low power dedicated signal processing systems. *Proceedings of the IEEE 2001 Custom Integrated Circuits Conference* 545-548 (2001).

19 McEvoy, A., Markvart, T. and Castaner, L. Practical handbook of photovoltaics: fundamentals and applications. *Elsevier: New York*, pp. 72-74 (2003).

20 Cook-Chennault, K. A., Thambi, N. and Sastry, A. M. Powering MEMS portable devices - a review of non-regenerative and regenerative power supply systems with special emphasis on piezoelectric energy harvesting systems. *Smart Materials & Structures* **17**,043001 (2008).

21 Maalawi, K. Wind turbines (edited by Al-Bahadly I.). *InTech* **Cahper 1**, pp. 1-2 (2011).

22 Mostafaeipour, A. Wind turbines (edited by Al-Bahadly I.). *InTech* **Chapter 2**, pp. 27-28 (2011).

23 Hau, E. Wind turbines (2nd edition). *Springer: Germany*, pp. 86 (2006).

24 Knight, C., Davidson, J. and Behrens, S. Energy Options for Wireless Sensor Nodes. *Sensors* **8**, 8037-8066 (2008).

25 www.nrel.gov/ncpv [online access] 04/04/2015.

26 Myers, R., Vickers, M., Kim, H. and Priya, S. Small scale windmill. *Applied Physics Letters* **90**, 054106 (2007).

27 Hu, R. C., Cola, B. A., Haram, N. *et al.* Harvesting Waste Thermal Energy Using Carbon-Nanotube-Based Thermo-Electrochemical Cell. *Nano Letters* **10**, 838-846 (2010).

28 Martin-Gonzalez, M., Caballero-Calero, O. and Diaz-Chao, P. Nanoengineering thermoelectrics for 21st century: Energy harvesting and other trends in the field. *Renewable & Sustainable Energy Reviews* **24**, 288-305 (2013).

29 Leonov, V. Thermoelectric energy harvesting of human body heat for wearable sensors. *IEEE Sensors Journal* **13**, 2284-2291 (2013).

30 Tritt, T. M. and Subramanian, M. A. Thermoelectric materials, phenomena, and applications: A bird's eye view. *Mrs Bulletin* **31**, 188-194 (2006).

31 Cuadras, A., Gasulla, M. and Ferrari, V. Thermal energy harvesting through pyroelectricity. *Sensors and Actuators A-Physical* **158**, 132-139 (2010).

32 Ikeshoji, T. and Ratkje, S. K. Energy conversion in thermocells: Efficiency calculations. *Journal of the Electrochemical Society* **137**, 1193-1194 (1990).

33 Ujihara, M., Carman, G. P. and Lee, D. G. Thermal energy harvesting device using ferromagnetic materials. *Applied Physics Letters* **91**, 093508 (2007).

34 Smoker, J., Nouh, M., Aldraihem, O. and Baz, A. Energy harvesting from a standing wave thermoacoustic-piezoelectric resonator. *Journal of Applied Physics* **111**, 104901 (2012).

35 Uchida, K., Takahashi, S., Harii, K. *et al.* Observation of the spin: Seebeck effect. *Nature* **455**, 778-781 (2008).

36 Chen, G., Dresselhaus, M. S., Dresselhaus, G., Fleurial, J. P. and Caillat, T. Recent developments in thermoelectric materials. *International Materials Reviews* **48**, 45-66 (2003).

37 Chen, M., Lu, S.-S. and Liao, B. On the figure of merit of thermoelectric generators. *Journal of Energy Resources Technology, Transactions of the ASME* **127**, 37-41 (2005).

38 Chen, J., Yan, Z. and Wu, L. Influence of Thomson effect on the maximum power output and maximum efficiency of a thermoelectric generator. *Journal of Applied Physics* **79**, 8823-8823 (1996).

39 Wang, Z. L. and Wu, W. Z. Nanotechnology-enabled energy harvesting for self-powered micro-/nanosystems. *Angewandte Chemie-International Edition* **51**, 11700-11721 (2012).

40 Choday, S. H., Lu, C., Raghunathan, V. and Roy, K. *Twenty Ninth Annual IEEE Semiconductor Thermal Measurement and Management Symposium*, *Proceedings IEEE Semiconductor Thermal Measurement and Management Symposium* 99-104 (2013).

41 Buchanan, R. C. and Huang, J. Pyroelectric and sensor properties of ferroelectric thin films for energy conversion. *Journal of the European Ceramic Society* **19**, 1467-1471 (1999).

42 Capineri, L., Masotti, L., Ferrari, V. *et al.* Comparisons between PZT and PVDF thick films technologies in the design of low-cost pyroelectric sensors. *Review of Scientific Instruments* **75**, 4906-4910 (2004).

43 Ferrari, V., Ghisla, A., Marioli, D. and Taroni, A. Array of PZT pyroelectric thick-film sensors for contactless measurement of XY position. *IEEE Sensors Journal* **3**, 212-217 (2003).

44 Moulson, A. J. and Herbert, J. M. Electroceramics: Materials, properties and applications. *Chapman & Hall: London*, pp. 318-319 (1990).

45 Boisseau, S., Despesse, G., Monfray, S., Puscasu, O. and Skotnicki, T. Semi-flexible bimetal-based thermal energy harvesters. *Smart Materials and Structures* **22**, 025021(2013).

46 Xie, X. D., Wu, N., Yuen, K. V. and Wang, Q. Energy harvesting from high-rise buildings by a piezoelectric coupled cantilever with a proof mass. *International Journal of Engineering Science* **72**, 98-106 (2013).

47 Haddad, S. A. P., Houben, R. P. M. and Serdijn, W. A. The evolution of pacemakers. *IEEE Engineering in Medicine and Biology Magazine* **25**, 38-48 (2006).

48 Wu, W. W., Bai, S., Yuan, M. M. *et al.* Lead zirconate titanate nanowire textile nanogenerator for wearable energy-harvesting and self-powered devices. *Acs Nano* **6**, 6231-6235 (2012).

49 Sue, C. Y. and Tsai, N. C. Human powered MEMS-based energy harvest devices. *Applied Energy* **93**, 390-403 (2012).

50 Kymissis, J., Kendall, C., Paradiso, J. and Gershenfeld, N. Parasitic power harvesting in shoes. *2nd International Symposium on Wearable Computers - Digest of Papers* 132-139(1998).

51 Shenck, N. S. and Paradiso, J. A. Energy scavenging with shoe-mounted piezoelectrics. *IEEE Micro* **21**, 30-42 (2001).

52 Klimiec, E., Zaraska, K., Zaraska, W. and Kuczynski, S. Micropower generators and sensors based on piezoelectric polypropylene PP and polyvinylidene fluoride PVDF films - energy harvesting from walking. *Mechanical and Aerospace Engineering, Applied Mechanics and Materials* (ed W. Fan) **1-7**, 1245-1251 (2012).

53 Liu, W. T., Cheng, X. Y., Fu, X., Stefanini, C. and Dario, P. Preliminary study on development of PVDF nanofiber based energy harvesting device for an artery microrobot. *Microelectronic Engineering* **88**, 2251-2254 (2011).

54 Rivera, A., Edington, A., Zeller, J. and Anwar, M. Energy scavenging using ZnO nanorods grown on flexible substrates. *2012 Lester Eastman Conference on High Performance Devices, Proceedings IEEE Lester Eastman Conference on High Performance Devices* (2012).

55 Platt, S. R., Farritor, S. and Haider, H. On low-frequency electric power generation with PZT ceramics. *IEEE - Asme Transactions on Mechatronics* **10**, 240-252 (2005).

56 Pozzi, M. and Zhu, M. L. Plucked piezoelectric bimorphs for knee-joint energy harvesting: modelling and experimental validation. *Smart Materials & Structures* **20**, 055007 (2011).

57 Renaud, M., Sterken, T. and Fiorini, P. *et al.* Scavenging energy from human body: Design of a piezoelectric transducer. *Transducers '05, Digest of Technical Papers* **1-2**, 784-787 (2005).

58 Sun, K., Liu, G. Q. and Xu, X. Y. Nonlinear resonant generator for harvesting energy from human wrist vertical shaking. *Measuring Technology and Mechatronics Automation Iv, Applied Mechanics and Materials* (ed Z. X. Hou) **1-2**, 923-927 (2012).

59 Granstrom, J., Feenstra, J., Sodano, H. A. and Farinholt, K. Energy harvesting from a backpack instrumented with piezoelectric shoulder straps. *Smart Materials & Structures* **16**, 1810-1820 (2007).

60 Papatheou, E., Green, P., Racic, V., Brownjohn, J. M. W. and Sims, N. D. A short investigation of the effect of an energy harvesting backpack on the human gait. *Active and Passive Smart Structures and Integrated Systems 2012, Proceedings of SPIE* (ed H. A. Sodano) **8341**, 83410F (2012).

61 Xie, L. H. and Du, R. X. Harvest human kinetic energy to power portable electronics. *Journal of Mechanical Science and Technology* **26**, 2005-2008 (2012).

62 Reichenbach, M., Fasl, J., Samaras, V. A. *et al.* Evaluatin vehicular-induced bridge vibrations for energy harvesting applications. *Nondestructive Characterization for Composite Materials, Aerospace Engineering, Civil Infrastructure, and Homeland Security 2012, Proceedings of SPIE* (eds A. L. Gyekenyesi *et al.*) **8347**, 83472E (2012).

63 Zhao, H. D., Ling, J. M. and Yu, J. A comparative analysis of piezoelectric transducers for harvesting energy from asphalt pavement. *Journal of the Ceramic Society of Japan* **120**, 317-323 (2012).

64 Tang, X. D. and Zuo, L. Vibration energy harvesting from random force and motion excitations. *Smart Materials and Structures* **21**, 075025 (2012).

65 Singh, K. B., Bedekar, V., Taheri, S. and Priya, S. Piezoelectric vibration energy harvesting system with an adaptive frequency tuning mechanism for intelligent tires. *Mechatronics* **22**, 970-988 (2012).

66 Song, D., Yang, C. H., Hong, S. K. *et al.* Feasibility study on application of piezoelectricity to convert vibrations of Korea train express. *2012 International Symposium on Applications of Ferroelectrics Held Jointly with 11th Ieee Ecapd and Ieee Pfm, IEEE International Symposium on Applications of Ferroelectrics* (2012).

67 De Pasquale, G., Soma, A. and Fraccarollo, F. Piezoelectric energy harvesting for autonomous sensors network on safety-improved railway vehicles. *Proceedings of the Institution of Mechanical Engineers Part C-Journal of Mechanical Engineering Science* **226**, 1107-1117 (2012).

68 Pearson, M. R., Eaton, M. J., Pullin, R. *et al.* Energy harvesting for aerospace structural health monitoring systems. *Modern Practice in Stress and Vibration Analysis 2012, Journal of Physics Conference Series* **382**, 012025 (2012).

69 Pirisi, A., Grimaccia, F., Mussetta, M. and Zich, R. E. An Evolutionary Optimized Device for Energy Harvesting from Traffic. *2012 IEEE Congress on Evolutionary Computation* (2012).

70 Messineo, A., Alaimo, A., Denaro, M. and Ticali, D. Piezoelectric bender transducers for energy harvesting applications. *2011 2nd International Conference on Advances in Energy Engineering, Energy Procedia* (ed D. Zeng) **24**, 39-44 (2012).

71 Li, J. C., Jang, S. and Tang, J. Modeling and analysis of a bimorph piezoelectric energy harvester for railway bridge health monitoring. *Health Monitoring of Structural and Biological Systems 2012, Proceedings of SPIE* (ed T. Kundu) **8348**, 823827 (2012).

72 Beeby, S. P., Tudor, M. J. and White, N. M. Energy harvesting vibration sources for microsystems applications. *Measurement Science & Technology* **17**, R175-R195 (2006).

73 Lallart, M., Cottinet, P. J., Lebrun, L., Guiffard, B. and Guyomar, D. Evaluation of energy harvesting performance of electrostrictive polymer and carbon-filled terpolymer composites. *Journal of Applied Physics* **108**, 034901 (2010).

74 Williams, C. B. and Yates, R. B. Analysis of a micro-electric generator for microsystems. *Sensors and Actuators A-Physical* **52**, 8-11 (1996).

75 Cottinet, P. J., Lallart, M., Guyomar, D. *et al.* Analysis of AC-DC conversion for energy harvesting using an electrostrictive polymer P(VDF-TrFE-CFE). *IEEE Transactions on Ultrasonics Ferroelectrics and Frequency Control* **58**, 30-42 (2011).

76 Huang, H. L., Li, G. R., Huang, L. Z. *et al.* Energy harvesting using multilayer structure based on La-doped PMN-PT electrostrictive ceramics. *Physica Status Solidi a-Applications and Materials Science* **209**, 1965-1971 (2012).

77 Roundy, S., Leland, E. S., Baker, J. *et al.* Improving power output for vibration-based energy scavengers. *IEEE Pervasive Computing* **4**, 28-36 (2005).

78 Mitcheson, P. D., Yeatman, E. M., Rao, G. K., Holmes, A. S. and Green, T. C. Energy harvesting from human and machine motion for wireless electronic devices. *Proceedings of the IEEE* **96**, 1457-1486 (2008).

79 Kim, H. U., Lee, W. H., Dias, H. V. R. and Priya, S. Piezoelectric microgenerators-current status and challenges. *IEEE Transactions on Ultrasonics Ferroelectrics and Frequency Control* **56**, 1555-1568 (2009).

80 Sterken, T., Baert, K., van Hoof, C. *et al.* Comparative modelling for vibration scavengers. *Proceedings of the IEEE Sensors 2004, IEEE Sensors* (eds D. Rocha, P. M. Sarro, & M. J. Vellekoop) **1-3**, 1249-1252 (2004).

81 Wang, L. and Yuan, F. G. Vibration energy harvesting by magnetostrictive material. *Smart Materials and Structures* **17**, 045009 (2008).

82 Zhao, W., Choi, K., Bauman, S. *et al.* A radio-frequency energy harvesting scheme for use in low-power ad hoc distributed networks. *IEEE Transactions on Circuits and Systems Ii-Express Briefs* **59**, 573-577 (2012).

83 Hwang, J. H., Kang, T. W., Hyoung, C. H. and Kang, S. W. *2012 IEEE Antennas and Propagation Society International Symposium* (2012).

84 Hagerty, J. A., Helmbrecht, F. B., McCalpin, W. H., Zane, R. and Popovic, Z. B. Recycling ambient microwave energy with broad-band rectenna arrays. *IEEE Transactions on Microwave Theory and Techniques* **52**, 1014-1024 (2004).

85 Bond, D. R., Holmes, D. E., Tender, L. M. and Lovley, D. R. Electrode-reducing microorganisms that harvest energy from marine sediments. *Science* **295**, 483-485 (2002).

86 Mercier, P. P., Lysaght, A. C., Bandyopadhyay, S., Chandrakasan, A. P. and Stankovic, K. M. Energy extraction from the biologic battery in the inner ear. *Nature Biotechnology* **30**, 1240-1243 (2012).

87 Que, R. H., Shao, Q., Li, Q. L. *et al.* Flexible nanogenerators based on graphene oxide films for acoustic energy harvesting. *Angewandte Chemie-International Edition* **51**, 5418-5422 (2012).

CHAPTER 3. PIEZOELECTRIC MATERIALS

3.1 Ferroelectricity and Piezoelectricity

To date, it has been found that among the 32 classes of crystal point groups, 21 possess non-centrosymmetric unit cell structures, of which 20 have potentials to exhibit the piezoelectric effect[1]. This is a phenomenon that charge displacement (or electric potential) will be generated across the material when it is strained under applied force (defined as direct piezoelectric effect), while strain of the material will be induced when it is placed in external electric field (defined as converse piezoelectric effect)[2]. Figure 3-1 explains the piezoelectric effect.

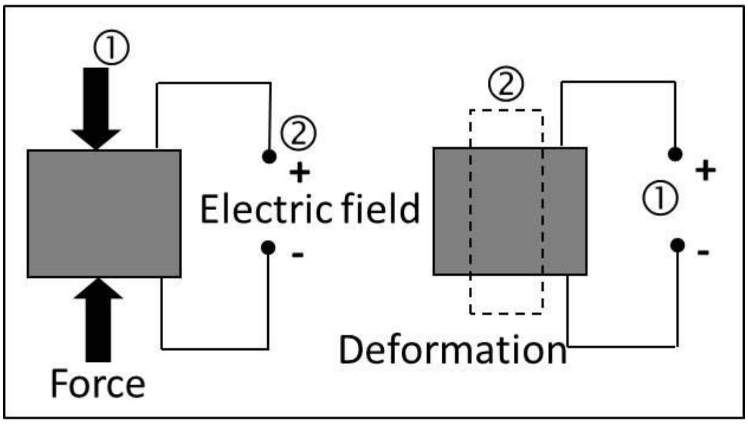

Figure 3-1. Schematic explanation of the piezoelectric effect.

Of the 20 piezoelectric crystal classes, 10 are said to be ‘ferroelectric’, as in their unit cells two or more spontaneous polarization orientation states are allowed without an external electric field but can be shifted between each other by an external electric field. Such a phenomenon is known as ‘ferroelectricity’[2]. The area in which spontaneous polarizations stay along the same direction is defined as a ‘domain’, whilst the boundary area between domains is called ‘domain wall’[3]. In a polycrystalline, domains are randomly arranged thus a piece of ferroelectric material does not exhibit piezoelectricity. But via a poling process (based on the behaviour of ferroelectricity), the domains will be forced to rotate and align along the direction of the field[3], thus giving a piezoelectricity.

The discovery of piezoelectricity dates back to 1880, when Jacques and Pierre Curie were working on crystals including quartz, Rochelle salt (potassium sodium tartrate) and tourmaline[4]. However, piezoelectric materials had not been actually used until Barium Titanate ($BaTiO_3$) ceramics were investigated, since before then piezoelectric materials were limited to single crystals and they were either easily soluble in water or only operated at ultra-low temperatures (< -100 °C), which prevented their application[5]. The discovery of $BaTiO_3$ ferroelectric ceramics was a milestone of piezoelectric materials development. The unit cell of $BaTiO_3$ is classified as the 'perovskite' structure (ABO_3), where 8 barium ions (Ba^{2+}) occupy the 8 corners of a cube (A site), 6 oxygen ions (O^{2-}) possess the 6 face centre positions and 1 titanium ion (Ti^{4+}) takes the body centre position (B site)[5], shown in Figure 3-2 (a). Above the Curie temperature (T_c), the unit cell has cubic symmetry where the centres of the positive and negative charges are coincident and thus no dipole moment exists. However, when the temperature drops below T_c, there is a relative shift between the O^{2-} octahedra and the Ba^{2+}/Ti^{4+} ions, destroying the cubic symmetry and resulting in a spontaneous polarization. The relative shift can produce various non-cubic perovskite phases depending on the distortion directions, including tetragonal, orthorhombic and rhombohedral, where temperature and ionic size are the driving forces to determine which exact phase will be generated[5,6]. Figure 3-2 (b) shows an example of a tetragonal perovskite structure.

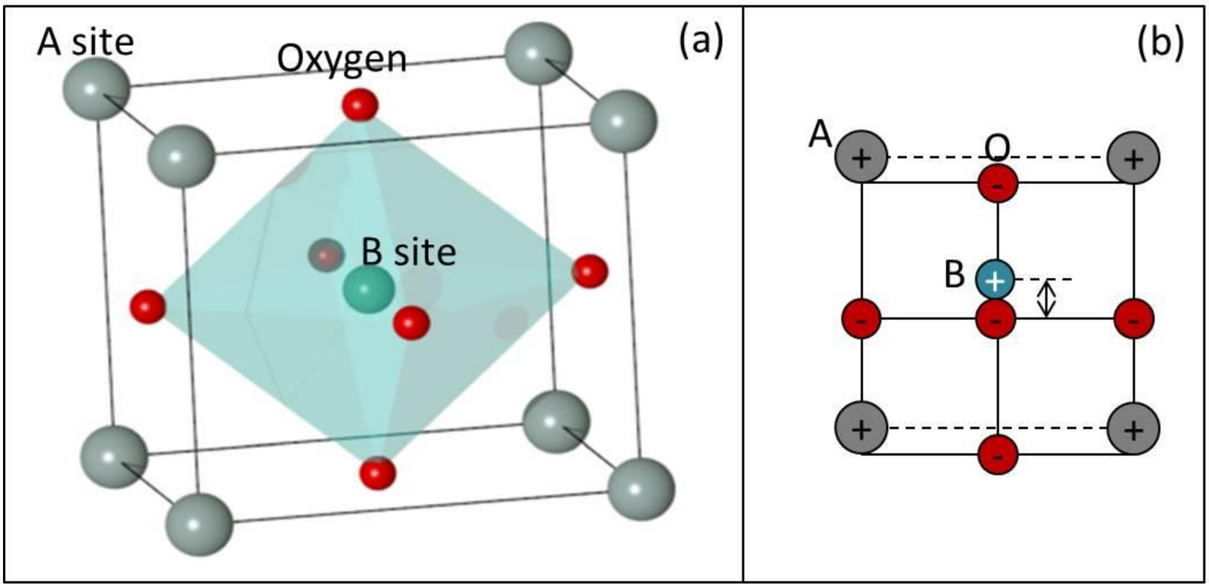

Figure 3-2. Schematics of a perovskite structure: (a) a cubic phase above T_c[6]; (b) side-view of a tetragonal phase below T_c.

In theory, other ions are able to replace Ba^{2+} or Ti^{4+} but still retain the overall perovskite structure. Equation 3-1[5,6] defines the tolerance factor (*tol.*) and indicates the requirements and relations of site A, B ions and oxygen ion, where r_A, r_B and r_O represent the radii of A, B site ions and oxygen ion, respectively, assuming the ions to be perfect spheres. For cubic perovskite phases, *tol.*=1, while 0.9<*tol.*<1.1 must be ensured in order to make other non-cubic perovskite phases stable[5,6]. This has provided a guide for exploring more perovskite piezoelectrics.

$$tol. = \frac{r_A + r_O}{\sqrt{2} \cdot (r_B + r_O)} \quad (3\text{-}1)$$

3.2 Properties and Relevant Parameters of Piezoelectric Materials

3.2.1 Definitions of Effective Directions

Before understanding piezoelectric properties, specific directions must be defined, as polarised piezoelectric materials do not perform the same with isotropic and anisotropic structures. Figure 3-3 shows the commonly accepted convention relating to piezoelectric materials. The poling axis is usually defined as the '3' direction, with the two orthogonal directions labelled as the '1' and '2' directions. The '4', '5' and '6' directions indicate rotations around the '1', '2' and '3' axes, respectively, thus representing shear. For piezoelectric materials, the properties along '1' and '2' are normally the same but different from those of '3'. The defined directions are normally notated with certain parameters, where two numbers are inserted as subscripts, first of which represents the input direction (stress or electric field), whilst the second matches the response direction. For example, parameter M_{31} is interpreted as material property M determined by the stress along '3' inducing charge displacement along '1' for the direct piezoelectric effect, or by the external electric field along '3' causing strain along '1' for converse piezoelectric effect. The parameters with the same root but different direction pairs possess various values[7].

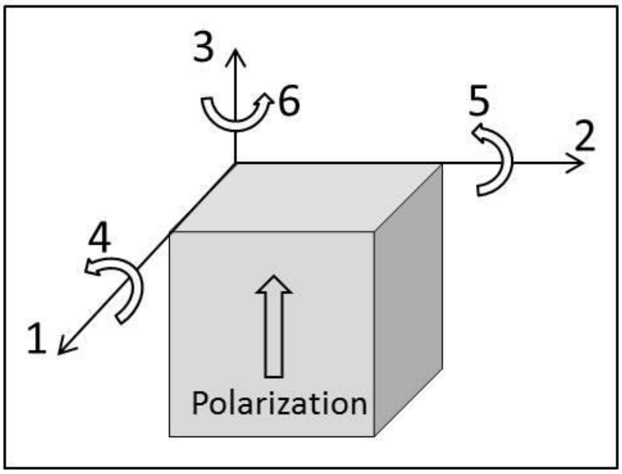

Figure 3-3. Schematic explanation of piezoelectric directions.

3.2.2 Elastic, Dielectric and Ferroelectric Properties

Piezoelectric materials are firstly elastic objects within a certain stress range, similar to other materials. However, unlike isotropic and fully anisotropic materials, polarized piezoelectric materials have 5 independent compliance or stiffness constants, which are s_{11}, s_{12}, s_{13}, s_{33}, s_{44} ($= s_{55}$) or c_{11}, c_{12}, c_{13}, c_{33}, c_{44} ($= c_{55}$)[1,5], respectively. Some compliance constants (s) are inverse to their corresponding stiffness constants (c) (e.g. $s_{11} = 1/c_{11}$, $s_{44} = 1/c_{44}$), and they link to normalised material elastic properties, including Young's modulus (Y), Poisson's ratio (Λ) and shear modulus (G), by Equation 3-2 to 3-4[1,8].

$$Y = {}^{1}\!/_{s_{11}} \quad (3\text{-}2)$$

$$\Lambda = -{}^{s_{12}}\!/_{s_{11}} \quad (3\text{-}3)$$

$$G = {}^{1}\!/_{s_{44}} \quad (3\text{-}4)$$

Second, piezoelectric materials also act as dielectrics. Because of polarization, piezoelectric materials have two independent values of permittivity, ε_{11} and ε_{33}[1,5]. For single-domain piezoelectric materials, ε_{11} and ε_{33} determine the permittivity of direction '1' (or '2') and '3', respectively. For multi-domain piezoelectrics, the permittivity of a certain direction is comprehensively contributed by ε_{11} and ε_{33} (dependent on domain arrangement) of each domain. Also, as other dielectric materials, the permittivity of piezoelectric materials are affected by temperature and phase, and peaks can be observed in phase transition regions in temperature-permittivity spectra. Figure 3-4 shows an example of temperature-relative permittivity relation of single crystal $BaTiO_3$. Relative permittivity ($\varepsilon_r = \varepsilon/\varepsilon_0$, ε_0 is vacuum permittivity of free space) is also known as the dielectric constant.

Dielectric loss is another significant property for dielectrics as well as piezoelectrics, which defines the dissipated energy caused by phase difference between the electric field and field-induced dipole displacement when a dielectric or piezoelectric material is subjected to an alternating external field[9]. The phase difference (δ) is known as the loss angle, while dissipation factor ($tan\delta$) is generally used to reveal the level of dielectric loss[9]. Larger dielectric loss is indicated by increased $tan\delta$.

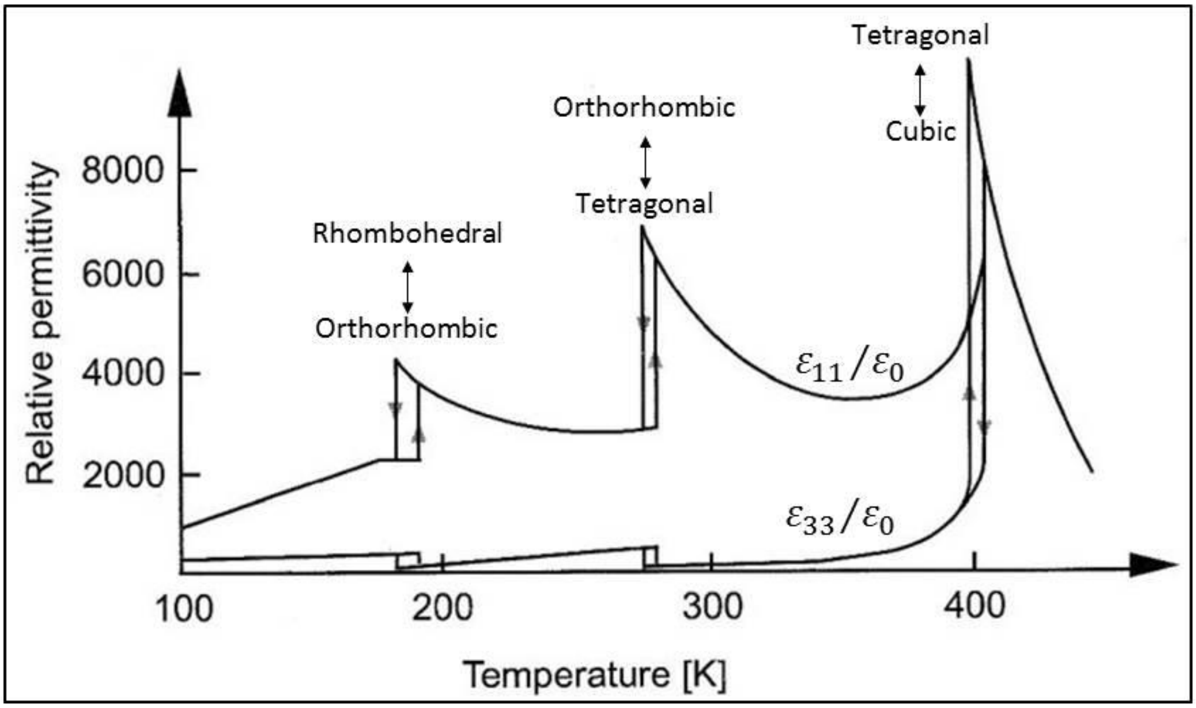

Figure 3-4. The dependence of relative permittivity on temperature for single crystal $BaTiO_3$[5].

Finally, as introduced above, the phenomenon whereby that the direction of polarisation in individual domains can be made to rotate with external electric field can be understood as ferroelectricity. Figure 3-5 shows the hysteresis loop of a ferroelectric material. As the electric field is increased from zero for the first time, the polarization rises from zero to its saturation or spontaneous value, but then falls to a non-zero value (remanent polarization) when the electric field is reduced to zero. In order to reduce the polarization to zero, a coercive electric field with an opposite direction is needed. If this field continues to increase, the polarization will reverse and reach the negative saturation. And in the same way, a positive coercive electric field is needed to reset the negative polarization.

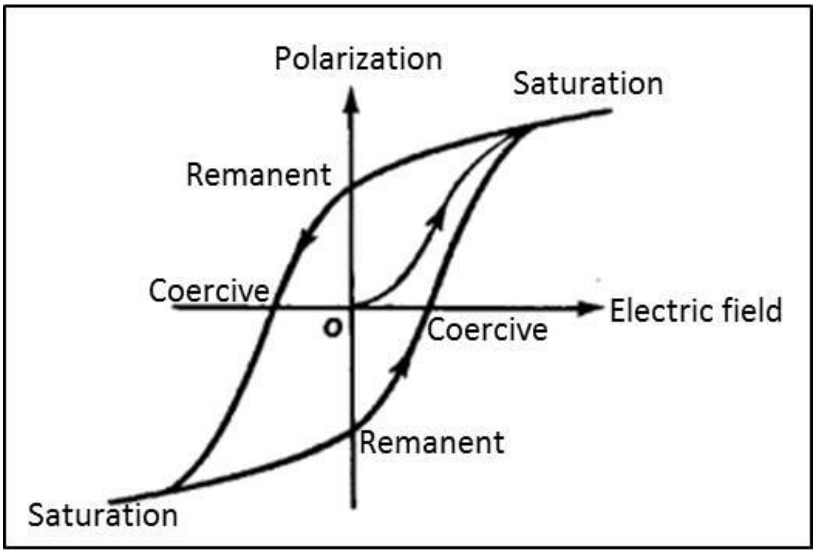

Figure 3-5. Example of ferroelectric hysteresis loop.

3.2.3 Piezoelectric Properties

3.2.3.1 Constitutive Equations, Piezoelectric Coefficients and Boundary Conditions

The piezoelectric effect can be fully described in theory by four equation groups, known as the constitutive equations (or relations), where Groups 1 to 4 are expressed by Equations 3-5 and 3-6, 3-7 and 3-8, 3-9 and 3-10, and 3-11 and 3-12, respectively. Different groups suit different boundary conditions (mentioned below) in which a piezoelectric material is situated.

Group 1: Gibbs free energy, free and short-circuit boundary[2,10]

$$D = d\sigma + \varepsilon^{\sigma} E \quad (3\text{-}5)$$

$$S = s^{E}\sigma + dE \quad (3\text{-}6)$$

Group 2: Electric Gibbs energy, clamped and short-circuit boundary[2,10]

$$\sigma = c^{E} S - eE \quad (3\text{-}7)$$

$$D = eS + \varepsilon^{S} E \quad (3\text{-}8)$$

Group 3: Elastic Gibbs energy, free and open-circuit boundary[2,10]

$$S = s^{D}\sigma + gD \quad (3\text{-}9)$$

$$E = -g\sigma + \beta^{T} D \quad (3\text{-}10)$$

Group 4: Helmholz free energy, clamped and open-circuit boundary[2,10]

$$\sigma = c^{D}S - hD \quad (3\text{-}11)$$

$$E = -hS + \beta^{S}D \quad (3\text{-}12)$$

In the equations, D, σ, E and S mean the charge displacement, stress, electric field and strain of a piezoelectric material, respectively; β^{T} and β^{S} are the inverses of ε^{T} and ε^{S}; and d, g, e and h are four piezoelectric coefficients. Such coefficients are mathematically defined by Equations 3-13 to 3-16[1], where T represents temperature. In addition, d is known as the piezoelectric charge coefficient; g is usually called the piezoelectric voltage coefficient; and e and h have rarely been referred to by special names, but only by piezoelectric coefficients contributing to Groups 2 and 4 constitutive relations.

$$\left(\frac{\partial D}{\partial \sigma}\right)_{E,T} = \left(\frac{\partial S}{\partial E}\right)_{\sigma,T} = d \quad (3\text{-}13)$$

$$-\left(\frac{\partial E}{\partial \sigma}\right)_{D,T} = \left(\frac{\partial S}{\partial D}\right)_{\sigma,T} = g \quad (3\text{-}14)$$

$$\left(\frac{\partial D}{\partial S}\right)_{E,T} = -\left(\frac{\partial \sigma}{\partial E}\right)_{S,T} = e \quad (3\text{-}15)$$

$$\left(\frac{\partial E}{\partial S}\right)_{D,T} = \left(\frac{\partial \sigma}{\partial D}\right)_{S,T} = -h \quad (3\text{-}16)$$

Also, according to the expression of the constitutive equations, some properties of a piezoelectric material are also affected by boundary conditions which the material is surrounded by, as certain parameters (e.g. ε, s, c and β) are presented with a superscript. The letters 'E', 'D', 'σ' and 'S' are not only used as tensors in the constitutive equations, but selected to represent electrical or mechanical boundary conditions when inserted as superscripts, meaning independent variables. In particular, the subscripts 'E' or 'D' corresponds to short- or open-circuit electric boundaries; and 'σ' or 'S' implies free- or clamped- mechanical boundaries, respectively[5]. For example, parameter M_{31}^{E} means material property M_{31} under short-circuit external electric conditions. Although property variations caused by different boundary conditions may not be as significant as those caused by directions, accurate parameter calculations still necessitate distinguishing such difference[5].

3.2.3.2 Electromechanical Coupling Coefficients (k)

The factor k indicates the effectiveness of the energy conversion between mechanical and electrical energy of piezoelectric materials. In general, the effective electromechanical coupling coefficient (k_{eff}) is defined by Equation 3-17[1]. And considering the effect of directions, other coupling coefficients including k_p (planar), k_{31} (transverse), k_{33} (longitudinal), k_{15} (shear), k_t (thickness), etc. have also been commonly introduced[11]. These coefficients will be mathematically defined by relevant equations in Section 3.3.

$$k_{eff}^2 = \frac{\text{mechanical energy converted to electrical energy}}{\text{input mechanical energy}}$$

$$= \frac{\text{electrical energy converted to mechanical energy}}{\text{input electrical energy}} \quad (3\text{-}17)$$

3.2.3.3 Mechanical Quality Factor (Q_M)

Q_M is defined by Equation 3-18, implying the level of mechanical energy loss when piezoelectric materials act as resonators under an applied electric field. Larger Q_M indicates less mechanical loss[12].

$$Q_M = 2\pi \cdot \frac{\text{Stored Mechanical Energy}}{\text{Dissipated Energy per Cycle}} \quad (3\text{-}18)$$

3.3 Characterisation Approaches

3.3.1 Vibration Modes and Sample Standards

As properties along different material directions vary significantly, samples with special shapes need to be processed before characterisation, in order to separate the frequency ranges of vibrations and provide a clear view of signal response. Typically, there are five vibration modes with matched sample standards, by which properties along all possible directions are able to be characterised[13-16]. Figure 3-6 shows the schematics of these standards with polarisation and vibration directions as well as electrode positions all marked. In transverse length mode and thickness shear mode, thin plate samples are used, where $\varepsilon_{33}^{\sigma}$, s_{11}^{E}, s_{11}^{D}, k_{31}, d_{31} and g_{31} can be obtained with the former whilst $\varepsilon_{11}^{\sigma}$, ε_{11}^{S}, s_{55}^{E}, s_{55}^{D}, k_{15}, d_{15} and g_{15} can be calculated with the latter. In radial mode and thickness extension mode, thin discs are utilised and the former can provide information of $\varepsilon_{33}^{\sigma}$, ε_{33}^{S}, s_{12}^{E} and k_p while the latter can reveal ε_{33}^{S}, s_{13}^{E}, s_{33}^{E}, s_{33}^{D} and k_t. In the last mode, longitudinal length mode, a cylinder is employed to gain values of $\varepsilon_{33}^{\sigma}$, s_{33}^{E}, s_{33}^{D}, k_{33}, d_{33} and g_{33}[11,13-16].

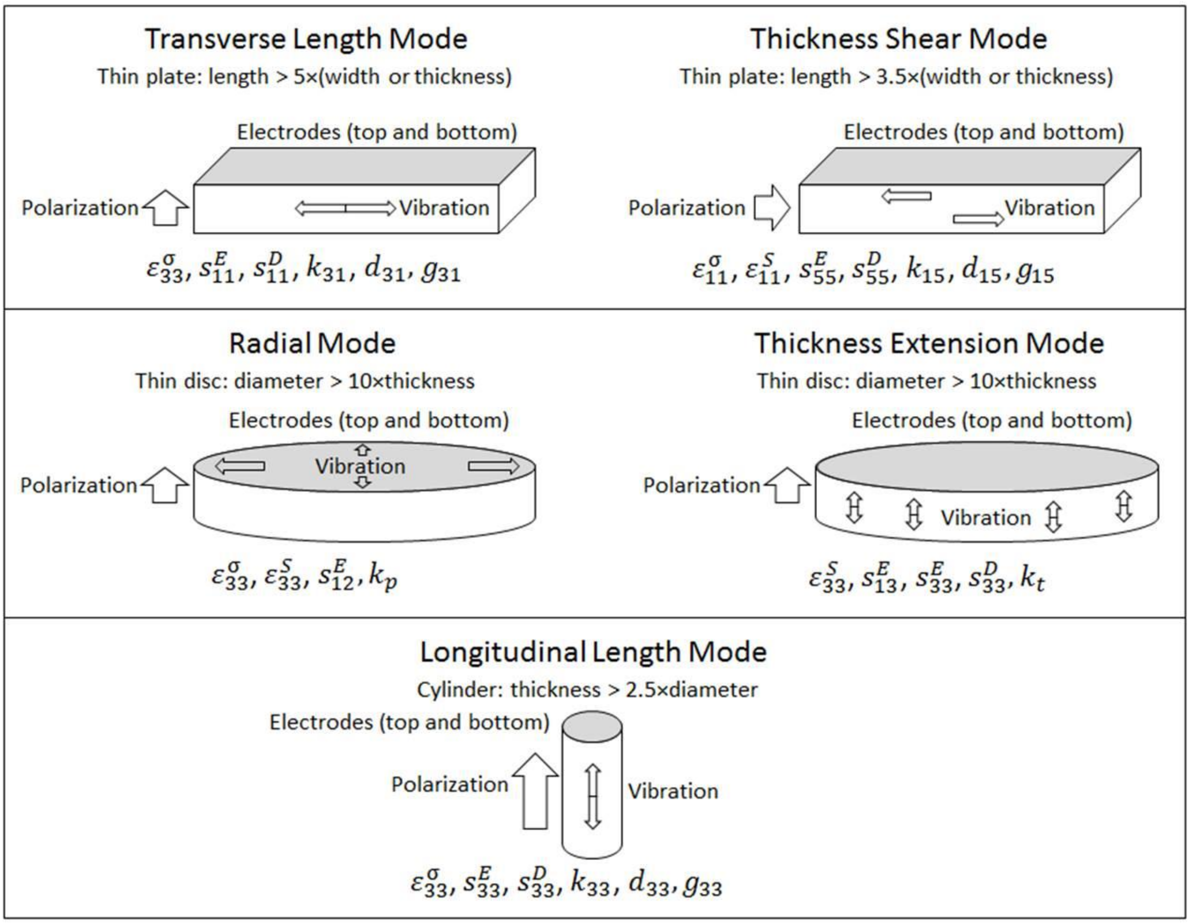

Figure 3-6. Schematics of piezoelectric vibration modes and sample standards[11,13-16].

3.3.2 Frequency Method

The frequency method is a comprehensive approach which provides a full scenario to obtain the complete matrix of the material coefficients. An impedance analyser is usually required and capacitance (C), resonant frequency (f_r) and anti-resonant frequency (f_a) of all the standard samples ideally made from the same batch of material must be accurately measured[5,11]. Figure 3-7 shows an example of an impedance-frequency plot measured by an impedance analyser. The parameter frequency constant (N) is defined as $N = f_r \cdot \alpha$, where α represents the dimension in parallel with the vibration direction. For the same piezoelectric material, the frequency constants of certain vibration mode should be the same value.

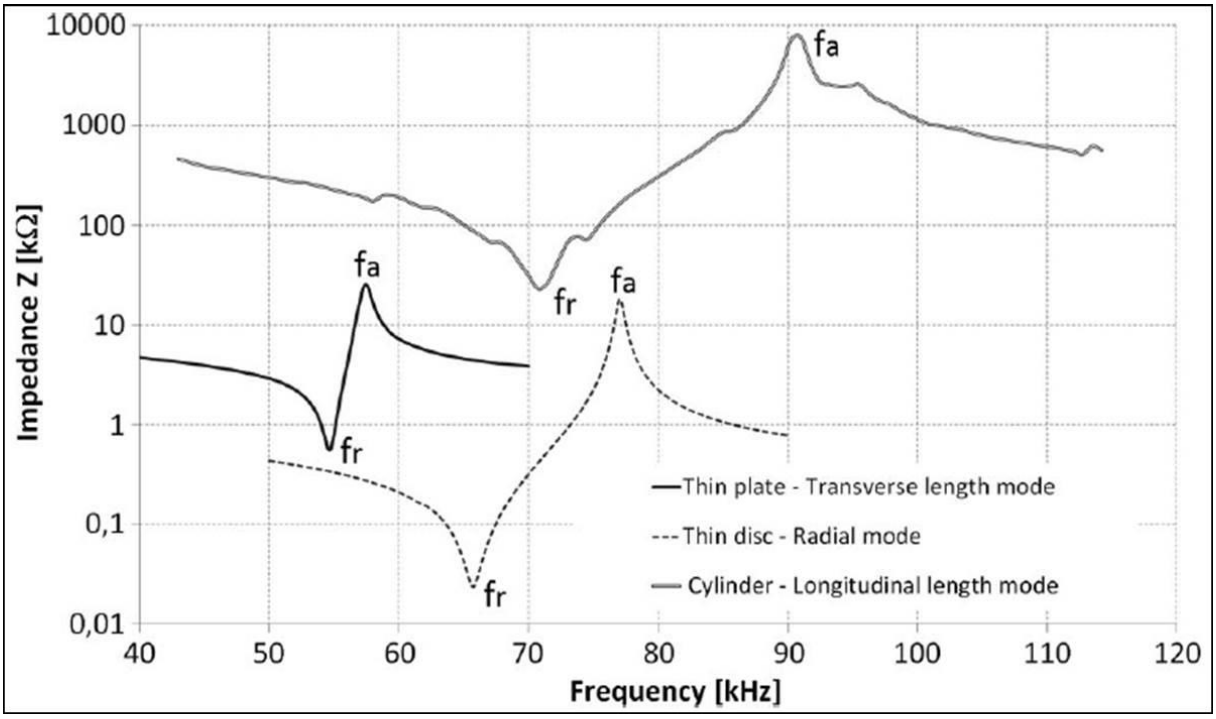

Figure 3-7. Resonance spectra of the transverse, radial and longitudinal length modes[11].

Other material constants can subsequently be calculated. Equations 3-19 to 3-36 fully express the calculation relations of all the material parameters[1,11,17,18]. It should be noted that the C, f_r and f_a cited in each equation should match the corresponding vibration mode[11]. In the equations, ρ, l, w, t and r represent density, length, width, thickness and radius of each sample, respectively. In Equation 3-28, J_0 and J_1 are Bessel functions[1], which make the specific expressions for the former equation considerably complex. However, as the curves induced by the functions are insensitive to Λ, in practice k_p can be approximately expressed by the second sub-equation in Equation 3-28[1,11]. The results strongly depend on the accuracy of the frequency measurement, and the disadvantage of this method is the complexity of sample preparation[11].

$$s_{11}^{E} = \frac{1}{4 \cdot \rho \cdot f_r^2 \cdot l^2} \quad (3\text{-}19)$$

$$s_{12}^{E} = -s_{11}^{E} \cdot \left(1 - \frac{2 \cdot k_{31}^2}{k_p^2}\right) \quad (3\text{-}20)$$

$$s_{13}^{E} = \left\{\frac{1}{2}\left[s_{33}^{E}(s_{11}^{E} + s_{12}^{E}) - \frac{s_{11}^{E} + s_{12}^{E}}{4 \cdot \rho \cdot f_a^2 \cdot t^2 \cdot (1 - k_t^2)}\right]\right\} \quad (3\text{-}21)$$

$$s_{33}^{E} = \frac{s_{33}^{D}}{1 - k_{33}^2} = \frac{\frac{1}{4 \cdot \rho \cdot f_a^2 \cdot t^2}}{1 - k_{33}^2} \quad (3\text{-}22)$$

$$s_{55}^{E} = \frac{s_{55}^{D}}{1 - k_{15}^2} = \frac{\frac{1}{4 \cdot \rho \cdot f_a^2 \cdot t^2}}{1 - k_{15}^2} \quad (3\text{-}23)$$

$$s_{66}^{E} = 2(s_{11}^{E} - s_{12}^{E}) \quad (3\text{-}24)$$

$$\varepsilon_{11}^{\sigma} = C \cdot \frac{t}{w \cdot l} \quad (3\text{-}25)$$

$$\varepsilon_{33}^{\sigma} = C \cdot \frac{t}{\pi \cdot r^2} \quad (3\text{-}26)$$

$$k_{eff}^2 \approx \frac{f_a^2 - f_r^2}{f_a^2} \quad (3\text{-}27)$$

$$\frac{k_p^2}{1 - k_p^2} = f\left(J_0, J_1, \sigma \cdot \frac{f_a - f_r}{f_r}\right) \qquad k_p^2 \approx 2.51 \cdot \frac{f_a - f_r}{f_r} - \left(\frac{f_a - f_r}{f_r}\right)^2 \quad (3\text{-}28)$$

$$k_{31}^2 = \frac{\pi}{2} \cdot \frac{f_a}{f_r} \cdot \frac{1}{\frac{\pi}{2} \cdot \frac{f_a}{f_r} - tan\left(\frac{\pi}{2} \cdot \frac{f_a}{f_r}\right)} \quad (3\text{-}29)$$

$$k_{33}^2 = \frac{\pi}{2} \cdot \frac{f_r}{f_a} \cdot tan\left(\frac{\pi}{2} \cdot \frac{f_a - f_r}{f_a}\right) \quad (3\text{-}30)$$

$$k_{15}^2 = \frac{\pi}{2} \cdot \frac{f_r}{f_a} \cdot tan\left(\frac{\pi}{2} \cdot \frac{f_a - f_r}{f_a}\right) \quad (3\text{-}31)$$

$$k_t^2 = \frac{\pi}{2} \cdot \frac{f_r}{f_a} \cdot tan\left(\frac{\pi}{2} \cdot \frac{f_a - f_r}{f_a}\right) \quad (3\text{-}32)$$

$$d_{33} = k_{33}(\varepsilon_{33}^{\sigma} \cdot s_{33}^{E})^{\frac{1}{2}} \quad (3\text{-}33)$$

$$d_{31} = k_{31}(\varepsilon_{11}^{\sigma} \cdot s_{11}^{E})^{\frac{1}{2}} \quad (3\text{-}34)$$

$$d_{15} = k_{15}(\varepsilon_{11}^{\sigma} \cdot s_{55}^{E})^{\frac{1}{2}} \quad (3\text{-}35)$$

$$g_{33} = \frac{d_{33}}{\varepsilon_{33}^{\sigma}} \qquad g_{31} = \frac{d_{31}}{\varepsilon_{33}^{\sigma}} \qquad g_{15} = \frac{d_{15}}{\varepsilon_{11}^{\sigma}} \quad (3\text{-}36)$$

3.3.3 Laser Interferometry Method

The laser interferometry method is based on the converse piezoelectric effect, where the displacement deflection (ΔL) of a sample is measured against the applied voltage (U_{in}). The piezoelectric coefficients (unit: pm/V) can be calculated by Equation 3-37, in which Δl should match the appropriate material direction of a standard sample[11]. For example, if d_{33} is the targeted parameter, the Δl should come from the length difference of the cylinder sample (longitudinal length mode) showed in Figure 3-6. Similar to the frequency method, high resolution (nanometre level) is compulsory for interferometers[11].

$$d_{ij} = \frac{\Delta l}{U_{in}} \quad (3\text{-}37)$$

3.3.4 Quasi-static (or Berlincourt) Method

A quasi-static method is more cost-effective than the above methods, as it does not require a complete set of standard samples and the measurement can usually accommodate a wide range of samples shapes and sizes[11]. The method is based on the direct piezoelectric effect[5], however both the response of direct and converse effects should be taken into account[11]. The piezoelectric coefficients (unit: pC/N) can be calculated using Equation 3-38, where Q (unit: pC) is the induced charge and F (unit: N) is the force along certain direction applied on the sample.[11]. In practice, a Berlincourt d_{33} or d_{31} metre is able to directly measure the charge and applied force, and thus the calculated values can usually be displayed on the equipment.

$$d_{ij} = \frac{Q}{F} \quad (3\text{-}38)$$

3.4 Lead-based Piezoelectric Ceramics

3.4.1 Lead-Zirconate-Titanate (PZT)

Although the discovery of $BaTiO_3$ (BT) was the start of the history of industrial application of piezoelectrics, it was still unable to meet all the requirements of actuators, sensors and transducers, which were potential consumers of these materials, as many of these applications demanded improved and/or tailored material performance. BT yielded neither high piezoelectric parameters nor could be optimised by adjusting compositions in a wide range[1,3,5]. Driven by this demand, PZT, a solid solution system of $PbTiO_3$ and $PbZrO_3$, was developed in the 1950s and has been dominating the market of piezoelectric ceramics until the present day[5,6]. Similar to BT, PZT unit cells also have perovskite structures (ABO_3), where Pb ions occupy the A sites and Zr and Ti ions occupy the B sites. The $PbTiO_3$-$PbZrO_3$ phase diagram is shown in Figure 3-8. The properties are very dependent on composition and temperature, and it has been well-established that properties such as the coupling coefficients and relative permittivity reach a peak near the morphotropic phase boundary (MPB), where an abrupt structural change occurs between the tetragonal and rhombohedral phases, allowing more polarisation directions (or increased ease of domain reorientation) when the material is being poled[5,19]. PZT outperforms BT in terms of piezoelectric properties and these properties can be widely tailored by adjustment of the Zr/Ti ratio and/or the addition of dopants[1,5].

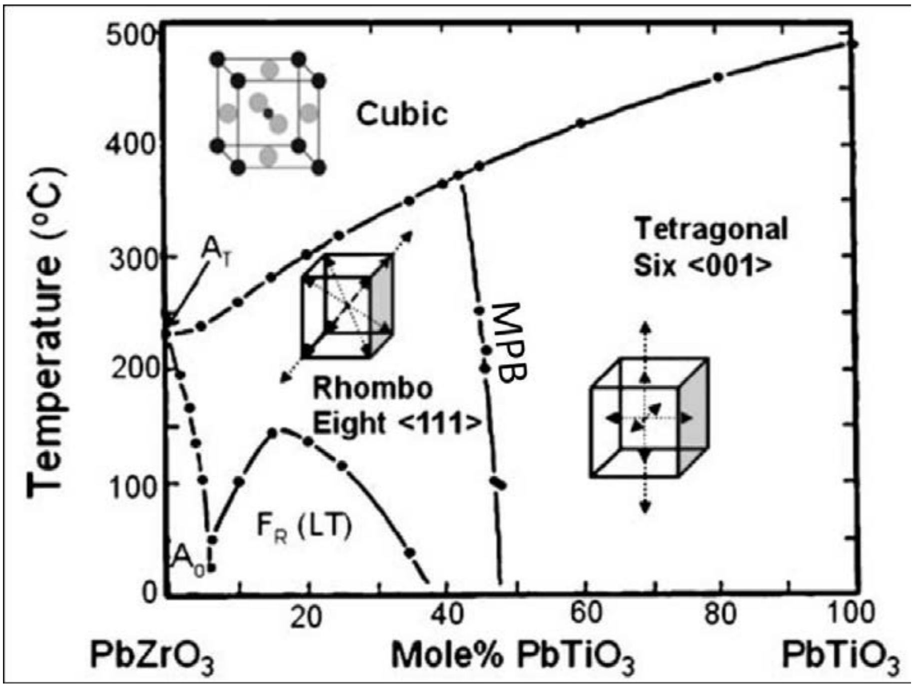

Figure 3-8. Low-temperature phase diagram of PZT[19].

With the rapid development of PZT, many other Pb-based perovskite solid solutions have been synthesized and they are mostly combined with the use of PZT, in order to further tailor properties. For example, the addition of $Pb(Zn_{1/3}Nb_{2/3})O_3$ (PZnN) can help enhance the d values and field-induced strain, which is required by high performance actuators and transducers for sensitive control[20]; the $Pb(Mg_xNb_{1-x})O_3$-$PbTiO_3$ (PMN-PT) system can provide higher electromechanical coupling coefficients[21], making the materials more suitable for energy conversion devices (e.g. energy harvesters)[22,23]; etc. Such compositional modifications have been usually referred to compensating valent substitutions[5].

3.4.2 Doping

Doping is also an approach used to enhance as well as tailor piezoelectric properties. The effect of doping can be quite complex, but it can be classified as four main types, including isovalent substitution of the A and/or B sites, donor doping and acceptor doping, respectively[5]. Firstly, some alkaline earth metal ions (e.g. Ca^{2+}, Sr^{2+}, Ba^{2+}, etc.), which are isovalent with Pb^{2+}, are able to randomly occupy a proportion of the A sites and replace the Pb^{2+} of PZT[5]. This substitution tends to decrease T_c, thus increase permittivity at room temperature[5]. In addition, it raises the d_{33} and coupling coefficients whilst a lower dielectric loss can be achieved[5]. Proper amount of such substitution is up to 10 at.%[5]. Similarly, some ions (e.g. Sn^{4+}, Hf^{4+}, etc.) are able to modify the composition by replacing the B sites (Zr^{4+} and Ti^{4+} of PZT)[5,24,25]. However, unlike the A site substitution where exists an suggested amount limit, the original B site ions can be partially as well as completely replaced by the introduced ions[5]. The B site isovalent substitutions normally do not significantly optimise specific piezoelectric properties as they nearly retain the initial perovskite structure of PZT[5], but they sometimes are able to shift the relative position of the MPB and adjust T_c, thus helping to tailor the properties[5,24,25].

Secondly, donor dopants (e.g. La^{3+}, Bi^{3+}, Nd^{3+}, Nb^{5+}, Ta^{5+}, Sb^{5+})and other possible rare earth metal ions), which carry higher charge than those of ions to be replaced, are also able to substitute into the perovskite structure (ion^{3+} replacing A site cations and ion^{5+} replacing B site cations), and are compensated by the creation of the cation vacancies[1]. The vacancies can be the A or B or both sites, which are comprehensively determined by the types of donor dopants and host structures, the actual doping amount and the exact processing conditions (e.g. atmosphere, pressure, etc.)[1]. The final composition after donor doping should be decided via microstructural characterisation methods. But for PZT, the A site (Pb^{2+}) vacancies are usually preferable because of the ease of PbO loss at high temperatures[5,26,27], and this can be proved by weight loss studies[5]. In the donor doped PZT, dipolar pairs combining the donor dopants and cation vacancies are formed, which are supposed to be immune to applied electric or spontaneous polarization, thus maintaining a relatively stable orientation status[1,5]. Such mechanism has few pinning effect on domain wall movement, because of which domains are likely to be more active thus domain motions are able to be driven by smaller external electric field or stress[1,5]. This tends to improve permittivity and compliance constants as well as increase dielectric and mechanical loss (lower Q_M)[1,5]. Also, as domains become more mobile, a larger number of them can be motivated along external electric field direction compared to that of pure PZT, resulting in stronger piezoelectric effect, e.g. larger coupling coefficients, but smaller coercive field[5]. In addition, the vacancies are able to help release residual stress of domain rotation, reducing the effect of ageing[5]. Ageing is the phenomenon whereby piezoelectric properties change with time after poling resulting from the relaxation and reorientation of the domains structure[1], which will be presented in detail in the next chapter. In addition, donor dopants increase the number of conduction band electrons compensating the vacancies, hence resistivity as well as the breakdown electric field of PZT tend to increase[1,5]. Donor doping is also called 'soft' doping, with amounts usually controlled within 5 at.%[1].

Finally, acceptors with lower charge (e.g. K^+, Rb^+, etc. replacing A site cations and Co^{3+}, Fe^{3+}, Cr^{3+}, Mn^{3+}, etc. replacing B site cations) are able to substitute the PZT perovskite structure and are compensated by the formation of oxygen vacancies[1]. As oxygen ions form a continuous lattice structure of PZT unit cells, the absence of oxygen is likely to cause shrinkage and distortion of the unit cells[5]. Opposite to the donor dopant-cation vacancy combinations, the dipolar pairs between acceptors and oxygen vacancies formed within the acceptor doped PZT can be reoriented by local or applied electric field[1]. As such dipolar pairs are able to provide a field contributing to the stabilization of the domain structures (pinning the domain walls), the permittivity, dielectric and mechanical loss and compliance constants of the doped PZT tend to be reduced[1,5]. Also, as the domain structures are rather stable, which means they are difficult to rotate with external electric field, the doped PZT usually have smaller coupling coefficients but higher coercive field than the undoped[1,5]. In general, acceptor doping induces opposite effects on relevant properties to those caused by donor doping[1,5]. Acceptor doping is also called 'hard' doping.

Other composition modification may involve the addition of Chromium and Uranium, which usually introduce more than one valence state, and hence cause comprehensive changes of piezoelectric properties[5]. In practice, a combination of the above methods may help properly design the properties for certain applications. For example, a standard set of hard and soft PZT has been developed, commercialised and commonly used in both laboratories and industries to meet the requirements of various applications. PZT-5A and PZT-5H are two types of standard 'soft' PZT. Benefiting from its high sensitivity, permittivity and time stability, PZT-5A has been widely used in receivers or generators such as hydrophones, ultrasonic transducers, vibration sensors and accelerometers, etc[28-31]. PZT-5H shares most of the features with PZT-5A, but it is even of higher quality, e.g. with extremely high permittivity, coupling and piezoelectric coefficients[28,29]. It has been widely used in not only all of the areas where PZT-5A has been applied, but also in sensitive ultrasonic transducers and ink jet printers, etc., where higher sensitivity is required[28,29,32-34]. PZT-4D and PZT-8 series are two types of standard 'hard' PZT. They exhibit extremely low dielectric and mechanical loss (low $tan\delta$ and high Q_M) and are able to generate large mechanical drive amplitudes[28,29]. Thus, they are suitable for high power acoustic applications such as ultrasonic cleaning, sonar, etc[28,29,35,36].

3.5 Lead-free Piezoelectric Ceramics

3.5.1 Introduction

Although PZT based piezo-ceramics have been dominating the application market, the issue of replacement of PZT becomes more and more urgent as a relevant EU legislation has prohibited the use of certain hazard substances, such as lead, mercury, cadmium, etc., in electrical and electronic equipment and devices[37,38]. Lead in piezoelectric materials has a current exemption from this ban, but the intention is for the maximum allowed concentration of lead to be 0.1 wt%[38], whereas PZT based piezoelectric materials usually contain more than 60 wt% of lead[6]. Once lead goes into human bodies, it accumulates in organs and can hardly be ejected, leading to potential fatal disease. Currently, lead-free piezoelectrics have not been able to substitute PZT on a broad basis, and this has triggered a huge amount of research to be undertaken to explore as many lead-free piezoelectrics as possible[39-42]. The consideration involves not only toxicity but also the cost of any alternative elements, their availability, and the structural tolerance between target atoms when designing and synthesizing lead-free materials[6]. According to such requirements, three main classes have received the most attention, namely Sodium Potassium Niobate (KNN) based, Bismuth Sodium Titanate (BNT) based and Barium Calcium Zirconate Titanate (BCZT) based ferroelectrics.

3.5.2 KNN Related Materials

KNN is a solid solution of $KNbO_3$ (KN) which possesses similar structures and phases to BT but higher phase transition temperatures[43], and $NaNbO_3$ (NN) which has antiferroelectric properties[44]. Both KN and NN are orthorhombic at room temperature[6]. Overall, pure KNN has shown comparable or even higher T_c (around 400 °C) but lower relative permittivity (200-500), k_p (0.2-0.4) and d_{33} (80-160 pC/N) than the PZT family[43,45-49]. Similar to PZT, doping (or chemical modification) is also helpful to optimise the properties. For instance, doping Li, Ta, Sb or introducing BT or BNT may help to comprehensively enhance permittivity, k_p and d_{33} (but still lower than PZT), while incorporating different amounts of $SrTiO_3$ may be able to adjust such properties in a wide range[6,39,50-55]. However, the expense of most doping is the decrease of T_c, affecting the highest working temperature of such materials[6].

3.5.3 BNT Related Materials

$Bi_{1/2}Na_{1/2}TiO_3$ (BNT) is also a perovskite ferroelectric[56], as well as its counterpart $Bi_{1/2}K_{1/2}TiO_3$ (BKT)[57]. The drawbacks of pure BNT or BKT refer to sintering complication, poling difficulty because of high leakage currents and high coercive fields, and poor dielectric and piezoelectric constants[6,56,58-62]. To optimise this, binary systems (e.g. BNT-BT, BKT-BT and BNT-BKT) and even ternary systems (e.g. BNT-BT-BKT and BNT-BT-KNN) have been developed[63-67]. BNT-BT can be easily sintered between 1100-1200 °C, with enhancement of piezoelectric and coupling coefficients[6]. In contrast, BKT-BT hardly shows advantages over pure BNT or BKT[64]. BNT-BKT exhibits higher T_c and T_d (depoling temperature) and slightly higher permittivity and d_{33}.[6] BNT-BKT-BT exhibits comparable properties to BNT-BT, though the highest d_{33} while lowest T_d is found among BNT based materials[6,68]. In fact, BNT-BKT-BT has been suggested to be a suitable material to replace PZT in some specific applications such as ultrasonic transducers[69] and accelerometers[70]. BNT-BT-KNN, combining an MPB between a rhombohedral phase (BNT) and a tetragonal phase (BT) together with an orthorhombic phase (KNN), possesses the highest external electric field induced strain due to easier domain rotation and domain wall movement of such structures[6,67], making them useful for actuators. Unlike PZT or KNN, doping of BNT related piezoelectrics shows few effects on property tailoring, in spite of decreased T_d and slight improvement of piezoelectric properties[6].

3.5.4 BCZT Related Materials

KNN and BNT related materials which have had a long history as candidates in the search for lead-free materials to replace PZT. However, since 2009, a solid solution of $(1-x)Ba(Zr_{0.2}Ti_{0.8})O_3-x(Ba_{0.7}Ca_{0.3})TiO_3$ (BZT-BCT or BCZT) has been investigated as another significant promising lead-free ferroelectric, with extremely high d_{33} (>600 pC/N, even higher than ‘soft’ PZT) being first reported for a 0.5BZT-0.5BCT (50BCZT) composition[42]. Figure 3-9 shows a prediction (based on X-ray diffraction and permittivity-temperature measurements) of the BZT-BCT phase diagram.

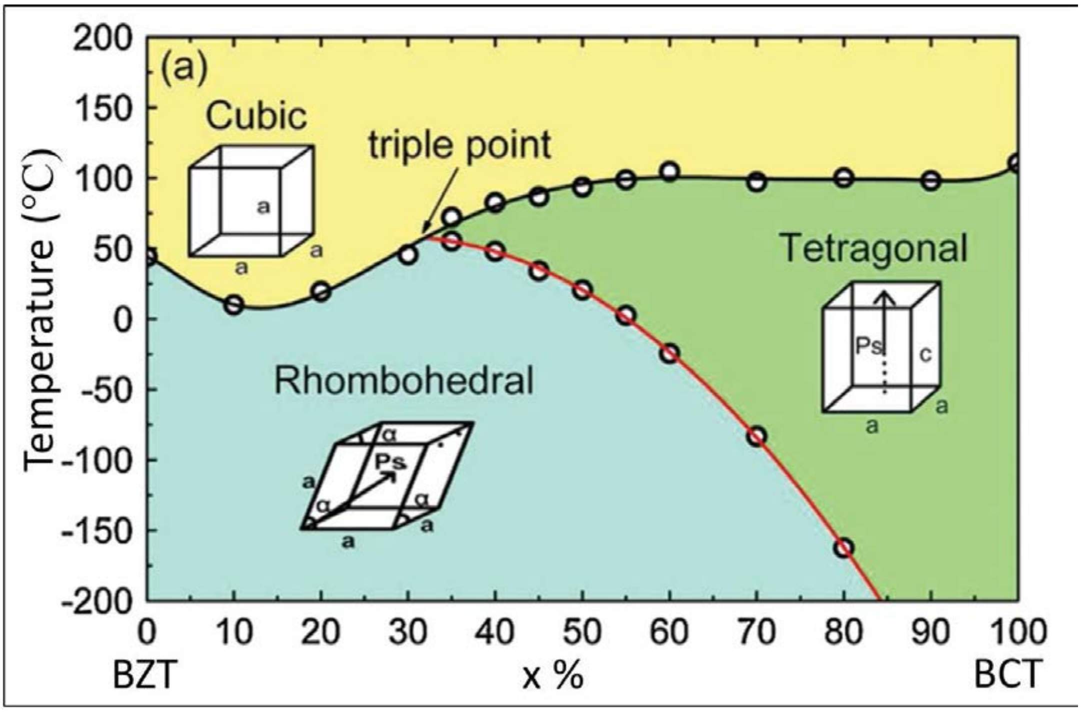

Figure 3-9. Predicted phase diagram BZT-BCT based on partial experiment[42,71].

Compared to that of PZT, the MPB of BCZT system is strongly curved, implying that the optimum properties near the MPB depend on not only composition but temperature, thus leading to poor temperature stability. However, in spite of this temperature instability, such a system has some similarity to PZT, meaning the properties vary with the ratio of BZT and BCT, with the optimum reaching comparable level to those of PZT, providing a possibility to tailor the material in a similar way to PZT[42]. However, the barrier preventing it to be widely used in the near future may be its low T_c (approximately 90 °C for 50BCZT), which is much lower than that of KNN based (around 400 °C)[6], BNT based (200-400 °C)[6] or PZT based piezoceramics (100-400 °C)[19].

The unit cell of BCZT has been treated based on that of BT, where Ca^{2+} ions occupy a part of the positions of Ba^{2+} whist some Zr^{4+} ions take places of Ti^{4+}. As only a few years have been devoted into BCZT related research, to the state of the art, effects of microstructure[72], fabrication and process methods (sintering[73], poling[74], annealing[75]), even the phase transition/diagram[76,77] is still under investigation and so is not yet well understood. Some preliminary doping trails have not shown any significant property improvements, although it has been shown that the sintering temperature can be lowered[78-80].

Table 3-1 lists a selection of reported properties of BCZT related materials and the comparison to those of typical PZT, KNN and BNT related materials.

Table 3-1. A selection of reported properties of PZT based and lead-free piezoceramics.

Composition	**Relative Permittivity**	**d_{33} (pC/N)**	**k_p**	**T_c (°C)**
$0.5Ba(Zr_{0.2}Ti_{0.8})O_3$-$0.5(Ba_{0.7}Ca_{0.3})TiO_3$[42]	~3000	~600	N/A	~93
$(Ba_{0.85}Ca_{0.15})(Ti_{0.9}Zr_{0.1})O_3 + CeO_2$[79]	4843	600	0.51	~90
$(Ba_{0.85}Ca_{0.15}Ti_{0.90}Zr_{0.10})O_3 + Pr_2O_3$[81]	4638	460	0.476	~80
$(Ba_{0.82}Sr_{0.03}Ca_{0.15})(Zr_{0.1}Ti_{0.9})O_3$[82]	N/A	534	0.477	72
Textured $(Na,K)NbO_3$-$LiTaO_3$-$LiSbO_3$[39]	1570	416	0.61	253
$Li_{0.03}(Na_{0.53}K_{0.48})_{0.97}Nb_{0.8}Ta_{0.2}O_3 + BiFeO_3$[83]	N/A	340	0.47	~300
$0.98(Na_{0.5}K_{0.5})NbO_3$-$0.02Ba(Zr_{0.52}Ti_{0.48})O_3$[84]	1951	217	0.41	~425
$(Bi_{0.5}Na_{0.5})_{0.94}Ba_{0.06}TiO_3 + CeO_2 + La_2O_3$[85]	831	162	N/A	~280
$Bi_{0.5}(Na_{0.84}K_{0.16})_{0.5}TiO_3 + SrTiO_3 + Nb_2O_5$[86]	868	185	0.343	292
PZT ceramic family (soft and hard)[19,39]	2000-8000	200-1000	0.5-0.7	400-100

3.6 Fabrication of Piezoelectric Ceramics

The fabrication of piezoelectric ceramics utilises processes in common with other ceramics, generally consisting of the mixing and milling of the raw materials, calcination, re-milling, shaping and sintering[1,5,87,88]. In addition, piezoelectric ceramics need to undergo electroding and poling after sintering[5]. An ageing process is sometimes added to the end of the process for industrial manufacturing.

3.6.1 Powder

3.6.1.1 Raw Materials

Inorganic powders (e.g. metal-oxides, alkaline earth-carbonate, etc.) are commonly utilised as starting materials to fabricate piezoelectric ceramics[88]. Purity, particle size, particle size distribution, and reactivity are the main criteria in the selection of the raw materials, in addition to availability and cost which may be considered by industrial manufacturers[1,5,88]. Purity is likely to affect final piezoelectric properties, as certain impurities may contain ‘soft’ or ‘hard’ doping elements which are able to cause a change of the designed compositions and corresponding final properties. Therefore, highly-purity powders (usually >99 %) are required to control the impurity level[5], especially for those forming the frame compositions of ABO_3, e.g. PbO, ZrO_2 and TiO_2 for synthesizing PZT, where much larger quantity would be used than those to be doping additives. Particle size affects reactivity during calcination and densification during sintering[5,88]. Also, the choice of particle size and size distribution of the raw materials will be dependent on the specific shaping method selected[88]. In general, smaller particles without agglomerates are desired[5]. Reactivity is affected by chemical elements and particle size of powders, both of which define the temperature and time needed in the calcination process[5,88]. For doping additives where only minor percentages are used, reactivity becomes more important[5].

3.6.1.2 Mixing and Milling

The different raw material powders need to be evenly mixed in their appropriate stoichiometric proportions before calcination. Also, the mixed powders need to be milled before and after reaction in order to control the particle size and size distribution. In practice, mixing and milling are usually completed in one step, which is selected from various mechanical and chemical mixing/milling methods for different particle size ranges. Vibratory milling is usually able to produce finer particles than ball milling due to the higher energy imparted to the suspensions, but both methods are suitable to make μm-sized particles[88]. However, if nm-sized particles are required, chemical methods, of which sol-gel[88] is an example, are usually applied. After mixing and milling, for those processes which are carried out in the presence of a liquid solvent, a subsequent drying step needs to be incorporated prior to calcination.

3.6.1.3 Calcination

For most of the mixtures obtained from mechanical mixing and milling methods, high-temperature treatment (called calcination) is usually employed before shaping and sintering them. The purpose of such a process is to pre-form the desired phases and thus improve sample homogeneity and also reduce the volume shrinkage in the sintering step[5]. In calcination, the target solid solution does not have to be fully synthesized, but the calcinations product must be able to react to the final phase during sintering[1]. Hence, the ideal calcination temperature should be high enough to drive the appropriate reactions but low enough to suppress chemical loss. For example, PbO evaporation is a common issue in the calcination process of PZT[1]. Several steps have been adopted in research and industry to avoid such evaporation loss, including using covered crucibles to load the powders, and adding appropriate amount of excess PbO in the starting materials, etc.[1] This issue still exists in the sintering process, and more steps to solve the problem will be presented in Section 3.6.3. Also, the ideal calcination temperature should prevent the powder becoming too hard to re-mill[1,5]. After calcination and re-milling, the first stage of fabrication is complete and the processed powders are ready for further steps.

3.6.2 Shaping

3.6.2.1 Dry Pressing

Before sintering, the calcined powders must be formed into specific shapes similar to the final product designs. Dry pressing (or uniaxial pressing) is the most commonly used way to obtain thin bulk samples with simple shapes and constant cross-sectional areas[1,87]. This method is able to achieve high production rates as well as close tolerances[88]. However, although double-ended pressing can provide a more even density distribution than single-ended, the green bodies made though dry pressing still tend to suffer large density variation, especially for thicker or larger samples[1,87,88]. To address this issue, hot pressing and/or isostatic pressing are also widely applied in both laboratory and industry[1,87,88]. These two methods are sometimes combined (hot-isostatic pressing) in order to further improve the density and minimise any variation throughout the sample[1].

3.6.2.2 Doctor Blading and Screen Printing

In contrast to dry pressing which mainly suits the fabrication of bulk ceramics, doctor blading and screen printing are specially designed for shaping thin and thick films (thickness <100 μm). Rather than dry powder with binder, printable inks/pastes with appropriate rheological behaviour needs to be prepared in advance. The process of doctor blading is shown schematically in Figure 3-10, where it can be seen that tapes are used to control the planar dimensions as well as the thickness of the deposited film, and the substrate provides a platform to the film.

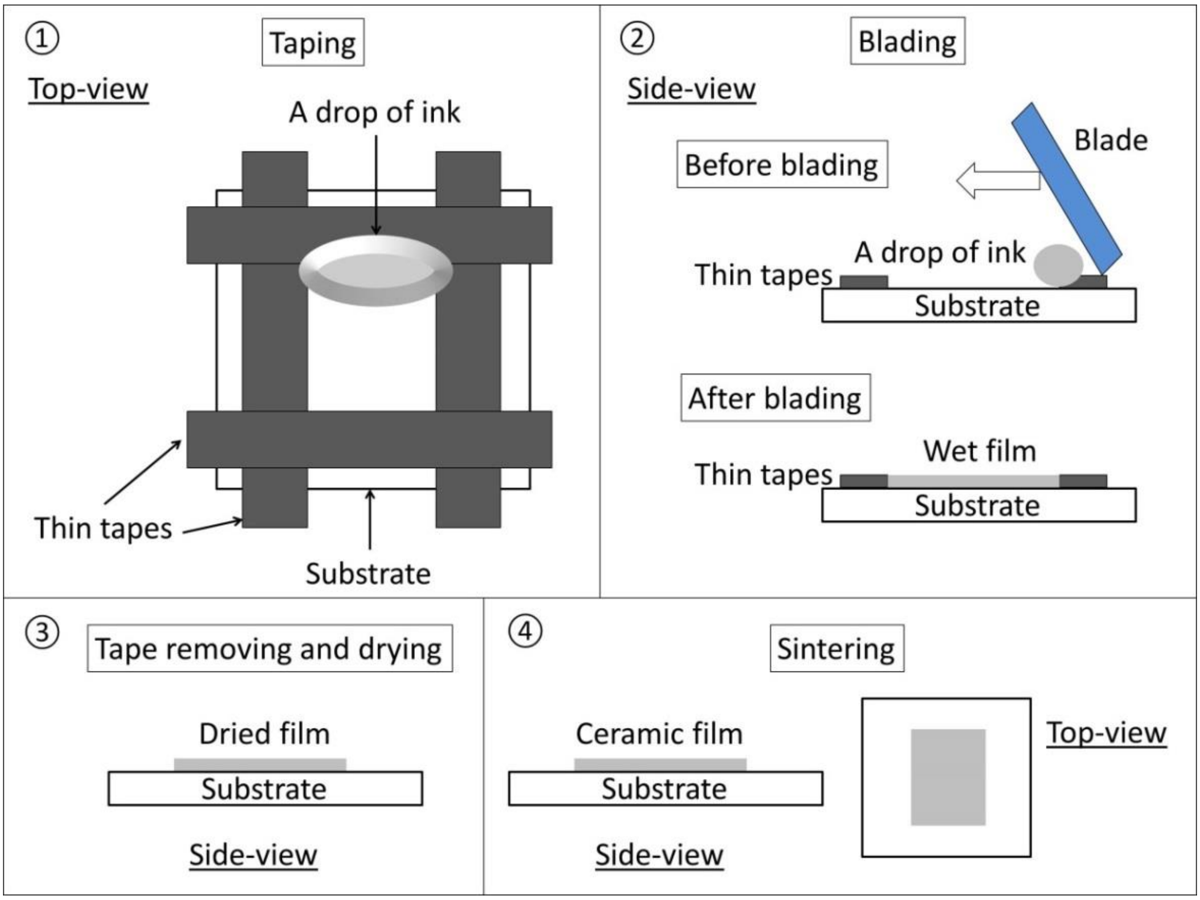

Figure 3-10. Schematic diagram of the doctor blading process.

Doctor blading is a flexible and cost-effective deposition method for producing ceramic films in laboratory conditions, while screen printing is another commonly used method (corresponding to doctor blading) to produce ceramic films in large quantity but at low cost in either laboratory or industry[89,90]. Inks similar to those used in doctor blading are squeezed with a rubber squeegee through pre-designed emulsion patterns on screens made from finely woven mesh, and are transferred onto supporting materials[89,90], followed by drying and sintering. The planar shape of a printed film is controlled by the pattern, whilst the thickness can be affected by the size and resolution of the mesh and/or the number of printing cycles.

There are also many other methods such as tape casting[10], extrusion[87,88], injection molding[87,88], slip casting[87,88] and gel-casting[91], which have been widely used to shape piezoelectric green bodies, but as they are not directly relevant to the work reported in this thesis, they will not be discussed here.

3.6.3 Sintering

3.6.3.1 Conventional Solid-state Sintering

Sintering is the process whereby the powder compacts (green bodies) are transformed to dense and robust ceramics by heating at elevated temperatures below the melting point of the material[92], and is the most important process determining density and grain size, thereby affecting the qualities and piezoelectric properties of the ceramic. In principle, sintering temperature and time comprehensively affect densification and grain growth[88]. At the right temperature, the density increases with time, then followed by grain growth. However, if the temperature is too low, full densification can never be reached. Although ceramics with high density but small and uniform grains possess excellent mechanical properties (e.g. high strength), piezoelectric ceramics are usually engineered to have larger grains (>1 μm) as higher d values can be obtained with increased grain size[61,93]. Such phenomenon is illustrated in Figure 3-11, where the parameters of d_{31} and spontaneous polarization of a Nb-doped piezoelectric ceramic were improved with increased grain size until about 1.5 μm, and then remained at the same level. Therefore, the sintering of piezoelectric ceramics requires more accurate selection and control of both temperature and time, in order to gain high density as well as appropriate grain sizes.

Also, following the discussion with calcination, PbO evaporation still retains an issue in the sintering process of lead-based piezoelectric ceramics[1]. In addition to the steps to avoid Pb loss mentioned above, the green bodies for sintering can also be surrounded or buried by a lead-rich powder (e.g. $PbZrO_3$), and again loaded in closed crucibles/vessels[1].

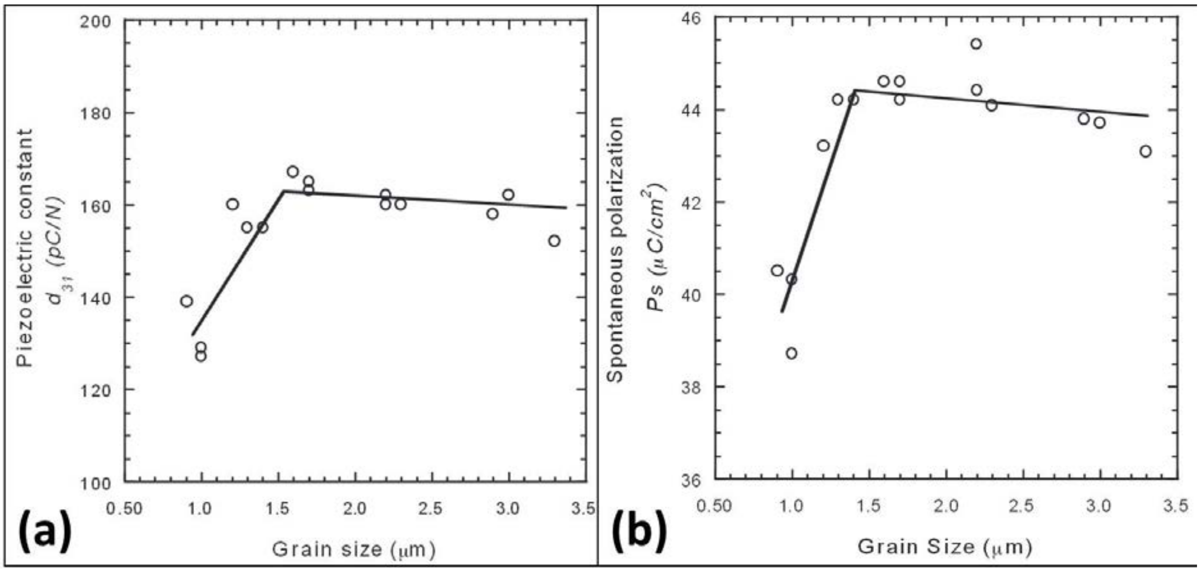

Figure 3-11. Dependence of (a) d_{31} (b) spontaneous polarization on grain size for a Nb-doped PZT ceramic[94].

3.6.3.2 Liquid-phase Sintering

Liquid-phase sintering involves the use of low melting point, often glassy, additions to the ceramic powder which, when molten, provide a mechanism to enhance atomic migration and diffusion, and enhance densification[92]. The first requirement for liquid-phase sintering to occur is that the liquid yields an appreciable solubility of the solid phase and is thus able to wet the solid particles[92]. When this happens, some of porosity will be filled by the liquid, and surface tension will tend to pull the neighbouring particles towards each other[92]. This mechanism not only enables ceramics to be densified at much lower temperatures than would be possible using conventional solid-state sintering, but also offers the advantages of much more rapid, uniform sintering and densification[92,95,96]. However, for piezoelectric ceramics, the existence of glassy film at grain boundaries after liquid-phase sintering may have detrimental effects on functional properties such as the d and k values[92,97-99]. Thus, the amount of sintering aid should be minimised in order to reach a balance point between high density and acceptable piezoelectric properties.

3.6.4 Electroding and Poling

Many electroceramics require the addition of thin layers of conductive materials on their surfaces in order to exploit their properties. In particular, for piezoelectric materials, electrodes are required on surfaces perpendicular to the intended polarisation direction to enable application of the appropriate external electric field, and also to allow voltage to be applied or extracted during the operation of the device[5]. In practice, any metal could be used, but common electrode materials are silver, gold, nickel, copper, palladium, platinum and alloys thereof, among which silver and gold are more commonly used in industry and laboratory, respectively[5]. The use of the platinum group metals is usually required if the electrodes are co-sintered with lead-oxide-based pizoelectrics, in order to withstand the sintering temperatures of the bulk ceramic materials, although silver can be used with thick film materials designed to sinter at and below 900 °C[90,95].

Poling is implemented by applying a large electric field to the piezoelectric ceramics via the electrodes (contacting poling) or without electrodes (Corona poling), and maintaining it for a certain period of time[5]. The field can be continuous, intermittent or alternating in either strength or direction, but must exceed the coercive field and approach the spontaneous polarisation while being smaller than the breakdown electric field[5]. The quality of poling is a vital factor that influences the percentage of the domains which are able to rotate and re-align along the direction of the applied electric field, thus affects the strength of piezoelectric response. In practice, poling can be done at the temperatures close to, but below, the Curie temperature where the domain wall movement becomes more active and poling is easier to achieve[51,74,100]. Often the sample is cooled with the electric field still applied[101,102]. Contacting poling usually takes places in silicone oil[1]. For ‘soft’ PZT, the oil temperature and the applied electric field are typically controlled at 100-150 °C and 1-4 kV/mm, respectively[1,101]. However, because of the domain wall pinning effect, as presented in Section 3.4, 'hard' PZT is more difficult to be well poled in the normal conditions applied to 'soft' PZT. Therefore, 'hard' PZT can be quenched from a temperature well above the T_c (e.g. 500 °C) or de-pinned by applying a high temperature (below the T_c) and a high periodic field (below the maximum allowed field) for hundreds or thousands of cycles, before being poled under the same conditions as those applied to 'soft' PZT[102]. Corona poling is an advantageous method to some degree, as it does not required electrodes to be deposited before poling, does not contact the surfaces of the samples, and can diminish the risk of electrical breakdown[1,103]. Such a poling method is done in the air atmosphere and elevated temperatures (100-150 °C for PZT), with applied voltages at ~10^4 V[103]. In general, poling is the last process in the fabrication of piezoelectric ceramics.

3.6.5 Aging

The functional properties of a piezoelectric ceramic can change with time after poling, and this effect is known as ageing[1,5]. It is not caused by any external mechanical stress or electric field or temperature variation[1,5], but may be due to the relief of residual stresses among domain re-aligned during poling[5] or the reduction in the mobility of domain walls and the gradual formation of inhibiting structures (e.g. internal fields induced by dipole alignment formed from impurity ions or lattice defects, redistributed internal strains because of crystal anisotropy or defect accumulation in domain wall areas)[1]. Such an effect usually leads to a reduction of the relative permittivity, dielectric loss and k, with a corresponding increase of Q_M and stiffness of the poled piezoelectric ceramics[5,104]. Equation 3-39 indicates the relation of property change and time in ageing, where M represents certain property and t_0, t_1 are two measurement time points after poling respectively[1,5].

$$\frac{M_{t1} - M_{t0}}{M_{t0}} = A \cdot \log_{10}\left(\frac{t_1}{t_0}\right) \quad (3\text{-}39)$$

For example, if the k_p value of a piezoelectric disc is measured on the 1st day after poling ($k_{p,1}$) and re-measured on the 10th day ($k_{p,10}$), Equation 3-39 can be written as Equation 3-40. Factor A can be defined as the ageing effect constant, of which the absolute value implies the ageing rate. The larger $|A|$ becomes, the faster a certain property changes with time. However, different time gaps as well as properties result in various A values.

$$\frac{k_{p,10} - k_{p,1}}{k_{p,1}} = A_{10} \cdot \log_{10}\left(\frac{10}{1}\right) \quad \text{(3-40)}$$

Also, Equations 3-41 and 3-42 can be deduced according to Equations 3-39 and 3-40, proving that the percentage of a property change is constant for the time gap of $(t_1^{n+1} - t_1^n)$ $(n = 0,1,2,3,\ldots)$.

$$\begin{aligned} & A_{10} \cdot \log_{10}\left(\frac{10}{1}\right) = A_{10} \cdot \log_{10}\left(\frac{100}{10}\right) = A_{10} \cdot \log_{10}\left(\frac{1000}{100}\right) = \cdots \\ & = \frac{K_{p,10} - K_{p,1}}{K_{p,1}} = \frac{K_{p,100} - K_{p,10}}{K_{p,10}} = \frac{K_{p,1000} - K_{p,100}}{K_{p,100}} = \cdots \quad \text{(3-41)} \end{aligned}$$

$$\frac{M_{t_1^{n+1}} - M_{t_1^n}}{M_{t_1^n}} = A_{t1} \cdot \log_{10}(t_1), n = 0,1,2,3,\ldots \quad \text{(3-42)}$$

Ageing is a detrimental effect, leading to the poorer stability of material properties over time and a corresponding unstable performance of final assembled devices. In practice, ageing can be minimised or controlled by, for example, using ‘soft’ doped material compositions presented in Section 3.4 and heat treatment at specially selected temperatures to help relieve internal stresses[5]. In addition, commercial materials would normally only be supplied in an ‘aged’ (at certain temperature and for certain time) so that any subsequent deterioration is small.

3.7 Summary

This chapter has comprehensively reviewed the backgrounds and up-to-date knowledge of piezoelectricity, from the basic principles to materials and corresponding fabrication processes, all of which are directly related to this project. Although piezoelectricity and piezoelectric materials are relatively old concepts, there are still several areas which need to explore, such as the investigation of the replacement of the lead-based by lead-free materials, and the selection of the mature lead-based and the emerging lead-free materials for the application of energy harvesting. The next chapter will give a specific review of the combination of piezoelectric materials and the energy harvesting technology.

References

1 Moulson, A. J. and Herbert, J. M. Electroceramics: Materials, properties and applications. *Chapman & Hall: London*, pp. 58-61, 76-77, 87-113, 265-284, 285-288 (1990).

2 Burfoot, J. C. Ferroelectrics: An introduction to the physical principles. *D. Van Nostrand: London*, pp.1-12, 46-54 (1967).

3 Lines, M. E. and Glass, A. M. Principles and applications of ferroelectrics and related materials. *Oxford University Press: Oxford*, pp. 1-2, 87-128 (1977).

4 Mason, W. P. Piezoelectric crystals and their application to ultrasonics. *D. Van Nostrand: New York*, pp. 2 (1950).

5 Jaffe, B., Cook, W. R. and Jaffe, H. Piezoelectric ceramics. *Academic Press Inc.: London*, pp. 1-9, 20-46, 30-35, 50-74, 83-85, 135-170, 253-267 (1971).

6 Rodel, J., Jo, W., Seifert, K. T. P. *et al.* Perspective on the development of lead-free piezoceramics. *Journal of the American Ceramic Society* **92**, 1153-1177 (2009).

7 van Randeraat, J. and Setterington, R. E. Piezoelectric ceramics. *Mullard Limited: London*, pp. 4-13 (1974).

8 Wortman, J. J. and Evans, R. A. Young's modulus, shear modulus, and Poisson's ratio in silicon and germanium. *Journal of Applied Physics* **36**, 153-156 (1965).

9 Böttcher, C. J. F. Theory of electric polarisation. *Elsevier: Amsterdam*, pp. 228-233 (1952).

10 Holmes, J. E. Novel piezozlectric structures for sensor and actuator applications. *Ph.D. Thesis, University of Birmingham*, pp. 19-20, 34-35 (2002).

11 Fialka, J. and Benes, P. Comparison of methods for the measurement of piezoelectric coefficients. *IEEE Transactions on Instrumentation and Measurement* **62**, 1047-1057 (2013).

12 Jackson, R. G. Novel sensors and sensing (online access). *IOP Publishing Ltd.: Bristol*, Chapter 2 (2004).

13 Piezoelectric properties of ceramic materials and components part 2: methods of measurement - low power. *European Standard EN 50324-2* (2002).

14 Guide to dynamic measurements of piezoelectric ceramics with high electromechanical coupling. *International Standard CEI/IEC 60483*, pp. 40 (1976, 1997).

15 IEEE standard on piezoelectricity. *ANSI/IEEE Standard 176-1987* (1987).

16 Fialka, J., and Benes, P. Comparison of methods of piezoelectric coefficient measurement. *2012 IEEE International Instrumentation and Measurement Technology Conference, IEEE Instrumentation and Measurement Technology Conference* 37-42 (2012).

17 Mason, W. P. and Jaffe, H. Methods for measuring piezoelectric, elastic, and dielectric coefficients of crystals and ceramics. *Proceedings of the Institute of Radio Engineers* **42**, 921-930 (1954).

18 Du, X. H., Wang, Q. M. and Uchino, K. An accurate method for the determination of complex coefficients of single crystal piezoelectric resonators II: Design of measurement and experiments. *IEEE Transactions on Ultrasonics Ferroelectrics and Frequency Control* **51**, 238-248 (2004).

19 Shrout, T. R. and Zhang, S. J. Lead-free piezoelectric ceramics: Alternatives for PZT? *Journal of Electroceramics* **19**, 113-126 (2007).

20 Fan, H. Q. and Kim, H. E. Perovskite stabilization and electromechanical properties of polycrystalline lead zinc niobate-lead zirconate titanate. *Journal of Applied Physics* **91**, 317-322 (2002).

21 Rakbamrung, P., Lallart, M., Guyomar, D. *et al.* Performance comparison of PZT and PMN-PT piezoceramics for vibration energy harvesting using standard or nonlinear approach. *Sensors and Actuators A-Physical* **163**, 493-500 (2010).

22 Moon, S. E., Lee, S. K., Lee, Y. G. *et al.* Characterization of a high-power piezoelectric energy-scavenging device based on PMN-PT piezoelectric single crystals. *Journal of the Korean Physical Society* **60**, 230-234 (2012).

23 Kim, I., Joo, H., Jeong, S., Kim, M. and Song, J. Micro-power generation of PMN-PZT triple morph cantilever for electric harvesting devices *E-MRS 2009 Spring Meeting, Symposium F: Advances in Transparent Electronics: From Materials to Devices, June 8, 2009 - June 12, 2009.*9 edn 2331-2335 (2010).

24 Valenta, M. W., Johnson, V. J., Cowan, R. E., Douglass, R. M. and Doughert.Je. Ferroelectric studies on systems Pb[Sc0.5-(Nb,Ta)0.5)x(Ti,Zr,Hf,Sn)1-x]O3. *American Ceramic Society Bulletin* **46**, 383 (1967).

25 Yang, P. and Payne, D. A. Thermal-stability of field-forced and field-assisted antiferroelectric-ferroelectric phase-transformations in Pb(Zr,Sn,Ti)O3. *Journal of Applied Physics* **71**, 1361-1367 (1992).

26 Mohiddon, M. A., Kumar, A. and Yadav, K. L. Effect of Nd doping on structural, dielectric and thermodynamic properties of PZT (65/35) ceramic. *Physica B-Condensed Matter* **395**, 1-9 (2007).

27 Laurent, M., Schreiner, U., Langjahr, P. A., Glazounov, A. E. and Hoffmann, M. J. Microstructural and electrical characterization of La-doped PZT ceramics prepared by a precursor route. *Journal of the European Ceramic Society* **21**, 1495-1498 (2001).

28 www.trstechnologies.com/Materials [online access] 31/07/2014.

29 www.morgantechnicalceramics.com/materials/lead-zirconate-titanate-pzt [online access] 31/07/2014.

30 Young, Y. S., Kim, S. H., Lee, S. J., Kim, H. K. and Lee, M. J. Fabrication and frequency response of dual-element ultrasonic transducer using PZT-5A thick film. *Sensors and Actuators A-Physical* **125**, 463-470 (2006).

31 Cho, K. H., Seo, C. E. and Choi, Y. S. Effects of impact conditions on the shock response of pzt-5a ceramics for feg devices. *Journal of the Korean Physical Society* **57**, 975-979 (2010).

32 Jiang, Y., Demore, C. E. M., Meggs, C. *et al.* Micro-moulded randomised piezocomposites for high frequency ultrasound imaging. *2012 IEEE International Ultrasonics Symposium* (2012).

33 Chaplya, P. M. and Carman, G. P. Compression of PZT-5H piezoelectric ceramic at constant electric field: Investigation of energy absorption mechanism. *Smart Structures and Materials 2002: Active Materials: Behavior and Mechanics, Proceedings of the Society of Photo-Optical Instrumentation Engineers (Spie)* (ed C. S. Lynch) **4699**, 124-132 (2002).

34 Singh, P., Smith, L. S., Bezdecny, M. *et al.* Additive manufacturing of PZT-5h piezoceramic for ultrasound transducers. *2011 IEEE International Ultrasonics Symposium* (2012).

35 Alguero, M., Guiu, F. and Reece, M. J. Degradation of PZT-4D hard piezoceramics under moderate heating. *Journal of the European Ceramic Society* **20**, 2705-2711 (2000).

36 Prabakar, K. Acoustic emission from PZT-5A and PZT-8 ceramics during the application of AC field at different frequencies. *International Journal of Modern Physics B* **21**, 4707-4714 (2007).

37 EU-Directive 2002/96/EC: Waste Electrical and Electronic Equipment (WEEE). *Office Journal of the European Union* **46**, 24-38 (2003).

38 EU-Directive 2002/95/EC: Restriction of the Use of Certain Hazardous Substances in Electrical and Electronic Equipment (RoHS). *Office Journal of the European Union* **46**, 19-23 (2003).

39 Saito, Y., Takao, H., Tani, T. *et al.* Lead-free piezoceramics. *Nature* **432**, 84-87 (2004).

40 Zhang, Y. R., Li, J. F. and Zhang, B. P. Enhancing electrical properties in NBT-KBT lead-free piezoelectric ceramics by optimizing sintering temperature. *Journal of the American Ceramic Society* **91**, 2716-2719 (2008).

41 Ahn, C. W., Han, G., Ryu, J. *et al.* Composition design rule for high piezoelectric voltage coefficient in (K0.5Na0.5)NbO3 based Pb-free ceramics. *Japanese Journal of Applied Physics* **51**, 09MD10 (2012).

42 Liu, W. F. and Ren, X. B. Large piezoelectric effect in Pb-free ceramics. *Physical Review Letters* **103**, 257602 (2009).

43 Shirane, G., Newnham, R. and Pepinsky, R. Dielectric properties and phase transitions of NaNbO3 and (Na,K)NbO3. *Physical Review* **96**, 581-588 (1954).

44 Wood, E. A. Polymorphism in potassium niobate, sodium niobate, and other ABO3 compounds. *Acta Crystallographica* **4**, 353-362 (1951).

45 Egerton, L. and Dillon, D. M. Piezoelectric and dielectric properties of ceramics in the system potassium sodium niobate. *Journal of the American Ceramic Society* **42**, 438-442 (1959).

46 Birol, H., Damjanovic, D. and Setter, N. Preparation and characterization of (K0.5Na0.5)NbO3 ceramics. *Journal of the European Ceramic Society* **26**, 861-866 (2006).

47 Singh, K., Lingwal, V., Bhatt, S. C., Panwar, N. S. and Semwal, B. S. Dielectric properties of potassium sodium niobate mixed system. *Materials Research Bulletin* **36**, 2365-2374 (2001).

48 Du, H. L., Li, Z. M., Tang, F. S. *et al.* Preparation and piezoelectric properties of (K0.5Na0.5)NbO3 lead-free piezoelectric ceramics with pressure-less sintering. *Materials Science and Engineering B-Solid State Materials for Advanced Technology* **131**, 83-87 (2006).

49 Kosec, M. and Kolar, D. Activated sintering and electrical properties of NaKNbO3. *Materials Research Bulletin* **10**, 335-339 (1975).

50 Zhao, P. and Zhang, B. P. High piezoelectric d33 coefficient in Li/Ta/Sb-codoped lead-free (Na,K)NbO(3) ceramics sintered at optimal temperature. *Journal of the American Ceramic Society* **91**, 3824-3824 (2008).

51 Yoo, J., Lee, K., Chung, K. *et al.* Piezoelectric and dielectric properties of (LiNaK)(NbTaSb)O3 ceramics with variation in poling temperature. *Japanese Journal of Applied Physics Part 1-Regular Papers Brief Communications & Review Papers* **45**, 7444-7448 (2006).

52 Zuo, R. Z., Fang, X. S. and Ye, C. Phase structures and electrical properties of new lead-free (Na0.5K0.5)NbO3-(Bi0.5Na0.5)TiO3 ceramics. *Applied Physics Letters* **90**, 092904 (2007).

53 Du, H. L., Zhou, W. C., Zhu, D. M. and Fa, L. Sintering characteristic, microstructure, and dielectric relaxor behavior of (K(0.5)Na(0.5))NbO(3)-(Bi(0.5)Na(0.5))TiO(3) lead-free ceramics. *Journal of the American Ceramic Society* **91**, 2903-2909 (2008).

54 Ahn, C. W., Park, H. Y., Nahm, S. *et al.* Structural variation and piezoelectric properties of 0.95(Na0.5K0.5)NbO3-0.05BaTiO(3) ceramics. *Sens. Actuator A-Phys.* **136**, 255-260 (2007).

55 Park, H. Y., Ahn, C. W., Song, H. C. *et al.* Microstructure and piezoelectric properties of 0.95(Na0.5K0.5)NbO3-0.05BaTiO(3) ceramics. *Applied Physics Letters* **89**, 062906 (2006).

56 Smolenskii, G. A., Isupov, V. A., Agranovskaya, A. I. and Krainik, N. N. New ferroelectrics of complex composition .4. *Soviet Physics-Solid State* **2**, 2651-2654 (1961).

57 Buhrer, C. F. Some properties of bismuth perovskites. *Journal of Chemical Physics* **36**, 798 (1962).

58 Wada, T., Fukui, A. and Matsuo, Y. Preparation of (K0.5Bi0.5)TiO3 ceramics by polymerized complex method and their properties. *Japanese Journal of Applied Physics Part 1-Regular Papers Short Notes & Review Papers* **41**, 7025-7028 (2002).

59 Sakata, K. and Masuda, Y. Ferroelectric and antiferroelectric properties of (Na0.5Bi0.5)TiO3-SrTiO3 solid-solution ceramics. *Ferroelectrics* **7**, 347-349 (1974).

60 Hiruma, Y., Aoyagi, R., Nagata, H. and Takenaka, T. Ferroelectric and piezoelectric properties of (Bi1/2K1/2)TiO3 ceramics. *Japanese Journal of Applied Physics Part 1-Regular Papers Brief Communications & Review Papers* **44**, 5040-5044 (2005).

61 Hiruma, Y., Nagata, H. and Takenaka, T. Grain-size effect on electrical properties of (Bi1/2K1/2)TiO3 ceramics. *Japanese Journal of Applied Physics Part 1-Regular Papers Brief Communications & Review Papers* **46**, 1081-1084 (2007).

62 Wada, T., Toyoike, K., Imanaka, Y. and Matsuo, Y. Dielectric and piezoelectric properties of (A(0.5)Bi(0.5))TiO3-ANbO(3) (A = Na, K) systems. *Japanese Journal of Applied Physics Part 1-Regular Papers Short Notes & Review Papers* **40**, 5703-5705 (2001).

63 Chen, M., Xu, Q., Kim, B. H. *et al.* Structure and electrical properties of (Na0.5Bi0.5)(1-x)BaxTiO3 piezoelectric ceramics. *Journal of the European Ceramic Society* **28**, 843-849 (2008).

64 Hiruma, Y., Aoyagi, R., Nagata, H. and Takenaka, T. Piezoelectric properties of BaTiO3-(Bi1/2K1/2)TiO3 ferroelectric ceramics. *Japanese Journal of Applied Physics Part 1-Regular Papers Short Notes & Review Papers* **43**, 7556-7559 (2004).

65 Sasaki, A., Chiba, T., Mamiya, Y. and Otsuki, E. Dielectric and piezoelectric properties of (Bi0.5Na0.5)TiO3-(Bi0.5K0.5)TiO3 systems. *Japanese Journal of Applied Physics Part 1-Regular Papers Short Notes & Review Papers* **38**, 5564-5567 (1999).

66 Zhang, S. J., Shrout, T. R., Nagata, H., Hiruma, Y. and Takenaka, T. Piezoelectric properties in (K0.5Bi0.5)TiO3-(Na0.5Bi0.5)TiO3-BaTiO3 lead-free ceramics. *IEEE Transactions on Ultrasonics Ferroelectrics and Frequency Control* **54**, 910-917 (2007).

67 Zhang, S. T., Kounga, A. B., Aulbach, E. *et al.* Lead-free piezoceramics with giant strain in the system Bi0.5Na0.5TiO3-BaTiO3-K0.5Na0.5NbO3. I. Structure and room temperature properties. *Journal of Applied Physics* **103**, 034107 (2008).

68 Takenaka, T., Nagata, H., Hiruma, Y., Yoshii, Y. and Matumoto, K. Lead-free piezoelectric ceramics based on perovskite structures. *Journal of Electroceramics* **19**, 259-265 (2007).

69 Choy, S. H., Wang, X. X., Chong, C. P. *et al.* 0.90(Bi1/2Na1/2)TiO3-0.05(Bi1/2K1/2)TiO3-0.05BaTiO(3) transducer for ultrasonic wirebonding applications. *Applied Physics a-Materials Science & Processing* **84**, 313-316 (2006).

70 Choy, S. H., Wang, X. X., Chan, H. L. W. and Choy, C. L. Study of compressive type accelerometer based on lead-free BNKBT piezoceramics. *Applied Physics a-Materials Science & Processing* **82**, 715-718 (2006).

71 Damjanovic, D., Biancoli, A., Batooli, L., Vahabzadeh, A. and Trodahl, J. Elastic, dielectric, and piezoelectric anomalies and Raman spectroscopy of 0.5Ba(Ti0.8Zr0.2)O3-0.5(Ba0.7Ca0.3)TiO3. *Applied Physics Letters* **100**, 192907 (2012).

72 Lin, Q., Jiang, M., Lin, D. M. *et al.* Effects of La-doping on microstructure, dielectric and piezoelectric properties of Ba0.85Ca0.15Ti0.90Zr0.10O3 lead-free ceramics. *Journal of Materials Science-Materials in Electronics* **24**, 734-739 (2013).

73 Mishra, P., Sonia and Kumar, P. Effect of sintering temperature on dielectric, piezoelectric and ferroelectric properties of BZT-BCT 50/50 ceramics. *Journal of Alloys and Compounds* **545**, 210-215 (2012).

74 Li, B. Z., Blendell, J. E. and Bowman, K. J. Temperature-dependent poling behavior of lead-free BZT-BCT piezoelectrics. *Journal of the American Ceramic Society* **94**, 3192-3194 (2011).

75 Shi, M., Zhong, J. G., Zuo, R. Z. *et al.* Effect of annealing processes on the structural and electrical properties of the lead-free thin films of (Ba0.9Ca0.1)(Ti0.9Zr0.1)O-3. *Journal of Alloys and Compounds* **562**, 116-122 (2013).

76 Haugen, A. B., Forrester, J. S., Damjanovic, D. *et al.* Structure and phase transitions in 0.5(Ba0.7Ca0.3TiO3)-0.5(BaZr0.2Ti0.8O3) from -100 degrees C to 150 degrees C. *Journal of Applied Physics* **113**, 014103 (2013).

77 Tian, Y., Wei, L. L., Chao, X. L., Liu, Z. H. and Yang, Z. P. Phase transition behavior and large piezoelectricity near the morphotropic phase boundary of lead-free (Ba0.85Ca0.15)(Zr0.1Ti0.9)O-3 ceramics. *Journal of the American Ceramic Society* **96**, 496-502 (2013).

78 Cui, Y. R., Liu, X. Y., Jiang, M. H. *et al.* Lead-free (Ba0.7Ca0.3)TiO3-Ba(Zr0.2Ti0.8)O-3-xwt % CuO ceramics with high piezoelectric coefficient by low-temperature sintering. *Journal of Materials Science-Materials in Electronics* **23**, 1342-1345 (2012).

79 Cui, Y. R., Liu, X. Y., Jiang M. H. *et al.* Lead-free (Ba0.85Ca0.15)(Ti0.9Zr0.1)O-3-CeO2 ceramics with high piezoelectric coefficient obtained by low-temperature sintering. *Ceramics International* **38**, 4761-4764 (2012).

80 Cui, Y. R., Yuan, C. L., Liu, X. Y., Zhao, X. Y. and Shan, X. Lead-free (Ba0.85Ca0.15)(Ti0.9Zr0.1)O-3-Y2O3 ceramics with large piezoelectric coefficient obtained by low-temperature sintering. *Journal of Materials Science-Materials in Electronics* **24**, 654-657 (2013).

81 Han, C., Wu, J. G., Pu, C. H. *et al.* High piezoelectric coefficient of Pr2O3-doped Ba0.85Ca0.15Ti0.90Zr0.10O3 ceramics. *Ceramics International* **38**, 6359-6363 (2012).

82 Bai, W. F., Li, W., Shen, B. and Zhai, J. W. Piezoelectric and strain properties of strontium-doped BZT-BCT lead-free ceramics. *High-Performance Ceramics Vii, Pts 1 and 2, Key Engineering Materials* (eds W. Pan & J. H. Gong) **512-515**, 1385-1389 (2012).

83 Zhou, J. J., Li, J. F., Cheng, L. Q. *et al.* Addition of small amounts of BiFeO3 to (Li,K,Na)(Nb,Ta)O3 lead-free ceramics: Influence on phase structure, microstructure and piezoelectric properties. *Journal of the European Ceramic Society* **32**, 3575-3582 (2012).

84 Lee, S. H., Lee, S. G. and Lee, Y. H. Electrical properties of lead-free 0.98(Na0.5K0.5)NbO3-0.02Ba(Zr0.52Ti0.48)O-3 piezoelectric ceramics by optimizing sintering temperature. *Nanoscale Research Letters* **7**, 15 (2012).

85 Wang, X. X., Chan, H. L. W. and Choy, C. L. (Bi0.5Na0.5)(0.94)Ba0.06TiO3 lead-free ceramics with simultaneous addition of CeO2 and La2O3. *Applied Physics a-Materials Science & Processing* **80**, 333-336 (2005).

86 Yoo, J. Y., Oh, D. G., Jeong, Y., Hong, J. and Jung, M. Y. Dielectric and piezoelectric characteristics of lead-free Bi-0.5(Na0.84K0.16)(0.5)TiO3 ceramics substituted with Sr. *Materials Letters* **58**, 3831-3835 (2004).

87 Rice, R. W. Ceramics fabrication technology. *Marcel Dekker Inc.: New York*, pp. 100-126 (2003).

88 Richerson, D. W. Modern ceramic engineering: Properties, processing and use in design (3rd edition). *CRC Press Taylor &Francis Group: FL*, pp. 371-399, 403-468, 477-498 (2006).

89 White, N. M. and Turner, J. D. Thick-film sensors: Past, present and future. *Measurement Science & Technology* **8**, 1-20 (1997).

90 Zhu, D., Glenne-Jones, P., White, N. *et al.* Screen printed piezoelectric films for energy harvesting. *Advances in Applied Ceramics* **112**, 79-84 (2013).

91 Garcia-Gancedo, L., Olhero, S. M., Alves, F. J. *et al.* Application of gel-casting to the fabrication of 1-3 piezoelectric ceramic-polymer composites for high-frequency ultrasound devices. *Journal of Micromechanics and Microengineering* **22**, 125001 (2012).

92 Barsoum, M. W. Fundamentals of ceramics. *Taylor & Francis: New York*, pp. 302-345 (2003).

93 Huan, Y., Wang, X. H., Fang, J. and Li, L. T. Grain size effects on piezoelectric properties and domain structure of BaTio3 ceramics prepared by two-step sintering. *Journal of the American Ceramic Society* **96**, 3369-3371 (2013).

94 Sakaki, C., Newalkar, B. L., Komarneni, S. and Uchino, K. Grain size dependence of high power piezoelectric characteristics in Nb doped lead zirconate titanate oxide ceramics. *Japanese Journal of Applied Physics Part 1-Regular Papers Short Notes & Review Papers* **40**, 6907-6910 (2001).

95 Tick, T., Perantie, J., Jantunen, H. and Uusimaki, A. Screen printed low-sintering-temperature barium strontium titanate (BST) thick films. *Journal of the European Ceramic Society* **28**, 837-842 (2008).

96 Rajesh, S., Jantunen, H., Letz, M. and Pichler-Willhelm, S. Low temperature sintering and dielectric properties of alumina-filled glass composites for LTCC applications. *International Journal of Applied Ceramic Technology* **9**, 52-59 (2012).

97 Yoo, J. Y., Lee, C., Jeong, Y. H. *et al.* Microstructural and piezoelectric properties of low temperature sintering PMN-PZT ceramics with the amount of Li2CO3 addition. *Materials Chemistry and Physics* **90**, 386-390 (2005).

98 Wang, M. C., Huang, M. S. and Wu, N. C. Effects of 30B(2)O(3)-25Bi(2)O(3)-45CdO glass addition on the sintering of 12Pb(Ni-1/3 Sb-2/3)O-3-40PbZrO(3)-48PbTiO(3) piezoelectric ceramics. *Journal of the European Ceramic Society* **21**, 695-701 (2001).

99 Kok, S.-L., White, N. M. and Harris, N. R. Fabrication and characterization of free-standing thick-film piezoelectric cantilevers for energy harvesting. *Measurement Science and Technology* **20**, 124010 (2009).

100 Li, C. X., Yang, B., Zhang, S. T., Zhang, R. and Cao, W. W. Effects of sintering temperature and poling conditions on the electrical properties of Ba0.70Ca0.30TiO3 diphasic piezoelectric ceramics. *Ceramics International* **39**, 2967-2973 (2013).

101 Kamel, T. M., Kools, F. and de With, G. Poling of soft piezoceramic PZT. *Journal of the European Ceramic Society* **27**, 2471-2479 (2007).

102 Kamel, T. M. and de With, G. Poling of hard ferroelectric PZT ceramics. *Journal of the European Ceramic Society* **28**, 1827-1838 (2008).

103 Waller, D., Iqbal, T. & Safari, A. Poling of lead zirconate titanate ceramics and flexible piezoelectric composites by the corona discharge technique. *Journal of the American Ceramic Society* **72**, 322-324 (1989).

104 Kholkin, A. L., Tagantsev, A. K., Colla, E. L., Taylor, D. V. and Setter, N. Piezoelectric and dielectric aging in Pb(Zr,Ti)O-3 thin films and bulk ceramics. *Integrated Ferroelectrics* **15**, 317-324 (1997).

CHAPTER 4. PIEZOELECTRIC AND VIBRATIONAL ENERGY HARVESTING

4.1 Introduction

The concept of harvesting and converting kinetic energy into electricity by utilising piezoelectric energy harvesters (PEHers), especially for vibrational energy, was introduced in Chapter 2. A simplified spring-mass system is shown in Figure 4-1. Typically, elements of piezoelectric materials are the core components in PEHers to convert energy[1-3]. But configurations acting as an equivalent 'spring' (e.g. cantilever substrate, etc.) to transmit motion from the host to the core components, and stress/strain magnifiers (e.g. proof mass, magnets, etc.) used for maximising/adjusting deformations of piezoelectric materials thus optimising outputs, are also included in PEHers[1-3].

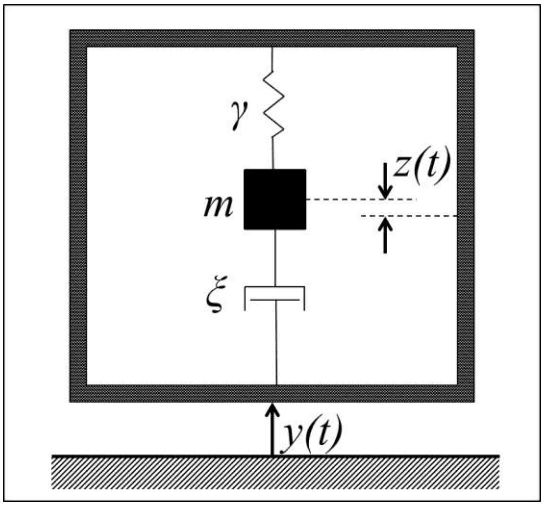

Figure 4-1. Schematic of a spring-mass system (reproduced according to reference[4])

Such structures mechanically perform as a spring-mass system, which can be mathematically expressed by Equation 4-1[4], where $y(t)$ is the housing vibration displacement, $z(t)$ is the relative motion of the seismic mass, and m, ξ, γ represent the seismic mass, damping constant and spring constant of the system, respectively. However, this is only a general assumption, and more accurate predictions of resonant frequency, generated voltage and power need further analyses, which will be introduced in the following sections.

$$m\ddot{z}(t) + \xi\dot{z}(t) + \gamma z(t) = -m\ddot{y}(t) \quad (4\text{-}1)$$

In addition to the main harvester structure presented above, a corresponding external circuit needs to be integrated into the system, providing voltage/power conditioning, rectification and regulation[5,6], as well as energy storage in certain cases[7]. Considering this, the performance of a PEHer, including output voltage, output power and energy conversion efficiency, may be affected by mechanical configurations, equivalent circuits and piezoelectric materials. These will also be introduced in the following sections.

4.2 Feasible Piezoelectric Energy Harvesting Configurations

4.2.1 Cantilever

The majority of the research involving PEHers to date has focused on cantilever configurations[8,9], as shown in Figure 4-2 (a). A piece of thin piezoelectric element is attached on a substrate, forming a unimorph cantilever. The direction of polarization is along the thickness of the piezo-element, and the cantilever is fixed on a base on one end while free on the other end where a tip mass is attached. In principle, when the fixed end of the cantilever vibrates upwards (Figure 4-2 (b)), the cantilever bends downwards because of inertia, causing the piezoelectric element to be deformed. Thus there will be an electric potential generated across the piezo-element. In a similar way, when the cantilever vibrates downwards (Figure 4-2 (c)), the piezo-element is compressed effectively, generating an electric potential with an opposite direction. Therefore, if the cantilever keeps vibrating, an AC output voltage will be generated.

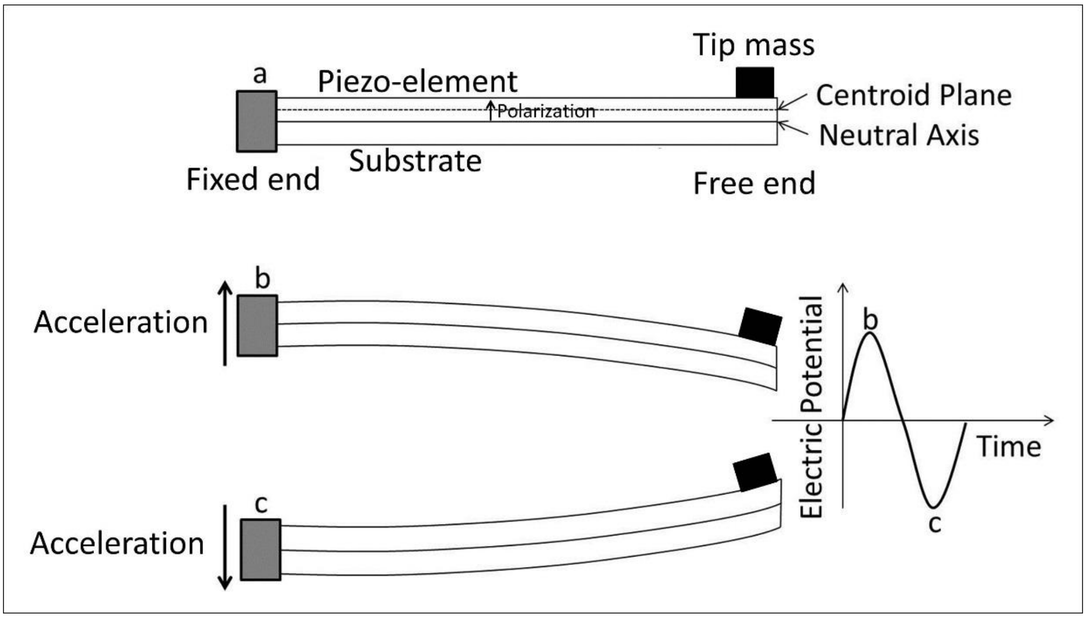

Figure 4-2. Schematics of cantilever configuration (side-view).

This working mode, commonly known as the '31-mode' (deformation is perpendicular to polarization), has been proved to be more efficient than the '33-mode' (deformation is parallel with polarization, which will be presented later), as although the '31' piezoelectric response is usually weaker than that of '33' ($d_{31} < d_{33}$), the '31' deformation tends to be much larger thus is able to induce a larger output[1,8]. It should be noted that the centroid plane of the piezo-element must not be coincident with the neutral axis of the entire cantilever (Figure 4-2 (a)), otherwise no voltage can be extracted[10].

In terms of actual designs, bimorph cantilevers, where two piezo-elements are attached on both surfaces of a substrate or to each other (Figure 4-3), are also commonly utilised in order to improve the open-circuit voltage[10] or output current (hence output power)[11,12]. It should be noted that in the case of the bimorph, a central electrode is needed, or the substrate for the bimorph (and for the unimorph) can be electrically conducting[13]. In addition, multi-morph configurations containing several piezoelectric elements can be occasionally considered[14,15], and element shapes can be tailored to optimise either output or efficiency. A rectangular shape is the most typical and can be simply fabricated[8]; whereas triangular or trapezoidal shapes allow more even strain distribution and thus are capable of increasing output power and efficiency[8,16]. The initial state of the cantilevers also has effect on the harvesting capability and working frequency range of PEHers. For instance, pre-stressed or pre-curved cantilevers are able to help enhance energy harvesting capability[17,18]; and pre-stressed beams clamped on both sides can exhibit a wider range of responses to excitation frequencies[19].

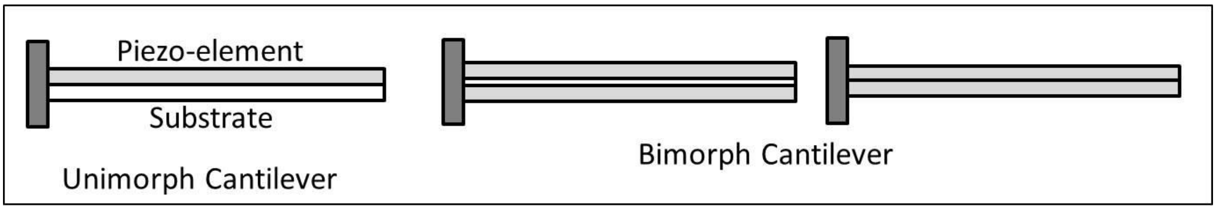

Figure 4-3. Schematics of unimorph and bimorph cantilevers.

4.2.2 Free-standing Thick-film Structure

For the ‘31-mode’ PEHers, piezoelectric bulk sheets have been conventionally fabricated separately then glued onto the substrates[1,20]. This process is simple to implement, however micro-scale dimensions are difficult to be achieved, making it incompatible with micro-electromechanical systems (MEMS) which are the one potential end use for PEHers. Also, it requires additional processing for reliable bonding in order to prevent fatigue and delamination in long-time use. As a result, thick-films co-sintered with substrates (e.g. silicon on insulator (SOI) or stainless steel), providing firm attachment between the piezo-elements and substrates, have been demonstrated, enabling integration of PEHers with MEMS[21]. However, the constraint effect caused by the substrate would lead to poor sintering and consequently reduced piezoelectric properties. During sintering, a piezoelectric thick film will shrink, whereas the supporting substrate is usually dense, and will not shrink further. When they are attached to each other and co-sintered, large residual stresses on the interface area are likely to prevent the film densifying fully, resulting in deteriorated piezoelectric properties. This may also lead to the piezoelectric layer fracturing easily when being poled. In this configuration, the substrate is purely a supporting structure and may absorb or dissipate the harvested energy, thus reducing the overall energy conversion efficiency. In addition, as the output of PEHers depend on relevant piezoelectric properties[3], but they are unable to be directly and accurately measured for the thick-films with substrates[22], theoretical modelling and design of the harvesters may become unreliable.

To solve the problem, a free-standing thick-film cantilever, firstly reported in 2008[23], may be helpful. The free-standing thick-film configuration was defined as ‘one that stands alone (or on its own foundation) and is free from external support or attachment to a non-electro-active platform’[24]. Figure 4-4 shows the schematics of the reported structure based on fabrication by screen printing. A carbon layer was incorporated into the normal multi-layer thick-film structure as the sacrificial layer, and this could be totally burnt off during co-sintering, thus producing a free-standing structure[24]. PZT paste and Ag/Pd paste were selected to be the piezo-elements and electrodes respectively[24], however the shrinkage rate of the electrodes did not match that of the PZT, leading to a delamination phenomenon. Despite that, the problem was temporarily solved by printing two non-active piezoelectric layers as the top and bottom layer. Unfortunately, few free-standing thick-film PEHers have been reported since then.

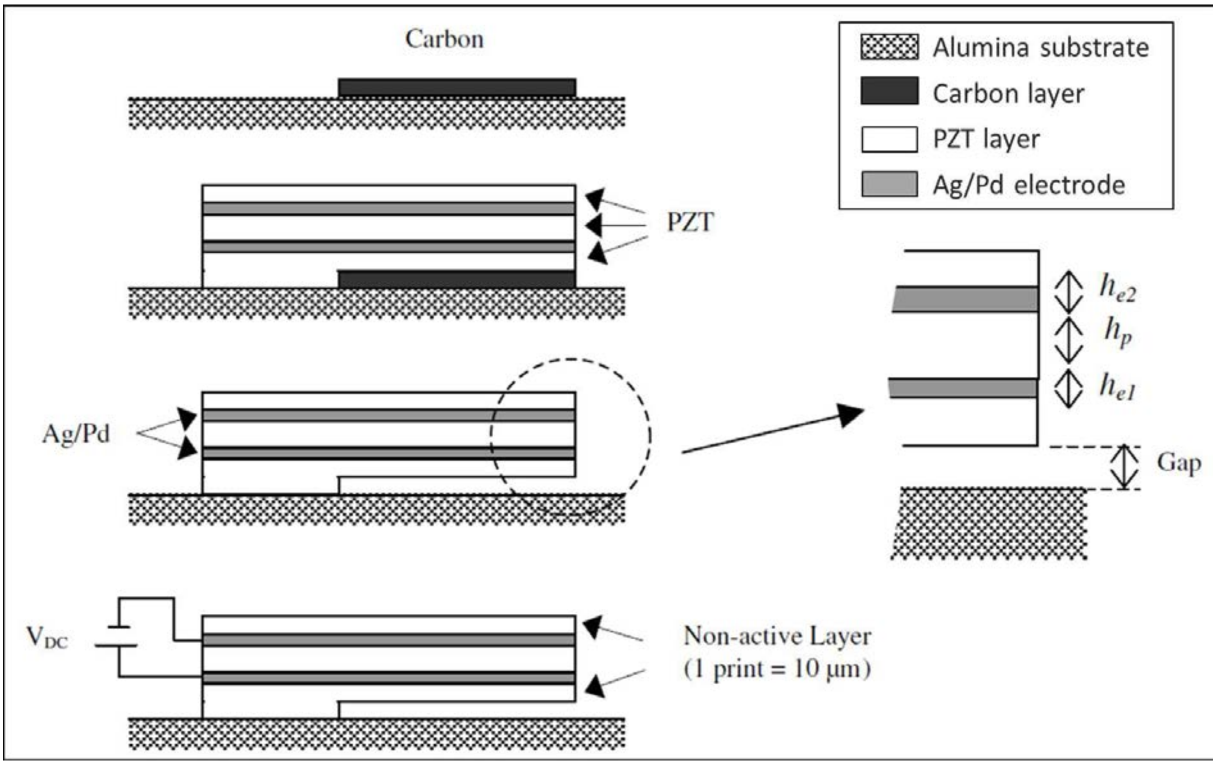

Figure 4-4. Schematics of fabrication and structure of the free-standing thick-film cantilever[24].

4.2.3 Other Structures

Other structures of PEHers have also been investigated to explore the energy generation capability and the effects of mechanical structures on output. Figure 4-5 shows a practical design of cymbal structure[25], consisting of a bulk PZT disc with electrodes (piezo-element), a pair of brass rings (for connection with external circuits) and a pair of convex steel plates (cymbal elastic elements). The force is vertically applied on the steel plates and is subsequently transferred to the disc, deforming it along the radial direction and effectively working in a '31 mode'[9,25]. This configuration is able to withstand higher loads than the cantilever[8,26], and is suitable for low working frequencies (several Hz)[25].

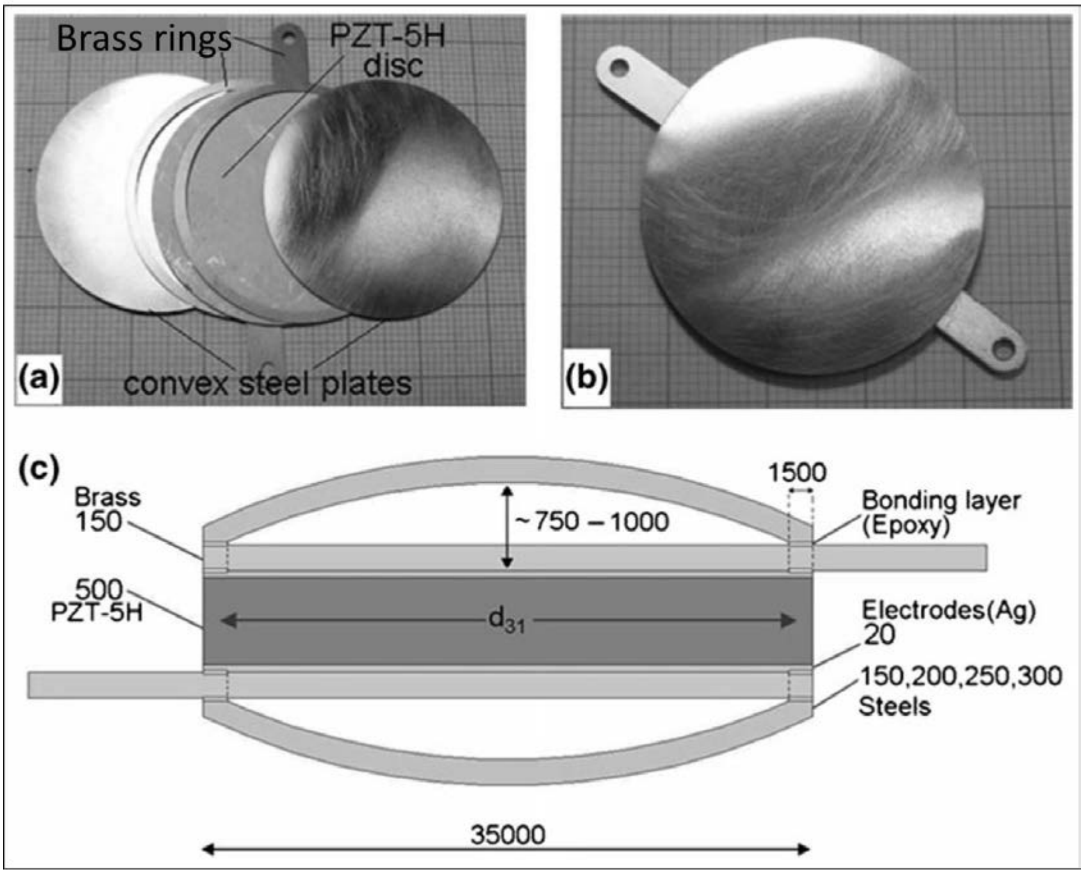

Figure 4-5. Pictures and schematic of a cymbal configuration (dimension unit in μm)[25].

Figure 4-6 shows a configuration of circular diaphragm, where a metal plate is clamped on a rigid base with attached piezoelectric disc and proof mass[27,28]. When the base vibrates, the inertia of the proof mass is able to force the metal disc as well as the piezoelectric disc bending up and down, generating charge across the piezo-element[27,28]. As the polarization of the piezoelectric disc is usually parallel to the thickness direction, this configuration in fact works in the '31 mode' as well, which is similar to the cantilever. With a metal support, this type of harvester tends to work with high accelerations or in fluctuating pressure environments[8].

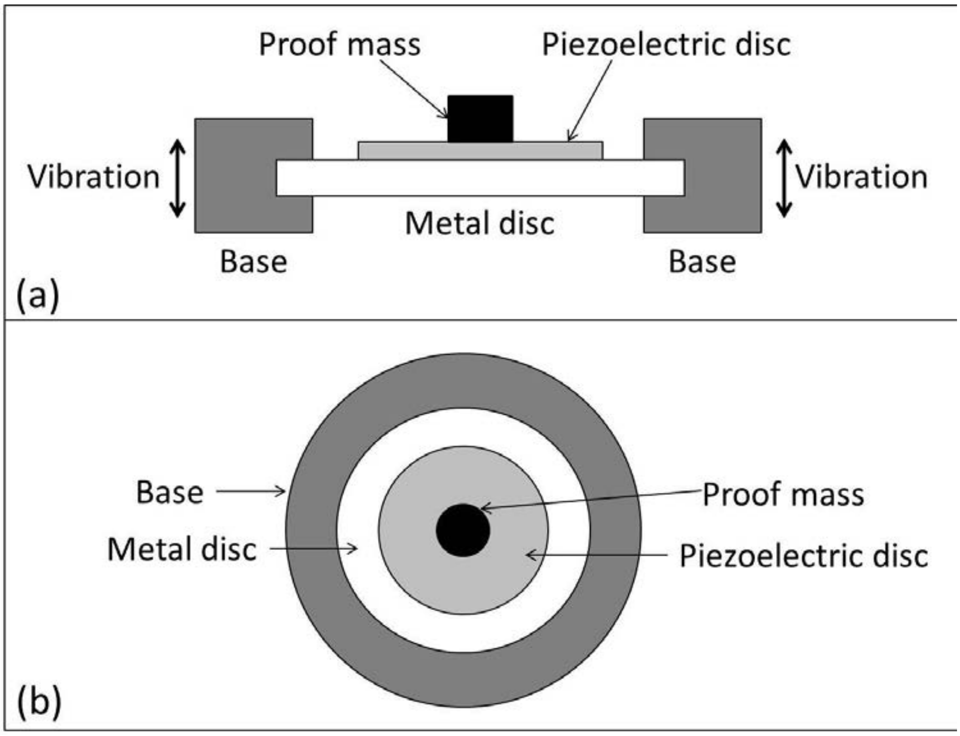

Figure 4-6. Schematics of circular diaphragm configuration: (a) side-view; (b) top-view (reproduced according to multiple sources[27,28]).

Although the '31 mode has' dominated the designs of PEHers, the '33 mode' can still be applied if the driving stress is large enough. For instance, a stack of thin piezoelectric elements combined together tends to generate a much higher power under large stress which is applied parallel to the polarization direction, as the piezoelectric response in '33 mode' (d_{33}) is usually a factor of about 2 larger than that in '31 mode' (d_{31})[29,30].

The '15 mode' (or shear mode) has recently been considered, of which the corresponding configuration is shown in Figure 4-7[31]. The polarization is parallel with the electrodes (while for 31 mode and 33 mode, the polarization is perpendicular to the electrodes), and the piezo-element is sandwiched by the proof mass and the base[31]. The vibration is also parallel to the polarisation direction, as shown in the figure, inducing a shear deformation of the piezo-element. This is a promising working mode to further enhance the output of PEHers due to the potentially higher energy harvesting factors in the '15 mode' than those in the '33 mode' or ‘31 mode’[31,32], though the fabrication of the materials (e.g. poling, re-electroding) may become more complex. This will be presented in detail in the following sections.

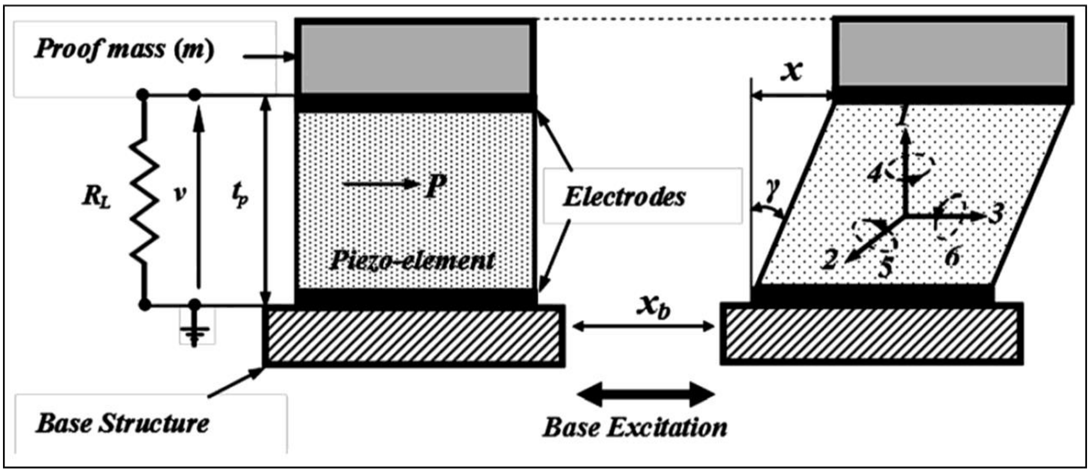

Figure 4-7. Schematics of shear mode harvester configuration (side-view)[31].

4.3 Beam Vibration Theory

4.3.1 Resonant Frequency

In terms of the design of the cantilever configuration, resonant frequencies where the amplitudes reach a maximum must be predicted in advance, as they define the optimum working conditions in which the PEHers should be operated in order to maximise the output. The Bernoulli-Euler beam theory is a reliable mathematical model for calculating the fundamental resonant frequencies of thin long cantilevers (length > 20×thickness)[33], according to which the fundamental frequency (f_0) of a multi-layer composite cantilever without tip proof mass can be illustrated by Equations 4-2, 4-3 and 4-4[34,35].

$$f_0 = \frac{\lambda_0^2}{2\pi L^2} \cdot \sqrt{\frac{YI}{m_{pul}}} \quad (4\text{-}2)$$

$$YI = \sum Y_\psi w \int y^2 \cdot dy \quad (4\text{-}3)$$

$$m_{pul} = \sum \rho_{\psi} w \int dy \quad (4\text{-}4)$$

In the equations, λ_0 is the function of fundamental resonant boundary conditions, which has a value of 1.8751 for a cantilever[34]; L and w are the length and width of the cantilever, respectively; Y is Young's modulus; I is the moment of inertia; m_{pul} is the mass per unit length of the cantilever; ρ is the material density; y is the distance from thickness neutral centre to each layer's boundary; and the subscript ψ represents a certain layer. A symmetric structure along the thickness direction is suggested[34]. When considering additional tip mass (m_{tip}), the overall natural resonant frequency (f) of the system can be expressed by Equation 4-5[24], where m_{can} is the mass of the entire cantilever.

$$f = f_0 \cdot \sqrt{\frac{0.236 m_{can}}{0.236 m_{can} + m_{tip}}} \quad (4\text{-}5)$$

According to the above model, the resonant frequency of a cantilever-based PEHer can be designed by tailoring either the dimensions and tip mass or the material physical/elastic properties.

4.3.2 Bandwidth

The bandwidth of a vibrational energy harvester can be defined as the full width at half maximum (FWHM) of its output-input frequency spectrum divided by its resonant frequency[36], as described in Figure 4-8.

For energy harvesters based on conventional beam-mass inertial systems (e.g. cantilever with tip mass), the bandwidth is considered extremely narrow (< 5%) due to the inherent working mechanism, with a resulting excellent performance only at or very close to their resonant frequencies[37,38]. However, a real environmental or machinery vibration normally has a wide bandwidth comprising several main frequencies mixed together and affecting each other, and even the main frequencies could shift slightly dependent on the circumstances[1,39]. Thus, in this situation, the efficiency of the harvesters are dramatically reduced, which is one of the major drawbacks of cantilever based PEHers.

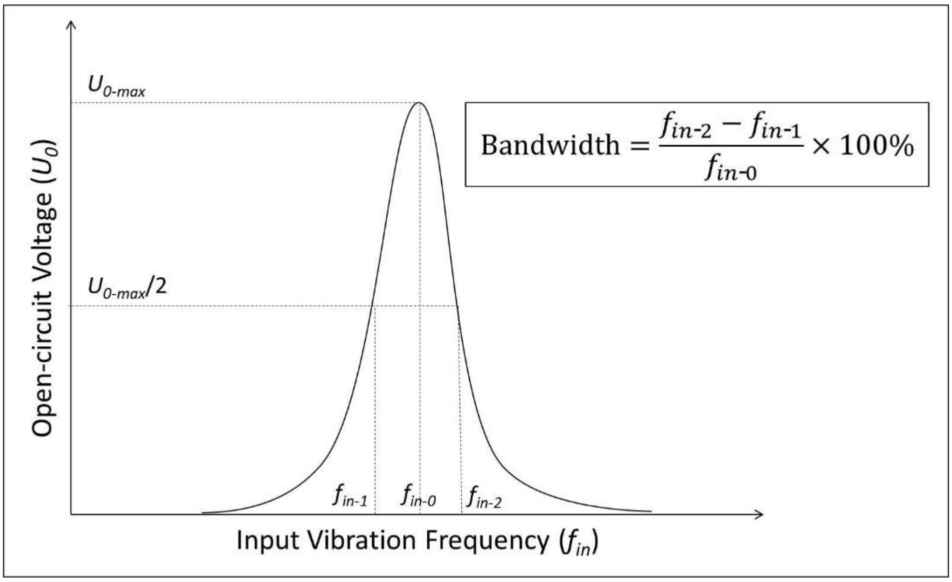

Figure 4-8. Definition of the bandwidth of vibrational energy harvesters.

To address this issue, non-linear technology[40-42] or harvester arrays[43,44], or a combination of both[45], can be utilised to widen the bandwidth of PEHers. In particular, for non-linear technology, single or multiple non-linear amplitude magnifiers have been applied on a typical piezoelectric cantilever. The magnifiers could be developed using a special tip mass (e.g. asymmetrically attached[46]), multiple spring-mass systems[47], magnetic coupled magnifiers[42], etc., or could be re-formed beams with specifically designed shapes, such as a multi-stage beam[48] or vertical placed beam[49]. The function of a non-linear magnifier is to create a bifurcation of the original output vs. frequency peak, or to suppress the optimum output but delaying its decrease, both of which tend to effectively widen the working frequency range[36]. In contrast, the method of integrating harvester arrays is more straightforward, by precisely designing the resonant frequencies of several individual harvesters with typical cantilever configurations[37]. The output peaks of the individual harvesters can be split in order to fit different major vibrations with frequencies far from each other, or can partially cover each other to obtain a wideband response, for vibrations where a major frequency co-exists with noise around the frequency[36]. The advantage of the array configuration over the non-linear method is that it is not only capable of a wide bandwidth, but also of enhancement of the overall output power, if two or more output peaks overlap[36]. However, the potential problem of the former one may involve that an array with multi-degrees of freedom tends to work in an unsynchronized regime because of mistuning stiffness[50]. This means if the individual harvesters in an array are connected directly to each other but via not any rectifiers, as the generated electric signals are alternating between positive and negative and their different stiffness cannot ensure synchronising vibration, the positive electric potential generated by an individual harvester may be affected that by another (or vice versa), thus reducing the overall output, especially when the individual harvesters are connected in series or share the same proof mass[50-52]. Although such a problem needs complex mathematical analyses[50], it has been practically solved by the use of a rectifier for each individual harvester before being connected together[43]. Also, as an array contains two or more individual harvesters, the overall size of the integrated harvester is likely to be larger.

4.4 Piezoelectric Cantilever Theory

4.4.1 Poling and Electric Connection of Bimorphs

Unimorph and bimorph cantilevers have be defined and distinguished in Figure 4-3. For a unimorph piezo-element with two layers of electrodes in parallel (like a capacitor), there is only one way to pole the material and connect the electrodes to external circuits if the cantilever is going to work in ‘31 mode’ (Figure 4-9 (a)). However, for a bimorph configuration, there are two different options to pole the two piezo-elements and connect the electrodes (Figures 4-9 (b), 4-9 (c)). Theoretically, the one poled in series and connected in parallel (called a parallel bimorph, Figure 4-9 (b)) tends to double the output current or power coupled with proper loads[38,53] compared to its unimorph counterpart, while the one poled in parallel and connected in series (called a series bimorph, Figure 4-9 (c)) is able to double the open-circuit voltage[10]. Either method can be applied in practice.

4.4.2 Electrodes

Depositing layers of continuous electrode materials on both surfaces of a piezo-element, known as ‘parallel plates’ type electrodes (PPE)[54], is a conventional electroding approach for cantilever-based PEHers, as presented above. This approach is simple and cost-effective, and suits a wide range of device dimensions (cm to µm level). However, another approach known as interdigitated electrodes (IDE) can also be considered, as shown in Figure 4-10. Rather than putting electrodes on both surfaces, two sets of electrode fingers are integrated on one surface of the piezo-element, across which a poling electric field is applied (Figure 4-10 (a))[54,55]. Therefore, the general polarization is along the length of the piezo-element, with opposite sub-directions between anodes and cathodes. As a result, the cantilever will work in a bending mode while the piezo-element will respond in ‘33 mode’ rather than ‘31 mode’[55]. As this configuration combines both the advantages of cantilever (larger deflection) and ‘33 mode’ (beneficial material parameters related to energy harvesting), the energy conversion capability tends to be improved, especially for MEMS applications[54,55]. However, much more complex factors, including the thickness of the piezo-element, the gaps between fingers, the length as well as the width/thickness ratios of the fingers, etc., must be carefully modelled and optimised in a practical design[54,55], leading to increased device cost. Other disadvantages involve the unpoled regions under the electrodes, and the piezo-element not fully poled through the thickness[55].

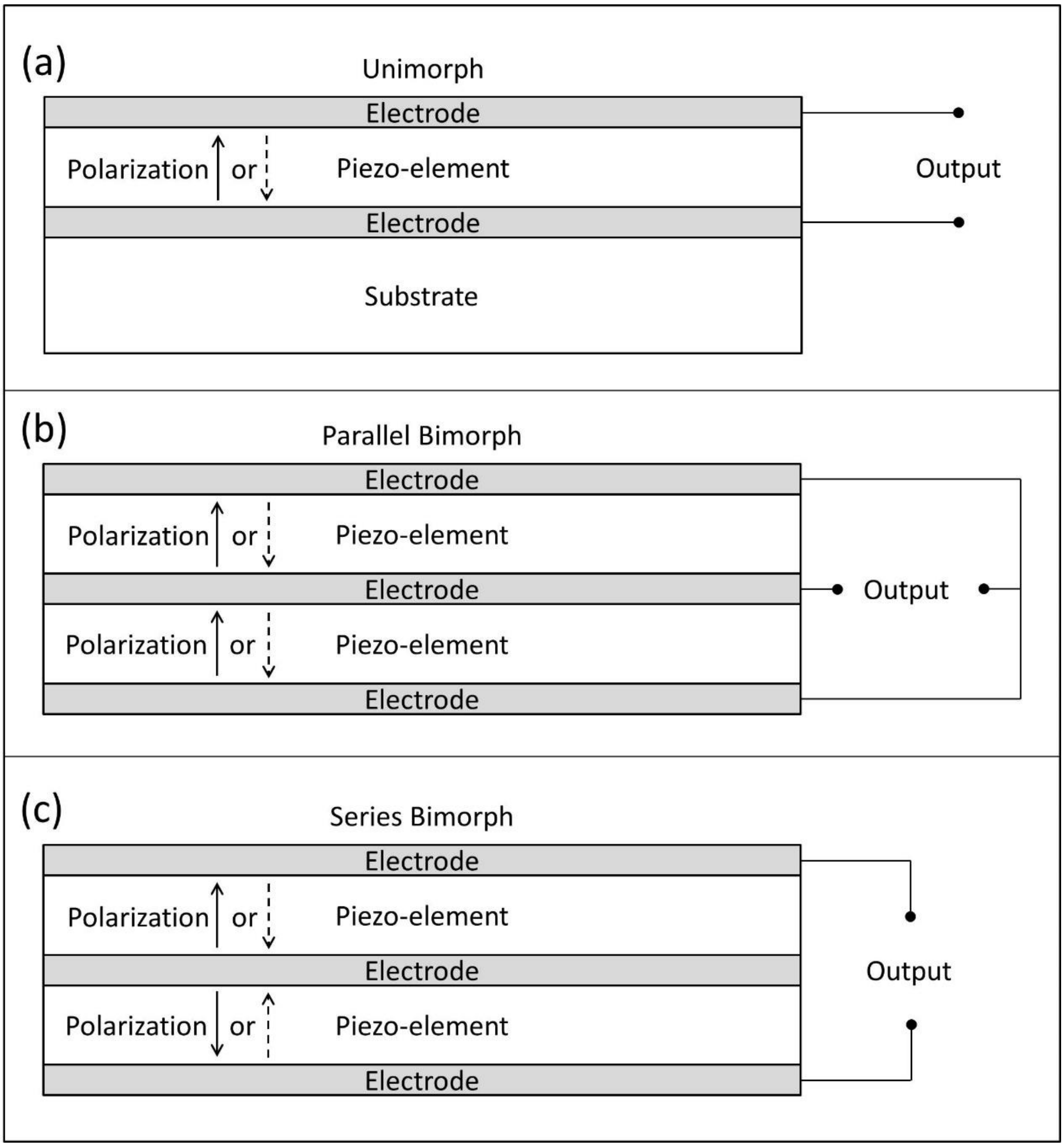

Figure 4-9. Schematics of poling and connecting methods (side-view): (a) unimorph; (b) bimorph poled in series, connected in parallel; (c) poled in parallel, connected in series.

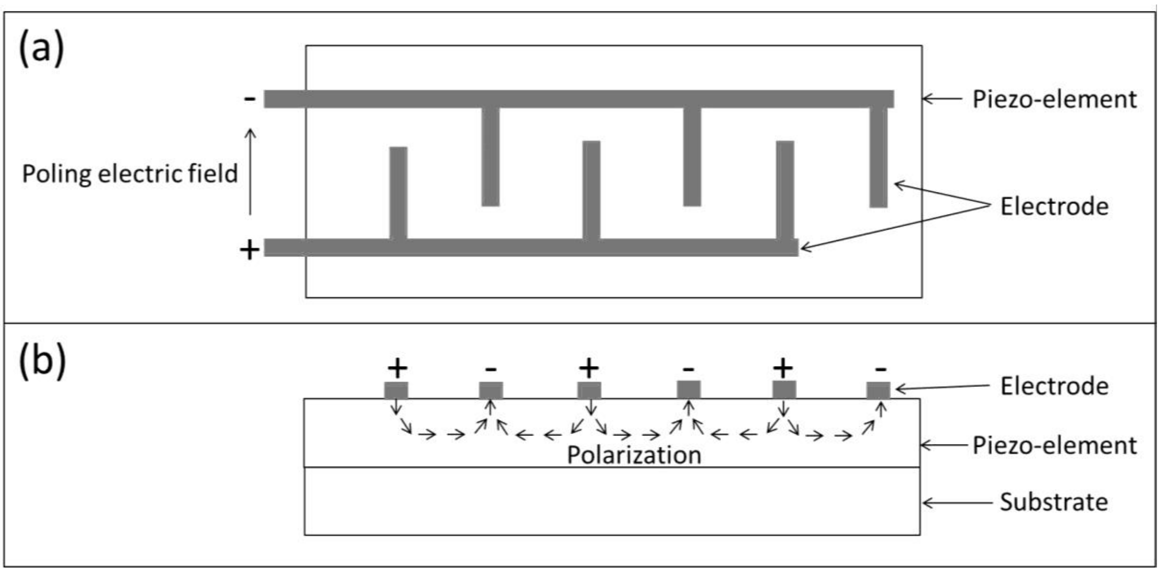

Figure 4-10. Schematics of IDE configuration: (a) top-view; (b) cross-sectional side-view (reproduced according to multiple sources[54,55]).

4.4.3 Equivalent Circuitry

Figure 4-11 shows examples of the equivalent circuit of a cantilever based '31 mode' PEHer in vibration and its corresponding external circuit, where Figure 4-11 (a) is focused on the details of the harvester, and Figure 4-11 (b) gives a general view of the entire harvesting system[38,56,57]. In Figure 4-11 (a), R_1, L_1 and C_1 are the effective resistance, inductance and capacitance of the mechanical segment of the harvester, which model the mechanical damping, mass and compliance, respectively[38]; and n is the turn ratio of the effective mechanical-electrical transformer[38]. With a vibration input v_{in}, an AC output voltage U is generated in parallel with the effective capacitance C_0 of the electric segment[38]. Such parameters are able to affect the output as well as energy conversion efficiency of the harvester[38], but they are actually determined by the parameters of the piezo-elements and/or the supporting substrate, as discussed in detail in the next section. However, as Figure 4-11 (b) shows, if the harvester is connected to a load or an energy storage medium in an application, a specially designed external circuit for conditioning, rectifying and regulating the chaotic AC output into stable and usable

DC signals must be placed between the harvester and the end uses[56,57]. Different external circuits will achieve various energy conversion efficiencies for different end users[57]. The design and investigation of external circuits are beyond the scope of this thesis, thus no further details will be given.

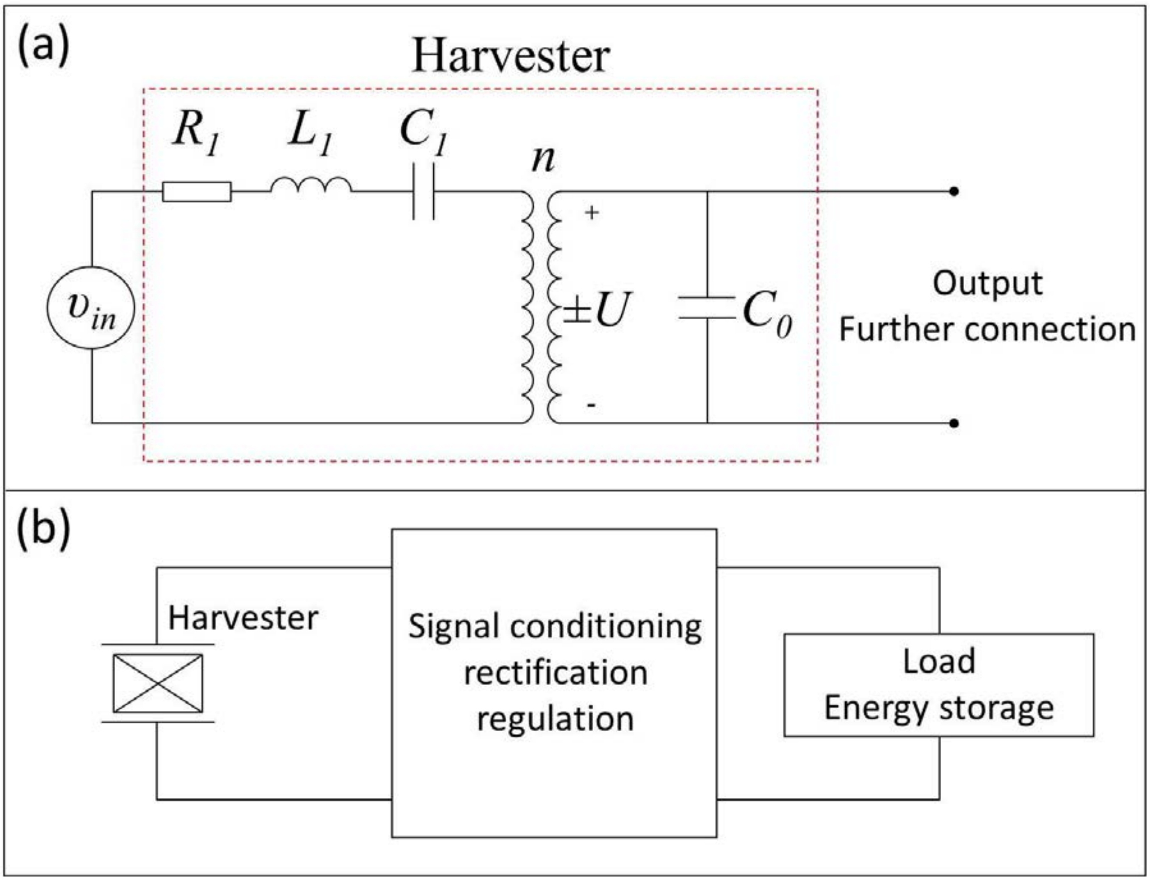

Figure 4-11. Schematics of the equivalent circuit of a cantilever based '31 mode' PEHer in vibration and the corresponding external circuit: (a) harvester; (b) general integration (reproduced according to multiple sources[38,56,57]).

4.4.4 Relationships of Material Properties and Energy Harvester Output

For an energy harvester which intends to be a power supply, open-circuit voltage, output power and energy conversion efficiency are the most significant criteria. It has been presented that such performance of a PEHer can be affected by factors related to the harvester structure and configuration and/or the electric circuitry. However, the overall capability of harvesting and converting energy is ultimately determined by the relevant properties of the piezoelectric materials utilised in the harvester. Even if the configuration and corresponding circuitry are very efficient, the absolute output of a PEHer is never able to be substantially improved if the full performance of the piezo-element is unavailable.

The open-circuit output voltage (U) of a unimorph cantilever in which the thickness of the substrate is equal to the total thickness of the electrodes and the piezo-element (as illustrated in Figure 4-9 (a)), or a symmetrical parallel bimorph cantilever (as illustrated in Figure 4-9 (b)), can be calculated using Equation 4-6[10]. In the equation, H and L represent the thickness and length of the entire cantilever, respectively; δz is the tip displacement when the cantilever is bending; and h_{31} is the effective transverse piezoelectric coefficient, which can be calculated by Equation 4-7[10]. The open-circuit voltage of a symmetrical bimorph cantilever connected in series (as illustrated in Figure 4-9 (c)) is likely to be double this value ($2U$)[10]. In general, the output voltage is dependent on the piezoelectric coefficients g_{33} and g_{31}, commonly named as piezoelectric voltage coefficients[24], the stiffness of the piezoelectric material, the dimensions of the structure and the deformation when vibrating.

$$U = \frac{3}{16}\left(\frac{H}{L}\right)^2 h_{31}\delta z \quad (4\text{-}6)$$

$$h_{31} = g_{31}(c_{11}^D + c_{12}^D) + g_{33}c_{13}^D \quad (4\text{-}7)$$

Compared to the voltage, the mathematic predictions of the output power have attracted stronger controversy[13,35]. Although the derivation of such equations is not appropriate here, it has been commonly agreed that certain general trends should be obeyed in practical harvester designs. For example, at frequencies far below the natural resonant frequency of a cantilever PEHer, the output power density, which is a comparable factor implying the ability to convert ambient vibrational energy, is likely to be positively related to $d{\cdot}g$ (e.g. $d_{31}{\cdot}g_{31}$)[3]. While at the resonant frequency, larger Q_M, k_{31} and relative permittivity tend to induce higher output power density[3]. It should be noted that at off-resonant frequencies smaller relative permittivity may be needed as $g_{31} = d_{31}/(\varepsilon_r \cdot \varepsilon_0)$,[58] however in the resonant situation the requirement is for a larger relative permittivity. This is the first conflict that should be balanced when designing and selecting the materials for PEHers.

In a similar way to the output power, the materials aspect of the energy conversion efficiency (η_m) may also suffer a conflict. Equation 4-8 provides an estimation[10,59], where Q is the total quality factor considering both the effects of mechanical part (Q_M) and dielectric part ($Q_d = 1/tan\delta$), and k' is expressed by Equation 4-9[10,59]. As indicated, the efficiency is positively contributed to by Q_M and k_{eff}. However, k_{eff} is normally inversely related to Q_M, as k_{eff} increases as the gap between the resonant and anti-resonant frequencies increases whereas Q_M decreases[10]. Therefore, a maximum multiplied value is desired.

$$\eta_m = \frac{Q \cdot k'}{2 + Q \cdot k'} \quad (4\text{-}8)$$

$$Q = Q_M + Q_d \qquad k' = \frac{k_{eff}^2}{1 - k_{eff}^2} \quad (4\text{-}9)$$

The above conflicts make choosing materials for PEHers complicated. Practical investigation needs to be done in terms of each material case.

4.5 Other Energy Harvesting Combining Piezoelectricity

Several examples of potential energy harvesters combining piezo-elements for harvesting other sources of energy rather than kinetic have been briefly mentioned in Chapter 2. These include a wind harvester, a pyroelectric or ferromagnetic thermal harvester, and a radioactive harvester. The design details of some wind harvesters with piezo-elements are shown in Figure 4-12. The first feasible configuration is shown in Figure 4-12 (a), where piezoelectric bimorphs are radially embedded on a cylindrical holder. The shaft is driven by wind causing the bumps to strike the bimorphs periodically and induce deformations[60]. Rather than bend the bimorphs by mechanical impact, the second configuration (Figure 4-12 (b)) employs permanent magnets mounted on the tip of the bimorphs and the shaft, which force the bimorphs to bend up and down by contact-less attractive and repulsive magnetic forces as the shaft is rotated by the wind[61]. The advantage of designs that combine piezoelectric elements and wind turbine structures, over the conventional electromagnetic wind turbine, is considered to be their potentially compact size which may suit the application of small and low-power devices. The energy harvesters involved in this project share similar cantilever configurations to those shown in Figure 4-12, and are thus compatible with wind turbine systems. The other possible structure incorporates flexible beams of soft piezoelectric polymers (e.g. PVDF – polyvinylidene floride), which can be straightforwardly placed in the air flow and thus deformed[62].

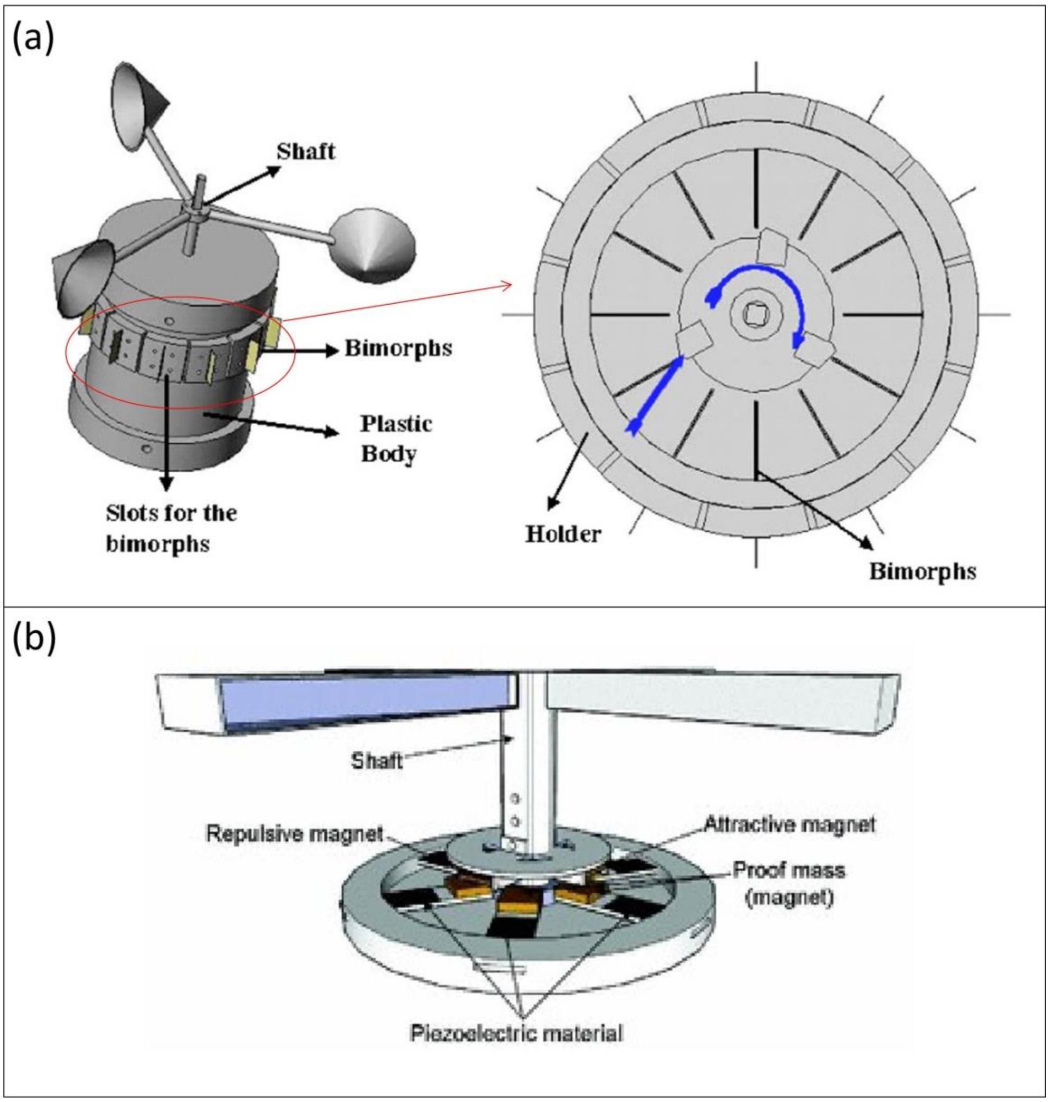

Figure 4-12. Schematics of wind harvesters combining piezo-elements: (a) striking design[60]*; (b) contact-less design*[61].

Also, ferroelectric materials are able to exhibit the pyroelectric effect which transfers temperature fluctuation into electricity. As this is a mechanically static procedure, the configuration of a pyroelectric harvester is relatively straightforward, where either bulk or film piezoelectric materials or a combination of both are directly employed as the harvester and connected with corresponding circuitry[10,63,64]. However, the other design of thermal energy harvester utilising the piezoelectric effect involves a more complex transfer structure, of which an example is shown in Figure 4-13[65,66]. A PEHer of any of the type introduced above is placed between cold and hot surfaces. A soft magnet (with a Curie temperature T_c) is attached to the 'hot' side of the PEHer, above a permanent magnet which is fixed on the hot surface. The temperature of the hot surface is higher than T_c while that of the cold side is lower. In the initial state, the soft magnet is ferromagnetic and is thus able to be attracted by the permanent magnet, inducing a deformation of the PEHer. When the two magnets contact each other, the temperature of the soft magnet increases above T_c and it enters the paramagnetic state, thus losing its attraction to the permanent magnet, causing release and oscillation of the PEHer. In such stage, the temperature gradient is transferred to mechanical displacement and then to electricity. When the soft magnet cools down, the cycle repeats. There are some important requirements to be noticed for the design of this harvester: (1) the T_c or T_d (depoling temperature) of the piezoelectric materials must be higher than the T_H (temperature of the hot surface); (2) the T_c of the soft magnet must be able to be tailored between the T_H and T_L (temperature of the cold surface). Such a configuration provides one option for the design of a thermal energy harvester incorporating piezoelectrics, though it is of slow cyclic operation[65,66] compared to piezoelectric energy harvesters designed for harvesting vibration energy.

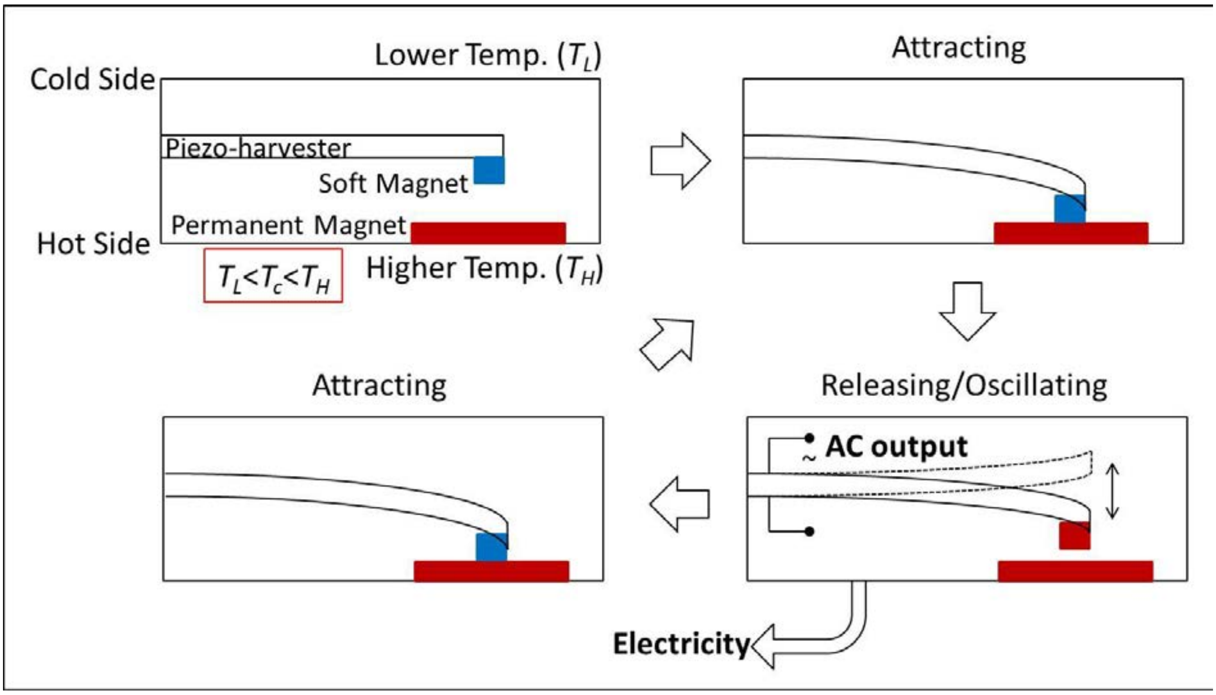

Figure 4-13. Example schematics of the configuration and operating mechanism of a thermal energy harvester combining piezoelectrics and magnetics (simplified according to multiple sources[65,66]).

The energy emitted by radioactive materials can also be harvested and converted to electricity through the piezoelectric effect. Figure 4-14[67] shows a promising design of such harvester, where there are many similarities compared to the harvester shown in Figure 4-13. The charge emitted by the piece of radioactive material (e.g. uranium, thorium) generates an electrostatic attraction to the conductive cantilever, forcing it to bend. When the two components contact each other, the charge differential is dissipated and the cantilever is released and starts to oscillate. Consequently, the piezoelectric patch attached to the cantilever transfers the radioisotope source into electricity[67,68].

Some quantification of output of different types of piezoelectric energy harvesters described above and some other (e.g. electromagnetic, electrostatic) vibrational energy harvesters are listed in Table 4-1 as reported for a brief comparison. In summary, PEHers are mainly suitable for harvesting vibration energy but, with suitable design configurations, they can be incorporated into harvesters of other energy sources.

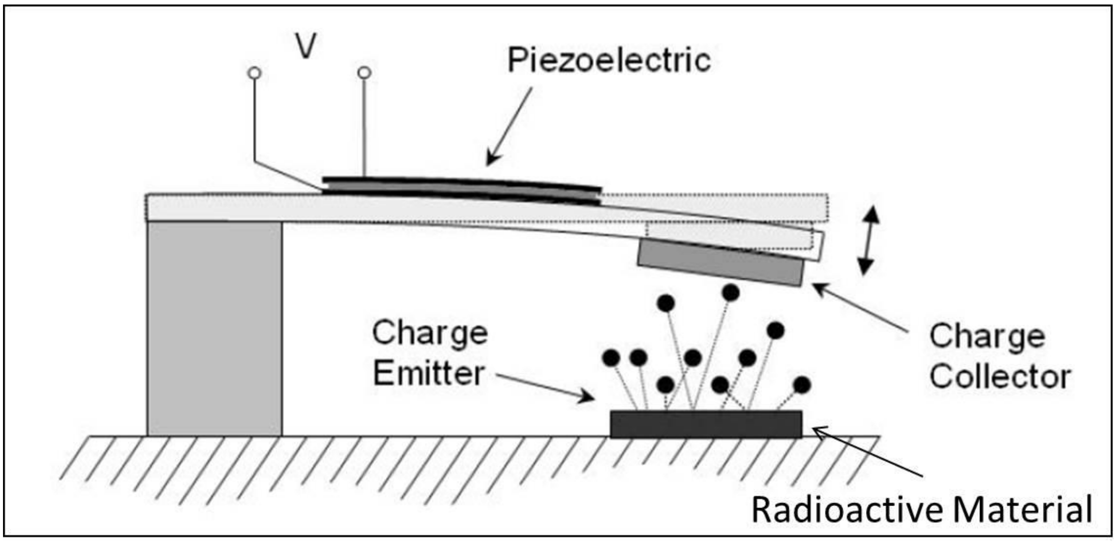

Figure 4-14. Schematic configuration of radioisotope harvester[67].

Table 4-1. Brief summary of different types of piezoelectric and vibrational energy harvesters.

Harvester Principle	**Energy Source and Condition**	**Harvester Configuration**	**Output Voltage (V)**	**Output Power (mW)**	**Power Density (mW/cm^3)**
Piezoelectric[69]	Vibration 243 Hz, 4.9 m/s^2	Thin-film cantilever on SOI, PPE	-	2.15×10^{-3}	2.02
Piezoelectric[70]	Vibration 67 Hz, 2.84 m/s^2	Screen printed thick-film on stainless steel	-	0.24	-
Piezoelectric[24]	Vibration 229 Hz, 9.8 m/s^2	Free-standing	-	0.28×10^{-3}	15.5×10^{-3}
Piezoelectric[69]	Vibration 243 Hz, 4.9 m/s^2	Thin-film cantilever on SOI, IDE	-	1.71×10^{-3}	1.61
Piezoelectric[25]	Cyclic pressure 1.19 Hz, 24.8 N	Cymbal, bulk ceramics	-	0.66	0.31
Piezoelectric[27]	Vibration 150 Hz, 9.8m/s^2	Diaphram array	-	28	14
Piezoelectric[32]	Vibration 63.8 Hz, 10m/s^2	Shear mode, bulk ceramics	127.6	9	42.25
Piezoelectric[60]	Wind 10 miles/h	18 bimorphs, striking type	-	5	0.386
Piezoelectric[61]	Wind 10 miles/h	6 bimorphs, contact-less type	-	0.75	1.04
Pyroelectric[64]	Cyclic heat flow 40-100 °C, 1 Hz	Piezoelectric thin-film	-	-	110
Piezoelectric[65]	Temperature gradient 50 °C difference	Integration of soft and permanent magnets	-	-	1.85-3.61 (mW/cm^2)
Piezoelectric[68]	Radioactive ^{63}Ni sourse	Cantilever, radioactive material	-	0.1×10^{-3}	0.1×10^{-3}
Electromagnetic[71,72]	Vibration Tailorable	Commercialised	Up to 8	Up to 27	-
Electrostatic[71]	Vibration Various conditions	-	-	2.4×10^{-3}-1.76	2.42×10^{-3}-56×10^{-3}
Electrostrictive[73]	Vibration 100 Hz, 0.2% transverse strain	-	-	7×10^{-3}	0.28

References

1 Roundy, S., Wright, P. K. and Rabaey, J. A study of low level vibrations as a power source for wireless sensor nodes. *Computer Communications* **26**, 1131-1144 (2003).

2 Beeby, S. P., Tudor, M. J. and White, N. M. Energy harvesting vibration sources for microsystems applications. *Measurement Science & Technology* **17**, R175-R195 (2006).

3 Priya, S. Advances in energy harvesting using low profile piezoelectric transducers. *Journal of Electroceramics* **19**, 167-184 (2007).

4 Williams, C. B. and Yates, R. B. Analysis of a micro-electric generator for microsystems. *Sensors and Actuators A-Physical* **52**, 8-11 (1996).

5 Ramadass, Y. K. and Chandrakasan, A. P. An efficient piezoelectric energy harvesting interface circuit using a bias-flip rectifier and shared inductor. *IEEE Journal of Solid-State Circuits* **45**, 189-204 (2010).

6 Dicken, J., Mitcheson, P. D., Stoianov, I. and Yeatman, E. M. Power-extraction circuits for piezoelectric energy harvesters in miniature and low-power applications. *IEEE Transactions on Power Electron.* **27**, 4514-4529 (2012).

7 Guan, M. J. and Liao, W. H. Characteristics of energy storage devices in piezoelectric energy harvesting systems. *Journal of Intelligent Material Systems and Structures* **19**, 671-680 (2008).

8 Anton, S. R. and Sodano, H. A. A review of power harvesting using piezoelectric materials (2003-2006). *Smart Materials & Structures* **16**, R1-R21 (2007).

9 Kim, H. S., Kim, J. H. and Kim, J. A review of piezoelectric energy harvesting based on vibration. *International Journal of Precision Engineering and Manufacturing* **12**, 1129-1141 (2011).

10 Moulson, A. J. and Herbert, J. M. Electroceramics: Materials, properties and applications. *Chapman & Hall: London*, pp. 274-336 (1990).

11 Erturk, A. and Inman, D. J. An experimentally validated bimorph cantilever model for piezoelectric energy harvesting from base excitations. *Smart Materials & Structures* **18**, 025009 (2009).

12 Wang, Q. M. and Cross, L. E. Constitutive equations of symmetrical triple layer piezoelectric benders. *Ieee Transactions on Ultrasonics Ferroelectrics and Frequency Control* **46**, 1343-1351 (1999).

13 Erturk, A. and Inman, D. J. Issues in mathematical modeling of piezoelectric energy harvesters. *Smart Materials & Structures* **17**, 065016 (2008).

14 Kim, I., Joo, H., Jeong, S., Kim, M. and Song, J. Micro-power generation of PMN-PZT triple morph cantilever for electric harvesting devices. *E-MRS 2009 Spring Meeting, Symposium F: Advances in Transparent Electronics: From Materials to Devices, June 8, 2009 - June 12, 2009.*9 edn **7**, 2331-2335 (2010).

15 Al Ahmad, M. and Jabbour, G. E. Electronically droplet energy harvesting using piezoelectric cantilevers. *Electronics Letters* **48**, 647-649 (2012).

16 Roundy, S., Leland, E. S., Baker, J. *et al.* Improving power output for vibration-based energy scavengers. *IEEE Pervasive Computing* **4**, 28-36 (2005).

17 Yoon, H. S., Washington, G. and Danak, A. Modeling, optimization, and design of efficient initially curved piezoceramic unimorphs for energy harvesting applications. *Journal of Intelligent Material Systems and Structures* **16**, 877-888 (2005).

18 Zhu, Y., Zu, J. and Su, W. Broadband energy harvesting through a piezoelectric beam subjected to dynamic compressive loading. *Smart Materials and Structures* **22**, 045007 (2013).

19 Marzencki, M., Defosseux, M. and Basrour, S. Mems vibration energy harvesting devices with passive resonance frequency adaptation capability. *Journal of Microelectromechanical Systems* **18**, 1444-1453 (2009).

20 Kymissis, J., Kendall, C., Paradiso, J. and Gershenfeld, N. Parasitic power harvesting in shoes. *2nd International Symposium on Wearable Computers - Digest of Papers* 132-139 (1998).

21 Glynne-Jones, P., Beeby, S. P. and White, N. M. Towards a piezoelectric vibration-powered microgenerator. *IEEE Proceedings: Science, Measuremetn and Technology 2 edn* **148**, 68-72 (2001).

22 Torah, R. N., Beeby, S. P. and White, N. M. Experimental investigation into the effect of substrate clamping on the piezoelectric behaviour of thick-film PZT elements. *Journal of Physics D: Applied Physics* **37**, 1074-1078 (2004).

23 White, N. M., Harris, N. R., Swee, L. K. and Tudor, M. J. Novel thick-film piezoelectric micro-generator based on free-standing structures *2008 2nd Electronics Systemintegration Technology Conference, ESTC, September 1, 2008 - September 4, 2008*, 589-592 (2008).

24 Kok, S. L., White, N. M. and Harris, N. R. Fabrication and characterization of free-standing thick-film piezoelectric cantilevers for energy harvesting. *Measurement Science and Technology* **20**, 124010 (2009).

25 Palosaari, J., Leinonen, M., Hannu, J., Juuti, J. and Jantunen, H. Energy harvesting with a cymbal type piezoelectric transducer from low frequency compression. *Journal of Electroceramics* **28**, 214-219 (2012).

26 Mo, C., Arnold, D., Kinsel, W. C. and Clark, W. W. Modeling and experimental validation of unimorph piezoelectric cymbal design in energy harvesting. *Journal of Intelligent Material Systems and Structures* **24**, 828-836 (2013).

27 Wang, W., Yang, T. Q., Chen, X. R. and Yao, X. Vibration energy harvesting using a piezoelectric circular diaphragm array. *IEEE Transactions on Ultrasonics Ferroelectrics and Frequency Control* **59**, 2022-2026 (2012).

28 Kim, S., Clark, W. W. and Wang, Q. M. Piezoelectric energy harvesting with a clamped circular plate: Experimental study. *Journal of Intelligent Material Systems and Structures* **16**, 855-863 (2005).

29 Li, X. T., Guo, M. S. and Dong, S. X. A flex-compressive-mode piezoelectric transducer for mechanical vibration/strain energy harvesting. *IEEE Transactions on Ultrasonics Ferroelectrics and Frequency Control* **58**, 698-703 (2011).

30 Platt, S. R., Farritor, S. and Haider, H. On low-frequency electric power generation with PZT ceramics. *Ieee - Asme Transactions on Mechatronics* **10**, 240-252 (2005).

31 Aladwani, A., Aldraihem, O. and Baz, A. Single degree of freedom shear-mode piezoelectric energy harvester. *Journal of Vibration and Acoustics-Transactions of the Asme* **135**, 051011 (2013).

32 Zhou, L., Sun, J., Zheng, X. J. *et al.* A model for the energy harvesting performance of shear mode piezoelectric cantilever. *Sensors and Actuators A-Physical* **179**, 185-192 (2012).

33 Wang, G. Analysis of bimorph piezoelectric beam energy harvesters using Timoshenko and Euler-Bernoulli beam theory. *Journal of Intelligent Material Systems and Structures* **24**, 226-239 (2013).

34 Blevins, R. D. Formulas for natural frequency and mode shape. *van Nostrand Reinhold Company: New York*, pp. 104-106 (1979).

35 Shafer, M. W., Bryant, M. and Garcia, E. Designing maximum power output into piezoelectric energy harvesters. *Smart Materials and Structures* **21**, 085008 (2012).

36 Bai, Y., Meggs, C. and Button, T. W. Investigation of using free-standing thick-film piezoelectric energy harvesters to develop wideband devices. *International Journal of Structural Stability and Dynamics* **14**, 1440016 (2014).

37 Zhu, D., Tudor, M. J. and Beeby, S. P. Strategies for increasing the operating frequency range of vibration energy harvesters: a review. *Measurement Science and Technology* **21**, 022001 (2010).

38 Al Ahmad, M., Elshurafa, A. M., Salama, K. N. and Alshareef, H. N. Determination of maximum power transfer conditions of bimorph piezoelectric energy harvesters. *Journal of Applied Physics* **111**, 102812 (2012).

39 Zhu, D. B., Harris, N. and Beeby, S. Performance of linear vibration energy harvesters under broadband vibrations with multiple frequency peaks. *26th European Conference on Solid-State Transducers, Eurosensor 2012, Procedia Engineering* (eds R. Walczak & J. Dziuban) **47**, 5-8 (2012).

40 Guyomar, D., Badel, A., Lefeuvre, E. and Richard, C. Toward energy harvesting using active materials and conversion improvement by nonlinear processing. *IEEE Transactions on Ultrasonics Ferroelectrics and Frequency Control* **52**, 584-595 (2005).

41 Lallart, M., Wu, Y. C., Richard, C., Guyomar, D. and Halvorsen, E. Broadband modeling of a nonlinear technique for energy harvesting. *Smart Materials and Structures* **21**, 115006 (2012).

42 Tang, L. H. and Yang, Y. W. A nonlinear piezoelectric energy harvester with magnetic oscillator. *Applied Physics Letters* **101**, 094102 (2012).

43 Liu, J. Q., Fang, H. B., Xu, Z. Y. *et al.* A MEMS-based piezoelectric power generator array for vibration energy harvesting. *Microelectronics Journal* **39**, 802-806 (2008).

44 Al-Ashtari, W., Hunstig, M., Hemsel, T. and Sextro, W. Enhanced energy harvesting using multiple piezoelectric elements: Theory and experiments. *Sensors and. Actuators A-Physical* **200**, 138-146 (2013).

45 Ferrari, M., Alghisi, D., Bau, M. and Ferrari, V. Nonlinear multi-frequency converter array for vibration energy harvesting in autonomous sensors. *26th European Conference on Solid-State Transducers, Eurosensor 2012*, *Procedia Engineering* (eds R. Walczak & J. Dziuban) **47**, 410-413 (2012).

46 Abdelkefi, A., Najar, F., Nayfeh, A. H. and Ben Ayed, S. An energy harvester using piezoelectric cantilever beams undergoing coupled bending-torsion vibrations. *Smart Materials & Structures* **20**, 115007 (2011).

47 Tang, L. H. and Yang, Y. W. A multiple-degree-of-freedom piezoelectric energy harvesting model. *Journal of Intelligent Material Systems and Structures* **23**, 1631-1647 (2012).

48 Berdy, D. F., Srisungsitthisunti, P. and Jung, B. *et al.* Low-frequency meandering piezoelectric vibration energy harvester. *IEEE Transactions on Ultrasonics Ferroelectrics and Frequency Control* **59**, 846-858 (2012).

49 Friswell, M. I., Ali, S. F., Bilgen, O. *et al.* Non-linear piezoelectric vibration energy harvesting from a vertical cantilever beam with tip mass. *Journal of Intelligent Material Systems and Structures* **23**, 1505-1521 (2012).

50 Litak, G., Friswell, M. I., Kwuimy, C. A. K., *et al.* Energy harvesting by two magnetopiezoelastic oscillators with mistuning. *Theoretical & Applied Mechanics Letters* **14**, 043009 (2012).

51 Kim, I. H., Jung, H. J., Lee, B. M. and Jang, S. J. Broadband energy-harvesting using a two degree-of-freedom vibrating body. *Applied Physics Letters* **98**, 214102 (2011).

52 Lin, H. C., Wu, P. H., Lien, I. C. and Shu, Y. C. Analysis of an array of piezoelectric energy harvesters connected in series. *Smart Materials and Structures* **22**, 094026 (2013).

53 Smits, J. G., Dalke, S. I. and Cooney, T. K. The constituent equations of piezoelectric bimorphs. *Sensors and Actuators A-Physical* **28**, 41-61 (1991).

54 Chidambaram, N., Mazzalai, A., Balma, D. and Muralt, P. Comparison of lead zirconate titanate thin films for microelectromechanical energy harvester with interdigitated and parallel plate electrodes. *IEEE Transactions on Ultrasonics Ferroelectrics and Frequency Control* **60**, 1564-1571 (2013).

55 Knight, R. R., Mo, C. K. and Clark, W. W. MEMS interdigitated electrode pattern optimization for a unimorph piezoelectric beam. *Journal of Electroceramics* **26**, 14-22 (2011).

56 Yang, Y. W. and Tang, L. H. Equivalent circuit modeling of piezoelectric energy harvesters. *Journal of Intelligent Material Systems and Structures* **20**, 2223-2235 (2009).

57 Szarka, G. D., Stark, B. H. and Burrow, S. G. Review of power conditioning for kinetic energy harvesting systems. *IEEE Transactions on Power Electron.* **27**, 803-815 (2012).

58 Fialka, J. and Benes, P. Comparison of methods for the measurement of piezoelectric coefficients. *IEEE Transactions on Instrumentation and Measurement* **62**, 1047-1057 (2013).

59 Richards, C. D., Anderson, M. J., Bahr, D. F. and Richards, R. F. Efficiency of energy conversion for devices containing a piezoelectric component. *Journal of Micromechanics and Microengineering* **14**, 717-721 (2004).

60 Myers, R., Vickers, M., Kim, H. and Priya, S. Small scale windmill. *Applied Physics Letters* **90**, 054106 (2007).

61 Bressers, S., Avirovik, D., Lallart, M., Inman, D. J. and Priya, S. Contact-less wind turbine utilizing piezoelectric bimorphs with magnetic actuation. *Proceedings of the IMAC-XXVIII, Structural Dynamics, Conference Proceedings of the Society for Experimental Mechanics Series 12* **3**, 233 (2010).

62 Li, S. G., Yuan, J. P. and Lipson, H. Ambient wind energy harvesting using cross-flow fluttering. *Journal of Applied Physics* **109**, 026104 (2011).

63 Cuadras, A., Gasulla, M. and Ferrari, V. Thermal energy harvesting through pyroelectricity. *Sensors and Actuators A-Physical* **158**, 132-139 (2010).

64 Cha, G. and Ju, Y. S. Pyroelectric energy harvesting using liquid-based switchable thermal interfaces. *Senors and Actuators A-Physical* **189**, 100-107 (2013).

65 Ujihara, M., Carman, G. P. and Lee, D. G. Thermal energy harvesting device using ferromagnetic materials. *Applied Physics Letters* **91**, 093508 (2007).

66 Chung, T. K., Shukla, U., Tseng, C. Y., Chen, C. C. and Wang, C. M. A magnetic/piezoelectric-based thermal energy harvester. *Active and Passive Smart Structures and Integrated Systems 2013, Proceedings of SPIE* (ed H. A. Sodano) **8688**, UNSP 86880M (2013).

67 Knight, C., Davidson, J. and Behrens, S. Energy options for wireless sensor nodes. *Sensors* **8**, 8037-8066 (2008).

68 Lal, A., Duggirala, R. and Li, H. Pervasive power: A radioisotope-powered piezoelectric generator. *IEEE Pervasive Computing* **4**, 53-61 (2005).

69 Kim, S. B., Park, H., Kim, S. H. *et al.* Comparison of MEMS PZT cantilevers based on d(31) and d(33) modes for vibration energy harvesting. *Journal of Microelectromechanical Systems* **22**, 26-33 (2013).

70 Zhu, D., Glenne-Jones, P., White, N. *et al.* Screen printed piezoelectric films for energy harvesting. *Advances in Applied Ceramics* **112**, 79-84 (2013).

71 Mitcheson, P. D., Yeatman, E. M., Rao, G. K., Holmes, A. S. and Green, T. C. Energy harvesting from human and machine motion for wireless electronic devices. *Proceedings of the IEEE* **96**, 1457-1486 (2008).

72 www.perpetuum.com/products/vibration-energy-harvester.asp [online access] 07/08/2014.

73 Cottinet, P. J., Lallart, M., Guyomar, D. *et al.* Analysis of ac-dc conversion for energy harvesting using an electrostrictive polymer P(VDF-TrFE-CFE). *IEEE Transactions on Ultrasonics Ferroelectrics and Frequency Control* **58**, 30-42 (2011).

CHAPTER 5. AIMS AND OBJECTIVES

This project covered broad but systematic and consecutive investigations on the topic of piezoelectric energy harvesting. These include material fabrication and characterisation, harvester fabrication and parametric selection, electric output and dynamic behaviour tests of energy harvesters, and the feasibility of utilising lead-free piezoelectric materials for energy harvesting. In this way the work was able to provide a general view of piezoelectric energy harvesting as well as create relevant background and an initial data base in the group. The aims and objectives are summarised as following:

- To fabricate and characterise bulk ceramic samples made from traditional 'soft' PZT and two other lead-based piezoelectric compositions, and compare their parameters related to energy harvesting.
- To investigate the feasibility of lowering the sintering temperature of the bulk materials, in order to be prepared for subsequent thick-film fabrication.
- To fabricate and characterise bulk ceramics made from a promising lead-free piezoelectric composition, and thus compare its energy harvesting parameters to those of traditional PZT, as well as investigate its capability for low-temperature sintering.
- To select, fabricate and characterise a lead-based piezoelectric candidate material for energy harvesting applications, and compare with PZT in the form of single-layer free-standing thick-films.
- To fabricate and characterise multi-layer free-standing thick-film cantilevers with PZT and the other lead-based candidate, and develop a reliable/repeatable process.
- To test electrical outputs of the cantilever harvesters under mechanical vibration without structural or electrical optimisation, in order to explore or confirm the theoretical relations between harvester performance and material properties.

- To improve the performance of the harvesters, and fabricate and demonstrate prototype devices.

CHAPTER 6. EXPERIMENTAL APPROACHES

6.1 Powder Synthesis

6.1.1 Lead-based Compositions

The compositions of PZT-5H, 3 mol% and 5 mol% La-doped PZnN-PZT were selected as the lead-based candidates, whose expected chemical formulas and short names used in this thesis are shown in Table 6-1.

Table 6-1. Summary of the selected lead-based compositions.

Short Name	Theoretical Chemical Formula
PZT	Commercial PZT-5H (TRS610C)
PZnN-P3LZT	$0.25Pb(Zn_{1/3}Nb_{2/3})O_3$-$0.75[0.03La+Pb(Zr_{0.55}Ti_{0.45})O_3]$
PZnN-P5LZT	$0.25Pb(Zn_{1/3}Nb_{2/3})O_3$-$0.75[0.05La+Pb(Zr_{0.53}Ti_{0.47})O_3]$

As presented in Chapter 3, La^{3+} is a 'soft' dopant that helps to improve permittivity, k, time stability (slower ageing), etc.[1], whilst the use of PZnN as well as various Zr/Ti ratios can properly tailor and balance other properties[1,2]. The selection of both La-doped compositions was based on the author's previous work and experience[3], where the PZnN-P3LZT was likely to provide higher g and Q_M, while the PZnN-P5ZT was intended to have higher $d{\cdot}g$ values as well as coupling coefficients. The PZT powder was 'TRS610C' (Batch No. 1321A, TRS Technologies, USA), but the two series of La-doped PZnN-PZT powders were synthesized through the conventional solid state reactions from PbO (> 98 %, Product No. 290404E, BDH Chemicals Ltd., USA), ZnO (> 99.5 %, Product No. 306174R, BDH Chemicals Ltd., USA), Nb_2O_5 (> 99.9 %, Product No. 72520, Fluka Chemika, UK), La_2O_3 (> 99 %, Product No. 29010, BDH Chemicals Ltd., USA), ZrO_2 (> 99.82 %, Minchem HMP Ltd., UK) and TiO_2 (> 99.9 %, Batch No. 06005KS, PI-KEM Ltd., UK).

Firstly, the raw material powders were weighed according to their calculated stoichiometric ratios (Table 6-1). In order to take account of the evaporation of PbO during calcination and sintering, empirically 1 wt% excess PbO was also added to each batch. The powders were then mixed and milled in a 500 mL polypropene bottle (Scientific Laboratory Supplies, UK) with ZrO_2 balls and distilled water ($\text{ball:powder:water} = 2:1:0.5\ wt\%$) on a ball milling machine (Machine No. 21735, Pascall Engineering, UK) for 24 hours. The actual amount of each raw powder is listed in Appendix I. Subsequently, the mixtures were dried at 90 °C in an oven (Lenton Thermal Designs, UK) for 24 hours and then calcined at 900 °C for 2 hours with a 5 °C/min ramp rate (up and down) in a muffle furnace (Serial No. 3967, Lenton Furnaces, UK). The powders for calcination were loaded in Al_2O_3 crucibles (99.99 %, Multi-lab Ltd., UK) with lids (sealed by ZrO_2/water paste). Finally, the calcined powders were re-milled and dried using the same processes, followed by being sieved through a 250 μm sieve mesh (Endecotts, UK).

6.1.2 Lead-free Composition

The 0.5BZT-0.5BCT composition, $0.5Ba(Zr_{0.2}Ti_{0.8})O_3$-$0.5(Ba_{0.7}Ca_{0.3})TiO_3$ (abbreviated as 50BCZT afterwards), which was selected because of its excellent potential piezoelectric properties[4], was also synthesized through a conventional solid state reaction. $BaZrO_3$ powder was fabricated first as a precursor. Stoichiometric amounts of $BaCO_3$ (> 99 %, Batch No. 237108-500G, Sigma-Aldrich, UK) and ZrO_2 raw powders were mixed and milled in a 125 mL polypropene bottle (Scientific Laboratory Supplies, UK) with ZrO_2 balls and Ethanol (99.99 %, Batch No. 1076733, Fisher Scientific, UK) ($\text{ball:powder:ethanol} = 2:1:0.8\ wt\%$) for 24 hours on the ball milling machine, followed by drying at 80 °C in the oven for 24 hours and heat treatment at 1400 °C for 10 hours with a 5 °C/min ramp rate (up and down) in another muffle furnace (Serial No. 5079, Lenton Furnaces, UK). It should be noted that as this project includes work on both lead-based and lead-free compositions, good laboratory procedures were used to avoid cross-contamination of lead-based and lead-free materials (and any other materials used in the group). Where equipment could not be thoroughly cleaned (e.g. mixing, heating etc.), separate equipment was dedicated to each material type. This was particularly important for the calcination and sintering furnaces. Subsequently, treating the synthesized $BaZrO_3$ as one of the starting materials, stoichiometric amounts of $BaZrO_3$, $CaCO_3$ (> 99 %, Batch No. C4830-100G, Sigma-Aldrich, UK), $BaCO_3$ and TiO_2 were mixed, milled and dried using the same procedures presented above, and calcined at 1350 °C for 2 hours with the same ramp rate in the same furnace as the $BaZrO_3$. Because the decomposition of $BaCO_3$ and $CaCO_3$ produces CO_2, the lead-free powder mixtures were calcined in open Al_2O_3 crucibles. Finally, the calcined powders were re-milled and dried using the same processes as those presented in Section 6.1.1, followed by being sieved through a 300 μm sieve mesh (VWR, UK). The actual batch compositions are listed in Appendix I.

6.1.3 Low-temperature Sintering Aid

A commercial borosilicate glass (Batch No. 2210, Particle Technology, UK) was selected as the sintering aid for investigations of low-temperature sintered lead-based and lead-free piezoelectric ceramics (bulk discs and thick-films). A part of the calcined powders presented in Section 6.1.1 and 6.1.2 were mixed with amounts of the glass additive ranging from 1 to 9 wt% for the lead-based to 1 to 3 wt% for the lead-free powders respectively, treating the calcined powder as 100 wt%. The powder mixtures were then milled with ZrO_2 balls and distilled water ($\text{ball:powder:water} = 2:1:0.5\ wt\%$) for 24 hours on the ball milling machine, dried at 90 °C for 24 hours in the oven, and finally sieved through meshes (250 μm for the lead-based, 300 μm for the lead-free). It should be explained here that the selection of the mesh sizes has no strict requirement, as the sieves were only used to avoid potential large agglomerates of the dried powders. Both sieves used in this project were chosen according to the availability in the group's laboratories. And separate sieve for each material type was applied in order to avoid cross-contamination of lead-based and lead-free compositions.

6.2 Shaping and Sintering

6.2.1 Bulk Discs

All of the green bodies of bulk disc samples both with and without glass additives were shaped by uniaxial single-ended dry pressing in a stainless steel die (P.T. No. 3000, Specac, UK) with 13 mm diameter. Before pressing, a combination of two water-based polyvinyl alcohol (PVA) binders, about 5 wt% DURAMAX B-1000 (Product No. 74821, Chesham Chemicals Ltd., UK) and about 5 wt% DURAMAX B-1007 (Product No. 74823, Chesham Chemicals Ltd., UK) (treating the powder as 100 wt%), was mixed with ZrO_2 balls and distilled water as well as the powder ($\text{ball:powder:water} = 2:1:0.5\ wt\%$) for 10-15 minutes on the ball milling machine, followed by drying at 90 °C for 24 hours in the oven and sieving through 250 μm (lead-based) or 300 μm (lead-free) meshes. The subsequent pressing was carried out on a 5507 Instron (UK) using pressures between 90-98 MPa (12-13 kN) applied for 1 minute for each disc. The mass of each green body was targeted on 0.8 g (lead-based) or 0.4 g (lead-free). Finally, the green bodies were sintered at:

(1) 1200-1270 °C for 2 hours, in Al_2O_3 rectangular crucibles (99.99%, Multi-lab Ltd., UK), covered by lead-oxide doped ZrO_2 sand (lead-based without glass);

(2) 900-1000 °C for 2 hours, on Al_2O_3 substrates (CeramTec North America, USA), in air atmosphere (lead-based with glass);

(3) 1400-1490 °C for 4 hours, on ZrO_2 substrates (Dynamic-Ceramic Ltd., UK), in air atmosphere (lead-free without glass);

(4) 900-1300 °C for 4 hours, on ZrO_2 substrates, in air atmosphere (lead-free with glass).

The sintering programme was set as follows:

1 °C/min ramp to 325 °C, dwell 1 hour;

1 °C/min ramp to 500 °C, dwell 1 hour;

5 °C/min ramp to targeted temperatures, dwell certain periods (presented above);

5 °C/min ramp to room temperature.

The initial slow heating procedures below 500 °C were used to burn off the binders without disruption to the ceramic green bodies. Also, it should be noted that the furnaces used for sintering the lead-based and lead-free samples should match the corresponding ones used for calcination presented in Section 6.1, to avoid Pb contamination on lead-free samples.

6.2.2 Fabrication of Printable Inks

The lead-based powders with appropriate amounts of glass additives were mixed with a commercial vehicle, the Blythe (M03MD10, Johnson Matthey, UK). The ratio of the powder and the Blythe were 80 wt% and 20 wt%, respectively. A 3-roll mill (G2996/84/484/2, Marchant Engineers, UK) with 100 μm rear and 30 μm front roller gaps was utilised to help mix the inks and reduce agglomeration. A silver ink comprising 70 wt% silver flake (FS2, Johnson Matthey, UK) and 30 wt% Blythe, and a carbon ink comprising 30 wt% carbon powder (Monarch 120, Johnson Matthey, UK) and 70 wt% Blythe used to produce electrode and sacrificial layers respectively, were manufactured using the same process.

6.2.3 Free-standing Thick-films and Cantilevers

Free-standing single-layer thick-films or multi-layer cantilevers were fabricated by a doctor blading process. Figure 6-1 shows the schematic fabrication processes.

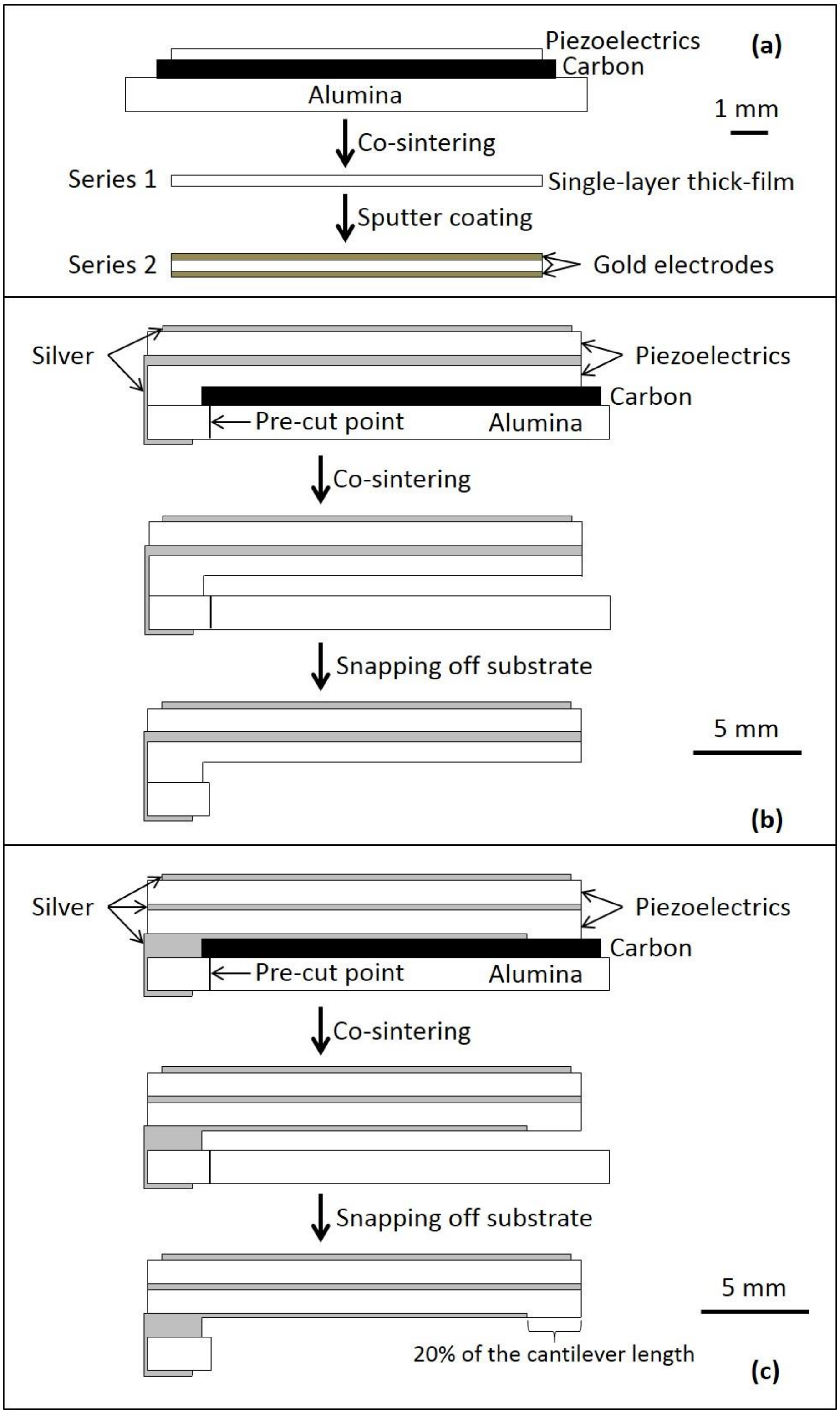

Figure 6-1. Side-view schematics of the fabrication processes of (a) free-standing single-layer thick-film; (b) free-standing thick-film unimorph cantilever; (c) free-standing thick-film bimorph cantilever.

A 70 µm thick tape (810 Magic, Scotch, UK) and a 140 µm thick tape (494-354, RS Components Ltd., UK) were employed to control the thickness of each bladed layer. First of all, a carbon layer was deposited on Al_2O_3 substrates (250-1000 µm thick, CeramTec North America, USA) (the substrates were also used as blades), followed by other layers as shown in the Figure 6-1. Each layer was dried at 70 °C for 30 minutes before printing the next layer. Subsequently, the layers were co-sintered at 875-950 °C for 0.5-2 hours. The ramping procedures were the same with those for bulk discs, while the dwell periods were cut to half because of smaller dimensions of the thick-films.

In further detail, as shown in Figure 6-1 (a), different from Series 2, Series 1 single-layer thick-films were not coated with gold electrodes (electroding will be presented in the next section), thus they were used for measurements of physical properties (e.g. density, shrinkage rate). The planar dimensions of wet films of Series 1 and 2 were 1 cm × 1 cm and 3 mm × 15 mm, respectively. Along with Series 1, several silver films with the same wet dimensions were also fabricated using the same process, for the investigation of shrinkage matching.

Besides, in Figure 6-1 (b) and (c), the substrates were pre-cut using a diamond scribe (RS, UK) (a pen with a diamond tip) thus could be snapped off by hand after sintering, in order to obtain free-standing structures. The top electrodes were slightly smaller (0.5 mm shorter as well as 0.5 mm narrower) than the piezoelectric layers, in order to avoid the potential shorting between the electrodes during high voltage poling. Also in practice, the bottom electrodes were connected to the other surfaces of the substrates by painting a conductive strip by hand using the tip of a 175 µm thick bare copper wire (Scientific Wire Company, UK), and soldering points were connected to the top, intermediate (bimorph only) and bottom electrodes, for convenience of further poling and wiring. Particularly, for the bimorph cantilevers, the bottom electrode was designed 20 % shorter than the piezoelectric layer (Figure 6-1 (c)), which was determined by many experimental trials and was proved to be able to prevent the tip from sticking to the substrate after sintering.

In order to adjust the performance of the harvester devices, lead (Pb) masses, selected because of their high density, were attached to the tips (bottom sides, piezoelectric surfaces uncovered by silver) of a part of the bimorph cantilevers with super glue (Power Flex GEL, Loctite, UK), shown in Figure 6-2. The joint areas between the cantilevers and the base substrates were also reinforced by the same glue, to avoid any crack and detachment in such weak areas during vibration, as Figure 6-2 shows. As the reinforcement was made by hand, the effective length of the free-standing part of a cantilever might be slightly shortened. Thus, the real free-standing length of the cantilever was measured after the reinforcement.

The dimensions of the unimorphs and bimorphs without tip mass for the first-stage material comparisons were about 11 mm length (free-standing part) and 3 mm wide, while the bimorphs used for output optimisation and frequency modelling were fabricated with a range of planar dimensions (free-standing length from 10 to 17 mm, width from 3 to 3.5 mm) and tip masses (0.05 to 0.2g) according to the theories presented in Chapter 3, in order to achieve different frequencies and integrate arrays on a test circuit board (433-832, RS, UK) to develop wideband harvesters.

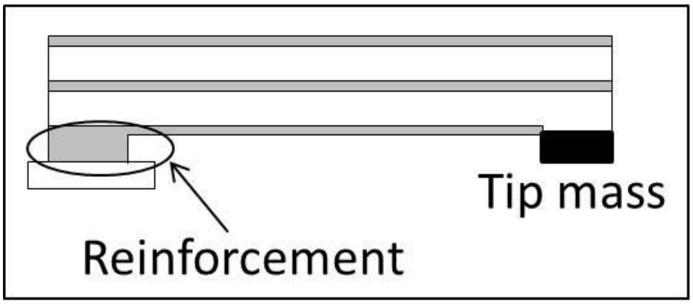

Figure 6-2. Schematic of tip mass attachment and joint area reinforcement.

6.3 Electrode Depositing and Poling

For the sintered lead-based discs without glass, the silver ink manufactured in Section 6.2.2 was painted on both surfaces as electrodes by hands. The wet electrodes were dried at 70 °C for 30 minutes in the oven and fired at 750 °C for 10 minutes with ramp rates (up and down) of 5 °C/min in the furnace for lead-based compositions. Also, as presented above, the unimorph and bimorph cantilevers were co-sintered with the same silver electrodes. However, for all of the remaining samples (discs and single-layer thick-films), Chromium (Cr) layers (thickness of 40 nm) then Gold (Au) layers (thickness of 200 nm) were successively sputtered as electrodes by a sputter coater (K575X, Emitech, UK).

Finally, all of the samples were poled using a contact poling method in silicone oil. The poling electric fields were 3 kV/mm and 10 kV/mm for disc samples and thick-films (including single-layers and cantilevers), respectively. The fields were provided by a power supply (Alpha III, Brandenburg Ltd., UK). In terms of poling temperature and period, all of the lead-based discs, single-layer thick-films and cantilevers were poled at 110 °C for 10 minutes, following which the samples were removed from the field and the oil immediately, while all of the lead-free discs were poled at 25, 50, 80 or 110 °C for 10 minutes with the field kept on during cooling to 25 °C. Additionally, a number of the bimorph cantilevers were poled in series whilst the others were poled in parallel.

6.4 Materials Characterisation

6.4.1 Density and Shrinkage

The density was calculated from the basic physical equation '$density = mass/volume$', where the mass was measured by an accurate electronic balance (R300S, Sartorius, USA) measuring to 4 decimal places, and the dimensions were obtained with:

(1) a Vernier caliper (Electronic Digital Caliper 0-150 mm/0.01 mm/±0.02 mm, RS, UK) - diameters of discs and length/width of thick-films/cantilevers;

(2) a micrometer (Electronic Digital Micrometer IP54, 0-30 mm/0.001 mm/±0.002 mm, TESA, Switzerland) - thickness of discs and free-standing single-layer silver films;

(3) a scanning electron microscope (SEM) (XL-30, Philips FEI, USA) - thickness of thick-films/cantilevers.

Each sample was randomly measured at (1) 3 positions (2) 5 points and (3) 4 fracture cross-sections then the average value was treated as the corresponding dimension.

Also, for disc samples the linear diameter shrinkage calculated by Equation 6-1 was used as the criterion, while for thick-films the planar area shrinkage calculated by Equation 6-2 was taken into account.

$$diameter\ shrinkage = \frac{(13\ mm - diameter\ after\ sintering)}{13\ mm} \times 100\% \quad (6\text{-}1)$$

$$planar\ shrinkage\ = \frac{(1\ cm^2 - planar\ area\ after\ sintering)}{1\ cm^2} \times 100\% \quad (6\text{-}2)$$

6.4.2 Particle Size, DSC, XRD and Microscopy

The particle sizes of all of the raw material powders as well as the calcined powders were analysed on a particle size analyser (Gracell, Sympa Tec, Germany).

The borosilicate glass powder was tested on a differential scanning calorimetry (DSC) and thermal gravimetric analysis (TGA) equipment (STA 449C, Netzsch, Germany), from room temperature to 900 °C with a ramp rate of 10 °C/min in air, in order to understand the thermal behaviour of this glass. Also, a part of the sintered lead-based discs were tested on a DSC equipment (DSC 404C, Netzsch, Germany), from room temperature to 500 °C with a ramp rate of 10 °C/min in argon atmosphere, in order to measure their phase transition temperatures.

All of the calcined powders and sintered discs/single-layer thick-films were measured on an X-ray diffractometer (XRD) (Equinox-3000, Inel, France) with Cu-Kα1 radiation (wavelength = 1.540560 Å) and diffraction angle ($\theta, 10° < 2\theta < 100°$), at room temperature. The resultant intensity - 2θ spectra were analysed with the help of the software 'Match!' integrated with the PDF-2 data base (copyright JCPDS-ICDD 2004, USA).

Also, all of the sintered discs, single-layer thick-films and cantilevers were observed using the SEM mentioned in Section 6.4.1. In particular, the fracture surfaces of the lead-based discs and the single-layer thick-films, whilst the polished then thermally etched (100-150 °C below the sintering temperature for 10 minutes) surfaces of the lead-free discs, were imaged. However, such a conventional SEM sample preparation method did not suit the observation of cross-sectional areas of the silver/piezoelectric multi-layer samples. As the silver layers were extremely soft and ductile, they could not be snapped off even in an ultra-low temperature environment (e.g. liquid nitrogen); in addition, the polished silver particles would cover the entire piezoelectric surface, and as a result only a large silver area could be seen under the SEM. This practical problem was solved by fixing the cantilevers in the hardened epoxy (EpoFix Resin + EpoFix Hardener, Batch No. 9081-2622/0216-1515, Struers, UK; $\text{resin:hardener} = 7:1\, wt\%$; hardened at room temperature in air), subsequently using a cutting machine (Accutom-50, Struers, UK) with a diamond cut-off wheel (M0D13, Struers, UK) to cut the cantilevers together with the epoxy. Figure 6-3 briefly explains the sample preparation process. It should be noted that both secondary electrons (SE) and back scatter electrons (BSE) were used as electron sources when imaging cantilevers, while only SE was employed for the discs and single-layer thick-films.

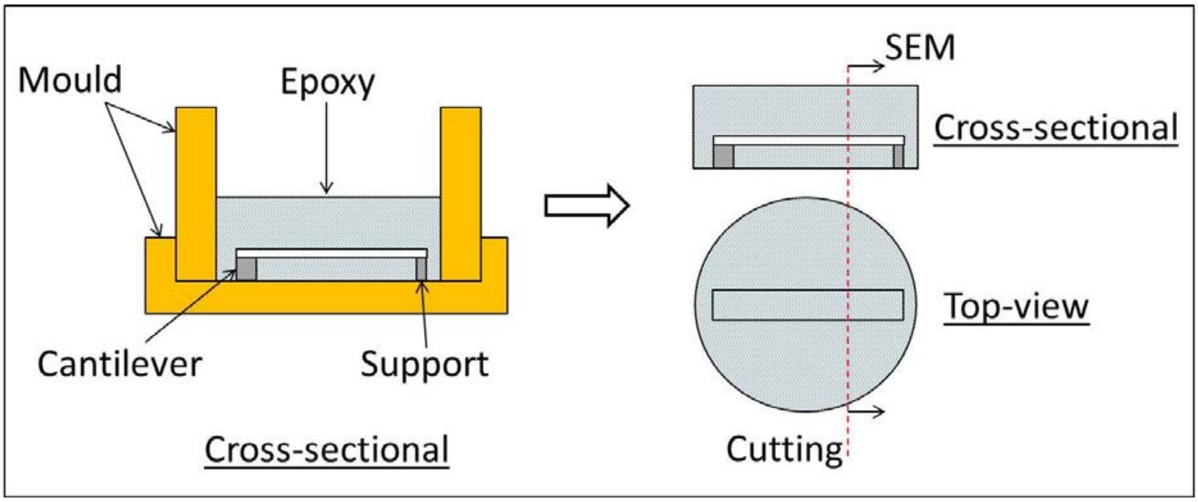

Figure 6-3. Schematics of SEM sample preparation process of the cantilevers.

6.4.3 Dielectric, Ferroelectric and Piezoelectric Properties

The capacitance (labelled as C_S on the equipment, corresponding to C^T in Chapter 3) and dielectric loss factor ($tan\delta$) at 1 kHz of a number of the lead-free discs were measured with an impedance analyser (4194A, Hewlett Packard, USA), at various temperatures (-50 °C to 120 °C) with ramp up rate of 60 °C/hour controlled by an environmental chamber (TJR, Tenney Environmental-SPX, USA). The measured capacitances were calculated to corresponding relative permittivity ($\varepsilon_r = \varepsilon_{33}^{\sigma}/\varepsilon_0$) by the Equation 3-26 in Chapter 3.

Also, the C^T and $tan\delta$ at 1 kHz of each sample, as well as the resonant/anti-resonant frequencies (f_r, f_a) and resonant impedance (Z_m) along the corresponding direction of certain sample shapes (presented in Chapter 3), were measured on another impedance analyser (4294A, Agilent, USA) at room temperature. Based on these, the Young's modulus (Y^E), compliance constant (s_{11}^E), ε_r, electromechanical coupling coefficients (k_{eff}, k_p, k_{31}), piezoelectric charge coefficient (d_{31}) and piezoelectric voltage coefficients (g_{33}, g_{31}) were calculated by the equations presented in Chapter 3. The mechanical quality factor (Q_M) was obtained from Equation 6-3[1].

$$Q_M = \frac{1}{2\pi f_r |Z_m| C^T \cdot \frac{f_a^2 - f_r^2}{f_a^2}} \quad (6\text{-}3)$$

The piezoelectric charge coefficient (d_{33}) was directly measured on a Berlincourt d_{33}-meter (YE2730A, Sinocera, China), where 6 random points of each sample were measured and the average value was treated as the true d_{33}. It should also be stated that as the single-layer thick-films were not robust enough to endure the forces applied by the d_{33}-meter, an entirely Au-coated Al_2O_3 substrate was introduced as a support, as Figure 6-4 shows.

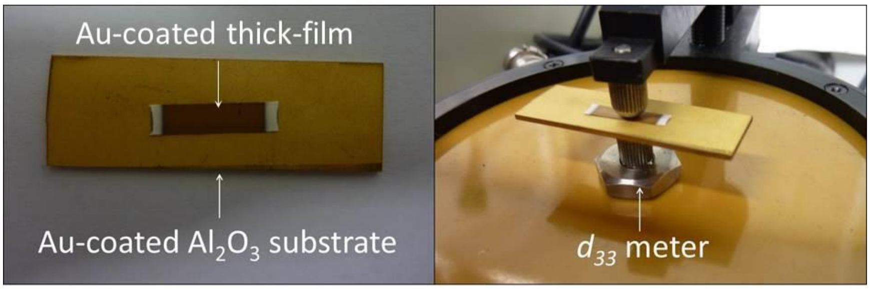

Figure 6-4. Picture illustration of the Au-coated substrate used to support the d_{33} *measurement of the single-layer thick-films.*

Obviously, the presence of the substrate caused an error, but it was not as significant as that of the films co-sintered with and firmly attached on a substrate, since the substrate used here only constrained the thickness deformation but not the transverse. A simple experiment was implemented to correct the error. As Figure 6-5 shows, a piezoelectric disc with Au electrodes was measured on the d_{33}-meter with free boundary conditions then re-measured with the same substrate used by the films, thus a difference was recognised. More than 20 discs were measured and the average measured d_{33} values with the substrate were proved about 78% of those without the substrate. As the boundary condition of the disc was similar to that of the thick-film, this error was applied to calculate the predicted real d_{33} value (named as effective piezoelectric coefficient, d_{33}^{*}). Therefore, for single-layer thick-films, d_{33}^{*} was calculated by '$d_{33}^{*} = measured\ d_{33}/78\%$'.

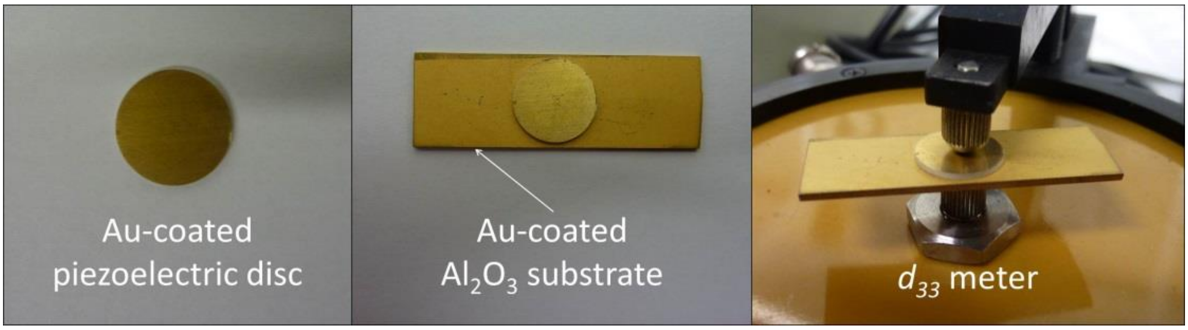

Figure 6-5. Picture explanation of the error eliminating experiment.

Finally, ferroelectric hysteresis loops of some of the lead-free discs were measured by a commercial characterisation company (aixACCT System GmbH, Germany).

6.5 Vibration Test

The cantilevers were mounted and tested as energy harvesters on an electromagnetic shaker (Gearing & Watson Electronics, UK). The setup of the testing system is shown in Figure 6-6 and Figure 6-7. The blue rigid clip in Figure 6-7 (b) was used as a support structure to conveniently fix the cantilever on and remove it from the vibrating component of the shaker. The cantilevers were attached on the clips by super glue in advance.

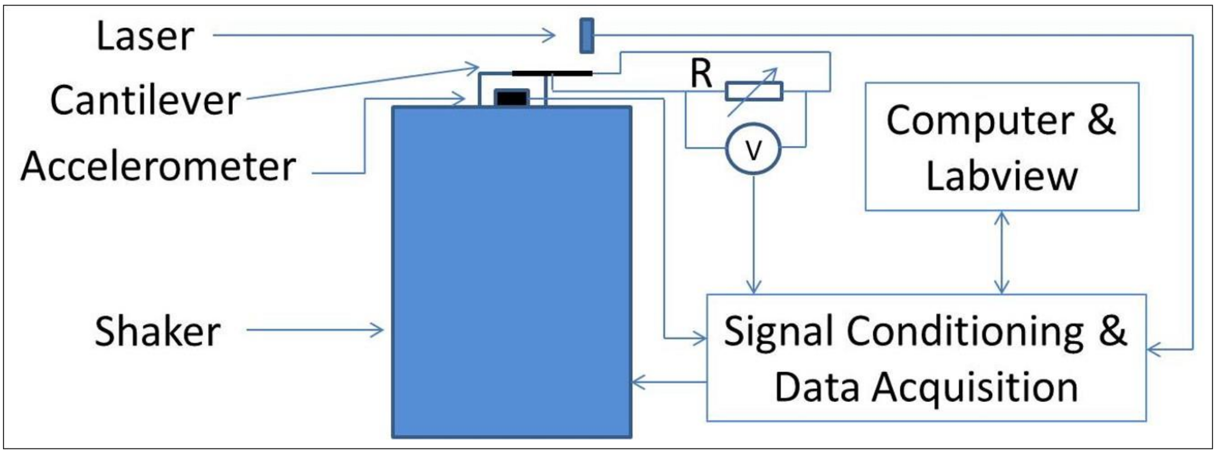

Figure 6-6. Schematic of the vibration testing system.

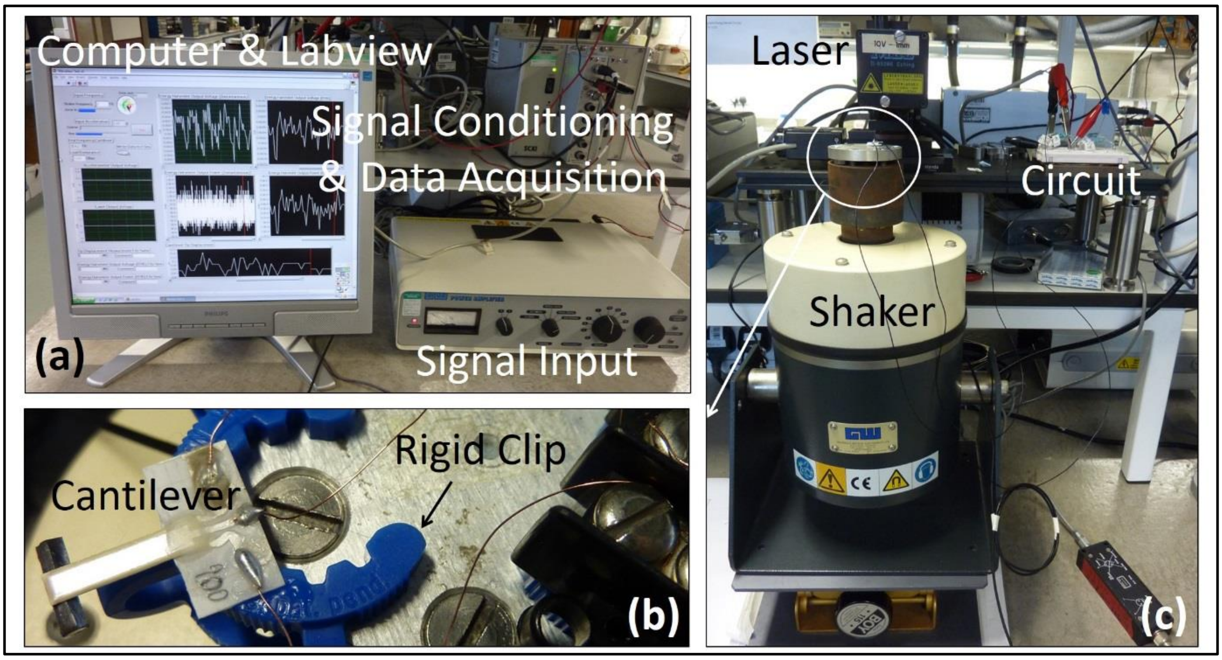

Figure 6-7. Pictures of the vibration testing system.

A sinusoidal input drove the shaker, providing a harmonic vibration to the individual harvester under test, which was directly connected to a resistive load (R) for measuring output voltage, power and tip displacement, or was connected to a 1000 μF capacitor through a diode bridge rectifier (1.5 A/200 V, W02G 948C, Vishay, USA) for observing charging behaviour. When connected to a 100 MΩ resistor, the voltage obtained was treated as the open-circuit voltage. Figure 6-8 shows the electric connections of the harvesters and external circuits.

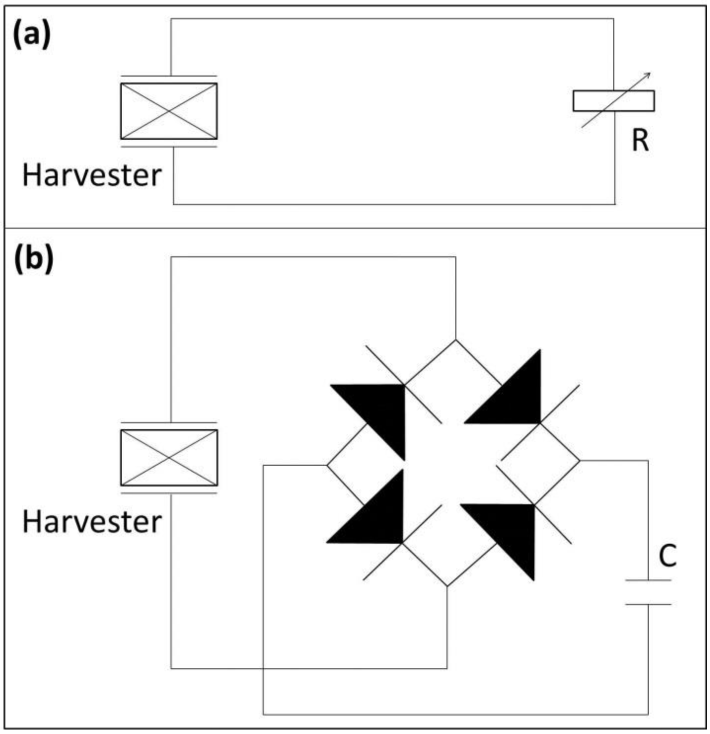

Figure 6-8. Schematics of connections used in the vibration test: (a) direct connection, for output voltage, power and tip displacement measurements; (b) connection with a diode bridge rectifier, for charging capacitors.

The input vibration frequency and acceleration as well as the tip displacement of the harvester were monitored by a laser vibrometer (M5L/2, MEL, Germany) and an accelerometer (4370, Brüel & Kjær, Denmark). When vibrating, the voltage across the resistor (V_R) or the capacitor (V_C) was measured, signal conditioned and recorded on a data-acquisition system (SCXI-1000 Chassis, SCXI-1305 Module, National Instruments, UK). Meanwhile, the output power (P) and power density (P_D) were automatically calculated by Equations 6-4 and 6-5, where P_{RMS} is the root mean square of P in 50 periods. The instantaneous data acquisition rate was 1 kHz. Also, in Equation 6-5, the cantilever volume of free-standing segment includes the inactive layers, e.g. electrode layers and bottom piezoelectric layer in unimorphs. Such a calculation method provides a convenience when comparing data with relevant references, which will be discussed in Chapter 8.

$$P = V_R^2/R \quad (6\text{-}4)$$

$$P_D = P_{RMS}/\text{cantilever volume of free-standing segment} \quad (6\text{-}5)$$

The entire procedure was controlled by the self-written Labview programme (Labview 8.5 software, National Instruments, UK), which is presented in detail in Appendix II.

In terms of harvester arrays, three individual harvesters were integrated into each harvester array, of which the connection is shown in Figure 6-9.

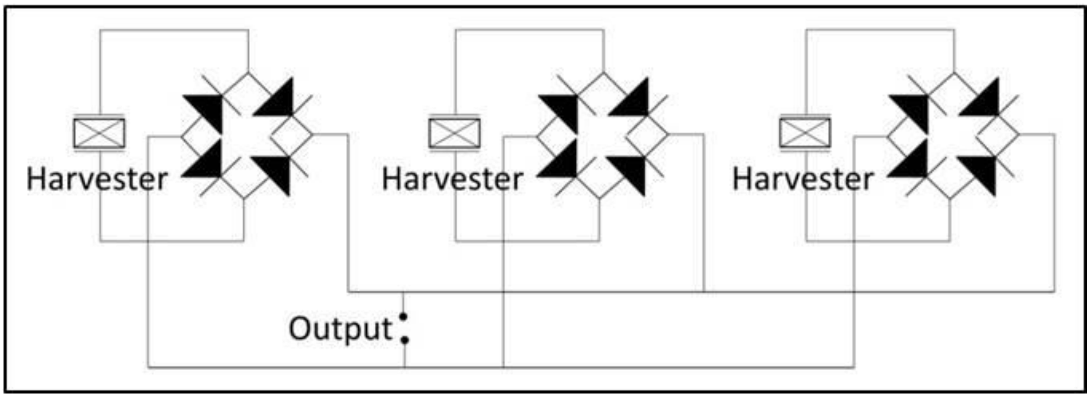

Figure 6-9. Schematic of electric connection of the integrated harvester array.

References

1 Moulson, A. J. and Herbert, J. M. Electroceramics: Materials, properties and applications. *Chapman & Hall: London*, pp. 276-282 (1990).

2 Fan, H. Q. and Kim, H. E. Perovskite stabilization and electromechanical properties of polycrystalline lead zinc niobate-lead zirconate titanate. *Journal of Applied Physics* **91**, 317-322 (2002).

3 Wang, N., Bai, Y., Ma, W. and Sun, Q. Unpublished Work. *Tianjin University of China* (2009-2011).

4 Liu, W. F. and Ren, X. B. Large Piezoelectric Effect in Pb-Free Ceramics. *Physical Review Letters* **103**, 257602 (2009).

CHAPTER 7. COMPOSITIONAL INVESTIGATIONS

7.1 PZT and La-doped PZnN-PZT

7.1.1 Material Analyses

7.1.1.1 Particles

Tables 7-1 and 7-2 summarise the particle sizes of the raw powders (starting oxides), PZT and two La-doped PZnN-PZT powders. All of the powders including starting oxides were separately ball milled with ZrO_2 balls and distilled water ($\text{ball:powder:water} = 2:1:0.5\ wt\%$) for 24 hours before measurements, and each datum was an average of 3 values from 3 independent measurements. There are not many strict issues for the particle sizes of the starting oxides, as long as they are well mixed prior to calcination. This can be achieved by the adequate ball milling described in Chapter 6. However, for the PZT and La-doped PZnN-PZT powders, the particle size needs to be suitable for forming the green bodies and sintering. According to Table 7-2, the particle sizes were considered to be acceptable for both calcination and sintering, hence no further crushing or grinding process was implemented.

Table 7-1. Summary of particle sizes of the starting oxides for lead-based composition.

Powder	**D_{50} (μm)**	**D_{90} (μm)**
PbO	2.80 ±0.64	7.60 ±0.91
ZnO	1.20 ±0.47	2.47 ±0.59
Nb_2O_5	2.06 ±0.53	5.15 ±0.73
La_2O_3	3.00 ±0.74	8.34 ±1.05
ZrO_2	3.14 ±0.56	7.46 ±0.81
TiO_2	2.97 ±0.67	7.33 ±1.05

Table 7-2. Summary of particle sizes of the calcined and milled lead-based powders.

Powder	**D_{50} (μm)**	**D_{90} (μm)**
PZT	1.22 ±0.40	3.41 ±0.50
PZnN-P3LZT	2.83 ±0.67	5.49 ±1.01
PZnN-P5LZT	2.54 ±0.57	5.70 ±0.82

7.1.1.2 Phase Structures

The XRD patterns of the starting oxides have been firstly checked. As the patterns matched well with the standard PDF database (presented in Chapter 6) and they are not the main research objectives of this project, no further information is provided here. Figures 7-1, 7-2 and 7-3 show the XRD patterns of the PZT, PZnN-P3LZT and PZnN-P5LZT powders and their disc counterparts sintered at different temperatures, respectively.

Pure tetragonal perovskite phases were revealed in both the powder and disc, with the evidence of a single diffraction peak (111) as well as the peak broadening (or potential split) near (100) and (200), as analysed in Figure 7-1. However, the 2θ values of the peaks from the sintered disc shifted about 1° towards the larger numbers compared to those of the powder, implying different lattice parameters (e.g. c/a, c and a are the lattice parameters along and perpendicular to the spontaneous polarization respectively) between the unit cells of the powder and the disc. According to the PDF database (presented in Chapter 6), the composition of this commercial PZT powder was extremely close to $Pb(Zr_{0.52}Ti_{0.48})O_3$ ($c/a \approx 1.014$), with no indication of obvious peak shifts or phase transition caused by doping. Nevertheless, the composition of the sintered disc matched a La-doped PZT ($c/a \approx 1.017$), which proved the 'soft' type claimed by the manufacturer. This might suggest that the La element was only physically doped into the powder but not chemically reacted.

During sintering, a chemical reaction between the La element and the pure PZT happened at the same time, resulting in altered lattice parameters and thus shifted peaks. Also, there appears to be a reversal of intensities of the (001)/(100) and (002)/(200) split peaks for the powder and disc respectively. This could be due to La reaction discussed above or lead loss during sintering. However, as the method of suppressing lead loss has been applied in the experiment (introduced in Chapter 6), the La reaction was considered as the preferable reason.

Compared to PZT, the phase structures of the other two compositions were more complex. In Figure 7-2, combinations of rhombohedral and tetragonal perovskite phases were observed in the PZnN-P3LZT powder and all of the sintered discs, with the evidence of peak broadening at (100), (111) and (200) peak positions. This was an expected result, as the designed Zr/Ti ratio (55:45) was near the MPB region in the PZT phase diagram. Besides, it was found that with the increased sintering temperature, the proportion of tetragonal phase increased, which was indicated by the gradually emerging peak split of the (002) reflection as the sintering temperature was increased. However, it was still quite difficult to recognise the main phase based only on the XRD patterns, and further details will be given in the next section as to how the relative permittivity was used to help the analysis. Also, as with other compositions containing lead zinc niobate, diffraction peaks identified as a pyrochlore phase (lead niobate) were observed along with the main phases. One reason for this might be due to the Nb ions being present in disordered regions caused by the abnormal growth of ZnNb regions and providing favourable formation conditions for pyrochlore[1].

Similar to the PZnN-P3LZT composition, it can be seen in Figure 7-3 that a rhombohedral and a tetragonal perovskite phase were also initially formed in the PZnN-P5LZT powder, with the evidence of the overlapped and/or split peaks at the (100), (111) and (200) orientations, due to the designed Zr/Ti ratio (53:47) being near the MPB. Meanwhile, the content of the tetragonal phase in the sintered discs also increased with the sintering temperature. In contrast to Figure 7-2 where the dominant phases were difficult to recognise, Figure 7-3 indicates that in the discs sintered at 1230 °C and 1250 °C, the tetragonal phase governed the main parts of the microstructures as the peaks belonging to the rhombohedral phase were not obvious, whilst in the disc sintered at 1270 °C there was mostly the tetragonal phase as the (111) orientation peak became sharp and single, and the rhombohedral phase peaks were hardly to be observed. This suggested that the doped La might be able to help the phase transition from rhombohedral to tetragonal with certain sintering temperatures[1,2]. However, the higher relative intensities of the pyrochlore peaks than those in Figure 7-2 indicated a larger percentage of the pyrochlore phase in the PZnN-P5LZT. This may also be due to the increased La content promoting the growth of (ZnNb) regions[1]. Excessive pyrochlore implies a risk of deteriorated piezoelectric properties. Consequently, the La doping needs to be carefully controlled in order to balance the increased c/a of the tetragonal phase with the deterioration of the piezoelectric properties due to the formation of pyrochlore.

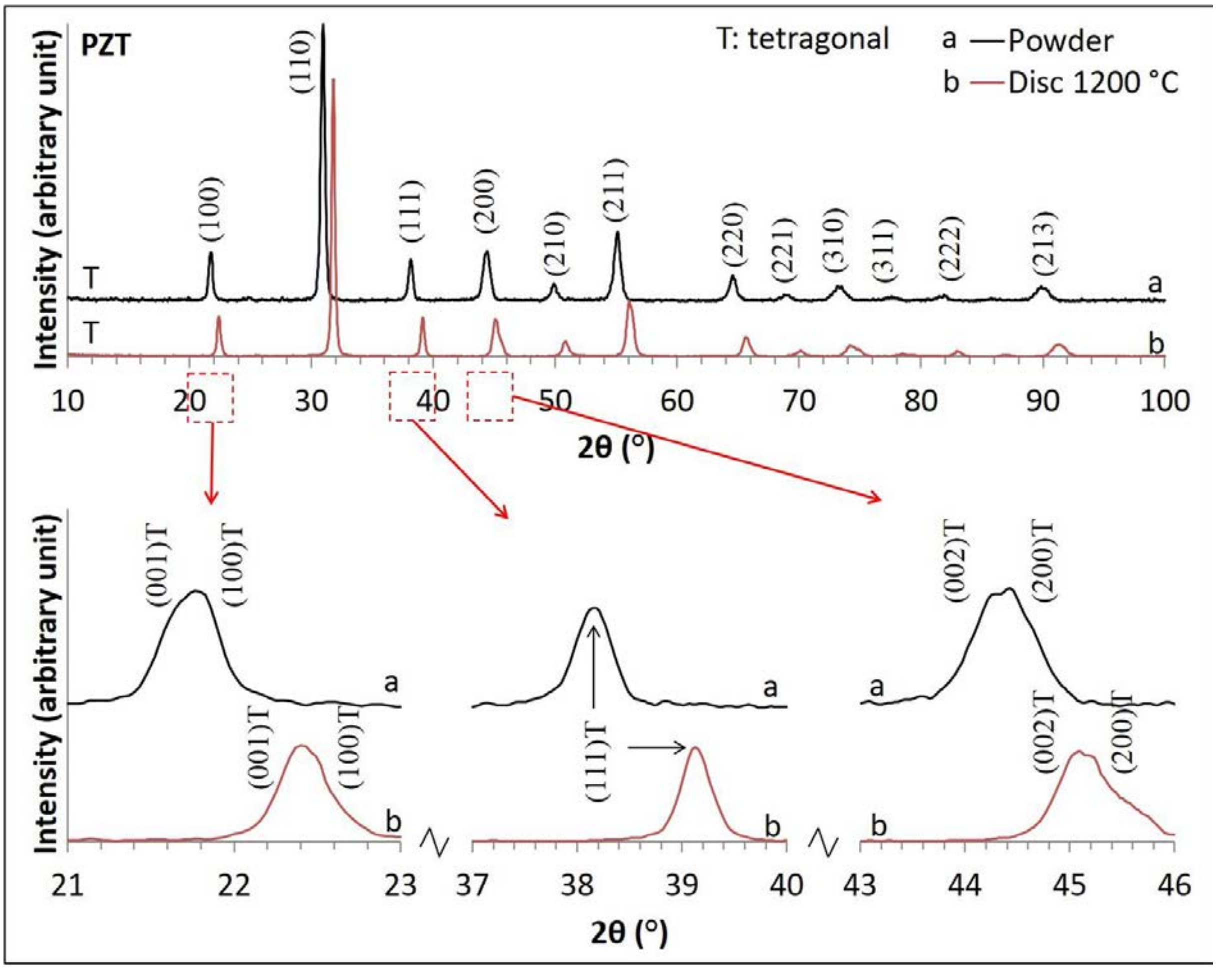

Figure 7-1. XRD patterns of the PZT powder and sintered disc with full-scale plotting and details of {100}, {111} *and* {200} *peaks.*

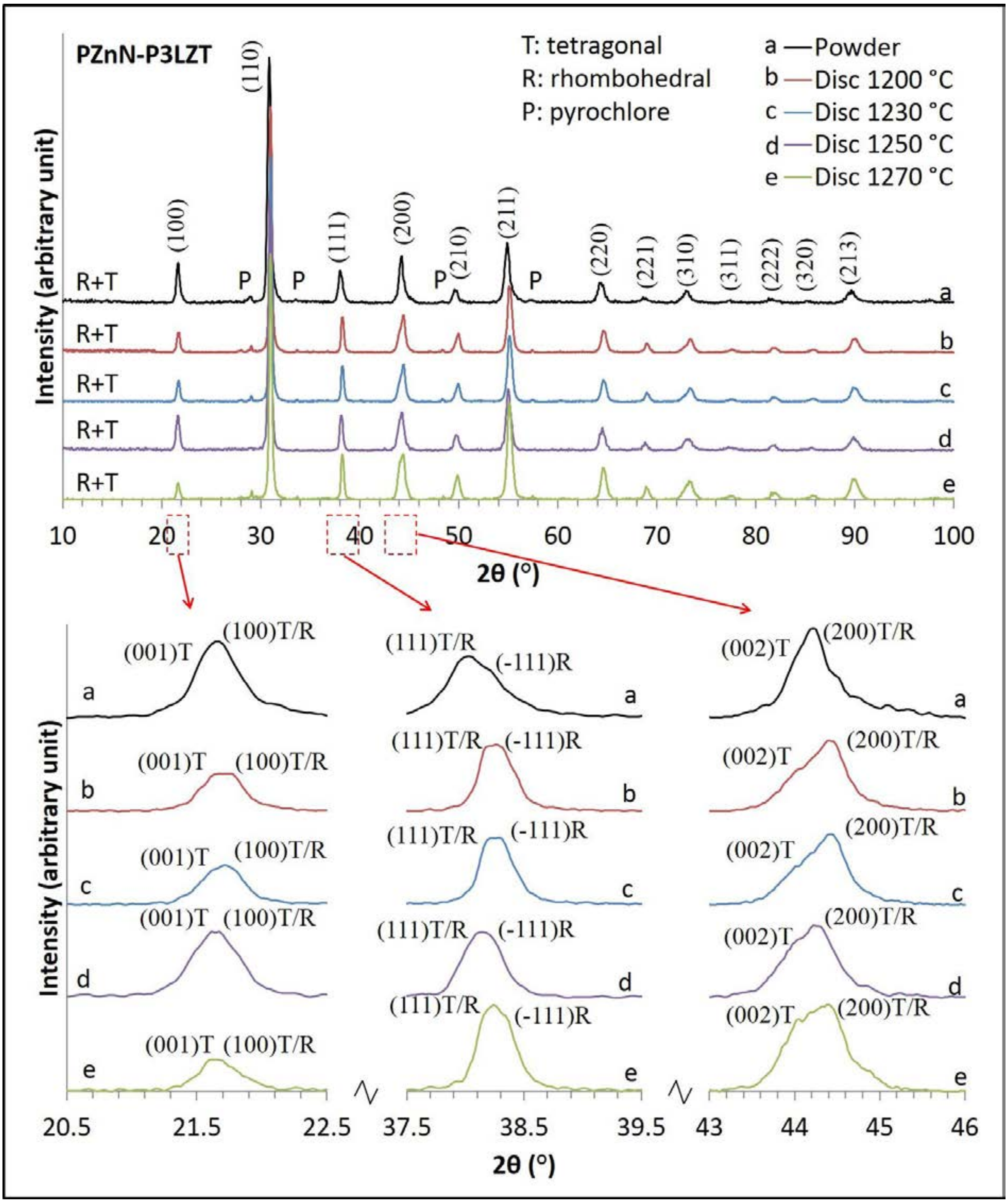

Figure 7-2. XRD patterns of the PZnN-P3LZT powder and sintered discs with full-scale plotting and details of $\{100\}$, $\{111\}$ *and* $\{200\}$ *peaks.*

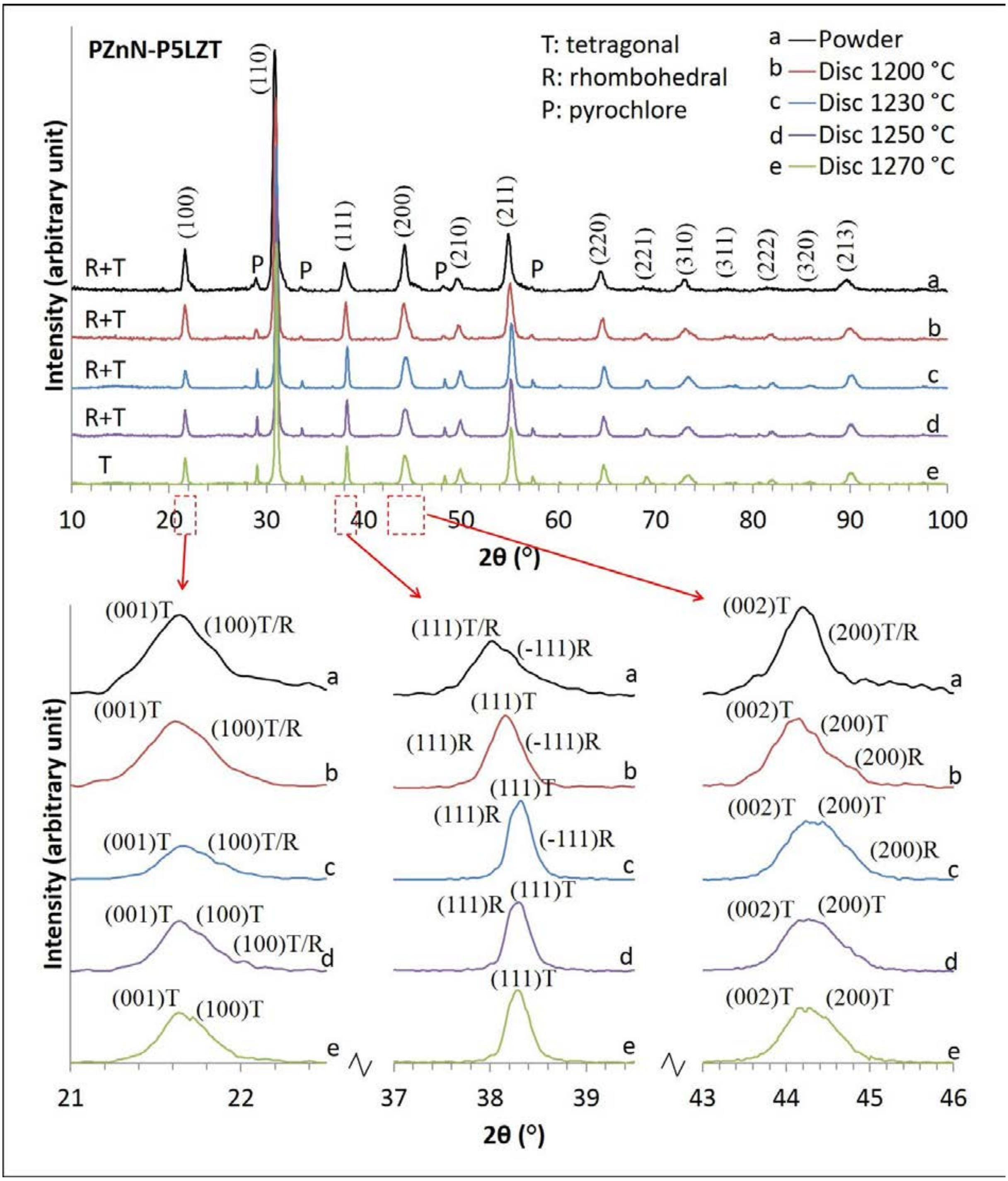

Figure 7-3. XRD patterns of the PZnN-P5LZT powder and sintered discs with full-scale plotting and details of $\{100\}$*,* $\{111\}$ *and* $\{200\}$ *peaks.*

7.1.1.3 Sintering Behaviour

Figure 7-4 shows the densities and diameter shrinkage of the sintered ceramic discs with different compositions and sintering temperatures. Each datum point was an average of 6 values from a batch of 6 samples.

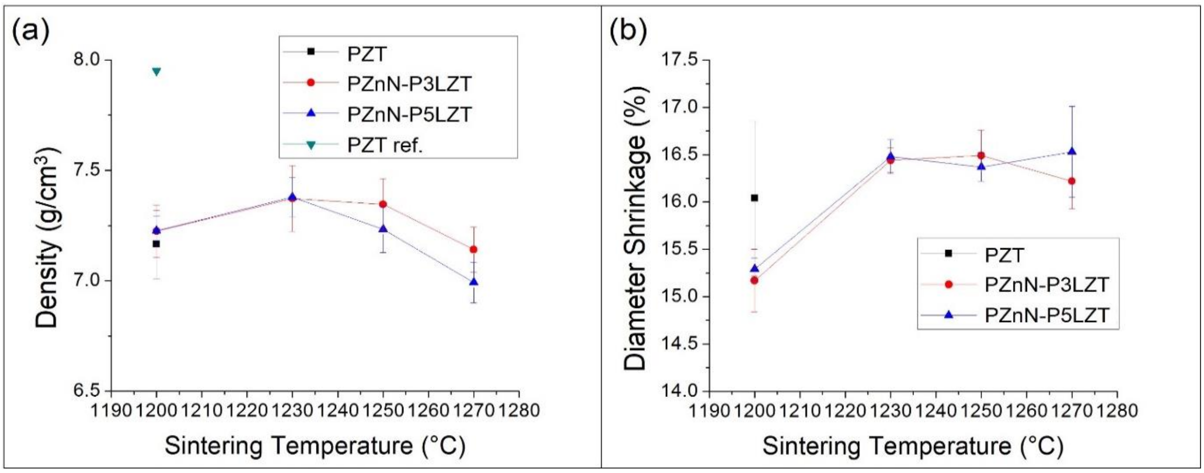

Figure 7-4. Dependence of (a) density and (b) diameter shrinkage on sintering temperature for sintered ceramic discs of different compositions.

The PZT samples were only sintered at 1200 °C, as this temperature was suggested by the manufacturer, with a reference density (PZT ref.[3]) provided. Although the experimental density of the PZT samples was not as large as the reference value, it was still able to be investigated and compared to those of the PZnN-P3LZT and PZnN-P5LZT samples, as the aim of this stage was to find out two compositions with obvious contrast and to use them to study the relations between piezoelectric properties and harvester performance, rather than discover better material options. According to Figure 7-4, for both the PZnN-P3LZT and PZnN-P5LZT samples, the optimum sintering temperatures were 1230-1250 °C with reasonable shrinkage, considering the deviations. Below 1230 °C, the energy provided by the furnace was not enough to induce a fully densification; while above 1250 °C, the grains continued to grow, leading to regenerated pores and decreased densities, despite the shrinkage remaining the same. Such phenomena were further investigated using SEM, as shown in Figures 7-5 and 7-6.

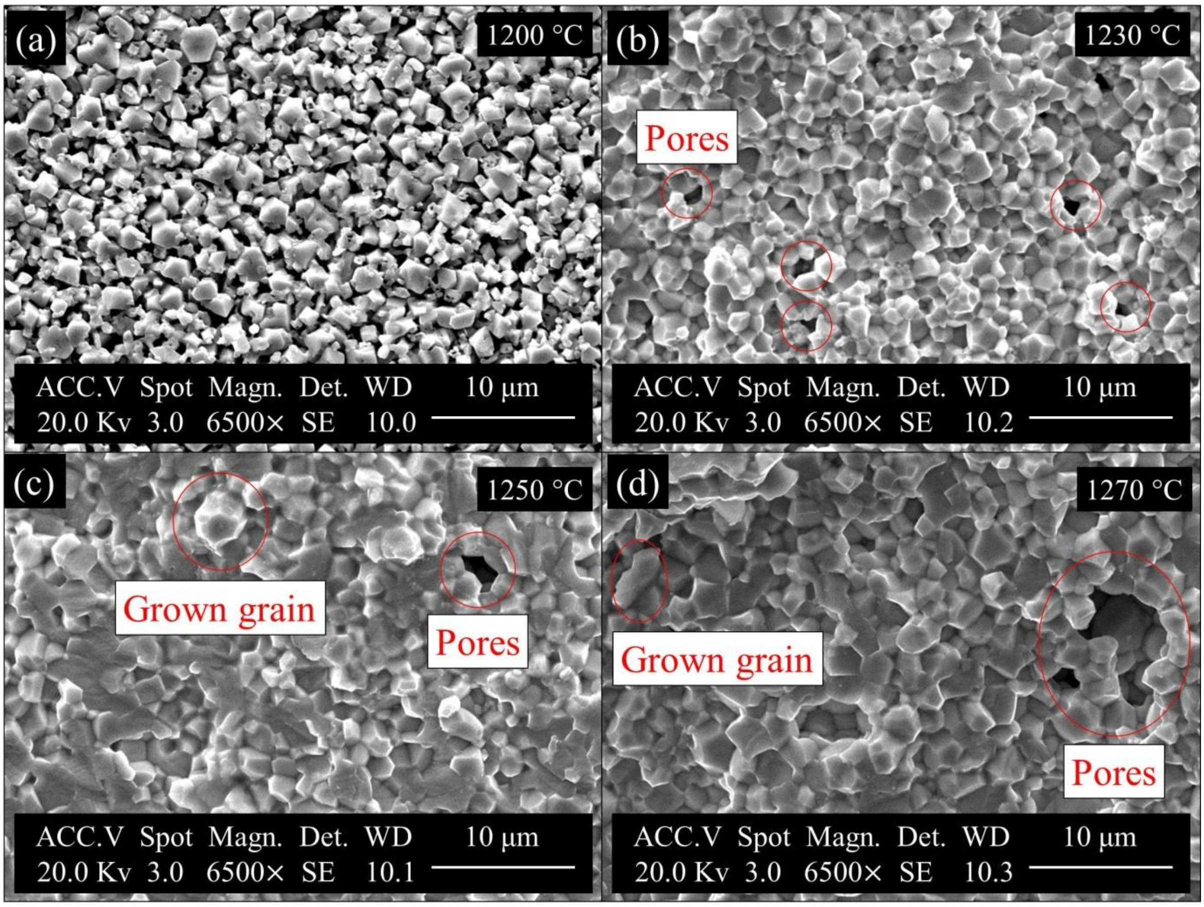

Figure 7-5. SEM images of fracture surfaces of the PZnN-P3LZT ceramic discs sintered at different temperatures.

For instance, in Figure 7-5, the microstructure of the PZnN-P3LZT sample sintered at 1200 °C (Figure 7-5 (a)) was unconsolidated, resulting in a smaller density and shrinkage rate, corresponding to the data points in Figure 7-4. When sintered at 1230 °C, the microstructures (Figure 7-5 (b)) were relatively densified with evenly distributed tiny pores and 1-2 μm average grain size. In the 1250 °C sintered sample (Figure 7-5 (c)), some larger pores and grains were observed in some areas, although most of the regions remained similar to those of the 1230 °C sintered sample (Figure 7-5 (b)). However, the situation deteriorated for the 1270 °C sintered sample (Figure 7-5 (d)), where much larger pores and grains were observed, with an average size of around 3 μm, leading to decreased densities as shown in Figure 7-4. The case shown in Figure 7-6 could be explained in a similar way.

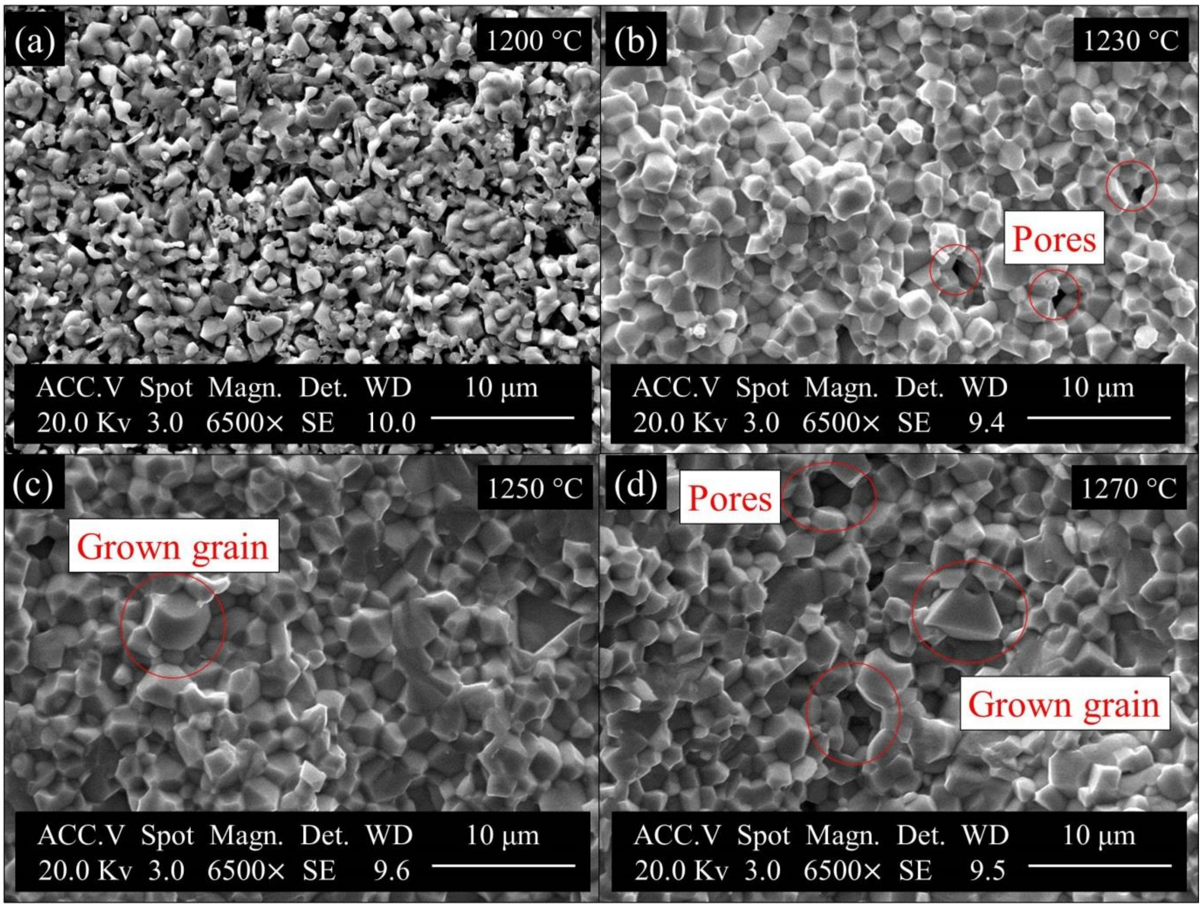

Figure 7-6. SEM images of fracture surfaces of the PZnN-P5LZT ceramic discs sintered at different temperatures.

Figure 7-7 shows the SEM image of a PZT sample as a reference, where 1-2 μm grains with evenly distributed pores could be observed. The existence of such pores might be the reason that the average density of the PZT discs shown in Figure 7-4 was smaller than that provided by the manufacturer. The difference of binder, shaping method and sintering conditions between the experimental samples and manufacturer samples could be responsible for the observed difference in density. Also, this might result in a reduction of other dielectric and piezoelectric properties, which will be discussed in the next section.

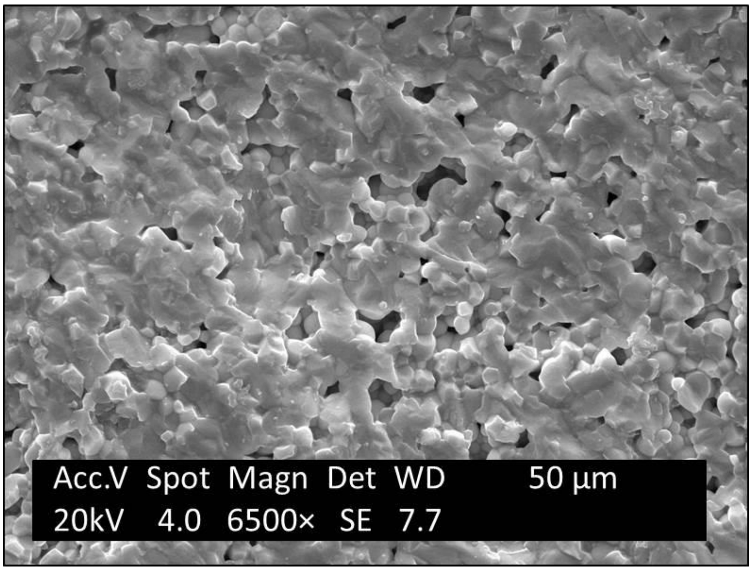

Figure 7-7. SEM image of fracture surface of the PZT ceramic disc sintered at 1200 °C.

7.1.1.4 Phase Transitions

The XRD patterns, results of density and shrinkage, as well as the SEM images of the sintered PZnN-P3LZT and PZnN-P5LZT discs indicated that 1250 °C was the optimum sintering temperature for these materials. Thus, one of each of such samples together with a PZT disc sintered at 1200 °C were selected to run the DSC test in the conditions presented in Chapter 6. Figure 7-8 shows the DSC plot, where the first gradient changes at 50-75 °C were regarded as the stabilisation of the equipment from relatively cold status to the heated internal circumstance. However, the second obvious gradient variations occurred in the range of 325-425 °C were considered as the thermal response of phase transitions. For the PZT sample, the phase transition started at around 325 °C and finished at about 425 °C, while for the PZnN-P3LZT and PZnN-P5LZT samples, they happened at approximately 350 °C and sustained until slightly below 400 °C. According to the PZT phase diagram shown in Chapter 3, these phase transitions were predicted to be rhombohedral/tetragonal to cubic transitions, and the temperature ranges were treated as their corresponding Curie temperatures (T_c). Although two phases (rhombohedral and tetragonal) co-existed in the PZnN-P3LZT and PZnN-P5LZT samples, no evidence of the transition between such phases was found in the DSC test, as in such a case the phase change is driven by composition rather than by temperature.

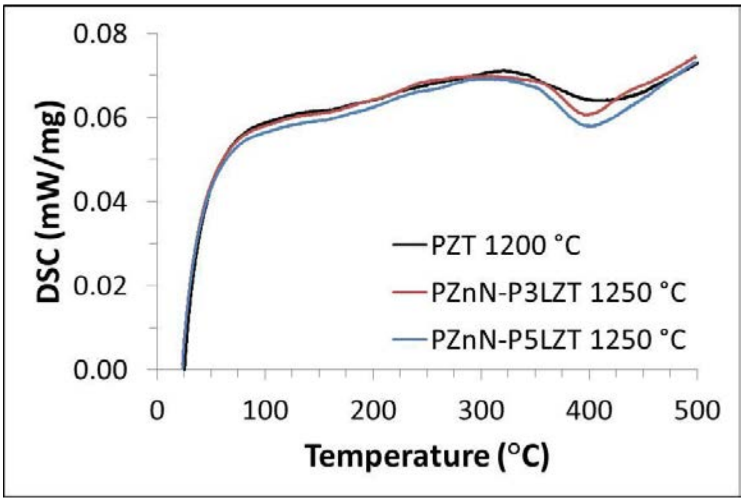

Figure 7-8. Dependence of DSC on temperature for the discs of PZT sintered at 1200 °C and PZnN-P3LZT and PZnN-P5LZT sintered at 1250 °C.

7.1.2 Basic Dielectric and Piezoelectric Properties

7.1.2.1 Permittivity and Dielectric Loss

Figure 7-9 shows the relative permittivity (ε_r) before and after poling and the dielectric loss factor ($tan\delta$) after poling, measured at room temperature, of the disc samples sintered at different temperatures. The measurements were taken at the 24th hour after poling had been completed, and each datum point was an average of a batch of 6 samples (each sample was measured 3 times independently in order to reduce errors caused by equipment). Firstly, it can be seen that the relative permittivity and dielectric loss of the PZT samples were lower and higher respectively, compared to the reference[3]. Presumably this is due to the lower density, but other factors such as lead loss may also contribute. Also, following the discussion of the dominant phases in the last section, Figure 7-9 (a) indicates that the disc samples of the PZT and PZnN-P5LZT compositions after poling yielded higher relative permittivity than those before poling, while an opposite trend happened for the PZnN-P3LZT samples. This might be evidence that in the PZnN-P3LZT disc samples, the rhombohedral phase possessed more content of the entire microstructures. And as Figure 7-9 (b) shows, the poled discs of the PZT and PZnN-P5LZT generally had lower dielectric loss than those of the PZnN-P3LZT.

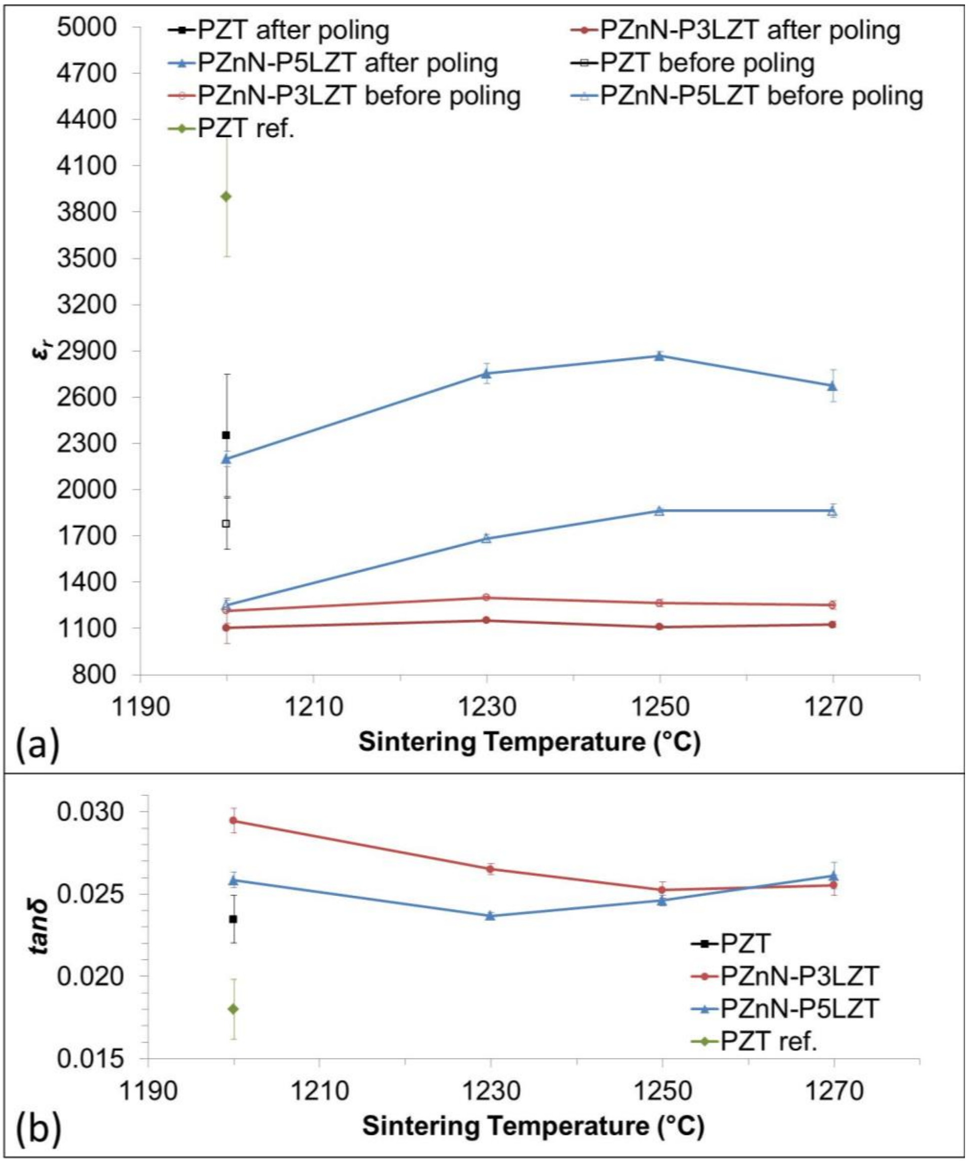

Figure 7-9. Dependence of (a) ε_r before and after poling (b) $\tan\delta$ after poling on sintering temperature for the lead-based ceramic discs of different compositions.

In theory, the domains in unpoled multi-domain piezoelectric ceramics can only co-exist with each other with angles of 180° and 90° in the tetragonal phase, as the possible dipole directions are along <100>, <$\bar{1}$00>, <010>, <0$\bar{1}$0>, <001> and <00$\bar{1}$>; or 180° and x°/(180-x)° (e.g. 71°/109° for PZT[4], called effective 90°) in the rhombohedral phase, because of possible dipole directions along <111>, <$\bar{1}\bar{1}\bar{1}$>, <$\bar{1}$11>, <1$\bar{1}$1>, <11$\bar{1}$>, <$\bar{1}\bar{1}$1>, <1$\bar{1}\bar{1}$> and <$\bar{1}$1$\bar{1}$>. Assuming that an unpoled multi-domain piezoelectric ceramic only consists of 180° domains, all of which are perpendicular to the electrodes (as shown in Figure 7-10 (a)), the effective overall $\varepsilon_{33}^{\sigma}$ of the ceramic should comprise a combination of the ε_{33}^{S} of each single domain. Similarly, if a multi-domain piezoelectric ceramic only contains 180° domains, all of which are in parallel with the electrodes (as shown in Figure 7-10 (b)), the effective overall $\varepsilon_{33}^{\sigma}$ should comprise a combination of the ε_{11}^{S} of each single domain. As the clamped domain is constrained by the domain walls, the ε_{33}^{S} value is predicted to be smaller than its corresponding $\varepsilon_{33}^{\sigma}$ value.[5] Therefore, in the situation of Figure 7-10 (a), the effective overall $\varepsilon_{33}^{\sigma}$ tends to increase after poling because of the disappearance of 180° domain walls. In contrast, according to empirical investigations[6,7], ε_{11} was usually larger than ε_{33} for a single domain, thus the effective overall $\varepsilon_{33}^{\sigma}$ after poling in Figure 7-10 (b) would probably decrease, as it will transfer to a combination of the individual $\varepsilon_{33}^{\sigma}$ values of each domain because of 90° domain rotation. Based on the above discussion, for a normalised unpoled multi-domain piezoelectric ceramic where the 180° and 90° (or effective 90°) domains co-exist, as shown in Figure 7-10 (c), if the 180° domains dominate the domain structure, the effective overall $\varepsilon_{33}^{\sigma}$ is likely to increase, while if the 90° (or effective 90°) domains are the majority, it tends to decrease. Also, based on the results in Figure 7-9 (a), as the microstructures of the PZT and PZnN-P5LZT were shown to be tetragonal-rich and their permittivity increased after poling, it implied that in such tetragonal phases 180° domains might dominate. Because the composition of PZnN-P3LZT was extremely close to that of the PZnN-P5LZT, the tetragonal phases were assumed to be similar. If in the PZnN-P3LZT samples the tetragonal phase still dominated, the permittivity should have a similar trend to those of the PZnN-P5LZT samples, however they varied with an opposite trend. Therefore, this could imply that the main phase in the PZnN-P3LZT samples was rhombohedral containing mainly effective 90° domains. It should be noted that the above discussion assumes that the poling direction is parallel to <100> where all the grains are nicely aligned, whereas in a real material the grain orientations will be random. However, such a discussion is still valid in real cases, although the effects might not be quite as great, as some domains may not be able to re-orientate.

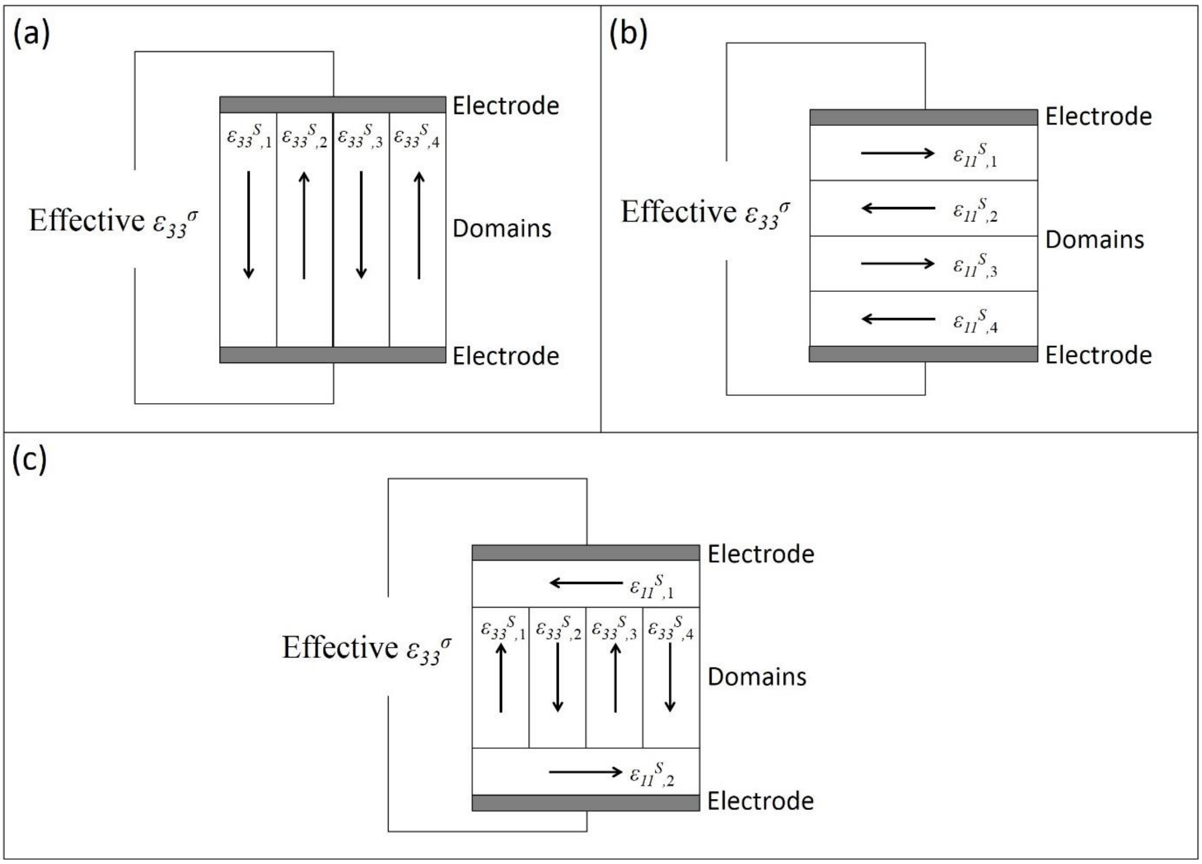

Figure 7-10. Schematics of explanation of effective $\varepsilon_{33}^{\sigma}$ of unpoled multi-domain piezoelectric ceramics.

7.1.2.2 Piezoelectric Coefficient, Electromechanical Coupling and Quality Factor

Figure 7-11 shows the impedance-frequency spectra (vibration along the diameter direction) of the discs based on which Q_M, k_{eff} and k_p were calculated. One of each batch of samples was selected and is shown as representative, and the average frequency constant (N) with deviation of each batch of samples is stated. The figure shows the fundamental resonance and three levels of harmonics of each sample when vibrating along the direction of the diameter driven by small electric signals, indicating that all of the samples exhibited typical piezoelectric response. The f_r, f_a and Z_m used for relevant calculation were obtained from the fundamental resonance.

In Figure 7-11, the frequency constants of the PZnN-P3LZT samples slightly increased with sintering temperature, implying possible internal change (e.g. phase transition) within the materials. This could be a supplementary evidence of the discussion with Figure 7-2, where a growth of tetragonal phase with the increase of sintering temperature was deduced. Also, for the PZnN-P5LZT samples, the frequency constants stayed similar until being sintered at 1250 °C, which implies no significant internal material change happened for the samples sintered below this temperature. However, the potential phase transition from rhombohedral to tetragonal as discussed in Section 7.1.1.2 within the samples sintered at and above 1250 °C might be the reason leading to the corresponding variation of the frequency constants.

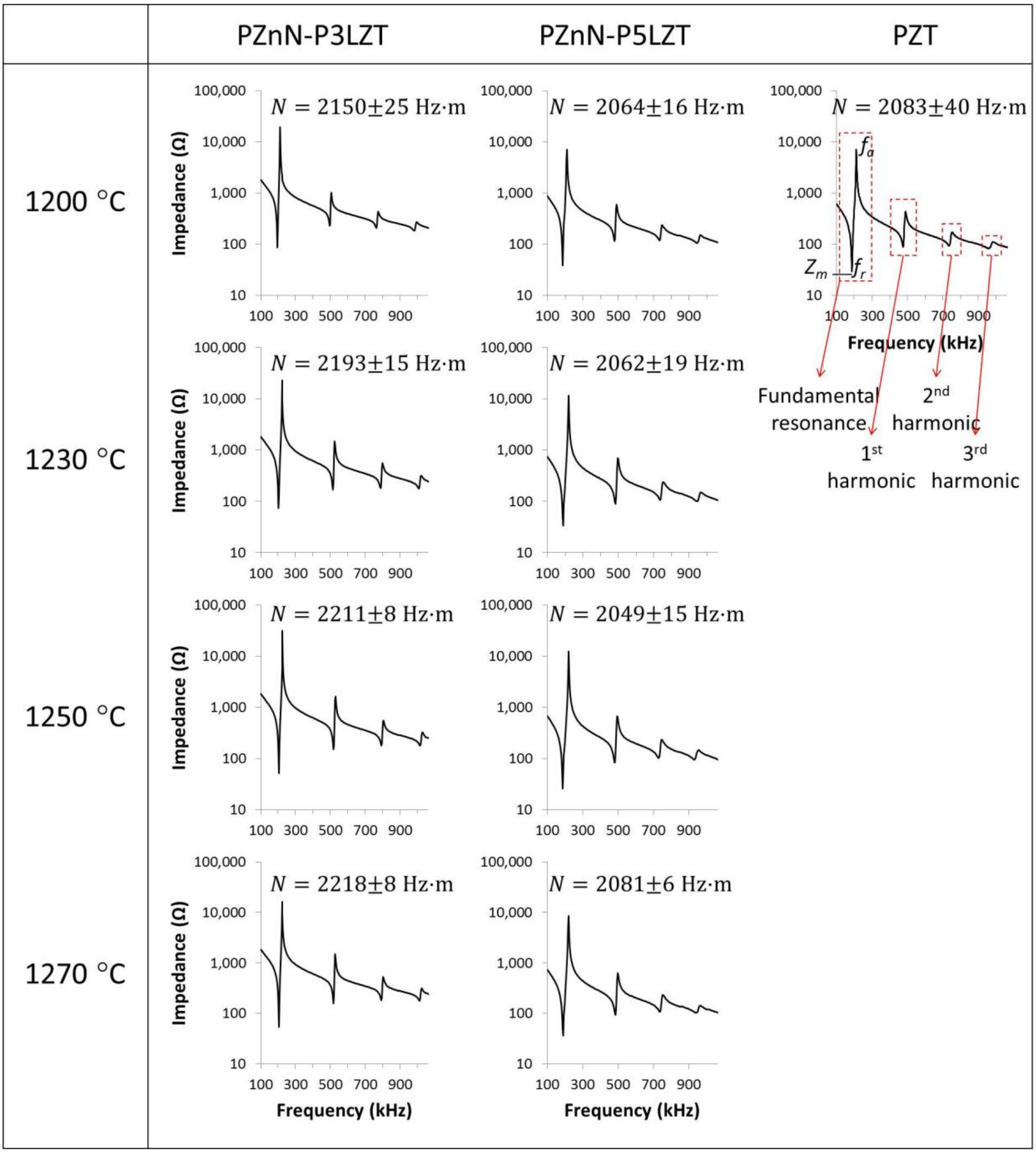

Figure 7-11. Dependence of impedance on frequency for the lead-based ceramic discs of different compositions sintered at different temperatures.

Figure 7-12 shows the d_{33}, Q_M, k_{eff} and k_p of the lead-based disc samples, of which the measurements were taken 24 hours after poling, and each datum point was an average of a batch of 6 samples (each sample was measured 3 times independently in order to reduce errors caused by equipment). The PZT and PZnN-P5LZT samples exhibited generally higher d_{33}, k_{eff} and

k_p, except that the PZnN-P3LZT samples exhibited higher Q_M. This could be because, on one hand, that larger amount of La doping made the PZT and PZnN-P5LZT rather 'soft', inducing enhanced d_{33} and electromechanical coupling coefficients; on the other hand, the Zr/Ti ratio in the PZnN-P3LZT composition was further away from the MPB than that of the PZT or PZnN-P5LZT, causing a partially pseudo-'hard' effect which increased Q_M but decreased d_{33}, electromechanical coupling coefficients as well as permittivity (Figure 7-9 (a)).

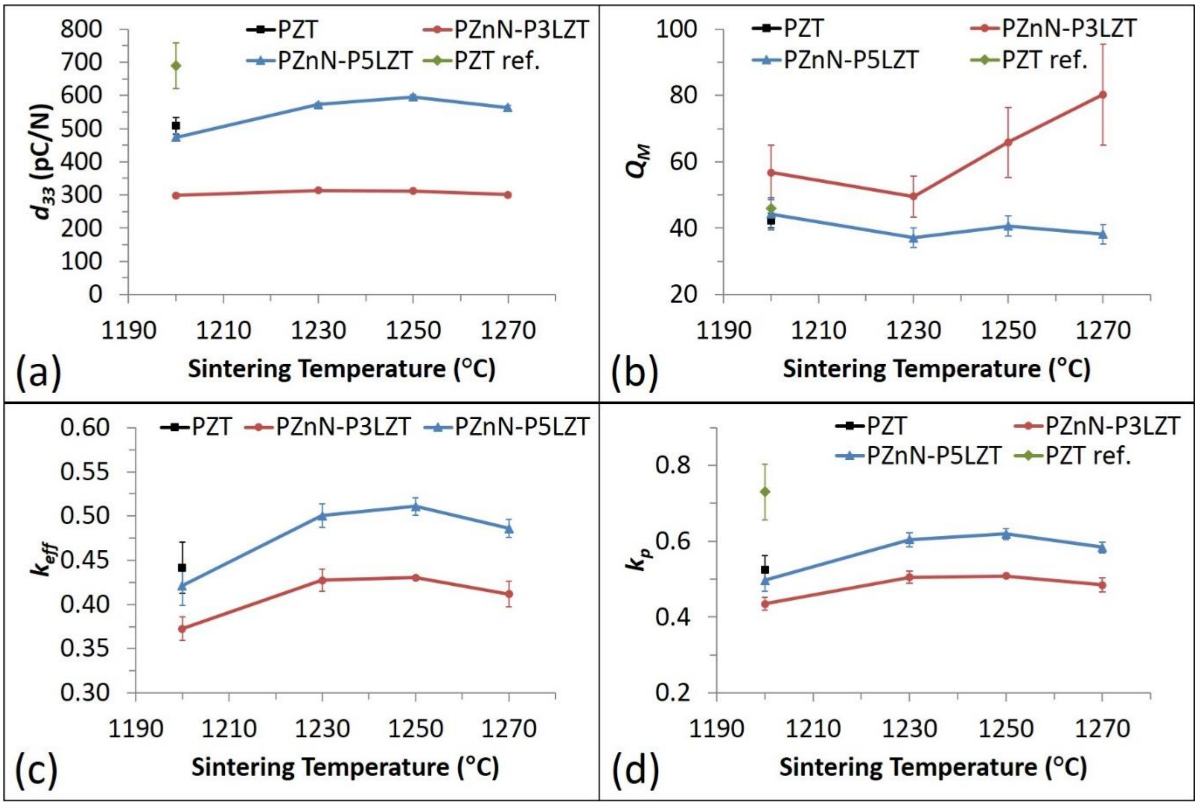

Figure 7-12. Dependence of (a) d_{33} (b) Q_M (c) k_{eff} and (d) k_p on sintering temperature for the lead-based ceramic discs of different compositions.

7.1.3 Energy Harvesting Related Parameters

Figure 7-13 shows the calculated results of g_{33} (Equation 3-36 in Chapter 3) and $d_{33}{\cdot}g_{33}$ of the disc samples. As expected, the PZnN-P3LZT samples possessed higher g_{33} values. This is because the pseudo-'hard' effect decreased the permittivity but the 'soft' La-doping compensated the reduction of d_{33} to some degree, resulting in increased g_{33}. However, the PZT and PZnN-P5LZT samples generally had higher $d_{33} \cdot g_{33}$ values. In principle, the parameter g has a positive effect on the generated voltage across a piezoelectric material (see Equations 4-6 and 4-7), while $d \cdot g$ (defined as figure of merit, FOM) is able to determine the overall capability of energy generation of a piezoelectric energy harvester. As shown in Equation 7-1, the energy storage of a piezoelectric energy harvester is positively related to the capacitance of a piezoelectric element (C) as well as the square of the generated voltage (U). Also as mentioned, C and U are proportional to the permittivity (ε) and voltage coefficient (g), respectively. As $g = d/\varepsilon$ (see Equation 3-36), the energy storage is consequently affected by the FOM. Considering the information provided in both Figures 7-12 and 7-13, a PEHer (piezoelectric energy harvester) made from the PZT or PZnN-P5LZT composition might have larger theoretical off-resonant output power density, while that made from the PZnN-P3LZT composition would hopefully generate higher open-circuit voltage. Nevertheless, which composition would reveal a larger energy conversion efficiency of the material sector was difficult to predict with the current results. A further discussion will be given with the real harvester test in Chapter 8.

$$\text{Energy Storage} = \frac{1}{2}CU^2 \propto \varepsilon \cdot g^2 = \varepsilon \cdot \left(\frac{d}{\varepsilon}\right)^2 = \frac{d^2}{\varepsilon} = d \cdot g \quad (7\text{-}1)$$

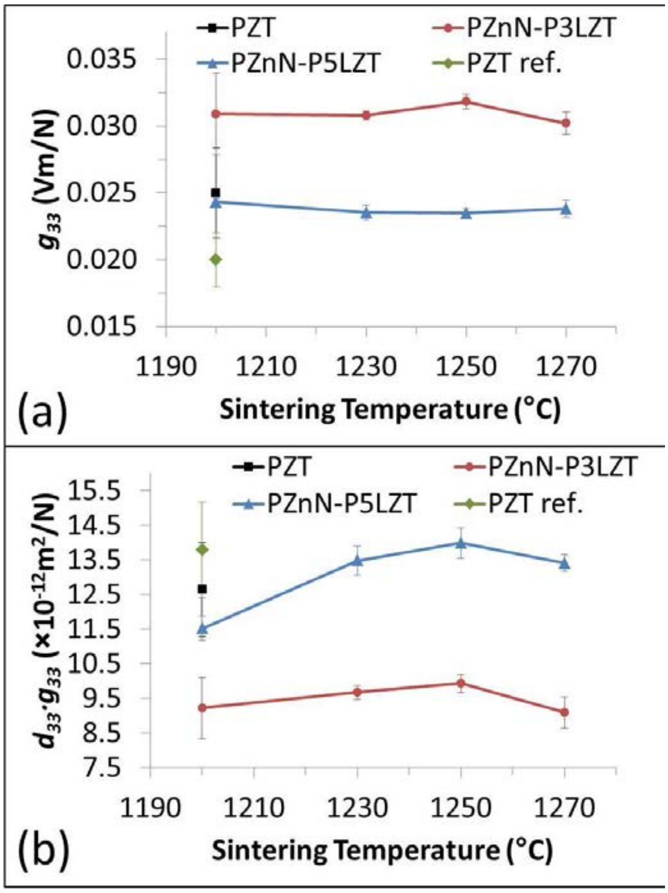

Figure 7-13. Dependence of (a) g_{33} (b) $d_{33} \cdot g_{33}$ on sintering temperature for the lead-based ceramic discs of different compositions.

At this stage, it could be summarised that the properties of the PZnN-P5LZT samples were quite similar to those of the PZT samples. As one of the aims of this project is to investigate the relations between material properties and harvester performance, rather than conduct further in depth research on different compositions, the PZT and PZnN-P3LZT compositions, which obviously differ each other, were selected to continue the device fabrication and test, with no further work about devices being carried out on the PZnN-P5LZT composition. This was only one of the reasons of such material selection, but the other reasons will be stated in the following sections.

7.1.4 Ageing

In order to observe the ageing behaviour, all of the disc samples were re-measured on the 180th day after being poled. Figure 7-14 summarises the 180-day ageing effect constants of parameters corresponding to those discussed in the above sections. The calculation was based on the relevant presentation in Chapter 3.

In the figure, the positive value means an increase of the parameter with time while the negative value indicates an opposite change. For $tan\delta$, ε_r and d_{33}, all of the three compositions showed decreasing trends, while for Q_M all of them showed an increasing trend. For the electromechanical coupling coefficients, all of the PZnN-P5LZT samples as well as the PZnN-P3LZT samples sintered at 1230 °C aged positively, while the others aged negatively. And for g_{33} and $d_{33}{\cdot}g_{33}$, only the PZT samples showed a positive change.

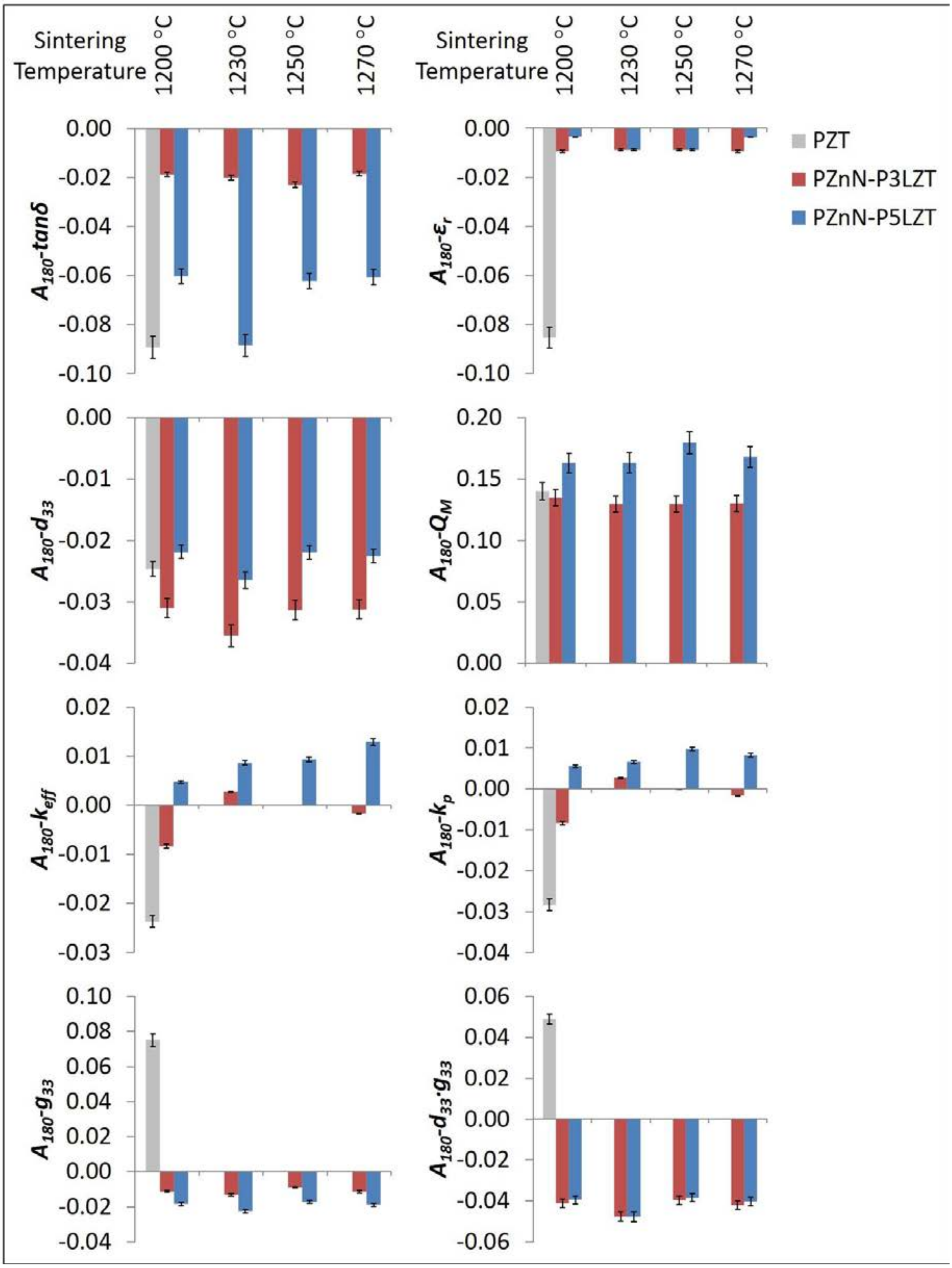

Figure 7-14. Dependence of 180-day ageing effect constants of $tan\delta$, ε_r, d_{33}, Q_M, k_{eff}, k_p, g_{33} and $d_{33}{\cdot}g_{33}$ on sintering temperature for the lead-based ceramic discs of different compositions.

From a general point of view, the PZnN-P3LZT composition exhibited the weakest ageing effect (smaller absolute value of A_{180}) among all the compositions, indicating a better time stability, despite the exception of d_{33}. However, as for the PZT composition the d_{33} decreased slower than the ε_r, the g_{33} and d_{33}·g_{33} which are two significant criteria for energy harvesting increased with time, which was actually a beneficial trend if the materials were selected to fabricate energy harvesters. As the 24-hour properties of the PZT and PZnN-P5LZT samples were similar but the ageing behaviour of the former was beneficial, this was the second reason to choose the PZT for further device investigations, rather than the PZnN-P5LZT. As the PZT had such ageing advantage, it was suggested that the PEHers made from the PZT and PZnN-P3LZT would better be tested and compared as soon as possible after being poled, in order to avoid significant errors caused by ageing.

7.2 $0.5Ba(Zr_{0.2}Ti_{0.8})O_3$-$0.5(Ba_{0.7}Ca_{0.3})TiO_3$

7.2.1 Material Analyses

7.2.1.1 Particles

Tables 7-3 and 7-4 summarise the particle sizes of the raw powders, pre-reacted $BaZrO_3$ powder and calcined 50BCZT powder. All of the powders were ball milled for 24 hours before measurements, and each datum was an average of 3 values from 3 independent measurements. The particle size of the calcined 50BCZT powder was larger than that of the lead-based powders listed in Table 7-2 as well as the empirical data of practical ceramic fabrication. This might be because of the larger starting particles of the $BaCO_3$ powder as well as the higher calcination temperature (1350 °C compared to 900 °C for the lead-based compositions). Although other milling methods (e.g. vibratory milling) may help to further reduce the particle size, this calcined powder was used for the preliminary investigation of the general properties of sintered

50BCZT ceramics, in order to maintain the compatible fabrication process with the lead-based ceramics discussed above, as well as keeping the process as simple as possible and thus avoiding errors or perturbations caused by additional procedures.

Table 7-3. Summary of particle sizes of the starting oxides for lead-free composition.

Powder	D_{50} (μm)	D_{90} (μm)
$BaCO_3$	4.04 ±0.87	9.59 ±1.38
ZrO_2	3.14 ±0.56	7.46 ±0.81
$CaCO_3$	2.73 ±0.79	6.90 ±1.05
TiO_2	2.97 ±0.67	7.33 ±1.05

Table 7-4. Summary of particle sizes of the calcined and milled lead-free powders.

Powder	D_{50} (μm)	D_{90} (μm)
$BaZrO_3$	1.47 ±0.44	3.38 ±0.56
50BCZT	4.58 ±0.69	11.60 ±1.07

7.2.1.2 Phase Structures and Transitions

Figure 7-15 shows the XRD results of the synthesized $BaZrO_3$ powder, calcined 50BCZT powder and disc ceramics sintered at different temperatures. In general, all of the patterns indicate perovskite phase structures. In particular, the $BaZrO_3$ powder was proved a simple cubic phase without peak broadening or split. However, the 50BCZT powders and the sintered discs were more complicated to analyse.

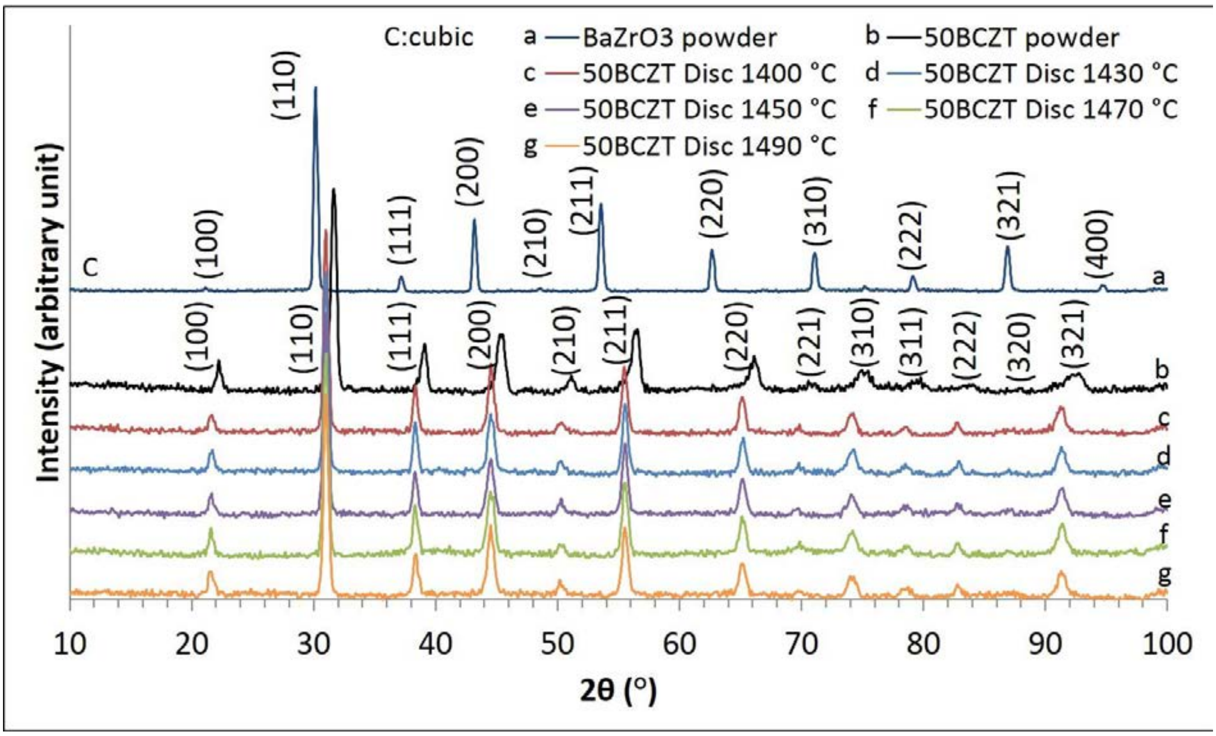

Figure 7-15. XRD patterns of the $BaZrO_3$ powder, 50BCZT powder and discs sintered at different temperatures – full scale.

Figure 7-16 provides the details of certain peaks that could help identify specific phases of the powder and discs. Although the peak positions shifted towards smaller diffraction angles after sintering, which might imply increased c/a ratios, both the powder and the discs formed orthorhombic/tetragonal-combined multi-phase structures according to the peak positions as well as broadening and splitting as shown in Figure 7-16. In detail, the first reported phase diagram of BZT-BCT system[8] (presented in Chapter 3) suggested a strongly curved MPB between tetragonal phase and rhombohedral phase, and the 50BCZT composition at room temperature is situated in this MPB region. This should result in a binary phase structure as shown in Figure 7-15 and 7-16. However, in more recent studies using either X-ray diffraction[9] or neutron diffraction[10] measurement which is more sensitive, partially revised MPBs of the system[9,10] were proposed with an additional orthorhombic phase between the tetragonal and rhombohedral phase regions, as in the parent compound $BaTiO_3$ (presented in Chapter 3). This was a supplementary clue[9,10] when analysing and indexing the XRD patterns. In order to investigate the phases in more detail as well as determine the phase transition temperatures, the temperature dependence of ε_r and $tan\delta$ of one sample of each batch of sintered discs were measured between -50 °C and 120 °C, and the data are shown in Figure 7-17.

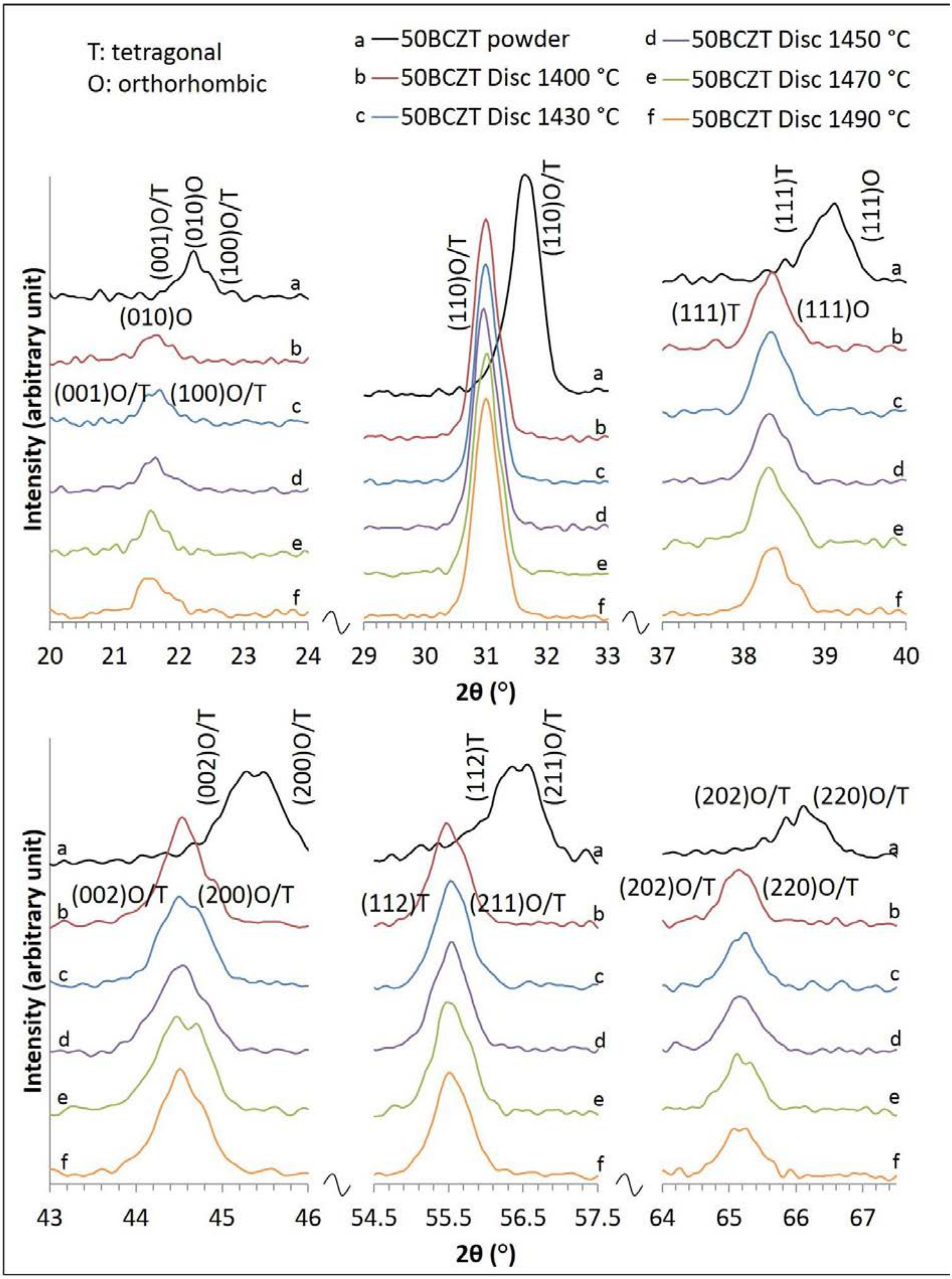

Figure 7-16. XRD patterns of 50BCZT powder and discs sintered at different temperatures - detail of the {100}, {110}, {111}, {200}, {211} *and* {220} *peaks.*

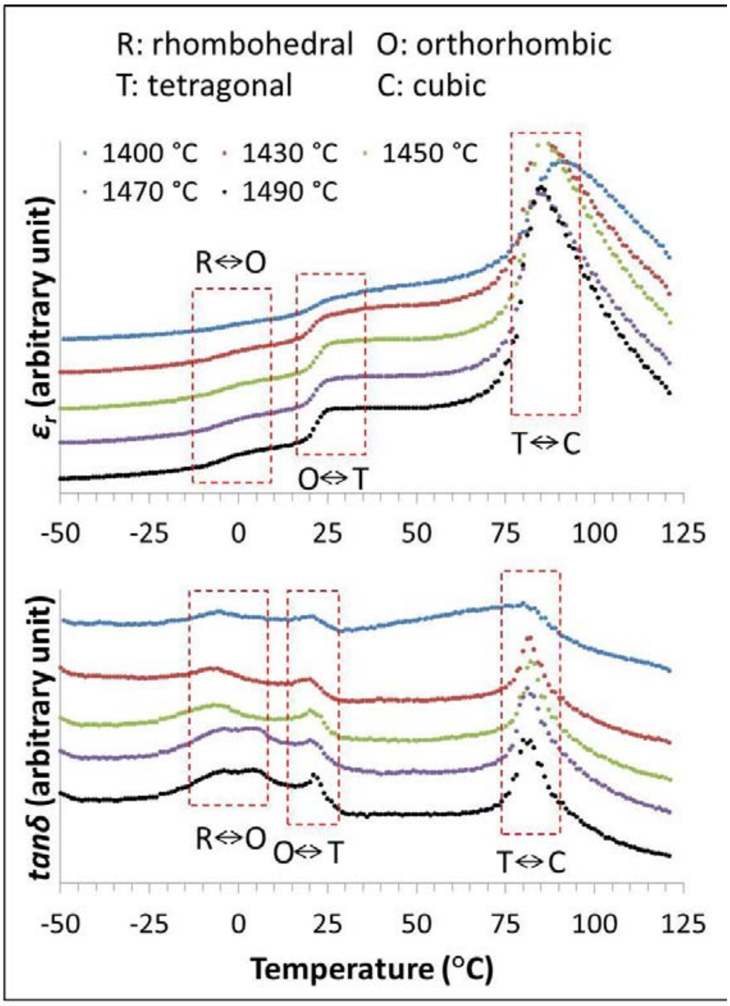

Figure 7-17. Dependence of relative permittivity and dielectric loss factor on temperature for the 50BCZT discs sintered at different temperatures.

The phase transition between the tetragonal and cubic phases can be recognised with the peaks in both ε_r and $tan\delta$ around 88 °C, which was also considered as the T_c of the 50BCZT composition. Two other phase transition regions can also be observed at around -5 °C and 23 °C, respectively. The first transition is only visible in the $tan\delta$ data, whilst the second transition is visible by gradient variations in both the ε_r and $tan\delta$ data around 23 °C. These phenomena indicate two phase transitions, which were interpreted as the rhombohedral-orthorhombic and orthorhombic-tetragonal transitions, respectively. As the XRD was carried out at room temperature (approximately 20 °C) which is in the phase transition region, a co-existence of orthorhombic and tetragonal phases of the sintered discs at room temperature could be expected, as shown by the indexing of the peaks in Figure 7-16.

7.2.1.3 Sintering Behaviour

Figure 7-18 shows the densities and diameter shrinkage rates of the 50BCZT discs sintered at different temperatures.

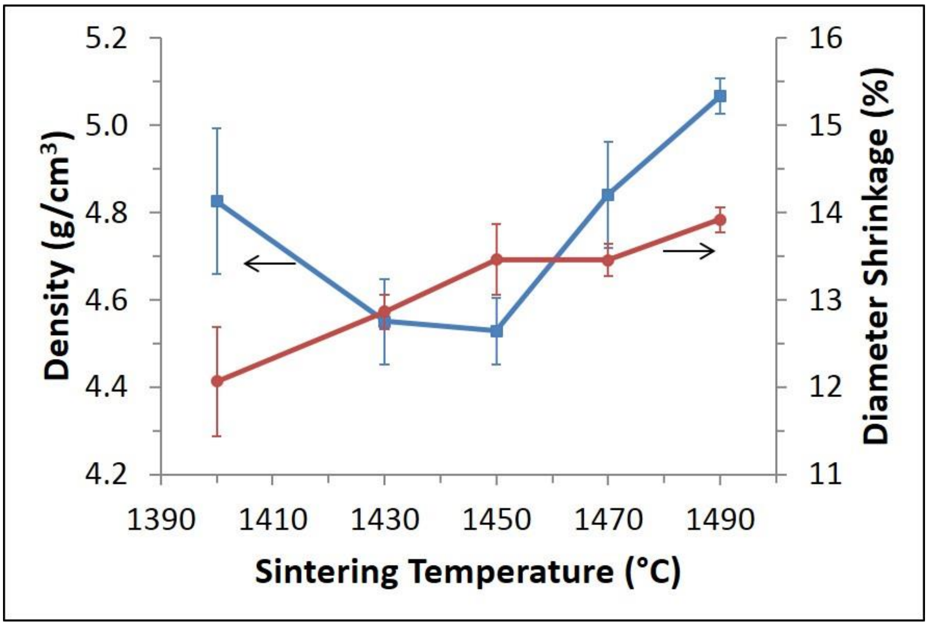

Figure 7-18. Dependence of density and diameter shrinkage on sintering temperature for the 50BCZT discs.

The shrinkage exhibited a similar trend to the lead-based samples discussed above, which was that the samples tended to shrink more with increased sintering temperature, indicating better densification at higher temperatures. However, the measured densities firstly decreased for the samples sintered up to 1450 °C, then increased to about 5 g/cm^3 sintered at 1490 °C. In principle, this might be due to grain growth dominating over densification for the samples sintered between 1400 °C and 1450 °C, thus resulting in much retained porosity and leading to decrease in density. However, when being sintered above 1450 °C, the densification dominates the sintering behaviour again, thus leading to an overall reduction in porosity. SEM micrographs of the sintered samples are shown in Figure 7-19.

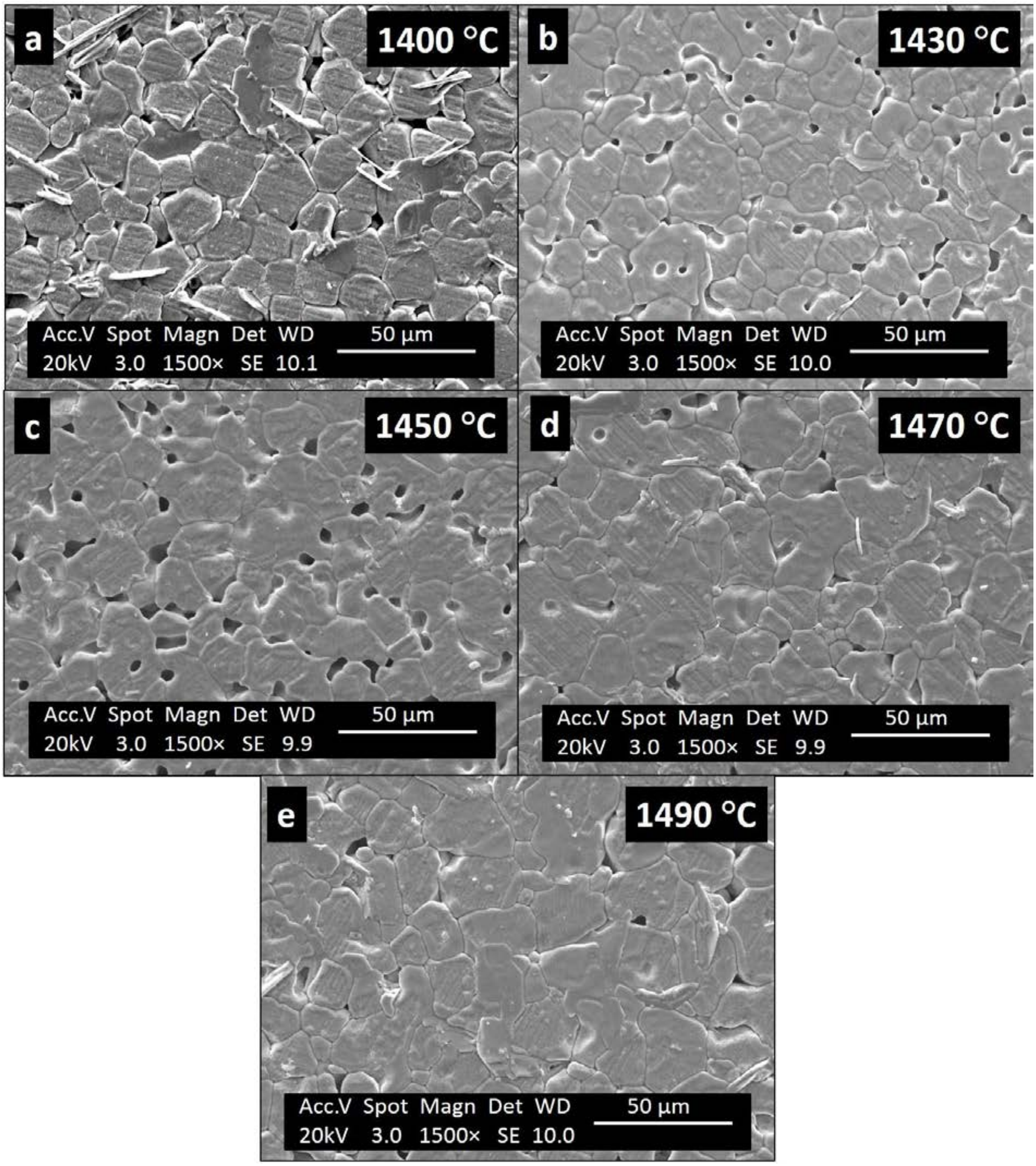

Figure 7-19. SEM images of polished and thermal-etched surfaces of the 50BCZT discs sintered at different temperatures.

For the samples sintered at 1400 °C (see Figure 7-19 (a)), the grain sizes are evenly distributed in the range of 15-20 μm with small amount of small pore between grains. When being sintered at 1430 °C (Figure 7-19 (b)), the grains continued to grow and dominated over densification, with more small pores retained than that sintered at 1400 °C. Such a behaviour sustained until 1450 °C (Figure 7-19 (c)), where the grain growth started to slow down and the average grain size maintained in the range of 25-30 μm. When the sintering temperature continued to ramp up, significant grain growth could hardly be observed in the samples sintered at 1470 °C (Figure 7-19 (d)) and 1490 °C (Figure 7-19 (e)), while most of the pores were eliminated due to densification dominating grain growth, resulting in more consolidated microstructures hence higher densities (see Figure 7-18). It should be noted that the average grain sizes of the 50BCZT discs were considerably larger than those of the lead-based discs presented in Section 7.1. This might be caused by the larger particle size of the calcined powder, as well as the higher sintering temperature which is the theoretical driven force of grain growth. Also, $BaTiO_3$ ceramics have been well known for rapid grain growth[11].

7.2.2 Effect of Sintering Temperature on Dielectric, Piezoelectric and Energy Harvesting Properties

7.2.2.1 Permittivity and Dielectric Loss

The relative permittivity and dielectric loss factor of the 50BCZT discs sintered at different temperatures, poled at 25 °C and tested at the 24th hour after poling are shown in Figure 7-20. Each datum point was an average of measurements on 6 samples. Overall, the relative permittivity increased while the dielectric loss decreased with increased sintering temperature. According to previous research regarding to the parent composition, $BaTiO_3$, both density and grain size have influence on relative permittivity[12]. When sintered below 1450 °C, as the grain growth dominated over densification, although the density decreased with increased sintering temperature (see Figure 7-18), the relative permittivity did not decrease but increase with growing grains. A corresponding opposite trend was observed in $tan\delta$. This might suggest that for the 50BCZT ceramics, dielectric properties (e.g. ε_r and $tan\delta$) may be strongly dependent on grain size rather than density. Considering the errors, little difference could be found in the temperature range of 1450 to 1490 °C in terms of the relative permittivity and dielectric loss.

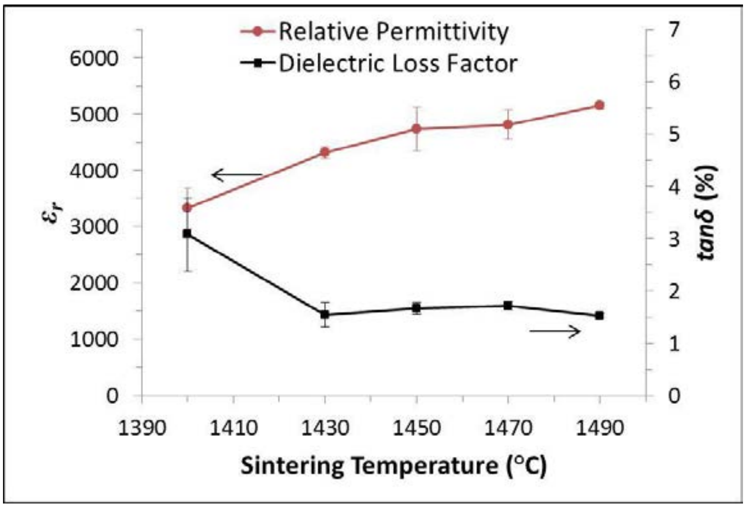

Figure 7-20. Dependence of relative permittivity and dielectric loss factor after poling on sintering temperature for the 50BCZT discs.

7.2.2.2 Piezoelectric Coefficient, Electromechanical Coupling and Quality Factor

The impedance-frequency spectra of planar vibration of the discs sintered at different temperatures are shown in Figure 7-21. These data were used to calculate the coupling coefficients. Each spectrum was from a sample sintered at the indicated temperature. The average frequency constants are also marked in the figure. This figure confirmed that all of the samples sintered at different temperatures exhibited piezoelectric activity with planar resonance. The frequency constants of the samples sintered at 1430-1490 °C were similar, considering reasonable errors, implying similar material qualities. However, those of the sample sintered at 1400 °C showed not only a larger average value but also huge deviation, indicating an unstable or inhomogeneous status at this sintering temperature.

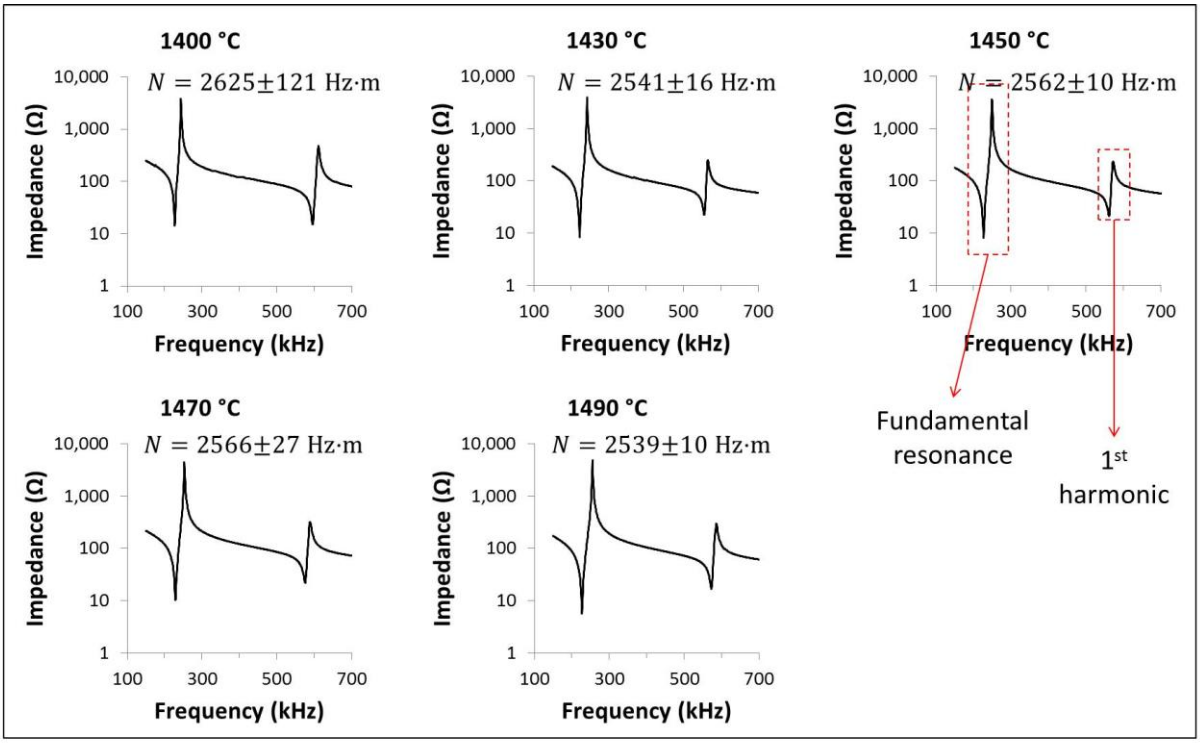

Figure 7-21. Dependence of impedance on frequency for the 50BCZT discs sintered at different temperatures.

The d_{33}, Q_M, k_{eff} and k_p of the 50BCZT discs sintered at different temperatures are shown in Figure 7-22. Each datum represents an average of measurements from 6 samples. Similar to the situation in Figure 7-21, the samples sintered at 1400 °C exhibited obviously different d_{33} and coupling coefficients with lower average values and larger deviations compared to the samples sintered at 1430-1490 °C. The d_{33}, k_{eff} and k_p showed similar trends to that of ε_r (see Figure 7-20), where the variation of these parameters was probably not resulted from change of density but was likely to be positively related to grain size. This might suggest that grain growth may also have a more significant influence on piezoelectric properties than density, which is consistent with the discussion in Section 3.6.3.1. Exclusively, the Q_M showed rather a stable trend when taking the deviations into account, which may suggest an independence on density or grain size. In summary, the dielectric and piezoelectric properties showed a rather good consistency to those in the published report[8].

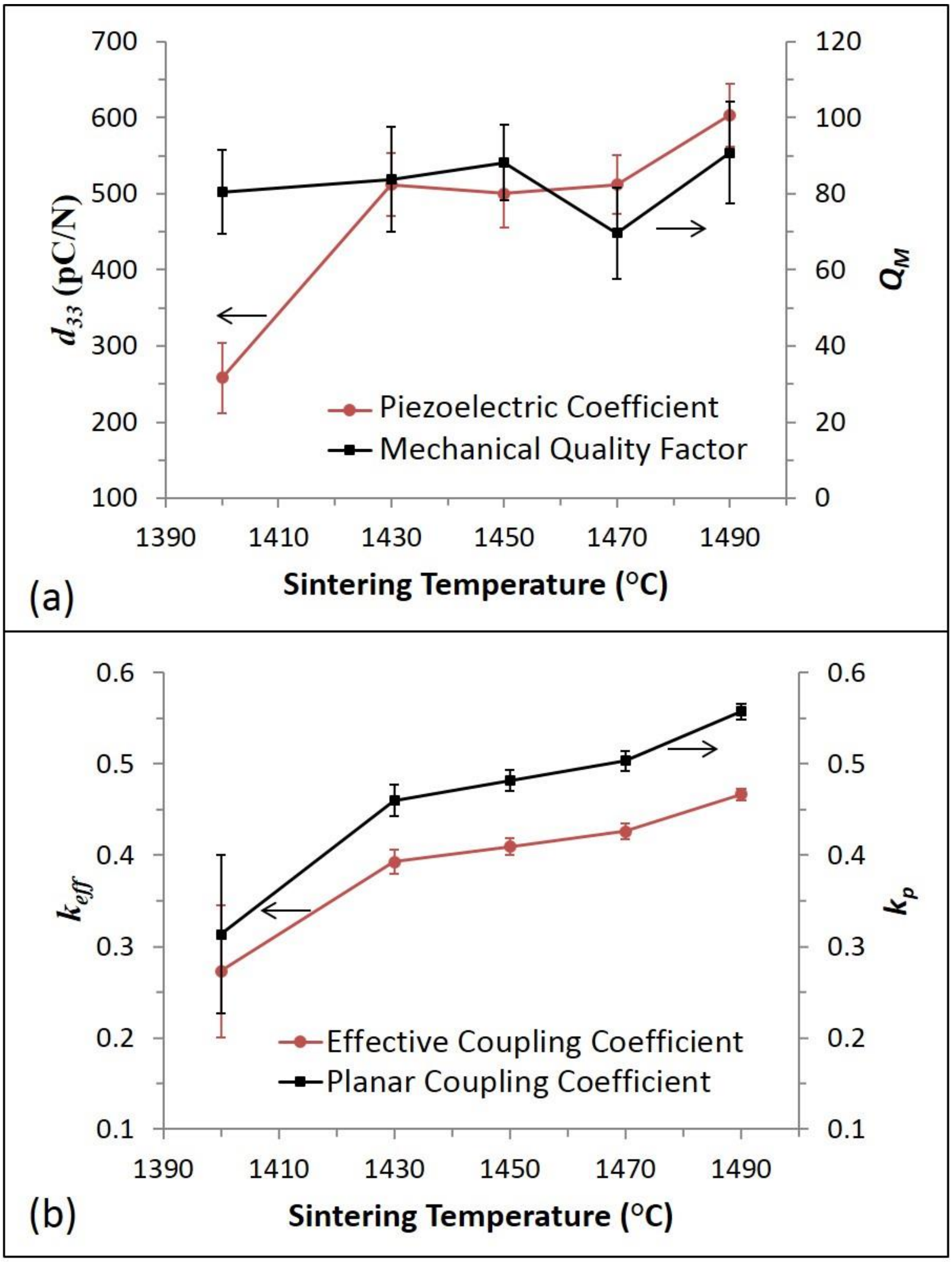

Figure 7-22. Dependence of (a) d_{33} and Q_M (b) k_{eff} and k_{31} on sintering temperature for the 50BCZT discs.

7.2.2.3 Energy Harvesting Related Parameters

The d_{33}·g_{33} and g_{33} values of the discs sintered at different temperatures are shown in Figure 7-23. Both parameters varied with similar trends to the d_{33} (see Figure 7-22 (a)), where the samples sintered at 1490 °C generally exhibited the best average properties. Therefore, as the d_{33}, coupling coefficients and energy harvesting parameters increased with sintering temperature, the samples sintered at 1490 °C were selected for further investigations.

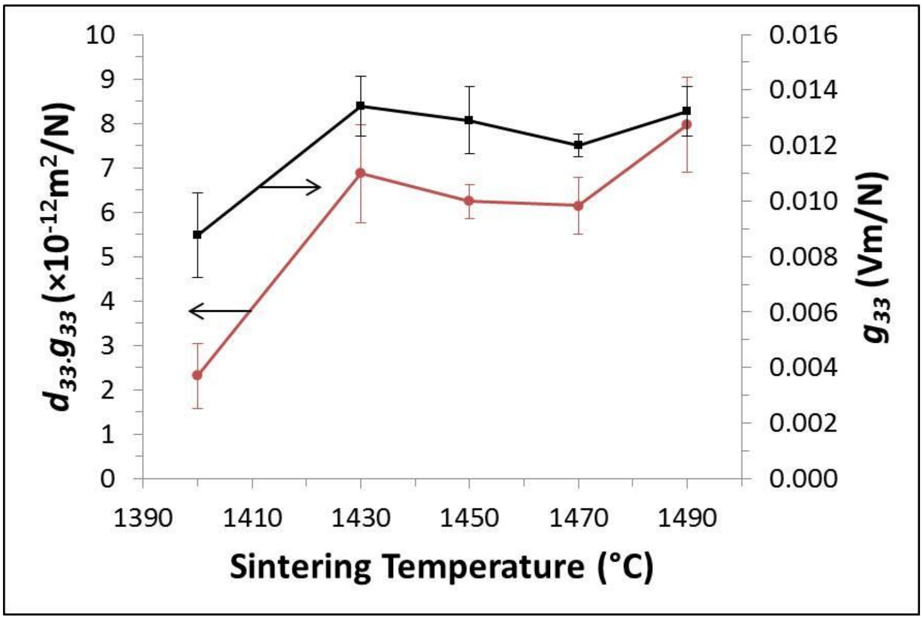

Figure 7-23. Dependence of d_{33}·g_{33} *and* g_{33} *on sintering temperature for the 50BCZT discs.*

7.2.3 Effect of Measurement Temperature – Temperature Stability

Polarization/electric field hysteresis loops measured at a range of temperatures are shown in Figure 7-24 for disc samples No. 25 and No. 26, both of which are 50BCZT sintered at 1490 °C.

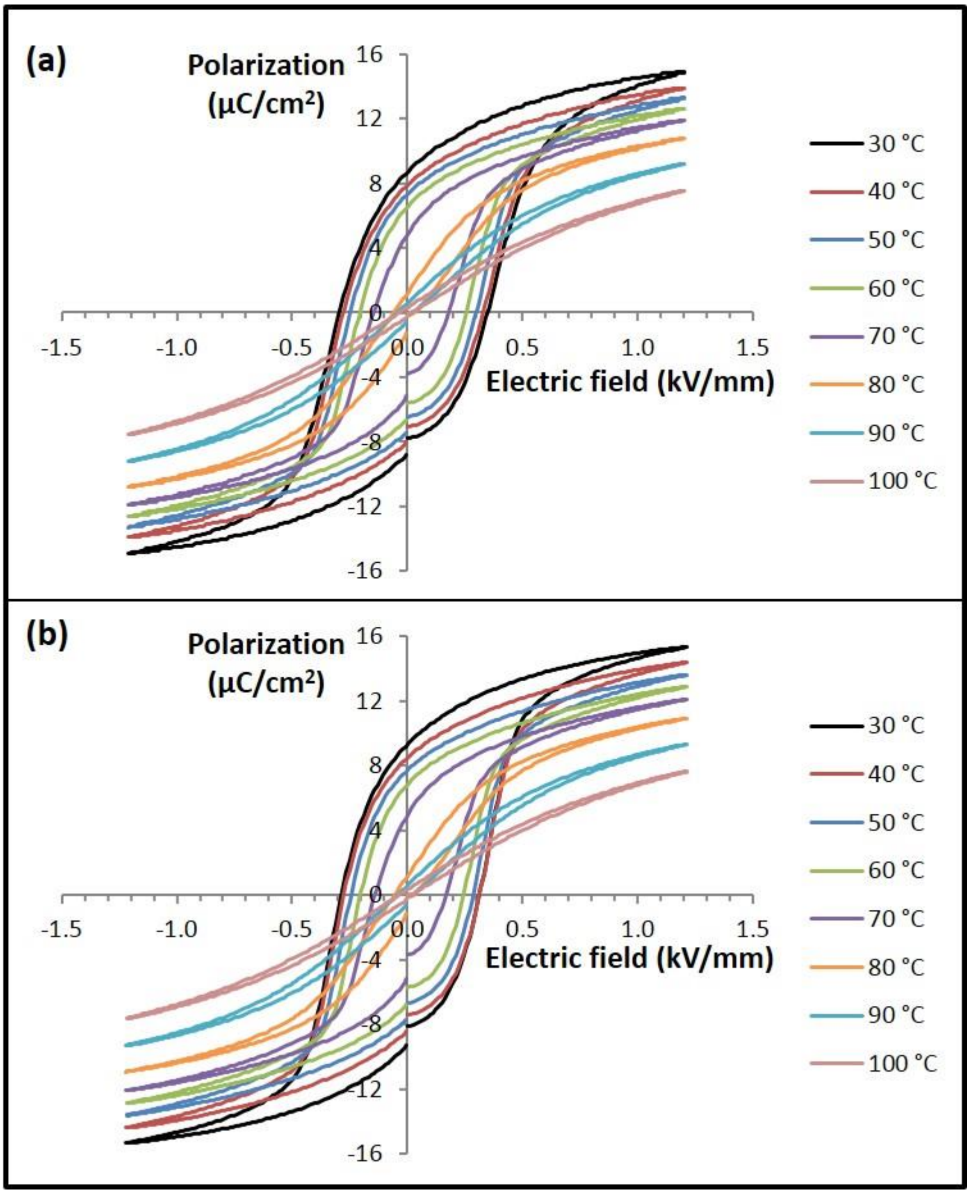

Figure 7-24. Dependence of polarization on bias electric field for (a) disc sample No. 25 and (b) disc sample No. 26 sintered at 1490 °C.

The results in Figure 7-24 (a) and (b) exhibit good consistency. As the two samples were randomly selected, the fabrication and measurement repeatability could then be confirmed. In the figure, the hysteresis loops measured at 30 °C possessed the largest spontaneous and remanent polarizations, which were about ±15 and ±9 μC/cm^2 in average, respectively. Also, they showed the largest coercive electric field of approximately ±350 V/mm. However, the both the spontaneous and remanent polarizations and the coercive electric fields decreased towards zero with the increase of temperature, especially for the loops measured at 70 °C and 80 °C where enormous deteriorations of the remanent polarizations and coercive electric fields were found between them. For the loops measured at 80 °C and above, the remanent polarizations and coercive electric fields were nearly zero, indicating that the perovskite ferroelectric phase had transferred to the paraelectric cubic phase and could not be poled any more, and thus no longer exhibiting piezoelectricity. The phase transition temperature (T_c) situated around 80 °C, is in agreement with that determined from the dielectric property data presented in Figure 7-17.

7.2.4 Ageing – Time Stability

In addition to the property measurements carried out on the 24th hour since being poled which were reported above, the 6 samples sintered at 1490 °C were subsequently measured on the 48th (2nd day), 72nd (3rd day), 96th (4th day), 240th (10th day) and 1440th (60th day) hours, respectively, in order to observe the ageing behaviour. The ageing process was completed at room temperature in air. Figure 7-25 shows the variations of the dielectric, piezoelectric and energy harvesting parameters with measurement time.

Overall, the 50BCZT ceramics exhibited the normal ageing behaviour expected of piezoelectric ceramics, with relative permittivity, dielectric loss, piezoelectric and coupling coefficients all decreasing with time, while the quality factor increased with time. The $d_{33}{\cdot}g_{33}$ showed a similar trend to the d_{33}, however the g_{33} trend was observed to be more complex, with the value dropping dramatically to a minimum value on the 4th day while then rising back to its initial value and remaining relatively stable. Amongst all of the parameters, the d_{33}, k_p, $d_{33}{\cdot}g_{33}$ and g_{33} became approximately constant on the 10th day after being poled, however other parameters still tended to keep changing. As the poling conditions which had been used for these experiments had not been optimised, further discussion of the ageing effects and comparisons to PZT ceramics will be given after the optimisation results are presented in the next two sections.

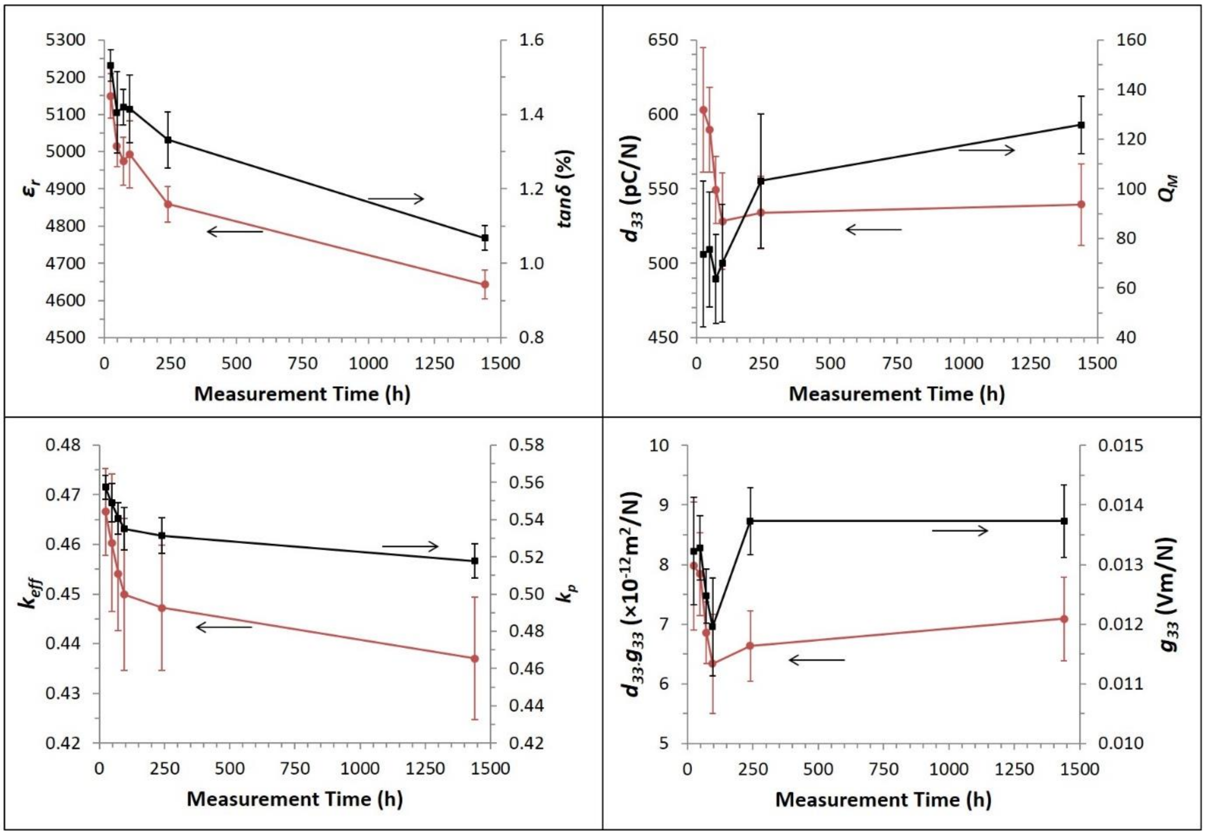

Figure 7-25. Dependence of ε_r, $tan\delta$, d_{33}, Q_M, k_{eff}, k_p, $d_{33} \cdot g_{33}$ and g_{33} on measurement time for the 50BCZT discs sintered at 1490 °C.

7.2.5 Effect of Poling Conditions

The optimum poling conditions for a piezoelectric material will be dependent on the precise relationship between phases and temperature for the composition of interest, and in particular the MPB. As the MPB of the BZT-BCT system is strongly dependent on temperature, and the presence of two phase transition regions above room temperature was observed for the 50BCZT composition as discussed in Section 7.2.1.2, a systematic investigation on the effect of poling temperature was undertaken with the disc samples sintered at 1490 °C. Four additional batches of discs were fabricated and each batch contained 3 samples. In order to minimise errors, each sample was measured 3 times independently, thus each data point in the figures of this section is an average of 9 measurements.

The 4 batches of samples were poled at 25 °C, 50 °C, 80 °C and 110 °C, respectively, on the same other conditions (at 3 kV/mm DC electric field, in silicone oil, keep field on during cooling and remove field at 25 °C) presented in Chapter 6. The poling temperatures were selected based on the phase transition behaviour presented in Section 7.2.1 and Figure 7-17, where 25 °C was in the phase transition region of two ferroelectric perovskite phases, 50 °C situated in a stable single-phase (tetragonal) region, 80 °C was near the T_c, and 110 °C was above T_c. In principle, the allowed polarization directions in the different phases have different crystallographic orientations. Thus around phase transition temperatures, there is a greater possibility for the polarisation direction of individual crystals or domains to align with the electric field direction. In addition, the process of keeping the voltage on whilst cooling down helps to maintain the optimum poled status. The poling taken above T_c was designed to induce the polarization with a preferred orientation when the paraelectric phase transferred to a ferroelectric phase. That is to say, when cooling through the cubic-ferroelectric phase transition with the electric field applied, this may give an additional driving force for the alignment of the polarization vectors. It should be noted here that as the breakdown electric field of the cubic phase of the 50BCZT ceramics was smaller than 3 kV/mm electric field, the poling at 110 °C was in fact carried out with 2 kV/mm field.

The dielectric and piezoelectric parameters of the additional samples poled at different temperatures are shown in Figure 7-26 for different time intervals after poling. Within the first 24 hours, increased poling temperatures resulted in decreased d_{33}, k_{eff} and k_p. Within the first 10 days, increased poling temperatures only led to a lower relative permittivity, and no significant effects on the other parameters were observed if the error bars are taken into account.

However, two variations were found on the d_{33} values measured on the 10th day and 60th day, where the values increased with poling temperature until 80 °C then became relatively stable. Also, despite the slight variations in terms of the average values, all of the parameters excluding d_{33} tended to be independent of poling temperature after being aged for 60 days.

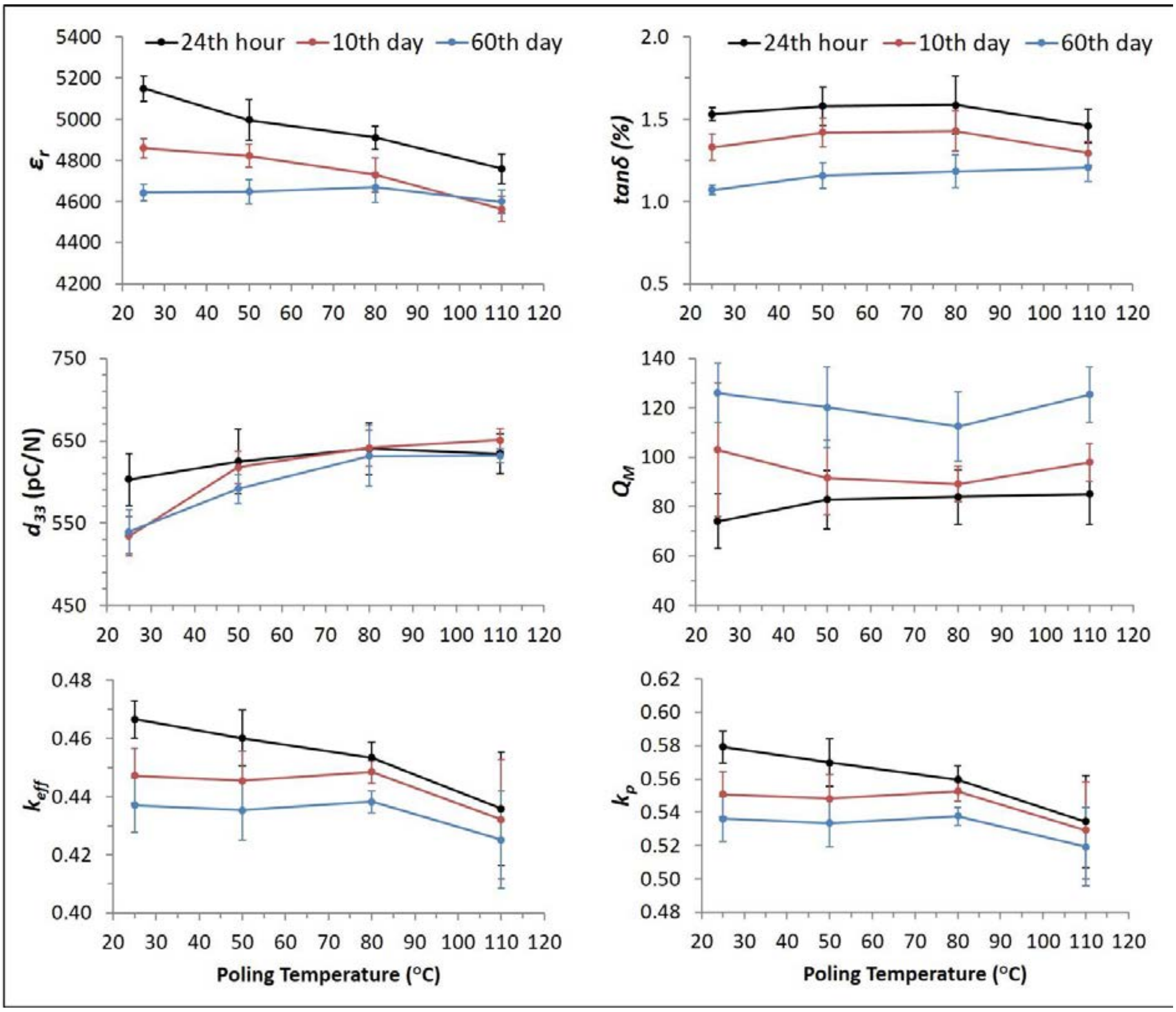

Figure 7-26. Dependence of ε_r, $tan\delta$, d_{33}, Q_M, k_{eff} and k_p on poling temperature for the 50BCZT discs sintered at 1490 °C measured at different times.

The remaining two energy harvesting related parameters, which exhibited slightly stronger dependence on poling temperature below 80 °C, especially when being aged, are shown in Figure 7-27. It should be noted here that the d_{33}·g_{33} and g_{33} were not always deteriorated with time, especially for the samples poled at 50 °C and above where no significant deterioration but even slight improvement with time can be observed. This is due to that the ε_r and d_{33} varied with different rates (see Figure 7-26), and thus the calculated $d_{33}{\cdot}g_{33}$ and g_{33} (see Equation 3-36) would follow a different trend.

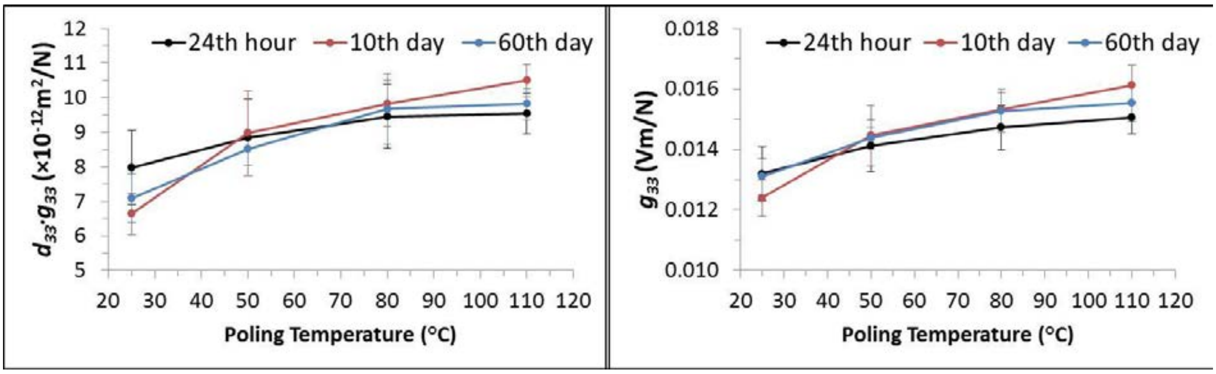

Figure 7-27. Dependence of $d_{33}{\cdot}g_{33}$ and g_{33} on poling temperature for the 50BCZT discs sintered at 1490 °C and measured at different times.

However, in Figures 7-26 and 7-27, a trend about the ageing effect could be generally viewed in that the samples poled at lower temperatures seemed to age more. Details are illustrated in Figure 7-28, where the 60-day ageing effect constants of different parameters with different poling temperatures are compared.

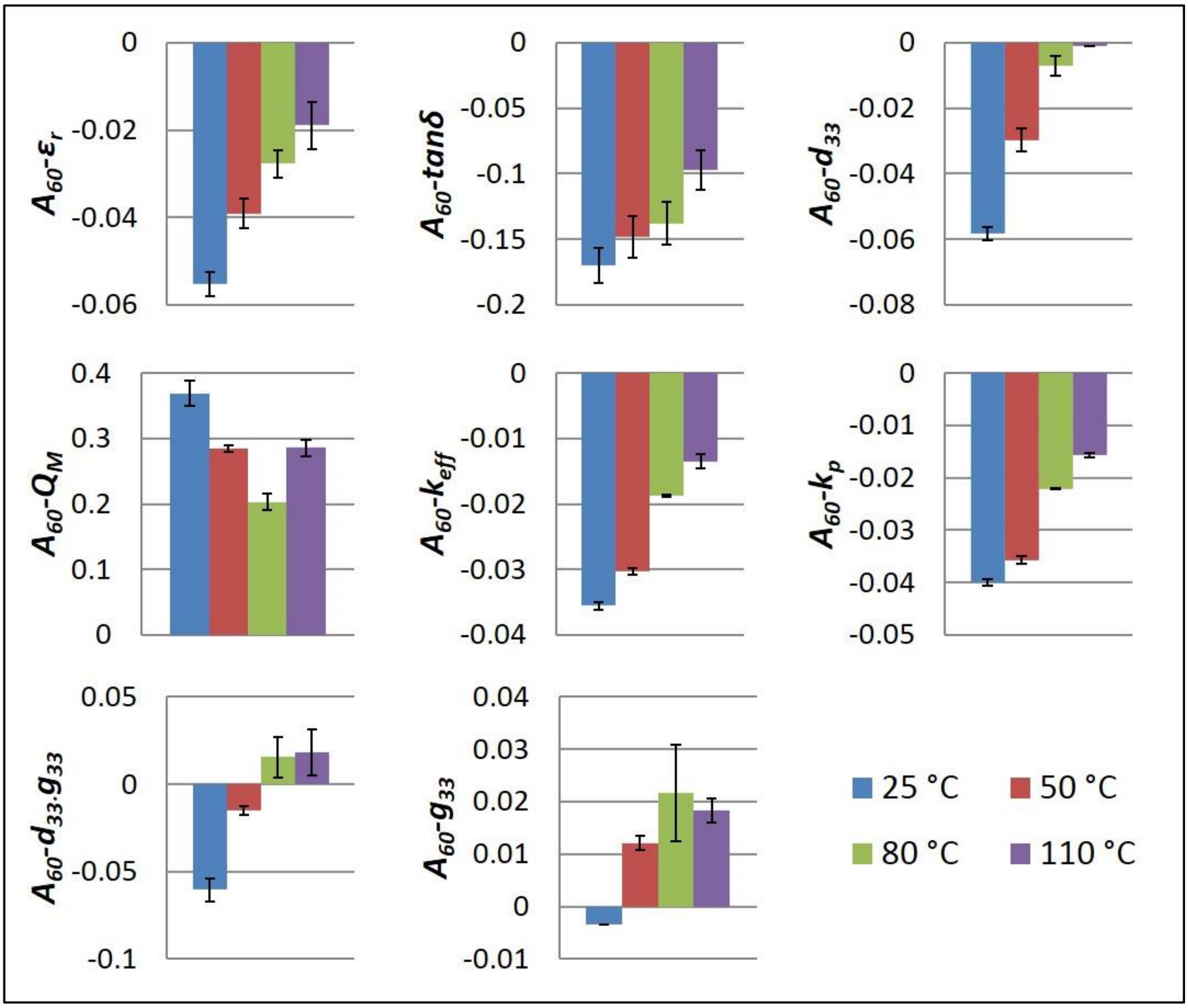

Figure 7-28. Dependence of 60-day ageing effect constants of ε_r, $tan\delta$, d_{33}, Q_M, k_{eff}, k_p, d_{33}·g_{33} and g_{33} on poling temperature for the 50BCZT ceramic discs sintered at 1490 °C.

In terms of the dielectric and piezoelectric parameters, the ageing effect constants decreased with the increase of poling temperature, excluding the Q_M where the smallest constants were found at 80 °C. Also, apart from Q_M, all of the parameters decreased with time. However, as the d_{33}·g_{33} and g_{33} were comprehensively determined by d_{33} and ε_r, both of their ageing effect constants showed irregular variation trends. In particular, for d_{33}·g_{33}, the values decreased with time when the samples were poled at 25 °C and 50 °C, but those for the latter aged less than the former. In contrast, a positive variation was observed for samples poled at 80 °C and 110 °C, the values being quite similar. For g_{33}, the values decreased only for samples poled at 25 °C, while those poled at 50, 80 and 110 °C showed increased properties after ageing, with samples from the latter two temperatures exhibiting similar values.

In summary, although the poling temperature had little effect on the absolute values of most properties, higher poling temperatures could help to eliminate ageing. Also, the key energy harvesting related parameters, $d_{33}\cdot g_{33}$ and g_{33} could even be increased with certain poling temperatures, which might be an advantage of using these materials to fabricate energy harvesters.

7.2.6 Comparison of 50BCZT and PZT Ceramics

As the proposed lead-free composition intends to substitute the commercial PZT as the material candidate for piezoelectric energy harvesters, the properties related to energy harvesting of both compositions were compared. The 50BCZT samples sintered at 1490 °C and poled at 80 °C were selected as the best samples, which were subsequently compared to the PZT samples sintered at 1200 °C which were presented in Section 7.1. Figure 7-29 shows the comparisons of relevant parameters of such samples, where the results were measured 24 hours after poling, and which have been extracted from Figures 7-9, 7-12, 7-13, 7-26 and 7-27.

It can be observed that for the two compositions, each has particular prominent features. The 50BCZT tends to have larger relative permittivity as well as mechanical quality factor, which in theory could provide higher resonant output power to a PEHer. The PZT exhibited larger $d_{33}\cdot g_{33}$ and g_{33} values, which might be helpful in respectively improving the theoretical off resonant output power and open-circuit voltage of a PEHer. However, as both compositions had comparable effective coupling coefficients, whilst the 50BCZT had a larger Q_M but smaller dielectric loss, all of which has a significant influence on the energy conversion efficiency of a PEHer, it is difficult to predict theoretically such performance. In addition, as the T_c of the 50BCZT composition was shown to be between 80 and 90 °C while that of the PZT was about

350-400 °C, the last disadvantage of the 50BCZT is considered as the much lower practical working temperature.

Overall, the 50BCZT composition shows a considerable potential to substitute traditional PZT in energy harvesters, especially when the predicted working temperature is lower than 80 °C.

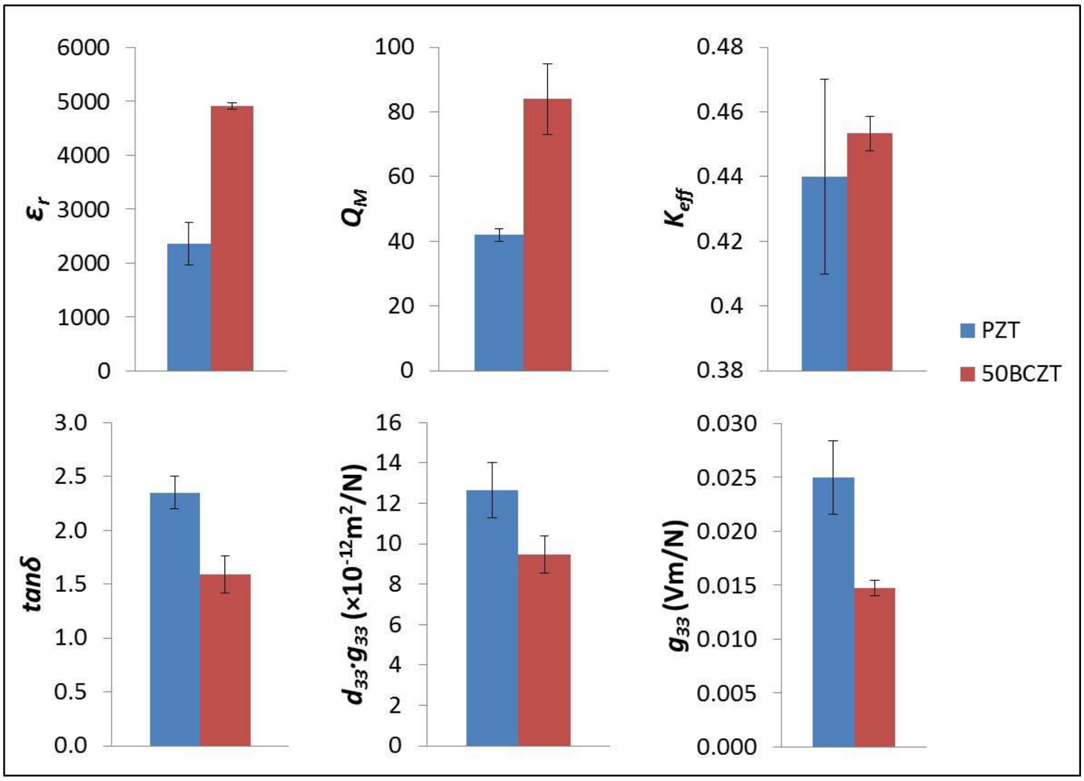

Figure 7-29. Comparisons of ε_r, Q_M, k_{eff}, $tan\delta$, $d_{33}{\cdot}g_{33}$ and g_{33} of the PZT and 50BCZT ceramics.

7.3 Low-temperature Sintering

7.3.1 Borosilicate Glass

In order to prepare for the subsequent fabrication of silver/piezoelectric multi-layer co-sintered thick-films, the low-temperature liquid-phase sintering behaviour and sintered piezoelectric properties of all of the lead-based and lead-free compositions discussed in Sections 7.1 and 7.2 were first investigated using bulk discs. The target sintering temperature was below 950 °C, as the melting point of silver is about 960 °C. Figure 7-30 shows the XRD pattern of the borosilicate glass used for this work. A single, very broad peak is observed on a very noisy background, indicative of a glassy material with extremely low level of crystallisation. The average results of 3 independent particle size analyses showed that the powder had D_{50} of 3.80 ± 1.30 µm and D_{90} of 9.89 ± 1.64 µm after 24-hour ball milling.

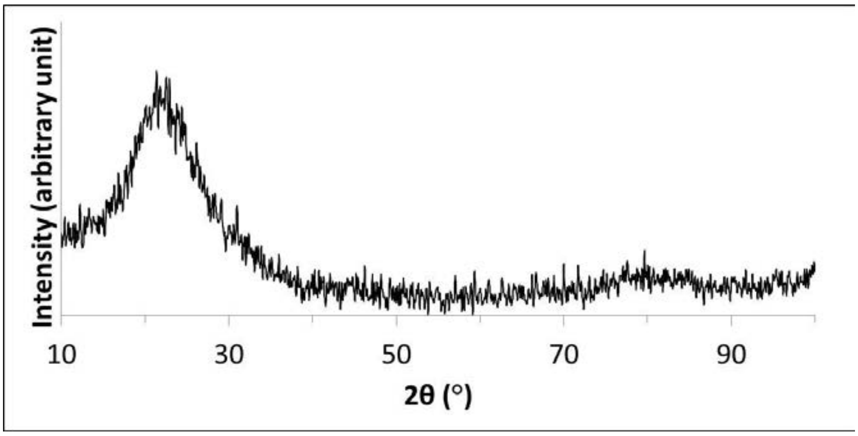

Figure 7-30. XRD pattern of the borosilicate glass utilised as sintering aid.

Figure 7-31 shows the results of a DSC/TGA test (introduced in Section 6.4.2) of the glass powder. Around 350 °C there was an endothermic event observed together with a weight loss of about 1.5 %. This might be caused by an impurity reaction that decomposed and emitted a gaseous product, or the evaporation of water chemically bound in the powder. However, at approximately 800 °C, an obvious exothermic reaction began without weight loss, and which was considered as the melting of the glass frit. Based on these observations, it was assumed that above 800 °C powdered materials containing this glass would be sintered in a liquid-phase environment.

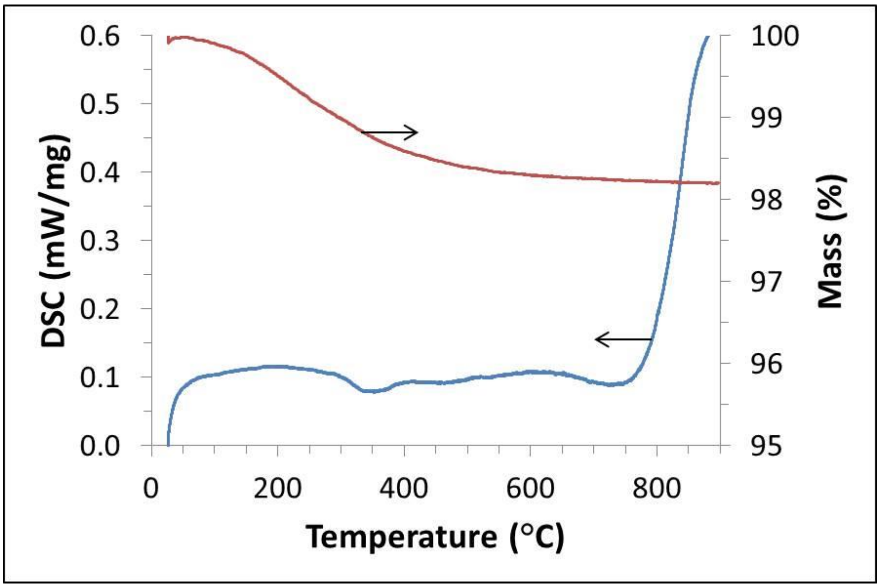

Figure 7-31. Dependence of DSC and mass on temperature for the borosilicate glass.

7.3.2 Lead-based Compositions

The PZT was used for an initial broad investigation to understand the sintering behaviour with the borosilicate glass. Figure 7-32 shows the density, diameter shrinkage, relative permittivity after poling and d_{33} of the PZT discs with different glass contents sintered at temperatures between 900 and 1000 °C. The measurements were taken 24 hours after poling, and each datum point is an average of 6 values from a batch of 6 measured samples.

In terms of ordinary ceramic sintering, targeting on a lower temperature, the highest density was achieved by the PZT discs with 5 wt% glass sintered at 950 °C, as indicated by the peaks in Figure 7-32 (a) and (b). The maximum average density and diameter shrinkage were approximately 85% and 93% respectively of those of the PZT discs without glass sintered at 1200 °C (see Figure 7-4), of which no shrinkage happened when sintered at 900-1000 °C. Therefore, the borosilicate glass was proved a successful sintering aid for the PZT composition. However, although the density and shrinkage increased with the content of glass addition (below 5 wt%), the dielectric and piezoelectric properties (ε_r and d_{33} as representatives) did not follow the same trend. For all of the samples shown in Figure 7-32 (c) and (d), obvious decreases of the ε_r and d_{33} were observed with the increase of the glass content, especially for the d_{33} where dramatic reductions occurred from 1 wt% to 3 wt% of glass content. This indicated that introduction of the non-crystalline glass composition had a detrimental influence on the dielectric and piezoelectric properties, thus the sintering densification and sintered material properties must be balanced in order to ensure a lower sintering temperature, a better densification and acceptable properties at the same time. In a comprehensive consideration, the glass content of 1 wt% was selected to be applied on other lead-based compositions.

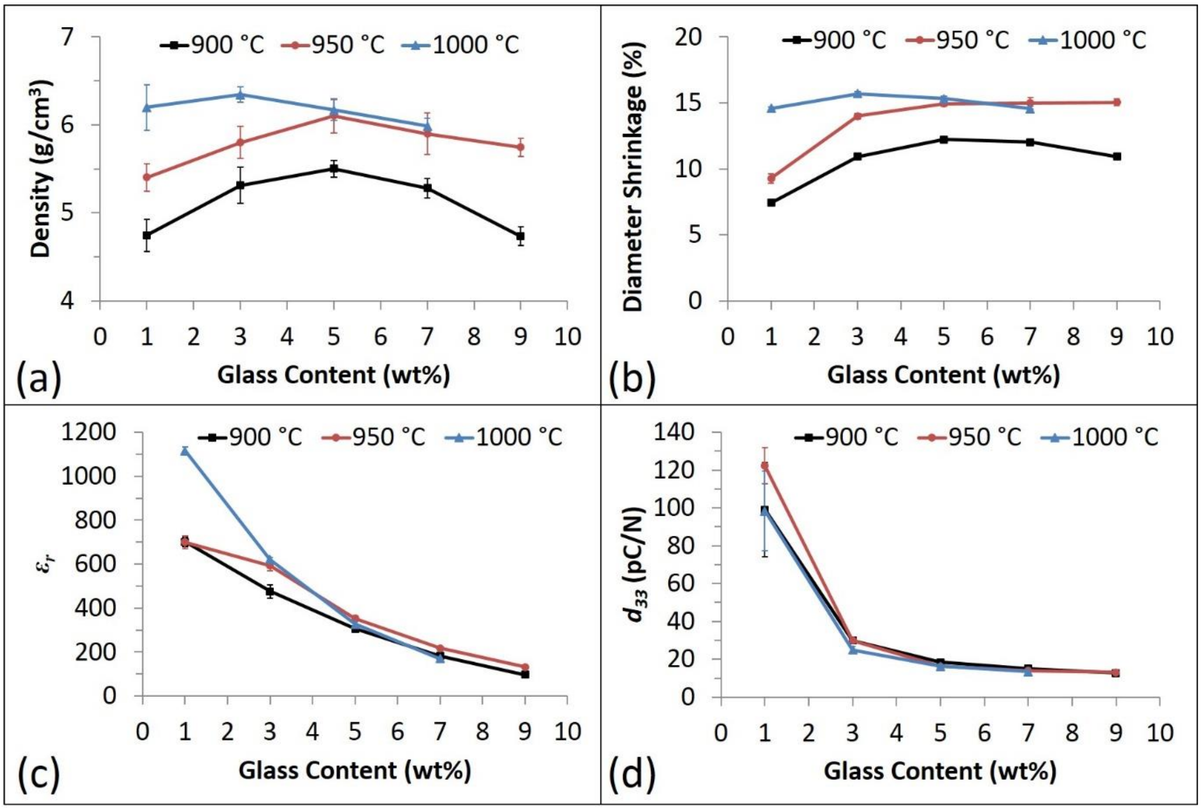

Figure 7-32. Dependence of (a) density (b) diameter shrinkage (c) ε_r and (d) d_{33} on glass additive content for PZT discs sintered at different temperatures.

The dielectric and piezoelectric as well as the energy harvesting related parameters, ε_r after poling, d_{33}, g_{33}, $d_{33}{\cdot}g_{33}$, k_{eff} and Q_M, of the PZT, PZnN-P3LZT and PZnN-P5LZT discs with 1 wt% glass and sintered at 900 °C and 950 °C are compared in Figure 7-33.

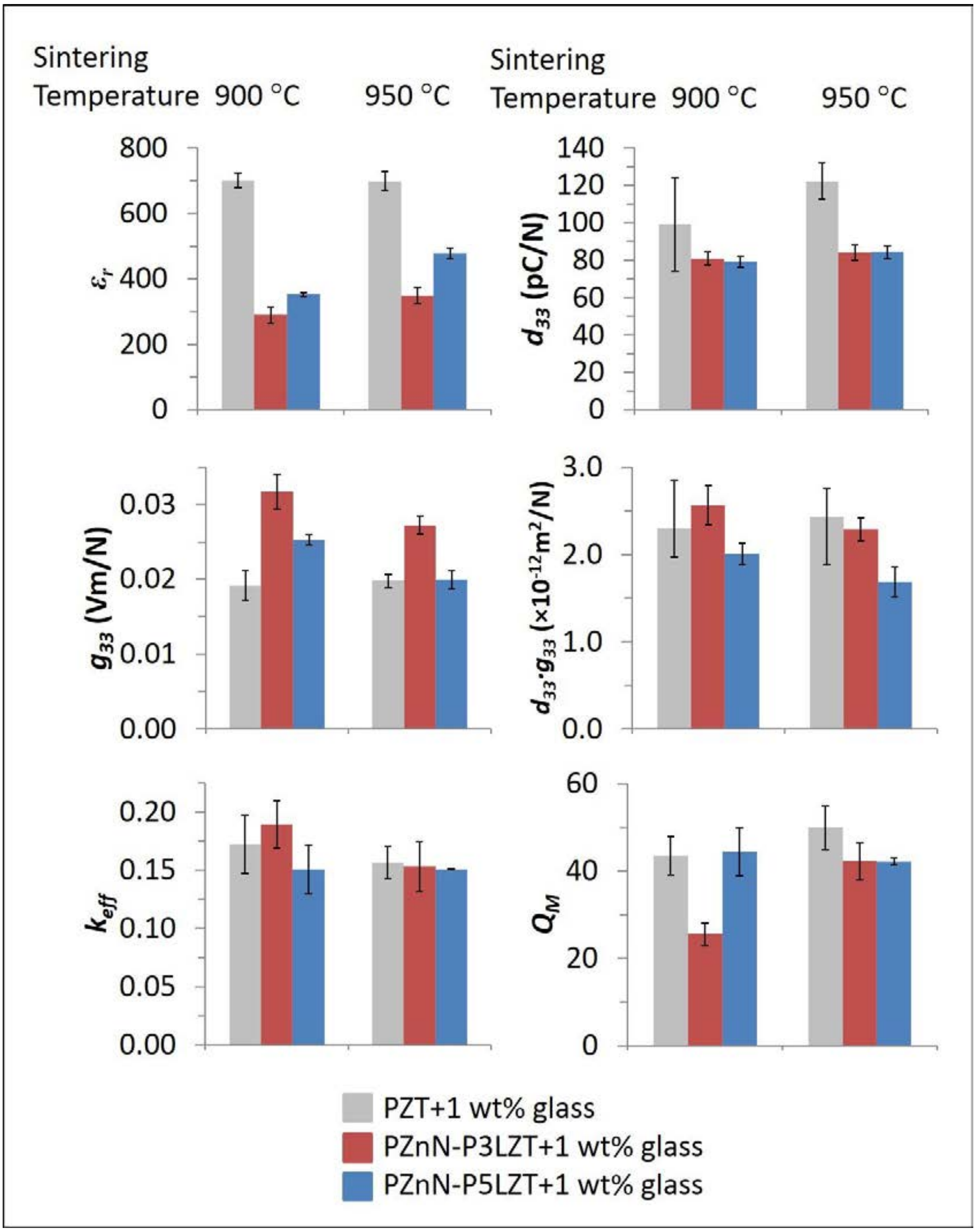

Figure 7-33. Comparisons of ε_r after poling, d_{33}, g_{33}, $d_{33}{\cdot}g_{33}$, k_{eff} and Q_M of the lead-based discs with 1 wt% glass additive sintered at 900 °C and 950 °C.

The first point to notice is that because of the imperfect sintering at low temperatures as well as the glass addition, all of the samples performed worse than their high-temperature, well-sintered counterparts. In particular, for PZT, the average ε_r, d_{33}, g_{33}, $d_{33}{\cdot}g_{33}$, k_{eff} and Q_M of the samples with 1 wt% glass sintered at 900-950 °C were about 30%, 19-24%, 77-80%, 18-19%, 36-39% and 105-114% respectively of those of the samples without glass and sintered at 1200 °C; for PZnN-P3LZT, the average values of the corresponding parameters were about 26-32% (ε_r), 26-27% (d_{33}), 86-99% (g_{33}), 23-26% (d_{33}·g_{33}), 35-44% (k_{eff}) and 39-64% (Q_M) respectively of those of samples without glass sintered at 1250 °C (best comprehensive properties); and for PZnN-P5LZT, they were about 12-16% (ε_r,) 13-14% (d_{33}), 85-108% (g_{33}), 12-14% (d_{33}·g_{33}), 29% (k_{eff}) and 102-107% (Q_M) respectively of those of the samples without glass sintered at 1250 °C (best comprehensive properties). Exclusively, for PZT and PZnN-P5LZT samples, the Q_M values were slightly enhanced by the addition of the glass and being sintered at low temperatures, whilst for all of the samples the least effect was seen on the g_{33} values. However, compared to the PZT and PZnN-P3LZT samples, the PZnN-P5LZT samples with glass dropped to extremely low levels (only around 15 %) in terms of the ε_r, d_{33}, and d_{33}·g_{33}, indicating that it was more difficult to sinter this composition at low temperatures whilst also maintaining the reasonable dielectric and piezoelectric properties.

Figures 7-34, 7-35 and 7-36 show the XRD pattern comparisons of the sintered samples with glass and the corresponding ones without glass together with those of the respective powders.

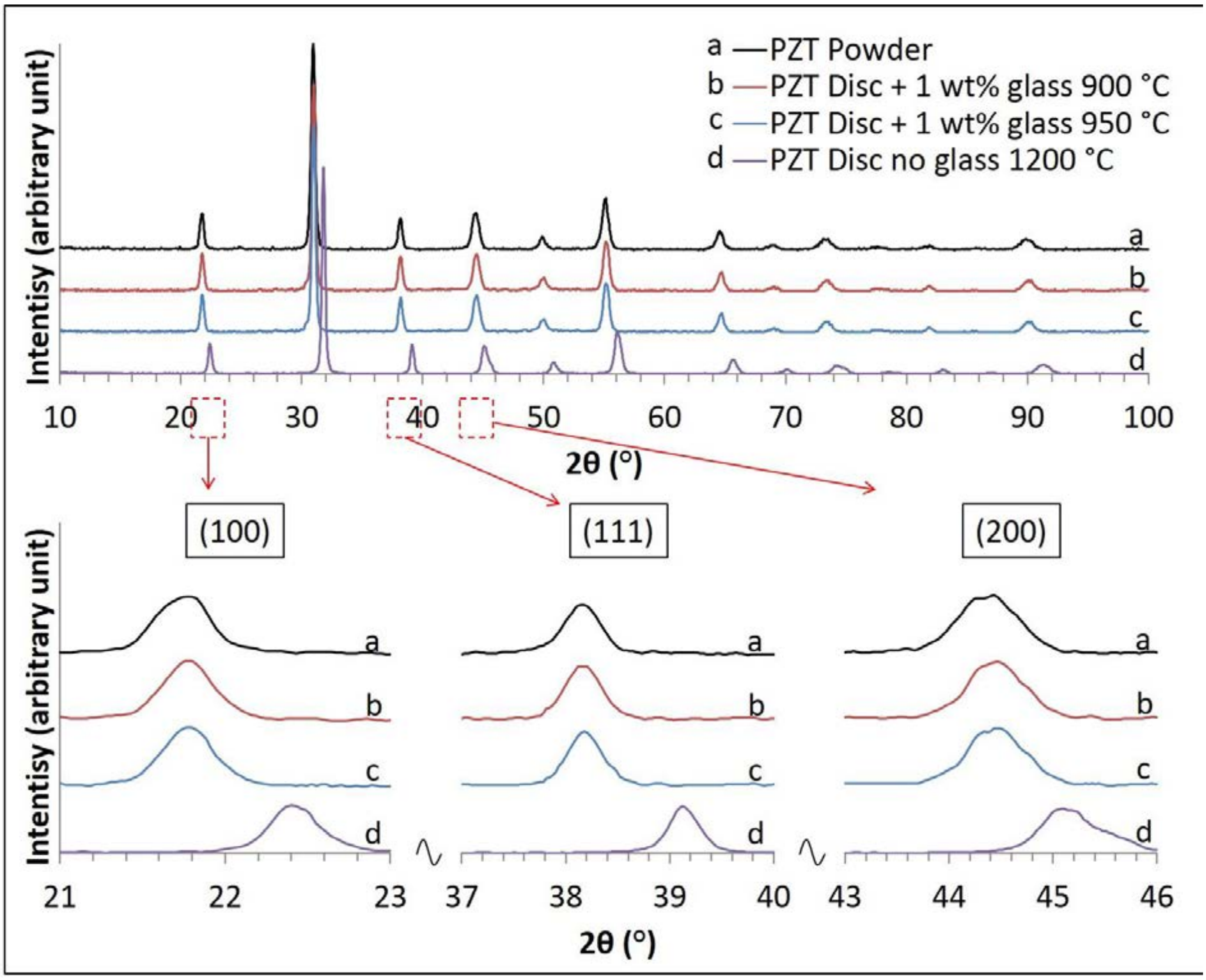

Figure 7-34. XRD patterns of the PZT powder, PZT discs with 1 wt% glass sintered at 900 °C and 950 °C and PZT disc without glass sintered at 1200 °C.

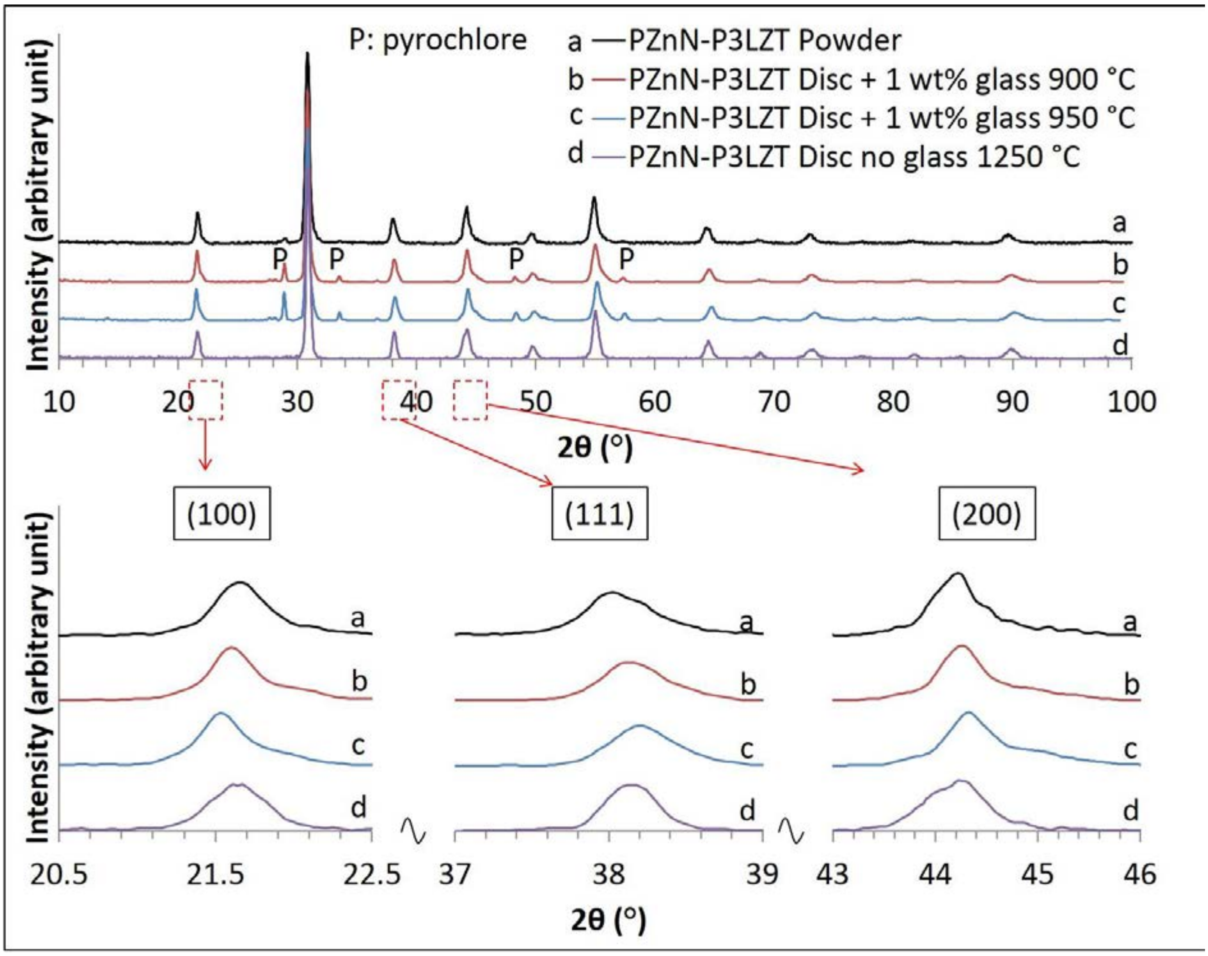

Figure 7-35. XRD patterns of the PZnN-P3LZT powder, PZnN-P3LZT discs with 1 wt% glass sintered at 900 °C and 950 °C and PZnN-P3LZT disc without glass sintered at 1250 °C.

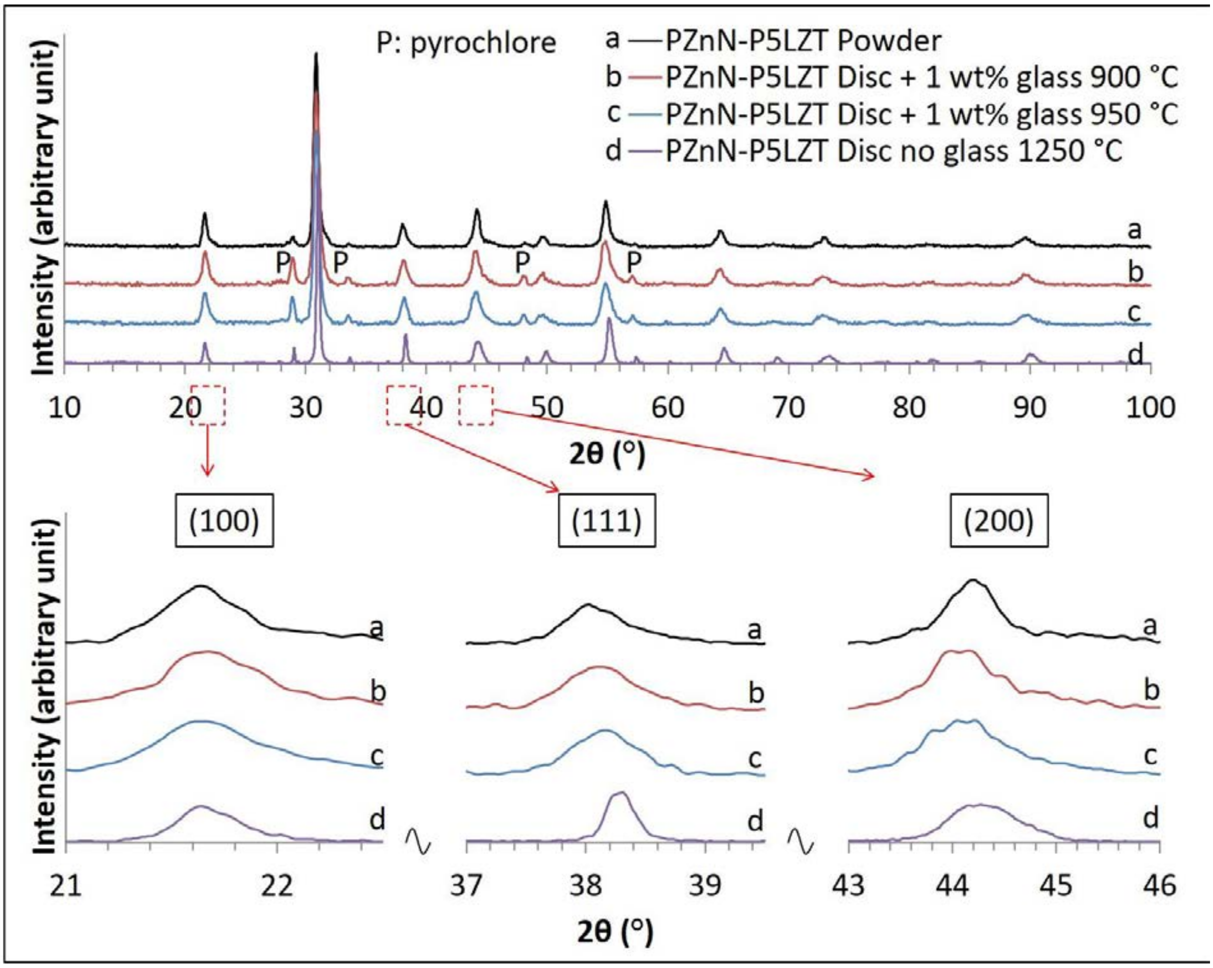

Figure 7-36. XRD patterns of the PZnN-P5LZT powder, PZnN-P5LZT discs with 1 wt% glass sintered at 900 °C and 950 °C and PZnN-P5LZT disc without glass sintered at 1250 °C.

Overall, all of the low-temperature sintered samples maintained similar phase structures to their corresponding powders, but did not achieve the properties of their high-temperature sintered counterparts. This could explain the reduction in the relevant material properties between the samples with glass and those without glass. It implies that the glass only promoted the ceramic densification at low temperatures, and had little effect on the phase transition or lattice parameter optimisation which were considered essential in order to obtain better dielectric/piezoelectric properties. Also, in Figures 7-35 and 7-36, the relative intensities of the XRD peaks of the samples with glass which were assigned to pyrochlore were magnified compared to the remaining peaks, indicating a higher proportion of the pyrochlore phases in these samples. This might be because the glass may not only help the densification but encourage the growth of pyrochlore at the same time. As the content of the glass utilised were only 1 wt%, no additional peaks related to the compositions of the glass were observed.

Finally, Figure 7-37 shows the fracture surface SEM images of the lead-based discs with 1 wt% glass sintered at 900 °C and 950 °C. All of the observed samples formed grains of 1-2 μm. However, although all of the samples were much more porous than their well-sintered counterparts presented in Section 7.1 (Figures 7-5, 7-6 and 7-7), the PZT samples showed relatively better densification than the PZnN-P3LZT and PZnN-P5LZT samples. This implies that it might be easier to sinter the PZT ceramics at low-temperatures in a liquid phase environment.

In a comprehensive consideration, the PZT and PZnN-P3LZT compositions were chosen for further study and the PZnN-P5LZT was abandoned, as: (1) the well-sintered PZnN-P5LZT samples performed extremely similarly to the PZT samples (presented in Section 7.1.3); (2) the PZnN-P5LZT composition showed worse time stability (faster ageing) than the other two compositions (presented in Section 7.1.4); and (3) the PZnN-P5LZT composition was more difficult to sinter at low temperatures in a liquid phase (presented in this section).

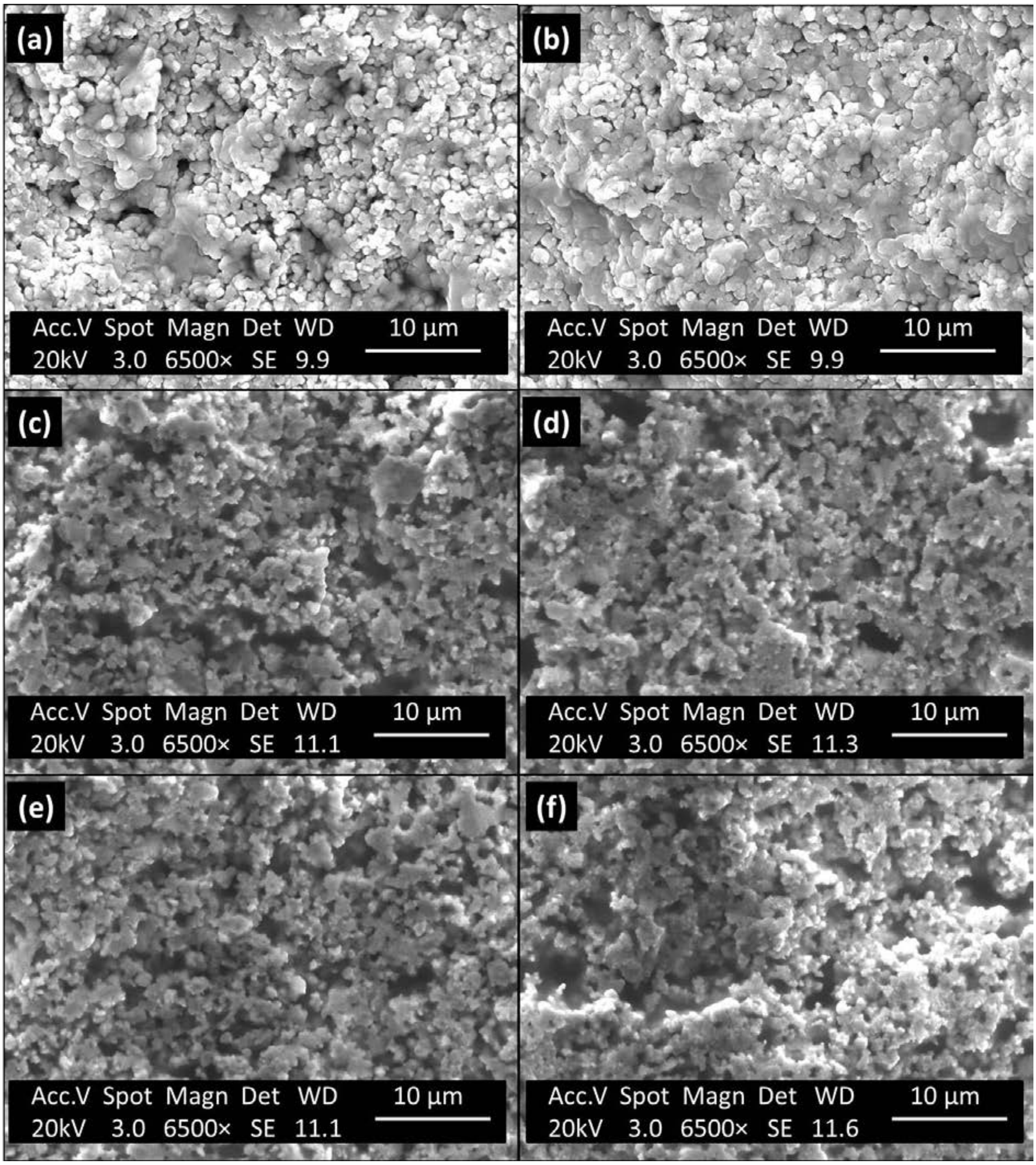

Figure 7-37. SEM images of fracture surfaces of the discs with 1 wt% glass sintered at different temperatures: (a) PZT, 900 °C; (b) PZT, 950 °C; (c) PZnN-P3LZT, 900°C; (d) PZnN-P3LZT, 950 °C; (e) PZnN-P5LZT, 900 °C; (f) PZnN-P5LZT, 950 °C.

7.3.3 $0.5Ba(Zr_{0.2}Ti_{0.8})O_3$-$0.5(Ba_{0.7}Ca_{0.3})TiO_3$

Figure 7-38 shows the densities and diameter shrinkage of the 50BCZT discs with glass contents of 1-3 wt% and sintered at different temperatures.

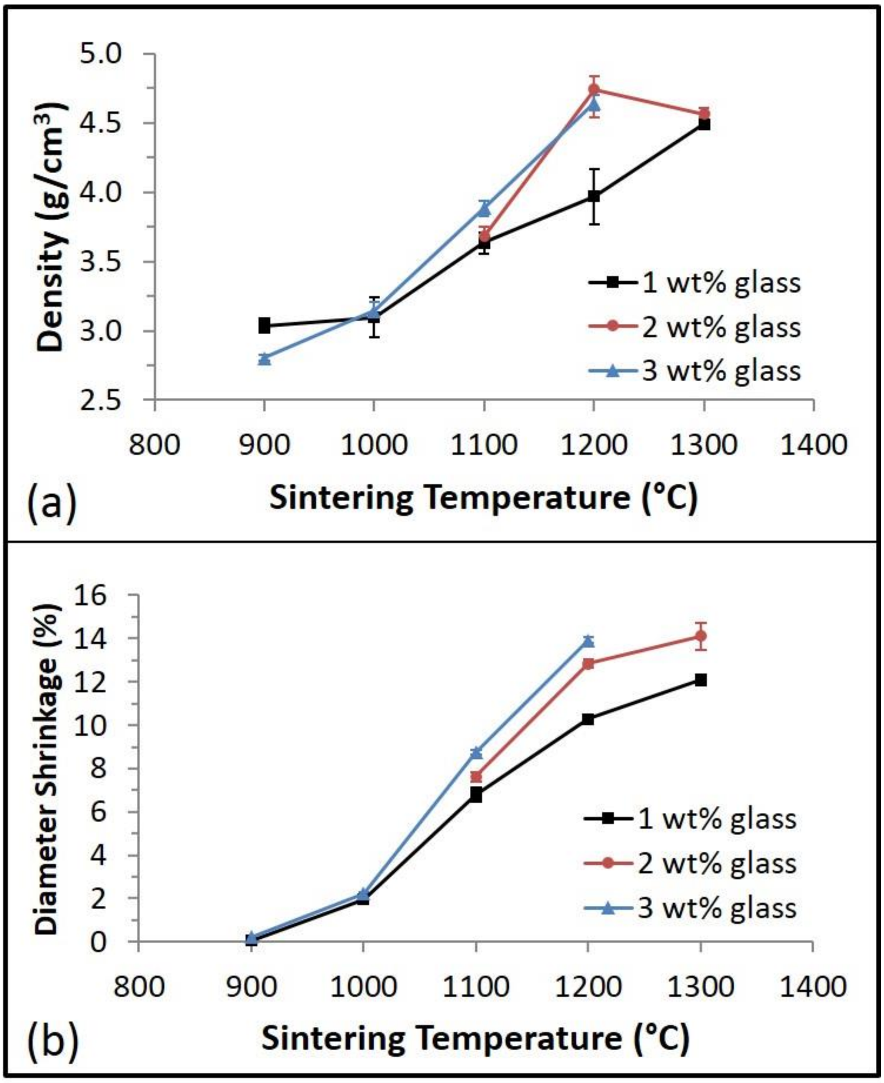

Figure 7-38. Dependence of (a) density (b) diameter shrinkage on sintering temperature for the 50BCZT discs with different glass contents.

In Section 7.2, it was shown that the principle sintering temperatures of the 50BCZT ceramics were much higher than that of PZT. They were also more difficult to sinter at the low temperatures achieved for PZT using the same glass type and contents. At 900-1000 °C, the 50BCZT samples were hardly sintered, even with 3 wt% glass additives, where the density and shrinkage were about 3.0 g/cm^3 and 0-2 % respectively, as shown in Figure 7-38. From 1100 °C, the samples started to be sintered as both the densities and shrinkage went up with the increase of temperature, indicating better densification. With 1100 °C sintering temperature, only small differences of density and shrinkage values were observed among the samples with 1 wt%, 2 wt% and 3 wt% glass addition, implying similar densification levels. At 1200 °C, the samples with 2 wt% and 3 wt% glass still showed similar density and shrinkage values, while the largest differences were observed between the 1 wt% and 2 wt% glass contents. This indicates that increase glass addition beyond 2 wt% may also help the sintering of the 50BCZT composition, but 2 wt% might be enough to obtain reasonable density and shrinkage. After being sintered at 1300 °C, the samples with 3 wt% glass addition were stuck onto the supporting substrate by the melted and re-solidified glass, which meant that 3 wt% addition was excessive for such a sintering temperature. In addition, being sintered at 1300 °C, the densities of the samples with 1 wt% and 2 wt% glass were similar and the difference in shrinkage reduced.

Figure 7-39 shows the variations of ε_r, d_{33}, g_{33} and $d_{33}{\cdot}g_{33}$ with sintering temperatures and glass contents for the 50BCZT samples. The poling was carried out at 25 °C, and the measurements were taken 24 hours after poling. Each datum point was an average of 9 values, which were from 3 samples but each sample was independently measured 3 times. The relative permittivity varied linearly with sintering temperature from 900 °C to 1300 °C, and the samples with less glass exhibited slightly larger relative permittivity values for a particular temperature, especially from 1100 °C upwards (see Figure 7-39 (a)). However, the situation for d_{33} was a little different, where all of the samples sintered at 900-1100 °C exhibited extremely low d_{33}. Noticeable enhancements only occurred with 1200-1300 °C sintering temperatures. Similar to what happened to the PZT samples, larger glass contents resulted in an obviously deterioration in d_{33} (see Figure 7-39 (b)). The trends of the $d_{33}{\cdot}g_{33}$ were nearly the same with those of d_{33}

(see Figure 7-39 (d)). In addition, interesting variations were found in g_{33}, where the values decreased until 1100 °C then increased with increasing temperature (see Figure 7-39 (c)). The larger g_{33} values at 900 °C were because of the smaller ε_r, while the larger values at 1200-1300 °C resulted from the larger d_{33}. However, considering the very poor ceramic sintering as well as extremely low $d_{33}{\cdot}g_{33}$ values, the samples sintered at 900-1100 °C were considered not suitable for further work.

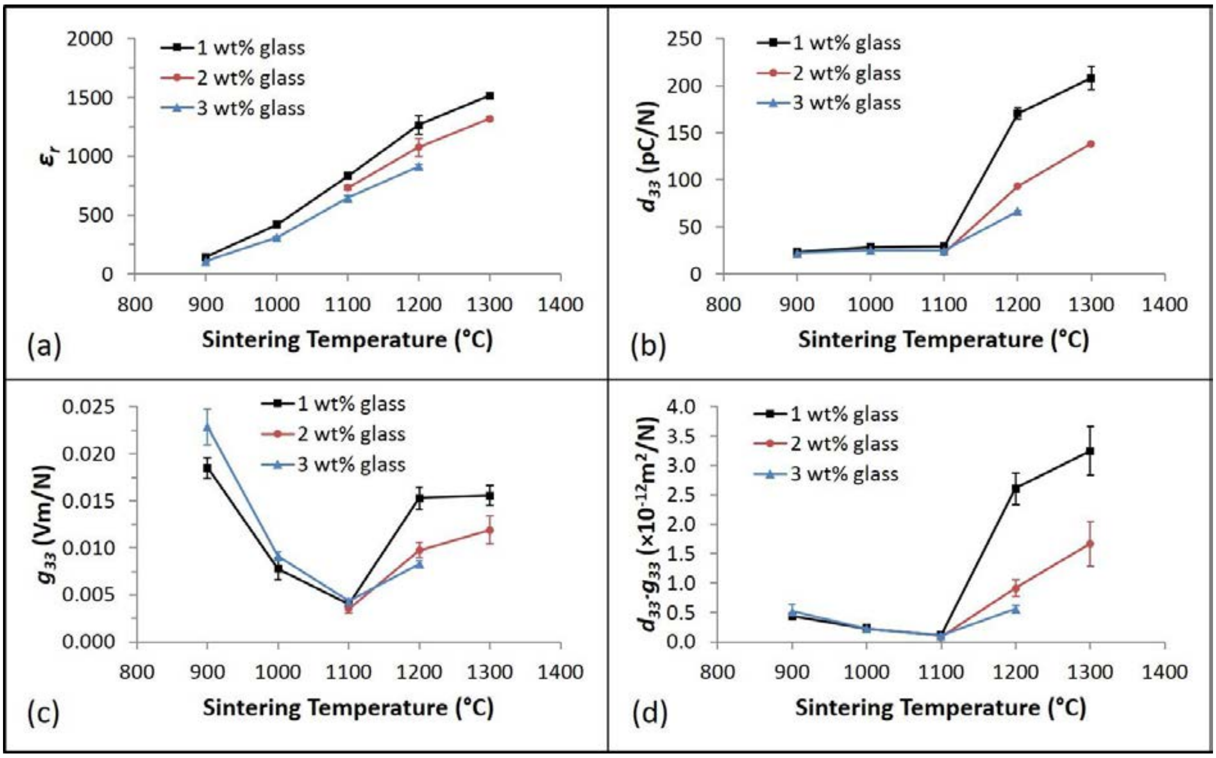

Figure 7-39. Dependence of (a) ε_r (b) d_{33} (c) g_{33} and (d) $d_{33}{\cdot}g_{33}$ on sintering temperature for the 50BCZT discs with different glass contents.

Figure 7-40 compares k_{eff} and Q_M of the 50BCZT samples with different glass contents sintered at 1200 °C and 1300 °C. Less glass tended to induce larger k_{eff}, while the Q_M varied in the opposite way. Considering a balance of densification and reasonable performance at reduced sintering temperatures, the best low-temperature sintered samples were determined as those with 1 wt% glass sintered between 1200 °C and 1300 °C.

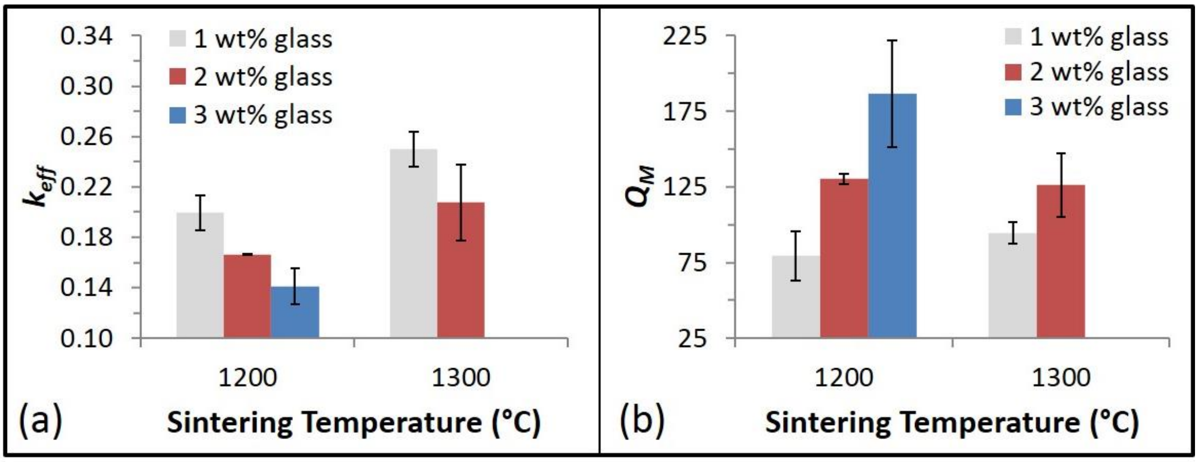

Figure 7-40. Dependence of (a) k_{eff} (b) Q_M on sintering temperature for the 50BCZT discs with different glass contents.

In summary, compared to the well-sintered samples at 1490 °C presented in Section 7.2, the low-temperature sintered 50BCZT samples performed about 74-86% of diameter shrinkage, 25-30% of ε_r, 28-35% of d_{33}, 43-54% of k_{eff}, 107-127% of Q_M, 116-117% of g_{33}, and 33-56% of $d_{33}{\cdot}g_{33}$, with approximately 200-300 °C lower sintering temperature, and under the same poling conditions (25 °C).

However, as 1200 °C was still too high for the use of silver electrodes, the subsequent investigations on real energy harvesters presented in Chapter 8 only involved the lead-based compositions. Potential methods for further reducing the sintering temperature of the 50BCZT composition will be discussed in the future work in Chapter 9.

References

1 Zeng, X., He, X. Y., Cheng, W. X., Zheng, X. S. and Qiu, P. S. Dielectric and ferroelectric properties of PZN-PZT ceramics with lanthanum doping. *Journal of Alloys and Compounds* **485**, 843-847 (2009).

2 Keve, E. T. and Bye, K. L. Phase identification and domain-structure in plzt ceramics. *Journal of Applied Physics* **46**, 810-818 321651 (1975).

3 www.trstechnologies.com [online access] 16/04/2014.

4 Ricote, J., Whatmore, R. W. and Barber, D. J. Studies of the ferroelectric domain configuration and polarization of rhombohedral PZT ceramics. *Journal of Physics-Condensed Matter* **12**, 323-337 (2000).

5 IEEE Standard on Piezoelectricity. *ANSI/IEEE Standard 176-1987* (1987).

6 Du, X.-h., Zheng, J., Belegundu, U. and Uchino, K. Crystal orientation dependence of piezoelectric properties of lead zirconate titanate near the morphotropic phase boundary. *Applied Physics Letters* **72**, 2421-2423 (1998).

7 Park, S.-E. and Shrout, T. R. Ultrahigh strain and piezoelectric behavior in relaxor based ferroelectric single crystals. *Journal of Applied Physics* **82**, 1804-1811 (1997).

8 Liu, W. F. and Ren, X. B. Large Piezoelectric Effect in Pb-Free Ceramics. *Physical Review Letters* **103**, 257602 (2009).

9 Tian, Y., Wei, L. L., Chao, X. L., Liu, Z. H. and Yang, Z. P. Phase transition behavior and large piezoelectricity near the morphotropic phase boundary of lead-free (Ba0.85Ca0.15)(Zr0.1Ti0.9)O-3 ceramics. *Journal of the American Ceramic Society* **96**, 496-502 (2013).

10 Keeble, D. S., Benabdallah, F., Thomas, P. A., Maglione, M. and Kreisel, J. Revised structural phase diagram of (Ba0.7Ca0.3TiO3)-(BaZr0.2Ti0.8O3). *Applied Physics Letters* **102**, 092903 (2013).

11 Lee, H. Y., Kim, J. S., Hwang, N. M. and Kim, D. Y. Effect of sintering temperature on the secondary abnormal grain growth of BaTiO3. *Journal of the European Ceramic Society* **20**, 731-737 (2000).

12 Huan, Y., Wang, X. H., Fang, J. and Li, L. T. Grain size effects on piezoelectric properties and domain structure of BaTiO3 ceramics prepared by two-step sintering. *Journal of the American Ceramic Society* **96**, 3369-3371 (2013).

CHAPTER 8. FREE-STANDING STRUCTURES AND NOVEL ENERGY HARVESTERS

8.1 Introduction

Chapter 4 has reviewed the principles, configurations and materials of piezoelectric energy harvesters (PEHers). This chapter presents the experimental results and corresponding discussions of piezoelectric free-standing thick-film structures and cantilever-based vibrational energy harvesters. The materials have been fully discussed in Chapter 7 using high-temperature and low-temperature sintered bulk ceramics. Following this, this chapter picks up two of the lead-based compositions (PZT and 3 mol% La-doped PZnN-PZT (PZnN-P3LZT)). Rather than bulk samples, these compositions were fabricated to single-layer and piezoelectric/silver multi-layer free-standing thick-films using the doctor blading process (see Section 3.6.2.2). The single-layer films were used for fabrication process investigation and material characterisation (Section 8.2), whilst the multi-layer film cantilevers were tested as individual energy harvesters under harmonic vibrations (Section 8.3). Also, the individual harvesters were mathematically analysed and modelled, and then used for energy harvester array design, fabrication and harmonic vibration test (Section 8.4). In addition, the individual harvesters were configured with a free-spinning fan and tested in air-flow (Section 8.5).

8.2 Inks and Thick-films

8.2.1 Ink Properties and Free-standing Structure Fabrication

As the fabrication process of the free-standing structures involved co-sintering silver/piezoelectric multi-layers, the first issue should be to gain a good knowledge of the shrinkage of the deposited films when subjected to various firing procedures, and the effects of them on the appearance and integrity of the sintered cantilevers. Figure 8-1 shows some examples of the sintered PZT, PZnN-P3LZT and silver free-standing single-layer thick-films (Series 1) which were used for shrinkage measurements. As presented in Chapter 6, Series 1 samples shown in Figure 8-1 were fabricated by printing a layer of piezoelectric or silver ink onto a carbon layer. After being sintered at 875-950 °C for certain period (see Section 6.2), the planar shrinkage and densities were characterised (see Section 6.4).

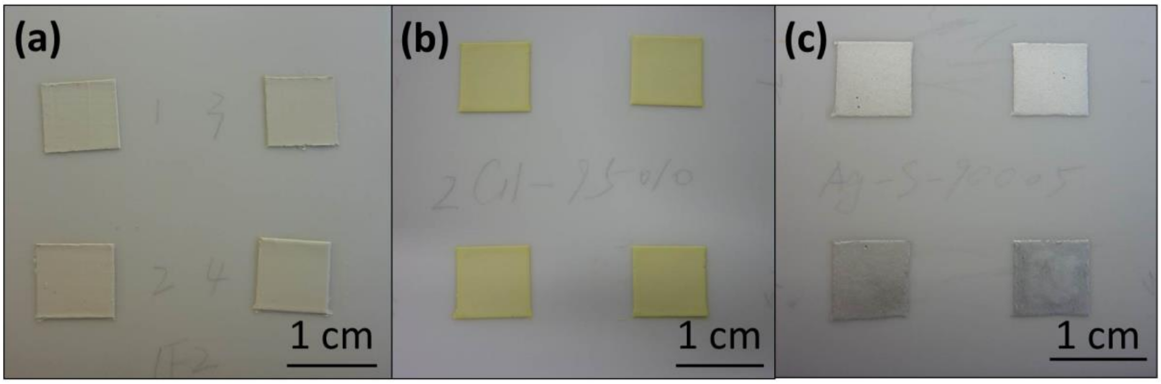

Figure 8-1. Pictures of the single-layer free-standing thick-films (Series 1) (a) PZT sintered at 900 °C for 1 hour, (b) PZnN-P3LZT sintered at 950 °C for 1 hour, and (c) silver sintered at 900 °C for 0.5 hour (top-view).

Figure 8-2 shows the planar shrinkage of the silver, PZT and PZnN-P3LZT inks at different sintering temperatures with different dwell durations (measured from Series 1 samples). The fabrication of the inks have been presented in Section 6.2.2. Each datum point was from an average of 10 samples.

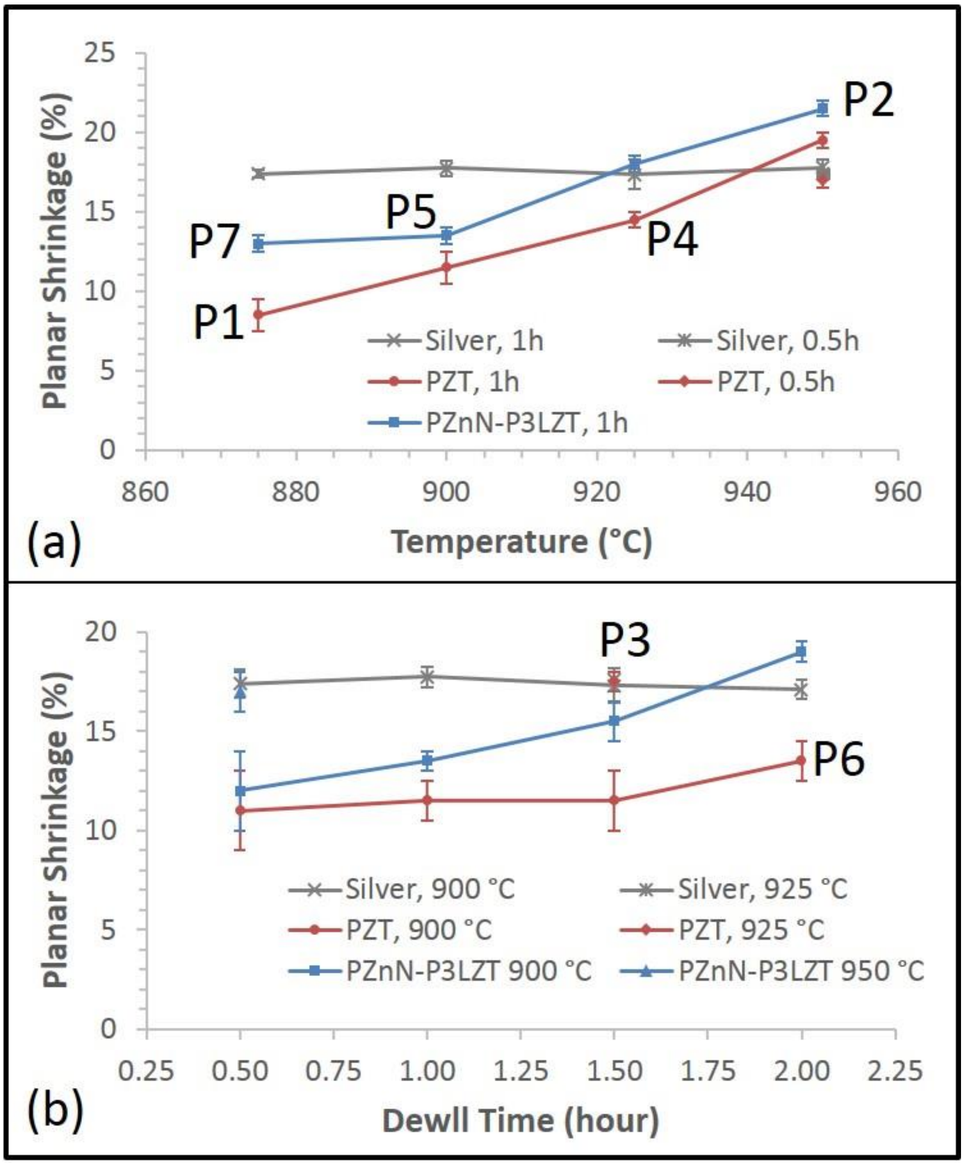

Figure 8-2. Dependence of planar shrinkage on (a) sintering temperature at various dwell times, and (b) dwell time at various sintering temperatures for single-layer thick-films of different compositions.

The silver ink had approximately the same shrinkage for all the conditions tested. Main contribution to the shrinkage of the silver ink is considered as polymer decomposition when heated to the sintering temperature. Also, as the tested temperatures shown in Figure 8-2 were rather close to the melting point of silver (about 960 °C), sintering of the silver ink is expected as well. However, sintering did not affect the shrinkage of the silver ink, implying that the silver had achieved the fullest densification under these conditions. In contrast, although polymer decomposition did not contribute to the differences of shrinkage under different conditions for the PZT and PZnN-P3LZT inks, the shrinkage varied for the different sintering procedures according to Figure 8-2 because of change of densification level. Both sintering temperature and dwell duration had significant influences on the shrinkage. In particular, for the PZT ink, the shrinkage increased linearly with sintering temperature (Figure 8-2 (a)) but retained at approximately the same level with dwell duration until being sintered for 2 hours where a slight shrinkage increase was observed (Figure 8-2 (b)). However, for the PZnN-P3LZT ink, the shrinkage increased linearly with both sintering temperature (Figure 8-2 (a)) and dwell duration (Figure 8-2 (b)), despite such a trend started from being sintered at 900 °C (Figure 8-2 (a)). Among all of the procedures, 7 of them (P1-P7 shown in Figure 8-2) were applied to the fabrication of the free-standing multi-layer thick-film cantilevers. Details of procedure P1 to P7 are summarised in Table 8-1, where adopted compositions and configurations, sintering temperatures and dwell durations are defined. The binder burning-off procedure and temperature ramping rate were mentioned in Section 6.2, which are:

(1) 1 °C/min ramping up to 325 °C, dwelling 1 hour;
(2) 1 °C/min ramping up to 500 °C, dwelling 1 hour;
(3) 5 °C/min ramping up to target sintering temperature, dwelling certain period;
(4) 5 °C/min ramping down to room temperature.

Table 8-1. Sintering temperatures and dwell durations of sintering procedure P1 to P7.

Procedure	**Composition and Configuration**	**Sintering Temperature (°C)**	**Dwell Duration (h)**
P1	PZT + Ag, unimorph	875	1.0
P2	PZnN-P3LZT + Ag, unimorph	950	1.0
P3	PZT + Ag, unimorph	925	1.5
P4	PZT + Ag, unimorph & bimorph	925	1.0
P5	PZnN-P3LZT + Ag, unimorph & bimorph	900	1.0
P6	PZT + Ag, unimorph	900	2.0
P7	PZnN-P3LZT + Ag, unimorph & bimorph	875	1.0

Figure 8-3 shows the pictures of the sintered cantilevers corresponding to the P1 to P7 procedures labelled in Figure 8-2 and listed in Table 8-1. As the cantilevers sintered with P3, P6 and P7 procedures looked similar to those sintered with P2, P4 and P5, respectively, the pictures were not re-presented.

As observed, if the shrinkage of the silver layer was much larger than that of the piezoelectric elements, a delamination problem was likely to occur (Figure 8-3 (a)). On the contrary, if the shrinkage of the silver layers were equal to or smaller than that of the piezoelectric layers, in addition to the effect of the material mass, the cantilever would deflect downwards and even stick onto the substrate during sintering, leading to a failure to obtain a free-standing structure (Figure 8-3 (b)). It was found empirically that only by maintaining a difference of 3 % to 6 % in the overall shrinkage of the silver and the piezoelectric elements could a flat, free-standing thick-film cantilever free from residual stress be obtained (Figure 8-3 (c), (d), (e) and (f)). This suggested that the PZT cantilever would better be sintered at 925 °C for 1 hour (P4) or at 900 °C for 2 hours (P6), and the PZnN-P3LZT cantilever could be sintered at 875 °C or 900 °C for 1 hour (P7 or P5).

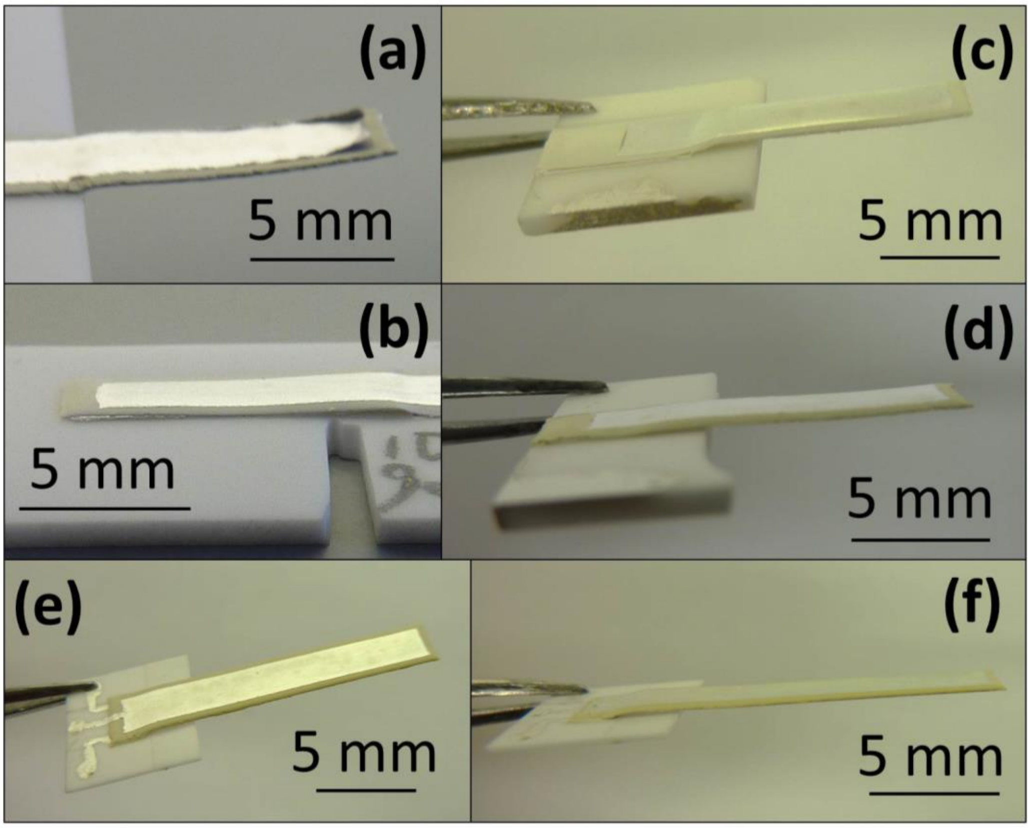

Figure 8-3. Pictures of the free-standing thick-film cantilevers sintered with different procedures: (a) the PZT unimorph sintered at 875 °C for 1 hour (P1); (b) the PZnN-P3LZT unimorph sintered at 950 °C for 1 hour (P2); (c) the PZT unimorph sintered at 925 °C for 1 hour (P4); (d) the PZnN-P3LZT unimorph sintered at 900 °C for 1 hour (P5); (e) & (f) the PZnN-P3LZT bimorph sintered at 900 °C for 1 hour (P5).

Figure 8-4 shows the cross-sectional SEM images of two successfully fabricated cantilevers: (a) a PZT unimorph sintered at 900 °C for 2 hours; (b) a PZnN-P3LZT bimorph sintered at 900 °C for 1 hour. In general, the individual layers and interfaces were clearly defined. For the unimorph, thicknesses of the silver and piezoelectric layers were about 35 μm and 80 μm, respectively, with the overall thickness of the unimorph being approximately 230 μm

(Figure 8-4 (a)). For the bimorph, the overall thickness was about 285 μm, with the individual silver and piezoelectric layers being about 35 μm and 90 μm, respectively. For the initial stage of the investigation concerning comparisons of the output generated by the harvesters made from the two piezoelectric compositions, the thickness of the layers were controlled around the above values. However, in later investigations concerning optimisation of the output and frequency tuning, various thickness combinations were utilised, which will be discussed later. It should be noted that all of the previous SEM images were generated using secondary electrons (SE) as the source, but Figure 8-5 shows the back scatter electron (BSE) images of a PZT unimorph and a PZnN-P3LZT bimorph, in order to observe any diffusion of silver. As shown in Figure 8-5, the silver diffused slightly into the piezoelectric layers with 5-10 μm diffusion interfaces (as marked in the figure), meaning good lamination between the silver layers and piezoelectric layers. No other evidence of deep silver diffusion was observed, thus confirming the success of the designed structures.

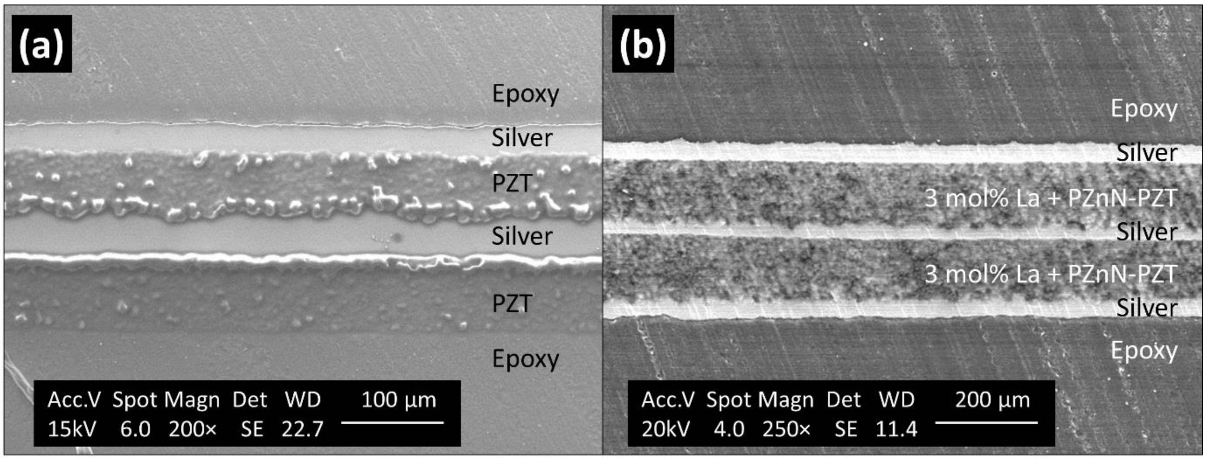

Figure 8-4. Cross-sectional SEM images (SE) of (a) PZT unimorph (b) PZnN-P3LZT bimorph.

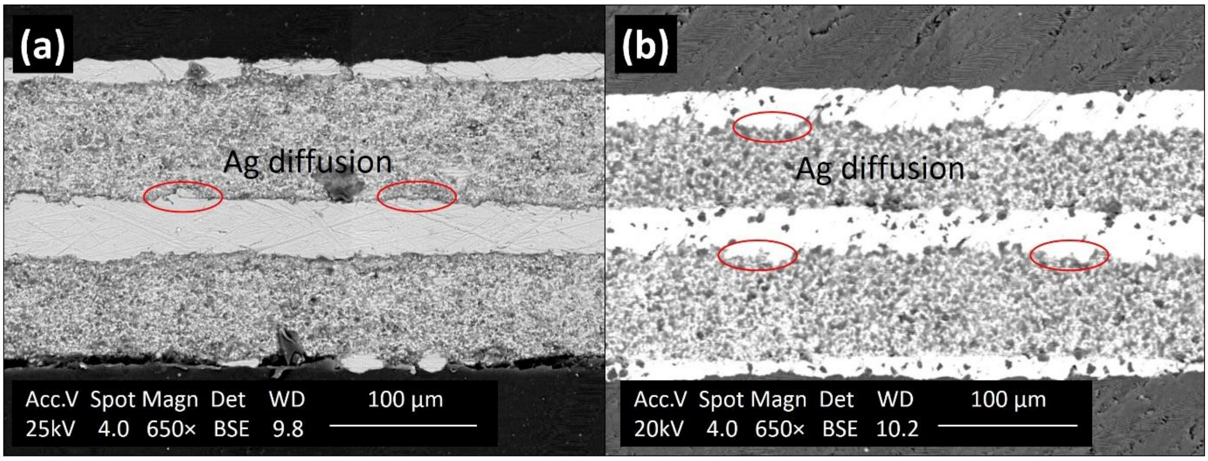

Figure 8-5. Cross-sectional SEM images (BSE) of (a) PZT unimorph (b) PZnN-P3LZT bimorph.

8.2.2 Properties of Single-layer Thick-films

Figure 8-6 gives an example of the upper and lower surfaces of a sintered and gold-sputtered free-standing single-layer thick-film (Series 2) used for property characterisations. The fabrication, dimensions and characterisation methods of Series 2 samples have been presented in Chapter 6. It can be seen that the electrode on each surface did not fully cover the entire surface of the piezoelectric layer, also the two layers of electrodes were not coincident with each other. This was to avoid electric shorting between the electrodes as well as preventing sparks during poling, as was presented and discussed in Chapter 3. However, the surface area used for permittivity calculation was taken as the smallest possible area which were covered by both electrodes at the same time, rather than that of the entire piezoelectric surface. For instance, the surface area used for calculating the permittivity of the sample shown in Figure 8-6 was $l_a \times l_b$ rather than $l_{a0} \times l_{b0}$, where l_a, l_b, l_{a0} and l_{b0} are defined in Figure 8-6.

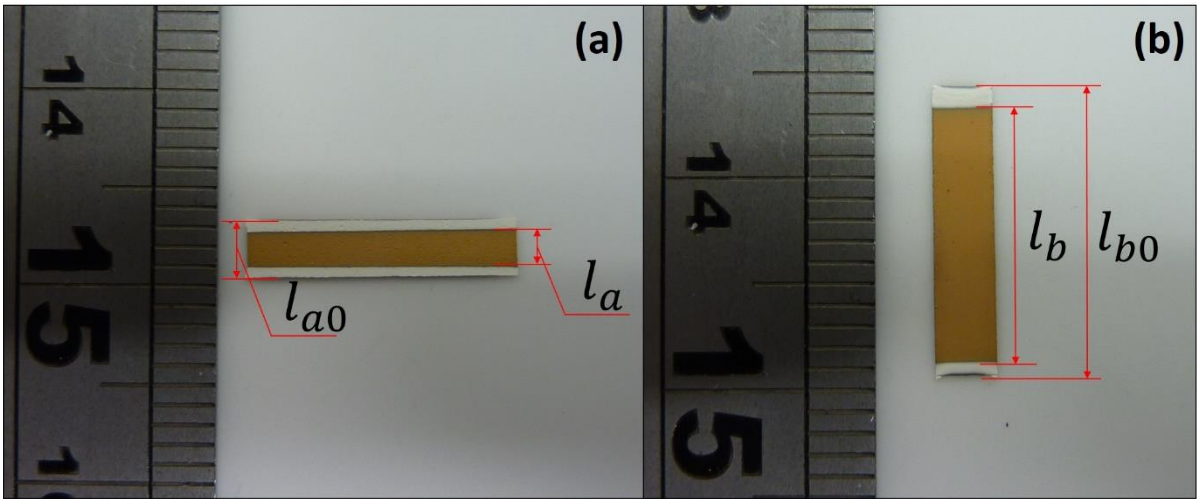

Figure 8-6. Pictures of a sintered and gold-sputtered PZT free-standing single-layer thick-film (Series 2): (a) upper surface; (b) lower surface (top-view).

The PZT thick-films sintered at 900 °C for 2 hours and the PZnN-P3LZT thick-films sintered at 900 °C for 1 hour were utilised to characterise the energy harvesting related properties of the materials, and thus provide a benchmark with which to correlate the harvester outputs in the vibration tests presented in the following sections. Table 8-2 briefly summarises the physical, dielectric and piezoelectric properties of the two types of thick-films. As with Series 1, each datum was an average of 10 samples, with the standard deviations indicated in the table. In general, the PZnN-P3LZT thick-films had larger d_{33}, d_{31}, g_{33} and g_{31} values and thus correspondingly larger d_{33}·g_{33} and d_{31}·g_{31}. This would imply a higher theoretical output voltage as well as off-resonant output power for the harvesters made from such thick-films compared to those made from the PZT thick-films with the same dimensions and peak deflections. However, the resonant output power density and energy conversion efficiency were difficult to evaluate theoretically due to the complex dependencies on the other parameters, k_{eff}, k_{31}, Q_M, ε_r and $tan\delta$. In addition, the data reported in a relevant publication[1], in which free-standing 'soft' PZT thick-films were fabricated with sintering temperatures of 850 to 950 °C, are also included in Table 8-2 as a reference. Overall, the free-standing PZT thick-film fabricated in this project exhibited smaller ε_r and Q_M but larger d_{33}, d_{31}, g_{33}, g_{31} and k_{31} compared to those in the literature. Further comparisons will be discussed in the following sections concerning real energy conversion tests.

Table 8-2. Summary of the average properties of the PZT and PZnN-P3LZT thick-films, and relevant data in reference.

	PZT	**PZnN-P3LZT**	**Reference[1]**
ρ (g/cm^3)	6.02 ±0.02	5.01 ±0.02	
Y^E (GPa)	13.9 ±1.3	19.4 ±1.7	
ε_r	383 ±19	328 ±16	336 to 617
$tan\delta$ (%)	2.4 ±0.1	2.4 ±0.2	
d_{33} (pC/N)	168 ±5	177 ±21	53 to 82
d_{31} (pC/N)	-97 ±3	-102 ±12	-20 to -29
g_{33} (mV·m/N)	49.4 ±1.5	60.8 ±7.0	17.8 to 21.2
g_{31} (mV·m/N)	-28.5 ±0.9	-35.2 ±4.1	-5.2 to -6.7
k_{eff}	0.18 ±0.01	0.23 ±0.01	
k_{31}	-0.20 ±0.01	-0.26 ±0.01	0.13 to 0.15
Q_M	32 ±4	19 ±3	98 to 130

Figure 8-7 shows the examples of the impedance-frequency spectra of a PZT thick-film and a PZnN-P3LZT thick-film, based on which the Y^E, d_{31}, k_{eff}, k_{31} and Q_M were calculated (for equations see Chapters 3 and 6). The resonance in the figure belonged to the length direction vibrations, which demonstrates the typical piezoelectric response of both samples.

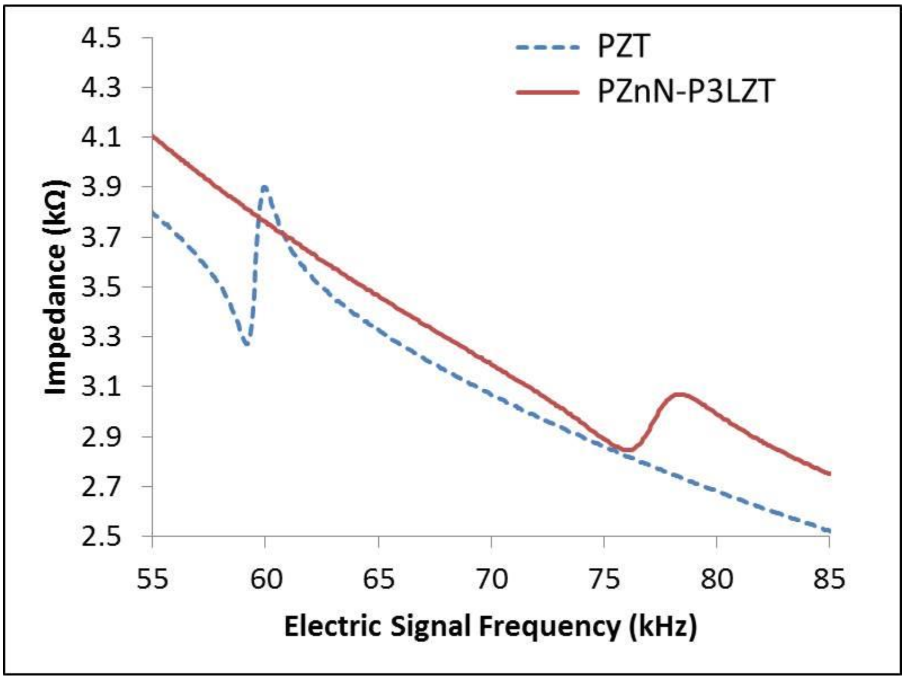

Figure 8-7. Dependence of impedance on electric signal frequency for a PZT thick-film sintered at 900 °C for 2 hour and a PZnN-P3LZT thick-film sintered at 900 °C for 1 hour.

Figure 8-8 shows the XRD patterns of the PZT and PZnN-P3LZT thick-films sintered with the same procedures presented above, together with comparisons to their powder and disc counterparts. For thick-films of both compositions, the main perovskite structures observed in the powders were maintained. The peak positions of the PZT thick-film shifted slightly (0.3°) towards larger diffraction angles. Although such a shift was not as significant as that for the PZT discs sintered at 1200 °C (presented with Figure 7-1), compared to the PZT discs with glass sintered at 900 °C for 2 hour where the peak shift could be hardly noticed (Figure 7-34), the low-temperature sintered PZT thick-films appeared to be closer to the high-temperature sintered discs. Such a microstructure also resulted in higher density, d_{33} and k_{eff} (listed in Table 8-2) than those of the low-temperature sintered discs (shown in Figure 7-33). However, nothing in the commercial vehicle used in the inks prevented the formation and growth of the pyrochlore in the PZnN-P3LZT thick-films, where the mixture of phases appeared almost the same as that for the corresponding low-temperature sintered discs.

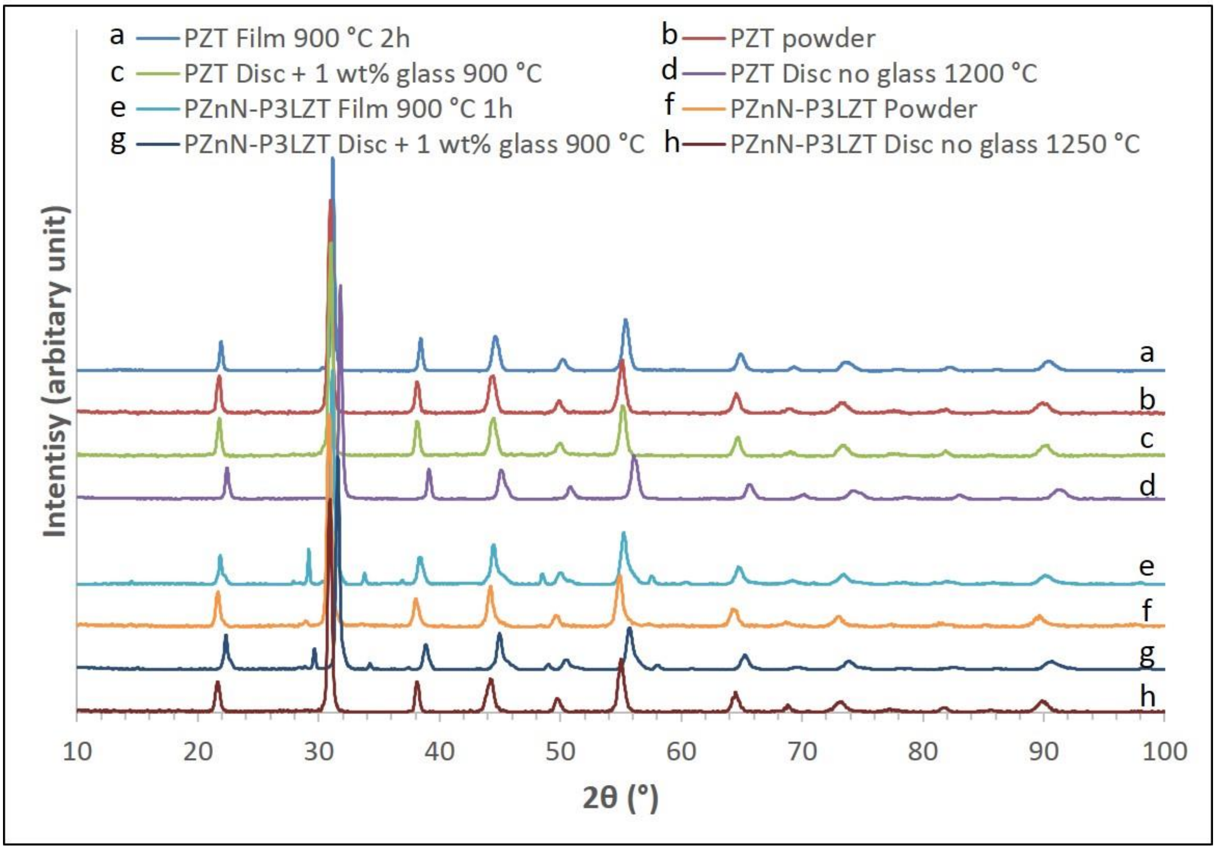

Figure 8-8. XRD patterns of the PZT thick-film sintered at 900 °C for 2 hours and the PZnN-P3LZT thick-film sintered at 900°C for 1 hour, and the corresponding powders, discs with glass addition sintered at 900 °C for 2 hours and discs without glass sintered at 1200 °C (PZT) and 1250 °C (PZnN-P3LZT) for 2 hours.

Figure 8-9 shows the SEM images of cross-sectional free-standing single-layer thick-films of the PZT and PZnN-P3LZT and their magnified fracture surfaces. Flat ceramic films of approximately 90 μm thick (PZT) and 80 μm thick (PZnN-P3LZT) were fabricated, with relatively dense microstructures compared to their low-temperature sintered disc counterparts (Figure 7-37). The grain sizes were 2-3 μm for both films, while some evenly distributed tiny pores were observed in the PZnN-P3LZT film, consistent with the lower measured density compared with that of the PZT film (Table 8-2).

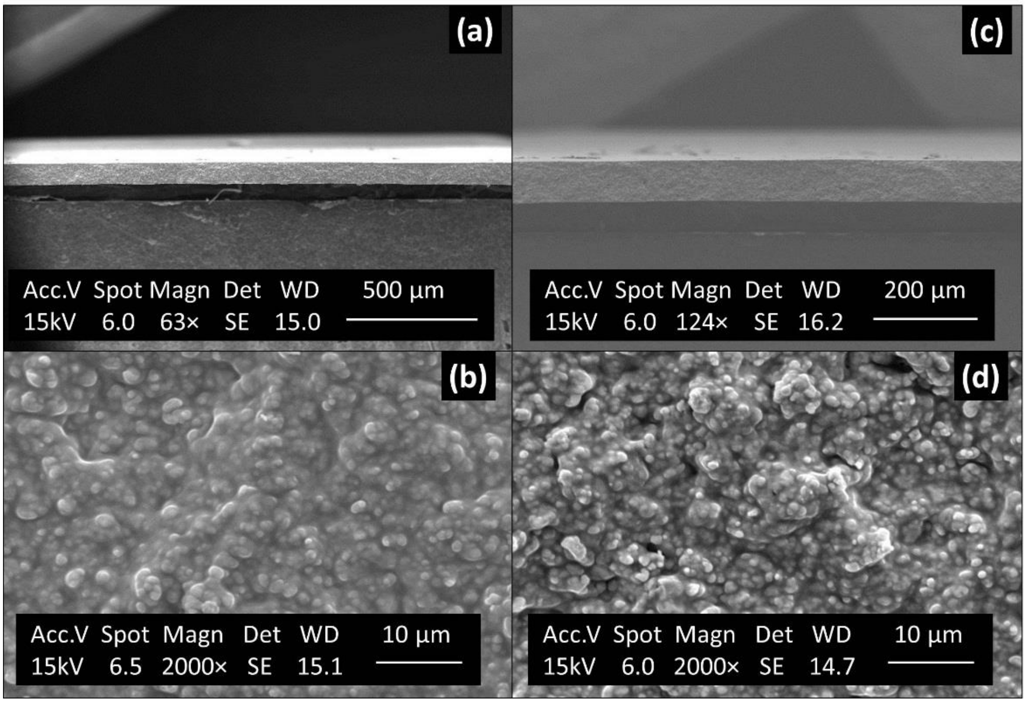

Figure 8-9. (a) & (c) cross-sectional and (b) & (d) fracture surface SEM images of free-standing single-layer thick-films of (a) & (b) PZT sintered at 900 °C for 2 hours and (c) & (d) PZnN-P3LZT sintered at 900 °C for 1 hour.

8.3 Vibration Tests of Single-element Energy Harvesters

8.3.1 Unimorph Harvesters without Proof Mass

The unimorph cantilevers made from the PZT and PZnN-P3LZT films were firstly tested and compared without tip proof masses. The root mean square (RMS) open-circuit voltage and RMS output power density measured with a range of accelerations at their individual resonant frequencies are shown in Figure 8-10 and 8-11, respectively. The calculation methods have been introduced in Section 6.5. In the figures, each datum was from an average of 3 samples, and each sample was tested 3 times independently within a week since being poled, in order to ensure the repeatability. Therefore, each datum point was actually an average of 9 values. The individual resonant frequencies of the PZT unimorph cantilevers were measured in the range of 431-436 Hz, while those of the PZnN-P3LZT unimorph cantilevers were about 470 Hz.

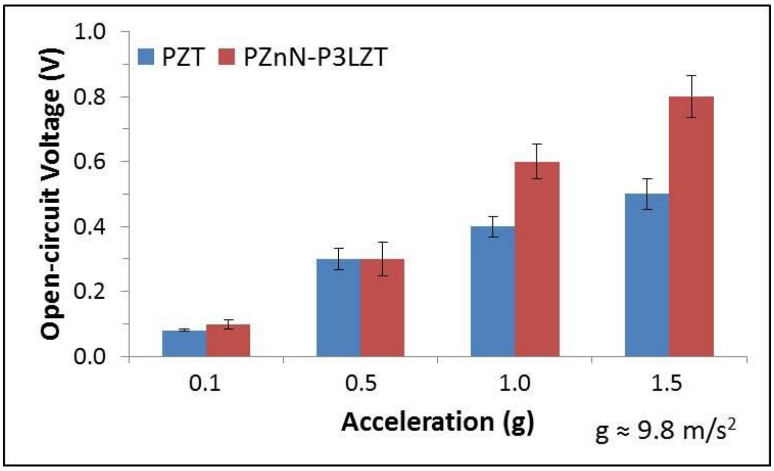

Figure 8-10. Dependence of RMS open-circuit voltage on acceleration (g ≈ 9.8 m/s^2) for the PZT and PZnN-P3LZT unimorph cantilevers vibrating at their individual resonant frequencies.

In Figure 8-10, as expected, the PZnN-P3LZT unimorph harvesters generated higher open-circuit voltage with relatively large accelerations (1.0g and 1.5g), resulting from the larger g_{33} and g_{31} of the piezoelectric elements. The peak to peak tip displacements of the PZT and PZnN-P3LZT samples at higher acceleration levels were not distinguishable, being in the range of 70-150 μm and 130-200 μm for accelerations of 1.0 and 1.5g, respectively. However, the PZnN-P3LZT harvesters did not exhibit advantages with smaller accelerations (0.1g and 0.5g) in terms of open-circuit voltage as shown in Figure 8-10. As the dimensions of the PZT and PZnN-P3LZT unimorphs were similar while the PZnN-P3LZT layers were stiffer (larger Y^E), the actual resonant frequencies of the PZnN-P3LZT cantilevers (approximately 470 Hz) were higher than those of their PZT counterparts (431-436 Hz), thus, with the same acceleration, the tip displacements of the former (20-30 μm for 0.1g, 40-60 μm for 0.5g) were smaller than the latter (30-40 µm for 0.1g, 50-70 µm for 0.5g), which might play a dominant role in generating output voltage at lower vibration levels.

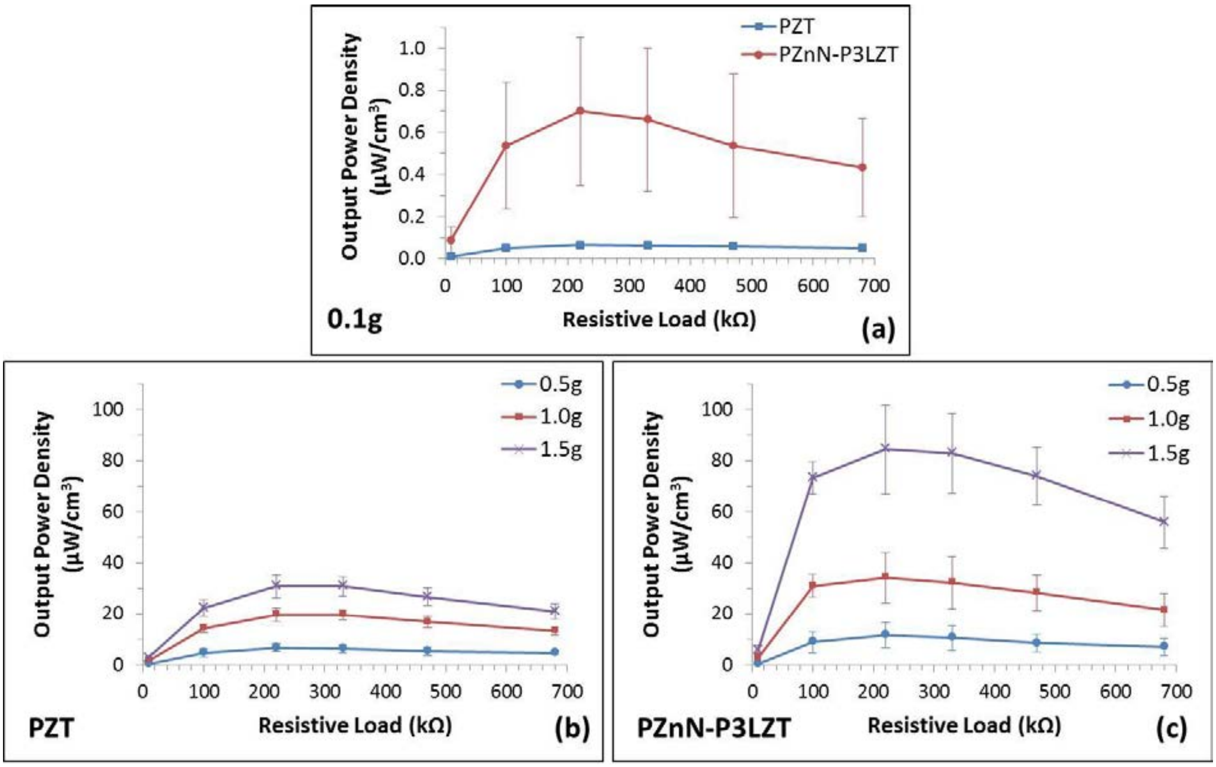

Figure 8-11. Dependence of RMS output power density on resistive load for: (a) the PZT and PZnN-P3LZT unimorphs vibrating at resonant frequencies with 0.1g acceleration; and (b) the PZT (c) the PZnN-P3LZT unimorphs vibrating at their individual resonant frequencies with different accelerations (g ≈ 9.8 m/s^2).

In Figure 8-11, it can be seen that the PZnN-P3LZT harvesters generally gave higher output power densities than the PZT samples with all values of resistive load, however they showed larger deviations. In order to identify whether such deviations were due to the measurement of different samples or repeat measurements on the same sample, Table 8-3 gives details of the data involved in Figure 8-11 (c) for acceleration of 1.5g with resistive load of 220 kΩ. Output power densities of three individual PZnN-P3LZT unimorph cantilevers (Samples 1, 2 and 3) obtained from three independent measurements (Tests 1, 2 and 3) are listed in the table. Also, deviations due to repeat measurements (Dev.-Test) and due to measurement of different samples (Dev.-Sample) are calculated. It can be seen that the Dev.-Sample values are about an order of magnitude larger than the Dev.-Test values, indicating that the larger overall deviations in Figure 8-11 (a) and (c) may be because of the larger deviations of the material parameters of the PZnN-P3LZT thick-films that were exhibited compared to those of the PZT thick-films, as listed in Table 8-2.

Table 8-3. Output power densities of three PZnN-P3LZT unimorph cantilevers obtained from three tests at their individual resonant frequencies with 1.5g acceleration and 220 kΩ resistive load, and deviations due to measurement of different samples and repeat measurements.

	Test 1	**Test 2**	**Test 3**	**Dev.-Test**
Sample 1	101.54	105.03	102.11	1.87
Sample 2	66.61	68.99	66.48	1.42
Sample 3	86.57	88.22	85.19	1.52
Dev.-Sample	17.53	18.03	17.82	15.47 (overall)

Unit: $\mu W/cm^3$

Despite these deviations, the outputs reached the peaks with a resistive load of 220 kΩ for both types of harvesters with all of the four input accelerations. Such an electrical matching may change as the materials, device dimensions/configurations or electrical connections differ. Also, the optimum average output power densities of the PZnN-P3LZT harvesters were calculated to be 900% (0.1g), 68% (0.5g), 73% (1.0g) and 173% (1.5g) better than those of the respective PZT harvesters. When compared to the reported data[1] obtained on a screen-printed PZT-5H free-standing thick-film unimorph energy harvester tested at its resonant frequency (around 230 Hz) with 60 kΩ resistive load, the advantages were even more remarkable, approaching to 25 %

(0.1g), 92% (0.5g) and 121% (1.0g). It should be noted that the output power densities of the reference[1] were re-calculated according to relevant data based on the same method used in this project (see Section 6.5).

The better performance of the PZnN-P3LZT harvesters compared to the PZT harvesters (Figure 8-11) might result from the PZnN-P3LZT unimorphs having either higher initial resonant power generation abilities (or energy densities) or higher energy conversion efficiencies, or a combination of both of them. Thus, the efficiency must be firstly determined in order to investigate and compare the initial/real energy densities. The effective efficiency (η_{eff}) of an energy harvesting system, which is expressed by Equation 8-1, consisted of three aspects: the material sector ($\eta_{material}$), the structural sector ($\eta_{structural}$) and the electric sector ($\eta_{electric}$).

$$\eta_{eff} = \eta_{material} \cdot \eta_{structural} \cdot \eta_{electric} \quad (8\text{-}1)$$

As the cantilevers were directly connected to resistors, the generated energy would be totally dissipated by the resistive load, thus $\eta_{electric}$ was assumed as 1. Meanwhile, because the configurations were the same, the $\eta_{structural}$ of the two types of unimorphs were assumed the same as well. Combining Equation 4-8 (Chapter 4) and Equation 8-1, the ratio of the efficiency of the PZT unimorph (η_{eff1}) and that of the PZnN-P3LZT unimorph (η_{eff2}) could be expressed by Equation 8-2, where Q_1 and Q_2 are total quality factors of the PZT and PZnN-P3LZT thick-films, respectively. And k'_1 and k'_2 are the factors of the PZT and PZnN-P3LZT thick-films related to electromechanical coupling coefficients. Factor k' has been defined by Equation 4-9 in (Chapter 4), whist Q could be estimated by Equation 8-3 (Q_M is mechanical quality factor, $tan\delta$ is dielectric loss factor).

$$\frac{\eta_{eff1}}{\eta_{eff2}} = \frac{2Q_1k'_1 + Q_1Q_2k'_1k'_2}{2Q_2k'_2 + Q_1Q_2k'_1k'_2} \quad (8\text{-}2)$$

$$\frac{1}{Q} = \frac{1}{Q_M} + tan\delta \quad (8\text{-}3)$$

Using the data of the thick-films in Table 8-2, η_{eff1}/η_{eff2} was calculated to be approximately 0.87. This means without considering the effects of the structure and circuit, the energy conversion efficiency of the PZT unimorph was smaller than that of the PZnN-P3LZT unimorph, suggesting that in order to obtain a higher efficiency, piezoelectric materials exhibiting larger $Q{\cdot}K'$ might be preferred.

The initial power generation abilities of the samples can now be compared after taking out the effect of efficiency. Taking the average output power densities vibrating at 0.5g with 220 kΩ resistive load as an example, the PZnN-P3LZT harvesters still outperformed the PZT harvesters by about 46% in terms of the initially generated power density. This confirmed that the PZnN-P3LZT composition could not only impart higher energy conversion efficiency, but better raw energy conversion ability, when applied in a piezoelectric free-standing thick-film energy harvester. Also, it suggested that the electromechanical coupling coefficients might have a more significant effect than Q_M on the output power density.

8.3.2 Bimorph Harvesters without Proof Mass

8.3.2.1 Output Power Density

Figure 8-12 shows the comparison of the RMS output power densities of the unimorphs and bimorphs made from the PZnN-P3LZT composition. Again, each datum was from an average of 3 samples and each sample was tested 3 times within a week. In addition it should be noted that, the bimorphs were poled in series while being connected in parallel for the harvester characterisations. In the figure, the average output power densities of the bimorphs with the optimum resistive load (100 kΩ) were about twice of those of the unimorphs when excited with accelerations of 1.0g and 1.5g. This is because the two pieces of piezoelectric layers of the bimorphs were electrically connected in parallel, which tended to double the current compared to the unimorphs. This is also the reason for the peak in bimorph output being at about half the resistive load compared to the unimorphs (electrical matching). However, at lower vibration levels (0.1g and 0.5g), the output power densities of the bimorphs were smaller than those of the unimorphs, where the reason might be that the bimorphs were thicker than the unimorphs thus their resonant frequencies were higher (about 610-625 Hz), leading to reduced amplitudes as well as tip displacements (around 10 μm for 0.1g and 30 μm for 0.5g) with weak vibrations. Although the same situation would also happen at higher vibration levels, the differences of the tip displacements between the unimorphs (70-150 μm for 1.0g, 130-200 μm for 1.5g) and bimorphs (90-130 μm for 1.0g, 160-180 μm for 1.5g) were not significant enough to markedly affect the absolute output. Table 8-4 gives the information of film thicknesses, planar dimensions and resonant frequencies for each sample of the PZnN-P3LZT unimorphs and bimorphs used for comparison in Figure 8-12. In the table, the thickness is expressed by the five individual layers, which are top electrode (E_T), top piezoelectric layer (P_T), middle electrode (E_M), bottom piezoelectric layer (P_B) and bottom electrod (E_B), respectively, from left to right. As introduced in Chapter 6, the volume used for calculating the output power density was the free-standing part taking into account all piezoelectric and silver layers (thickness of the whole device). This means, although the structure of the two configurations is almost identical apart from one electrode, the inactive piezoelectric layer in the unimorph case resulted in a half output power density compared to that in the bimorph case where both piezoelectric layers were active. This does not necessarily suggest the bimorph configuration is more efficient, but, based on the same materials, it is a better choice of chasing higher output compared to the unimorph. Also, unlike the unimorphs which had a relatively wide range of corresponding resistive loads (100-470 kΩ), the output of the bimorphs seemed more dependent on the loads. Sharp trends can be observed in Figure 8-12 (c), especially for measurements at 1.0g and 1.5g accelerations.

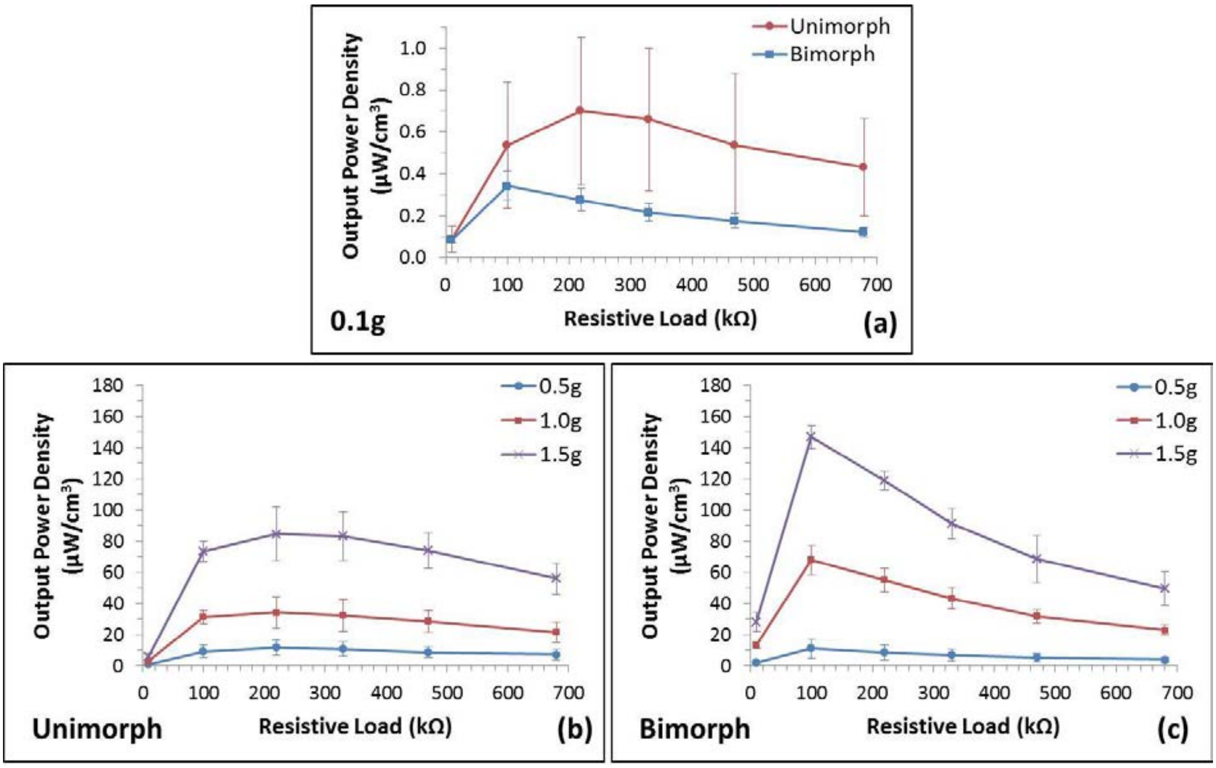

Figure 8-12. Dependence of RMS output power density on resistive load for: (a) the PZnN-P3LZT unimorphs and bimorphs vibrating at resonant frequencies with 0.1g acceleration; and the PZnN-P3LZT (b) unimorphs (c) bimorphs vibrating at resonant frequencies with different accelerations.

Overall, the PZnN-P3LZT bimorph individual harvesters performed a maximum average output power density of approximately 147±7 μW/cm^3, vibrating at resonant frequencies of 610-625 Hz with 1.5g acceleration and 100 kΩ resistive load, without any structural or electrical optimisation. Further experiments and discussions after this point are based on the bimorph structures made from the PZnN-P3LZT composition with various dimensions (planar and thickness) and different weights of tip proof masses.

Table 8-4. Length, width, thickness and resonant frequencies of each tested PZnN-P3LZT unimorph and bimorph cantilever (E_T – top electrode, P_T – top piezo-layer, E_M – middle electrode, P_B – bottom piezo-layer, E_B – bottom electrode).

	Length (mm) (free-standing part)	**Width (mm)**	**Thickness (µm) (E_T-P_T-E_M-P_B-E_B)**	**Resonant Frequency (Hz)**
Unimorph-1	11.4	2.94	37.8-73.8-28.4-79.4-n.a.	467
Unimorph-2	11.5	2.96	36.6-74.0-30.4-80.4-n.a.	470
Unimorph-3	11.4	2.93	34.0-82.5-25.5-84.4-n.a.	468
Bimorph-1	13.8	3.00	36.1-92.0-32.5-94.6-32.2	612
Bimorph-2	13.4	2.98	32.1-89.6-28.1-99.2-25.6	624
Bimorph-3	13.5	3.00	35.4-92.3-29.6-92.1-38.0	618

8.3.2.2 Effect of Shorter Bottom Electrode

It has been presented in Chapter 6 that in order to ensure successful fabrication, the bottom electrode of the bimorph should be at least 20% shorter than the entire cantilever. This would definitely cause a reduction to the output of the bottom piezoelectric layer, since only the part covered by both electrodes could be poled and activated. The influence of this will now be considered in more detail.

Figure 8-13 shows the lower side of a bimorph sample, where the bottom electrode was about 76% of the entire cantilever length. Figure 8-14 compares the instantaneous open-circuit voltage, output voltage with resistive load and output power of the top/bottom piezoelectric layers and the entire cantilever of this sample. In order to amplify the output thus make any differences more recognisable, a 0.12g mass was attached to the tip of this bimorph sample. The tip mass of 0.12g was chosen here because the value is at the average level among all of the masses used in the experiment, which is heavy enough to magnify the output but not to add risk of breaking the cantilever when vibrating.

According to Figure 8-14 (a), (b) and (c), the shorter bottom electrode did not obviously affect the open-circuit voltage. Both the top and bottom piezoelectric layers generated about 2 V peak voltages, close to that generated by the entire cantilever (about 2.2 V). This might be because that the very tip of the cantilever did not bend much[2], thus the inactive part close to the tip was not effective enough to drag down the output considerably. Indeed, it has been discussed that a thin-film PZT membrane on silicon substrate covered by 60% electrodes could offer the optimum electromechanical coupling[3], and a similar situation could exist for piezoelectric cantilevers.

However, when connected to a resistive load, the output difference of the layers could be easily recognised, as shown in Figure 8-14 (d), (e) and (f). The top and bottom layers only generated about 1.2 V and 1.0 V peak voltages across the load respectively, while the comprehensive value was about 1.5 V. This was mainly because the shorter bottom electrode made the effective resistance of the bottom piezoelectric layer smaller (only the aspect covered by both electrodes was active), and the resistive load matched only the overall resistance of the entire cantilever (effectively two resistors connected in parallel) but not each single-layer’s. The output power could provide more information of the real difference caused by the shorter bottom electrode. As Figure 8-14 (g) and (h) indicate, the output power of the bottom layer (nearly 3 μW) was about 67% of that of the top layer (nearly 4.5 μW), under the same vibrational and electric conditions. The overall output power (about 7.8 μW) shown in Figure 8-14 (i) was close to the sum of each layer’s value.

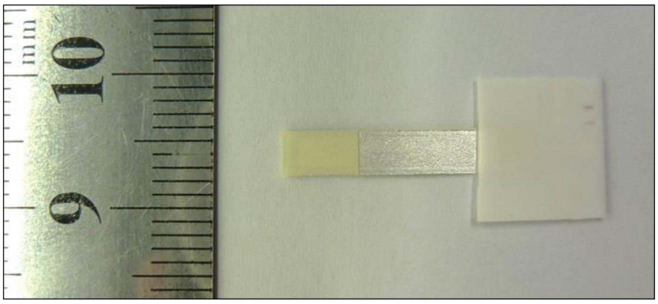

Figure 8-13. Picture of the lower side of a bimorph cantilever with the bottom electrode 76 % of the entire cantilever length.

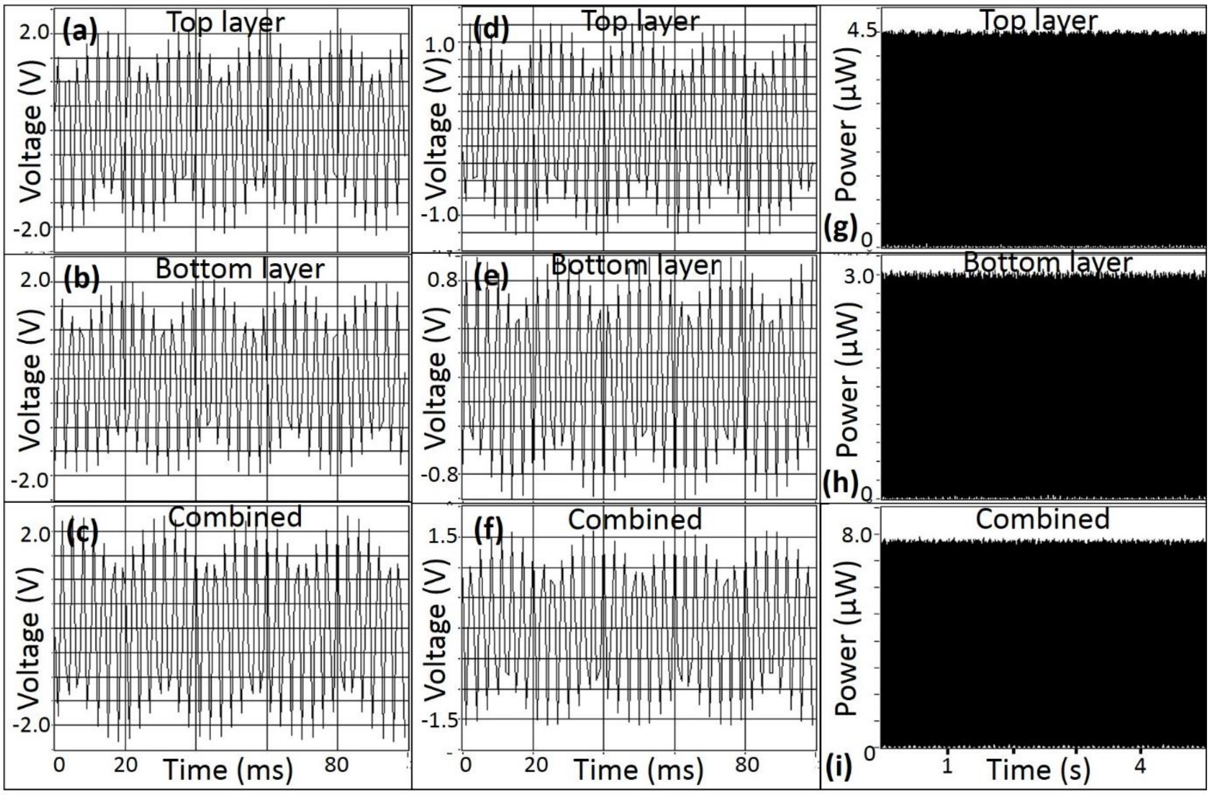

Figure 8-14. Dependence of (1) open-circuit voltage for (a) top piezoelectric layer (b) bottom piezoelectric layer (c) overall cantilever, (2) output voltage with 330 kΩ load for (d) top piezo-layer (e) bottom piezo-layer (f) overall cantilever, and (3) output power with 330 kΩ load for (g) top piezo-layer (h) bottom pizo-layer (i) overall cantilever, on real time, vibrating at resonant frequency (345 Hz) with 1.0g acceleration.

Consequently, considering the integrated two piezoelectric layers, the shorter bottom electrode would have a minimal effect on the overall open-circuit voltage, however it was likely to reduce the overall output power. In addition, it could be predicted that if the bottom electrode covered 100% of the cantilever bottom surface, the overall output power was likely to be twice of that of each single-layer, proving that the bimorphs poled in series while connected in parallel tend to double the output power, which has been estimated in Chapter 4.

8.3.3 Bimorph Harvesters with Proof Mass

8.3.3.1 Effect of Tip Mass Attachment

Tip masses of metallic lead were cut into tiny bar shapes with different weights, and attached to the cantilevers as described in Chapter 6 in either a symmetrical or asymmetrical configuration. Table 8-5 and 8-6 summarise the relevant information of dimensions, tip mass attachment and poling/connecting methods of all of the 6 samples used for the investigation on performance optimisation.

Table 8-5. Summary of the dimensions of the cantilever samples (E_T – top electrode, P_T – top piezo-layer, E_M – middle electrode, P_B – bottom piezo-layer, E_B – bottom electrode).

Sample ID	Free-standing Length (mm)	Width (mm)	Thickness (μm) (E_T-P_T-E_M-P_B-E_B)
H-1	10.71	3.16	32.3-116.7-22.0-115.0-30.8
H-2	14.10	3.21	31.4-71.2-23.2-66.1-29.3
H-3	16.75	3.50	18.6-76.0-17.0-67.3-19.0
H-4	14.25	3.22	18.3-76.5-16.6-67.0-18.9
H-5	16.00	3.50	19.0-76.0-16.5-67.5-18.5
H-6	15.00	3.25	18.5-75.5-17.9-67.4-19.6

Table 8-6. Summary of the tip mass attachment and poling/connection methods of the cantilever samples.

Sample ID	Tip Mass (g)	Attachment	Poling/Connection
H-1	0.122	Asymmetric	Series/Parallel
H-2	0.150	Symmetric	Series/Parallel
H-3	0.097	Asymmetric	Series/Parallel
H-4	0.095	Symmetric	Parallel/Series
H-5	0.104	Symmetric	Parallel/Series
H-6	0.120	Symmetric	Parallel/Series

As was presented with Table 8-3, the thickness in Table 8-5 is also expressed by the five individual layers, which are top electrode (E_T), top piezoelectric layer (P_T), middle electrode (E_M), bottom piezoelectric layer (P_B) and bottom electrod (E_B), respectively, from left to right. In Table 8-6, the poling scenario is indicated on the left of the poling/connection column whilst the connection is on the right. Figure 8-15 shows the schematics of the tip mass attachment methods corresponding to samples H-1 to H-3 in Table 8-3, and the pictures of a bimorph sample with a symmetrically attached tip mass.

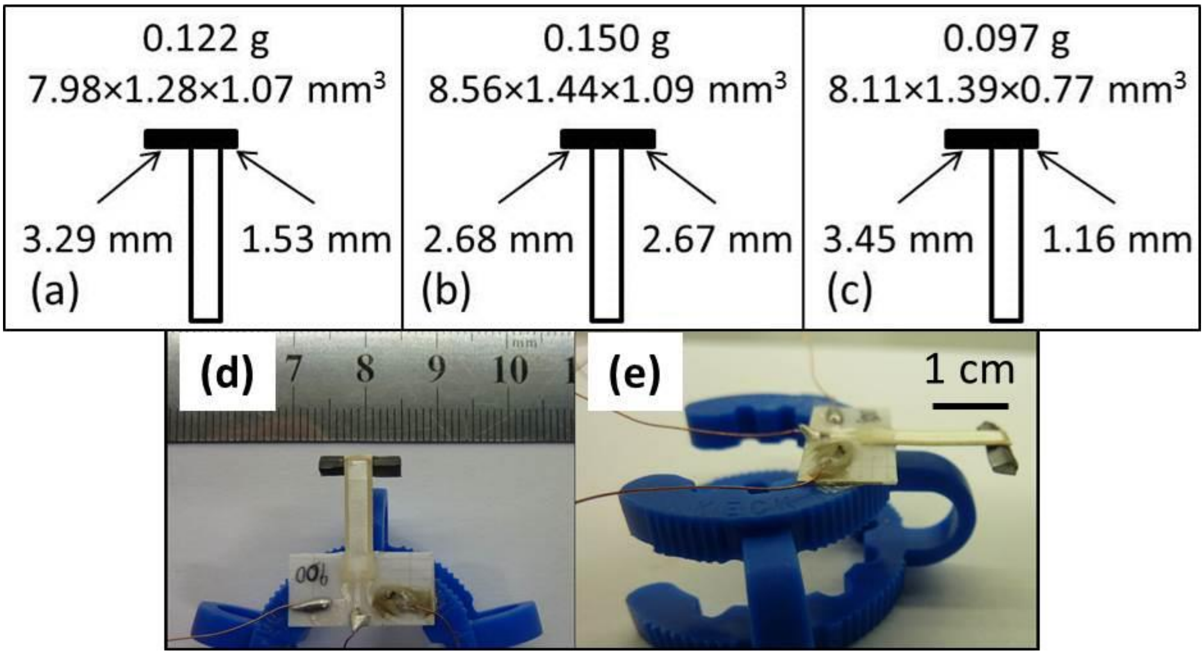

Figure 8-15. Schematics (top-view) of (a) H-1 (b) H-2 (c) H-3 for tip mass attachment methods; and (d) & (e) pictures of a bimorph with symmetrically attached tip mass.

Figure 8-16 shows the frequency dependence of the RMS output power for samples H-1 to H-3 with matched resistive loads (H-1 330 kΩ, H-2 470 kΩ, H-3 470 kΩ), and Figure 8-17 shows the frequency dependence of the RMS open-circuit voltage for samples H-1 to H-6, respectively, subjected to different accelerations ($g \approx 9.8 m/s^2$). The frequency dependence of the peak to peak tip displacement for samples H-3 (Figure 8-16 (c) and Figure 8-17 (c)), H-5 (Figure 8-17 (e)) and H-6 (Figure 8-17 (f)) is also shown. The frequency changes were made manually in discrete intervals of 1 Hz, either up or down. No lag in output with change of frequency was observed.

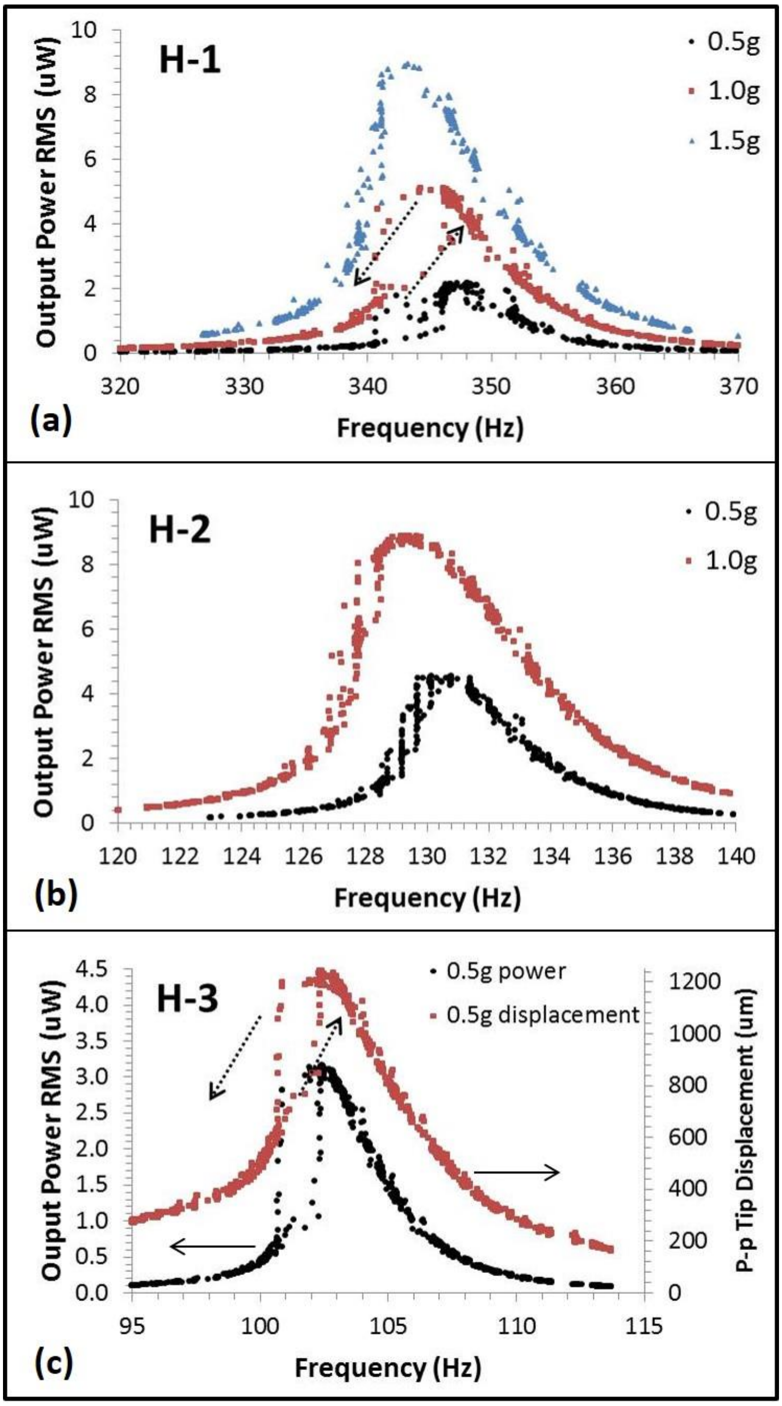

Figure 8-16. Dependence of RMS output power for samples H-1, H-2 and H-3, and peak to peak tip displacement for sample H-3, on input frequencies with different accelerations.

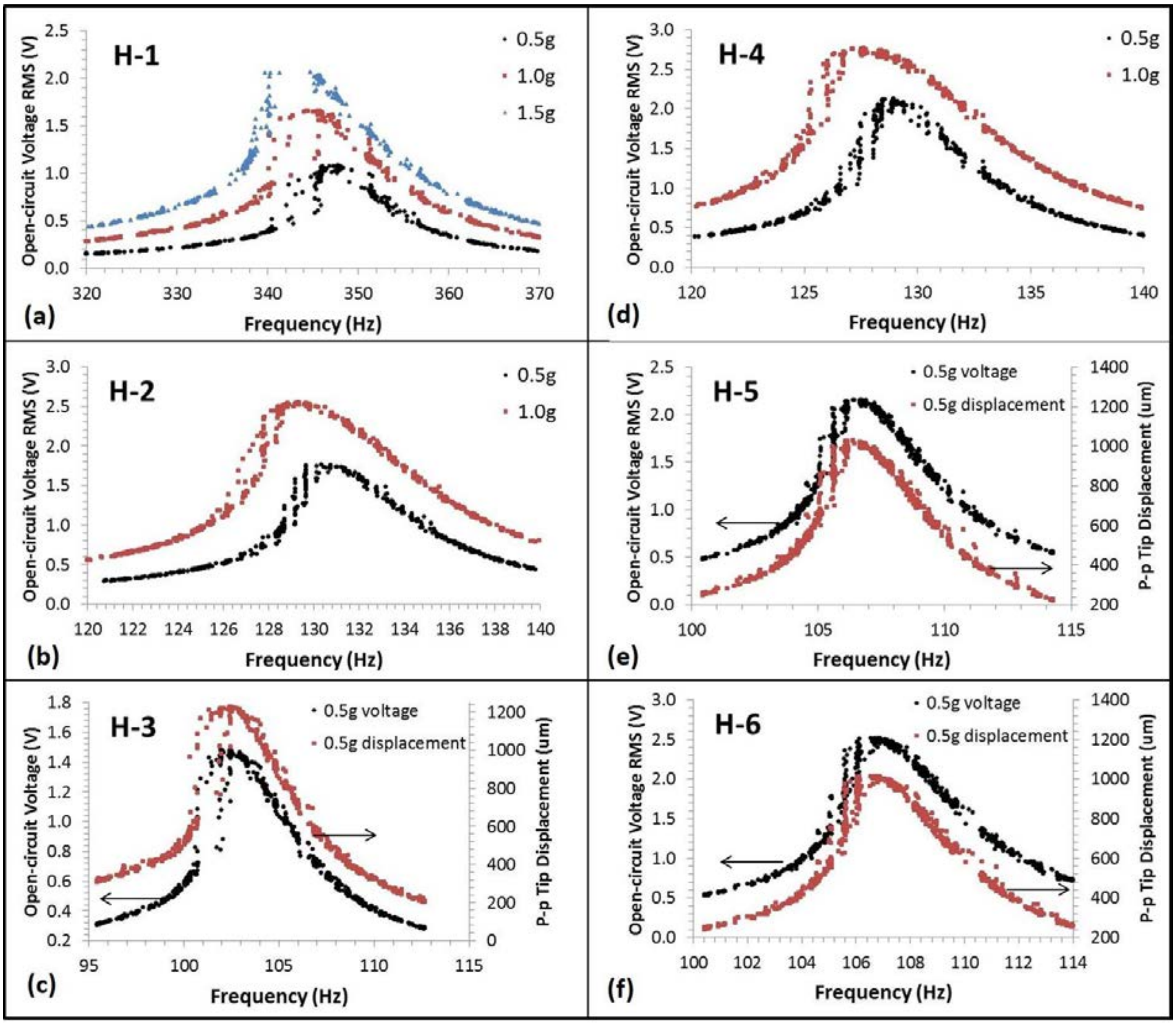

Figure 8-17. Dependence of RMS open-circuit voltage for samples H-1 to H-6, and peak to peak tip displacement for samples H-3, H-5 and H-6, on input frequencies with different accelerations.

As shown in the above figures, for the parallel connected individual harvesters (H-1, H-2 and H-3), maximum outputs of about 9 μW and 2-2.5 V with 1.0-1.5g accelerations, and 3-4.5 μW and 1.5-2 V with 0.5-1.0g accelerations were achieved when the harvesters were vibrating near the resonant frequencies. And the positions of the peaks were treated as the measured resonant frequencies. Meanwhile, for the series connected individual harvesters (H-4, H-5 and H-6), maximum outputs of 2-2.8 V with 0.5-1.0g accelerations were also generated when vibrating near resonant frequencies.

Comparing sample H-3 to samples H-5 and H-6, where the data of peak to peak displacement are shown, H-3 generated about 1.5 V peak open-circuit voltage with approximately 1200 μm displacement vibrating at 102 Hz with 0.5g acceleration, however H-5 and H-6 were able to provide the peaks of 2.2-2.5 V with nearly only 1000 μm with 107 Hz, 0.5g vibration. In another comparison, the open-circuit voltage of sample H-3 with 1000 μm tip displacement was only about 1.2 V, which was close to the half of those values of H-5 or H-6, under extremely similar conditions. This was to be expected according to the relevant introduction in Chapter 4, that is the bimorphs poled in parallel while connected in series tend to double the output voltage, though the best matched resistive loads were normally 4 times of those of the parallel connected counterparts. The point that the bimorphs poled in series while connected in parallel are able to double the output power has already been discussed in Section 8.3.2.

Furthermore, both the output power and open-circuit voltage shown in Figure 8-16 and Figure 8-17 were generally 5-10 times higher than those of the cantilever without tip mass. However, it should be noted that such an improvement does not necessarily mean a complete optimisation. As discussed in Chapter 4, tip displacement and dimensions of a cantilever are able to affect open-circuit voltage hence output power. Therefore, by precisely tailoring the dimensions (e.g. increase volume) or properly selecting tip masses (e.g. using heavier proof mass to increase tip displacement), further improvement on output could be expected. As output optimisation of energy harvesters is a complex procedure which requests advanced computational and modelling methods and this is not the main purpose of this project, the choice of tip mass was only used for frequency tuning and no further output optimisation was carried out.

In addition, it can also be observed in Figures 8-16 and 8-17 that at lower levels of vibration (0.5-1.0g acceleration) for samples H-1 and H-3, where the tip masses were asymmetrically attached, the output or tip displacement showed considerable inconsistency within the frequency ranges below the resonant frequencies. In particular, as indicated by the dashed arrows, when tuning up the input frequency, the output or displacement delayed to increase to the peak. On the contrary, when tuning down the input frequency, it delayed to decrease[4]. This phenomenon appeared as the asymmetric tip mass introduced a torsion degree of freedom[5], which made the entire bending-torsion system performing non-linear. However, when the vibration went to a higher level, e.g. H-1 with 1.5g acceleration, the inconsistency disappeared. This might be because the strong vibration compensated the difference between the bending amplitude and the torsion twisting angles[4]. In the opposite case, for samples H-2, H-4, H-5 and H-6 where the tip mass was symmetrically attached, the hysteresis phenomenon was hardly visible. The slight inconsistency might be because of the inaccuracy in precisely achieving a symmetrical attachment of the tip mass, as shown in Figure 8-15 (b). Such result suggested that an asymmetric tip mass was likely to increase the non-linearity of the spring-mass system to some degree, which might be valuable for designing a single-element non-linear energy harvester at low-level vibrations, in order to effectively widen the bandwidth[4].

8.3.3.2 Charging Behaviour in Real Applications

As the current development of energy harvesting technology has not been able to directly power most wireless sensor networks in real time because of insufficient energy generated, the potential applications of energy harvesters in the near future are predicted as two-stage power supplies – charging energy storage media firstly, then using such media to power final nodes when external energy sources are not available[6,7]. Therefore, sample H-3 and H-5 were selected as representatives to charge a 1000 μF capacitor, thus to explore the feasibility of applying such individual harvesters in certain scenarios.

Figure 8-18 shows the real-time instantaneous open-circuit voltage of sample H-3 and H-5 connected to diode bridge rectifiers (as shown in Figure 6-7 (b), Chapter 6), vibrating at their resonant frequencies (103 Hz and 107Hz, respectively) with 0.3g or 0.5g acceleration.

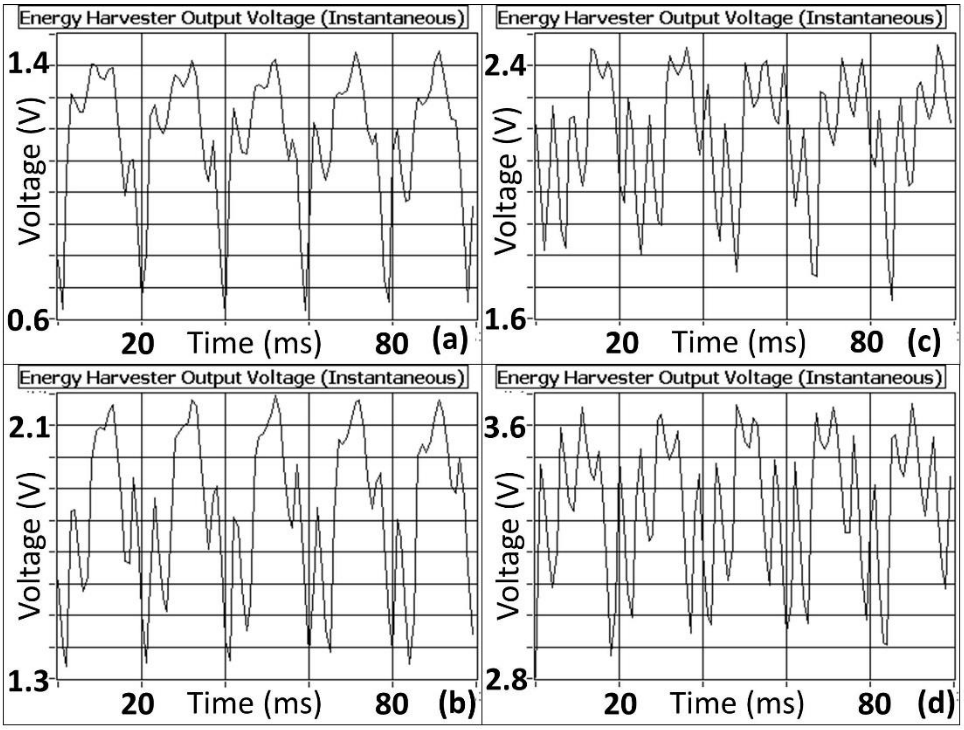

Figure 8-18. Dependence of instantaneous open-circuit voltage on real time for the individual harvesters connected with diode bridges vibrating at resonant frequencies with different accelerations: (a) H-3, 0.3g; (b) H-3, 0.5g; (c) H-5, 0.3g; and (d) H-5, 0.5g.

As observed, original AC outputs (switching between positive and negative potentials) were converted into positive outputs. Although they were not well-rectified DC outputs with stable voltage, they were still possible to charge capacitors. Similar to the un-rectified signals shown in Figure 8-17, sample H-5 offered higher open-circuit voltage than H-3, although it can be seen that the ratio was smaller than 2:1 which might be caused by electrical dissipation introduced by the rectifier.

Figure 8-19 shows the corresponding charging response using different samples with certain vibration conditions. As H-3 was poled in series while connected in parallel, it generated higher charging current, resulting in a faster charging rate in the first 25 minutes. However, although H-5 provided a slower charging rate at the early stage, it was able to charge the capacitor to a higher electric potential if the charging time was allowed long enough because of its higher open-circuit voltage (Figure 8-19). The charging voltage limits of H-5 (series connected) were 150-200% of those of H-3 (parallel connected). This result suggested that the proposed individual harvesters with either poling/connection method were feasible in terms of applications targeted on fast charging or high final electric potential.

In comparison, piezoelectric energy harvesters have also been used for charging energy storage devices in the literature[8]. For instance, a PZT-aluminum unimorph cantilever was used for charging a 40 mAh Ni-MH rechargeable button cell battery, where the voltage of the battery was charged from 0.5 V to 1.2 V in 60 minutes (11.7 mV/min) at the resonant frequency[8]. Although the charging rate of harvester H-3 with 0.5g acceleration shown in Figure 8-19 reached 38.3 mV/min in the first 60 minutes, it is considered less efficient than that of the literature as capacitance of the battery is much larger than the capacitor. However, the volume of the PZT element in the literature was also much larger (40mm × 62mm × 0.95mm), and the calculated average output power density was only 81 $\mu W/cm^3$, compared to 858 $\mu W/cm^3$ of the piezoelectric element of harvester H-3. From this point of view, it can be predicted that with increased volume of piezoelectric element, the proposed harvester is likely to be 10 times more efficient than that of the literature when charging the same battery.

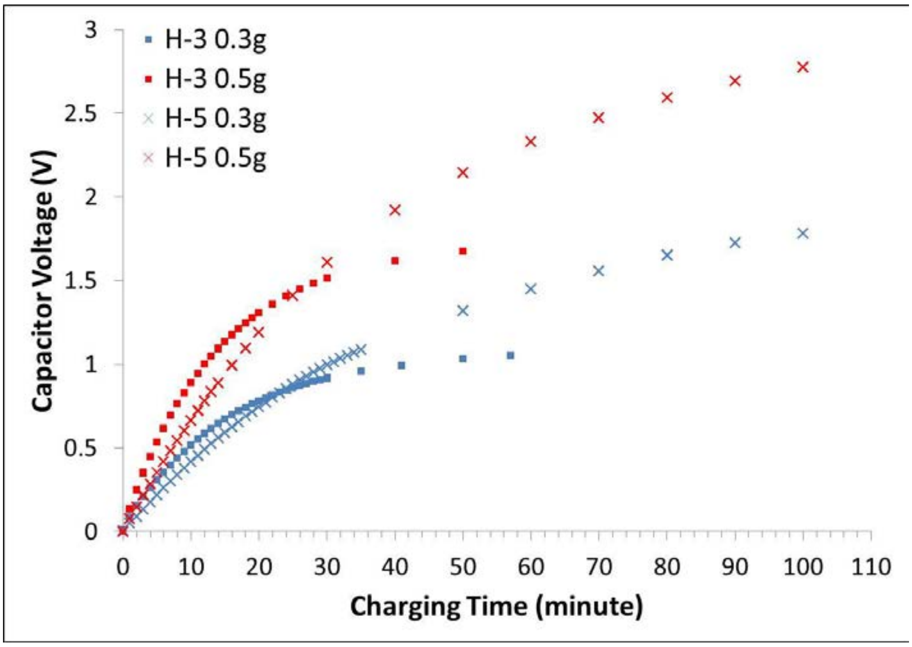

Figure 8-19. Dependence of capacitor voltage on charging time for samples H-3 and H-5 vibrating at resonant frequencies with 0.3g and 0.5g accelerations.

8.4 Design, Integration and Vibration Test of Harvester Arrays

8.4.1 Frequency Modelling

8.4.1.1 Young's Modulus of Silver Layers

The concept of an energy harvester array in which several single-element harvesters are integrated into a single device which could help to widen the overall bandwidth was introduced in Chapter 4. However, for this to be successful, the resonant frequency of each individual harvester must be carefully predicted and designed, in order to achieve either a very broad smooth shaped output-frequency spectrum partially overlapping neighbour peaks, or a saw tooth-shaped response extending the resonant frequencies into a wider range.

According to Equation 4-2 to 4-5 in Chapter 4, the unknown parameters for modelling the resonant frequency of a bimorph harvester until this point were the density (ρ_S) and Young's modulus (Y_S) of the silver layer. The density was obtained by measuring the single-layer silver film fabricated together with Series 1 samples, as shown in Figure 8-1 (c). The calculated value will be presented later with other relevant parameters used for frequency modelling. However, the Y_s was more complicated to be directly measured or calculated through the single-layer films. This issue was solved by taking converse calculations of Equations 4-2 to 4-5 with the measured resonant frequency of each bimorph sample and other known parameters. Specific details are provided here.

Figure 8-20 shows the cross-sectional SEM image of sample H-1, which reveals that the five layers were not perfectly symmetric to the neutral plane of the entire thickness. In order to make the equations still applicable, Equations 4-3 and 4-4 were treated specifically in terms of different layers.

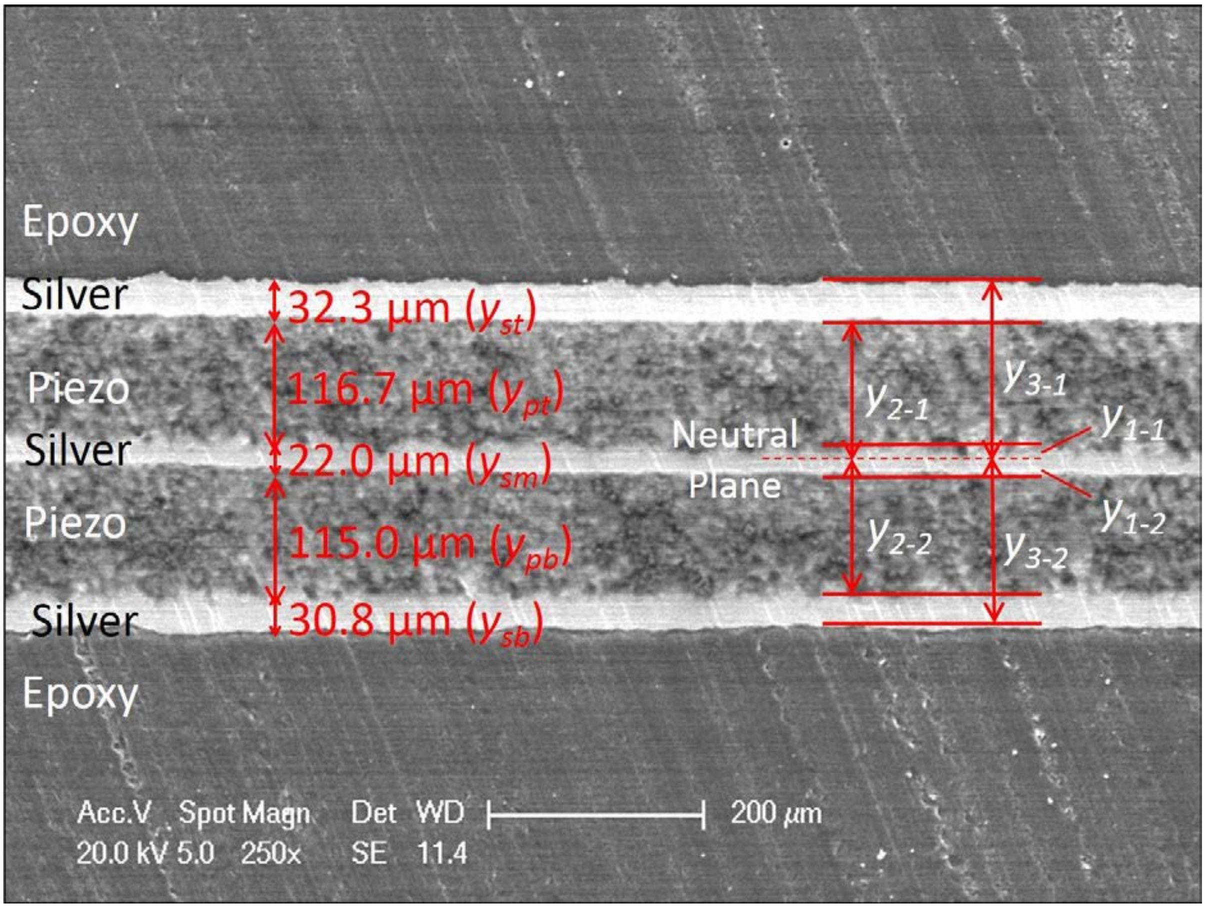

Figure 8-20. Cross-sectional SEM image with relevant dimensional markers of sample H-1.

Take sample H-1 as an example, although the neutral plane was determined, making $y_{3\text{-}1}$ equal to $y_{3\text{-}2}$, the middle silver later was not evenly divided by the neutral plane, where $y_{1\text{-}1}$ was about 9.4 µm while $y_{1\text{-}2}$ was about 12.6 µm, as shown in Figure 8-20. Also, the thickness difference between the top and bottom silver layers as well as the top and bottom piezo-layers exacerbated the asymmetry. In such a case, for sample H-1 (other samples obeyed the same principle), Equations 4-2 and 4-3 were replaced by Equations 8-4 and 8-5, where the dimensional parameters were marked in Figure 8-20, and ρ_p and Y_p represent the density and Young's modulus of the piezoelectric layers, respectively.

$$YI = \frac{w}{3} \cdot \begin{bmatrix} Y_s(y_{1\text{-}1}^3 + y_{1\text{-}2}^3 + y_{3\text{-}1}^3 - y_{2\text{-}1}^3 + y_{3\text{-}2}^3 - y_{2\text{-}2}^3) \\ +Y_p(y_{2\text{-}1}^3 - y_{1\text{-}1}^3 + y_{2\text{-}2}^3 - y_{1\text{-}2}^3) \end{bmatrix} \quad (8\text{-}4)$$

$$m_{pul} = w \cdot \left[\rho_s(y_{st} + y_{sm} + y_{sb}) + \rho_p\left(y_{pt} + y_{pb}\right)\right] \quad (8\text{-}5)$$

The above mathematical manipulation might introduce an error which was related to asymmetry. Define the degree of asymmetry ($D_{asy.}$) by Equation 8-6.

$$D_{asy.} = \frac{y_{3\text{-}1} - y_{st} - y_{pt} - \frac{y_{sm}}{2}}{y_{3\text{-}1} + y_{3\text{-}2}} \times 100\% \quad (8\text{-}6)$$

Table 8-7 and 8-8 summarise the relevant information of dimensions, tip masses, asymmetry, measured frequencies and calculated Y_s. A large number of samples were measured and calculated, but only 8 samples (C-1 to C-8) were listed in the tables which obtained similar calculated Y_s. The $D_{asy.}$ of such samples were found smaller than ±5%, compared to the full range of -8 % to 11 % for all of the measured samples. For other cantilevers where the $D_{asy.}$ were larger than ±5%, the calculated Y_s showed irregular variations. This probably implied that the mathematical model needed to be refined when modelling the samples with larger $D_{asy.}$.

Table 8-7. Summary of dimensions and tip masses of the cantilevers used for the calculation of Young's modulus of thick-film silver-layers.

Sample ID	Free-standing Length (mm)	Width (mm)	Thickness (μm) $d_{st}/d_{pt}/d_{sm}/d_{pb}/d_{sb}$	Tip Mass (g)
C1 (H-1)	10.71	3.16	32.3/116.7/22.0/115.0/30.8	0.122
C2	11.23	3.00	23.2/73.5/29.4/78.5/25.1	0.224
C3 (H-2)	14.10	3.21	31.4/71.2/23.2/66.1/29.3	0.150
C4	11.50	3.25	17.3/79.9/19.1/62.2/15.9	0.130
C5	12.97	3.25	20.0/71.7/16.9/59.5/20.4	0.113
C6	12.58	3.50	19.4/75.5/17.7/67.9/19.3	0.100
C7	13.65	3.50	17.7/77.0/15.4/67.9/18.9	0.130
C8	16.25	3.50	18.6/75.6/17.8/66.0/18.9	0.098

Table 8-8. Summary of degrees of asymmetry, measured resonant frequencies (open-circuit resonant behaviour with 0.5g acceleration) and calculated silver-layer Young's modulus of the cantilevers.

Sample ID	$D_{asy.}$ (%)	Measured Resonant Frequency (Hz)	Calculated Y_s (GPa)
C1 (H-1)	-0.51	347.76	46.26
C2	1.50	149.57	46.19
C3 (H-2)	-1.63	130.55	46.71
C4	-4.91	140.82	46.09
C5	-3.13	131.50	48.78
C6	-1.93	160.97	48.50
C7	-2.01	122.27	48.28
C8	-2.36	104.42	45.77

In order to simplify the analysis and target straightforward on the final purpose of designing harvester arrays of this project, rather than conduct professional mathematical and mechanical analyses, only the samples showing better consistency were discussed. In addition, the measured and calculated data in Table 8-8 were based on the open-circuit resonant behaviour with 0.5g acceleration.

During the fabrication of the initial bimorph samples used for this calculating stage, the thickness of each layer was not specifically controlled due to different tapes being used to define each layer during the printing stage. This may provide some explanation to the deviations that were observed. However, when fabricating the cantilevers for the following validation and array design stages, each layer was specially controlled, where the 70 μm tape was used for printing silver layers while the 140 μm tape was for piezoelectric layers. As a result, the average thickness of each layer was almost consistent for different samples, as shown in Figure 8-21. Meanwhile, the average degree of asymmetry was limited under ±5%.

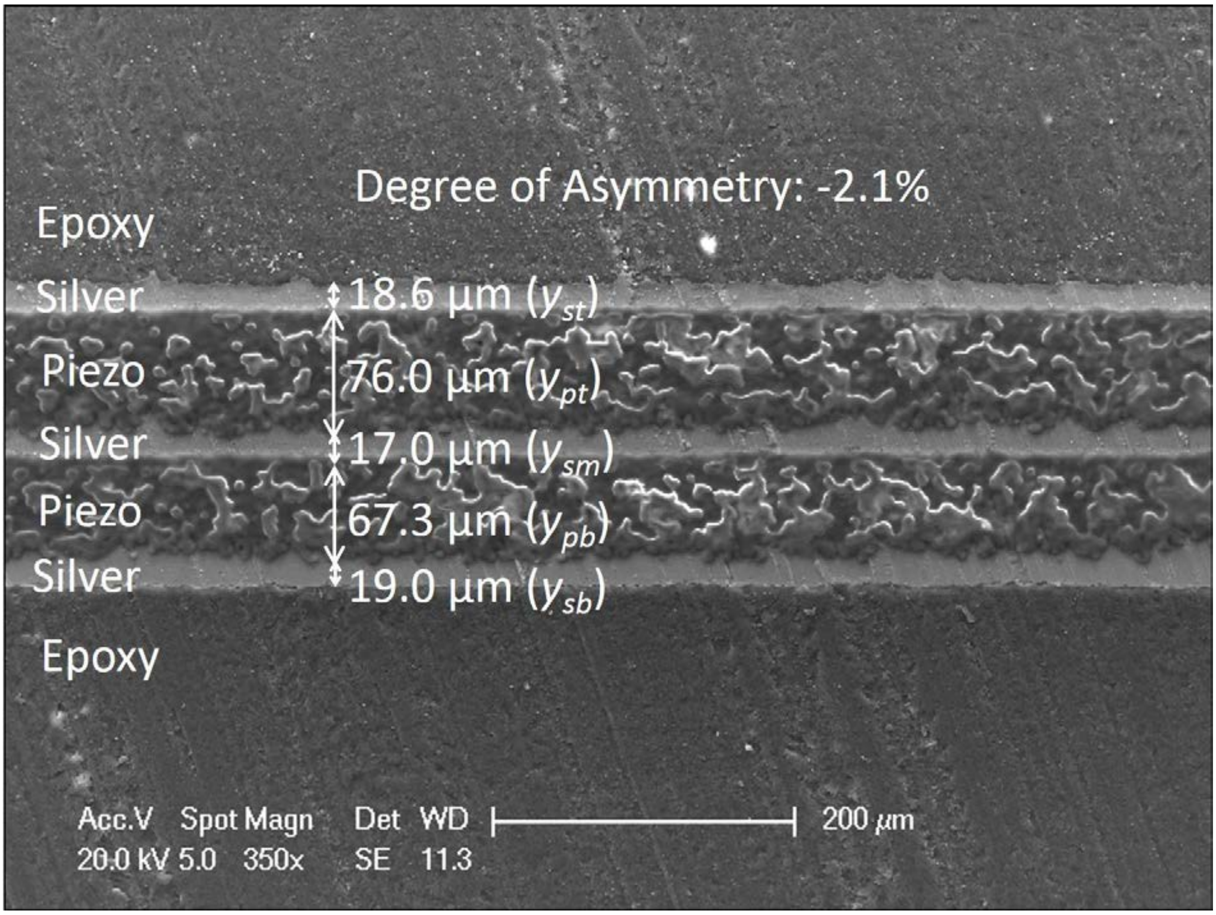

Figure 8-21. Cross-sectional SEM image with dimensional markers of a thickness-controlled cantilever.

Table 8-9 summarises the calculated values of density and Young's modulus of the piezoelectric and silver thick-film layers, which were used in the following validations and modelling. For the silver layer, both the density and Young's modulus are about 57 % of the bulk silver metal (10.49 g/cm^3 and 83 GPa, respectively)[9]. This may be because the silver layer was not fully densified during co-sintering with the piezoelectric layers. The piezoelectric layer is considered much softer than the bulk ceramics (for a commercial 'soft' PZT TRS 610, the Young's modulus is 69 GPa[10]), assuming the bulk PZnN-P3LZT ceramics exhibit similar mechanical properties to 'soft' PZT (according to similar compositions as well as densities shown in Figure 7-4). The piezoelectric layer is also softer than the reported screen-printed 'soft' PZT thick-films co-sintered with alumina[11] or silicon[12] substrates (calculated Young's modulus of 52±8 GPa[11] and 54±4 GPa[12] respectively). This may be due to larger porosity of the proposed thick-films, or the errors generated with the calculation methods used for the films attached with substrates. Corresponding to the supposed larger porosity, the density of the piezoelectric layer is about 69 % of their bulk counterparts (shown in Figure 7-4).

Table 8-9. Summary of calculated values of density and Young's modulus of the piezoelectric and silver thick-film layers.

	Piezoelectric Layer	**Silver Layer**
Density (g/cm^3)	5.01 ±0.02	5.98 ±0.29
Young's Modulus (GPa)	19.4 ±1.7	47.1 ±1.2

8.4.1.2 Validation and Modelling Results

Once the Y_s was obtained, Equations 4-2, 4-5, 4-4 and 4-5 were combined to calculate the theoretical resonant frequencies of 9 other cantilevers (M1-M9) fabricated with controlled thickness, and which were then compared with the actual measured resonant frequency values. The calculations and measurements were again based on the open-circuit electric condition and 0.5g acceleration. Figure 8-22 and Figure 8-23 shows the comparisons of the predicted and measured resonant frequencies of each sample, marked with free-standing length (L), cantilever width (w) and tip mass (M). It can be seen that the calculated frequencies did not exactly match the measured values, however, the deviation was smaller than 1.5 %. These deviations might result from a number of reasons. Firstly, despite the improved fabrication procedures noted above, the structures were not perfectly symmetric, which might affect the applicability of the beam theory. This effect should be minor because the asymmetry shown in Figure 8-21 is only -2.1 % (< ±5 % as discussed above) and relevant calculations were based on an improved model

(Equation 8-4). Secondly, both the density and the Young's modulus of each layer had non-negligible deviations according to Table 8-9, which could also affect the peak positions to some extent. The largest deviation in Table 8-9 occurs on the Young's modulus of piezoelectric layer, reaching ±8.8 %. However, as in Equation 4-2 the frequency is shown positively related to square root of Young's modulus whilst negatively related to square root of density, the deviations of other data (±0.4 %, ±4.8 % and ±2.5 %) are able to more or less compensate the large deviation of ±8.8 %. Finally, for convenience in the calculations it was assumed that all the layers in a cantilever had equal length and width. However, as also noted above, the bottom electrode was in fact shorter, which introduced small errors to the real mechanical status. As (a) it has been discussed in Section 8.3.2 that the very tip of the cantilever may not bend much, (b) in the real configuration the part where silver is absent was fulfilled by excessive piezoelectric components (shown in Figure 6-1 (c)), and (c) densities of the silver and piezoelectric layers are similar (Table 8-9), this should also be a minor influence. Therefore, the second reason, deviations of material properties, may have the most significant contribution to the errors. This is similar to the discussion in Section 8.3.1.

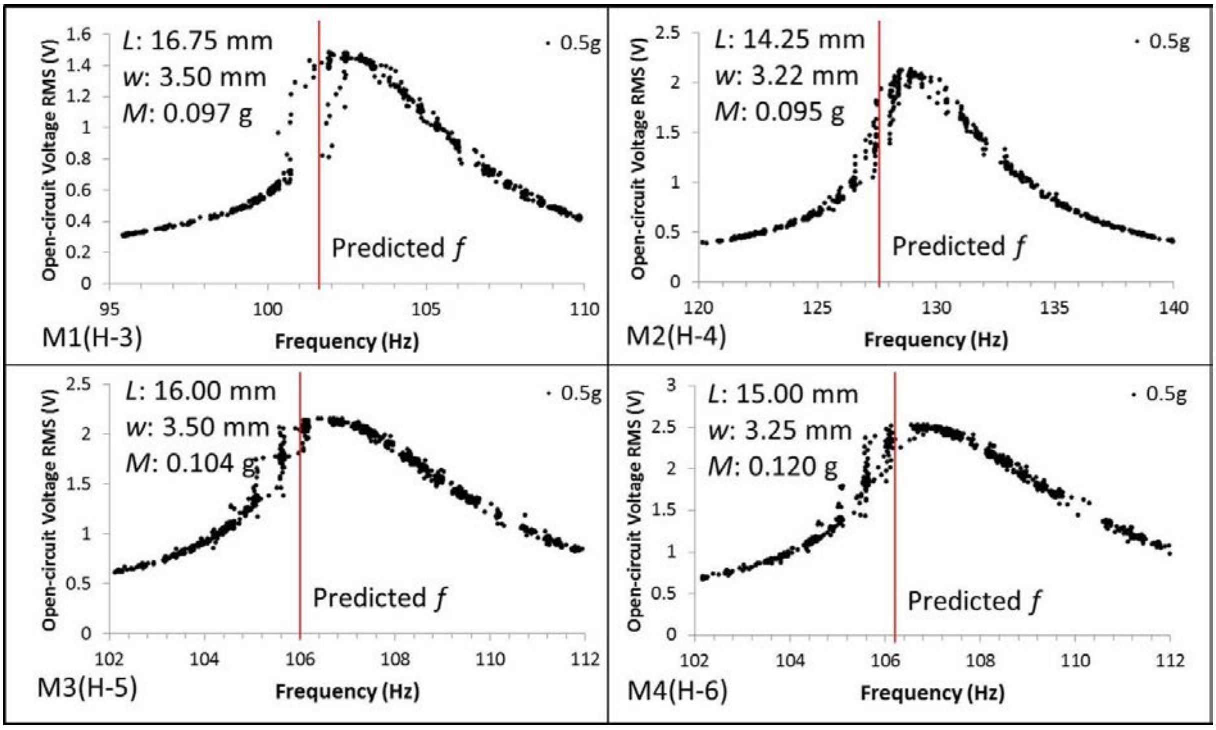

Figure 8-22. Dependence of RMS open-circuit voltage on input frequency for cantilevers (samples M1-M4) with marked predicted resonant frequencies (L – free-standing length, w – cantilever width, M – tip mass).

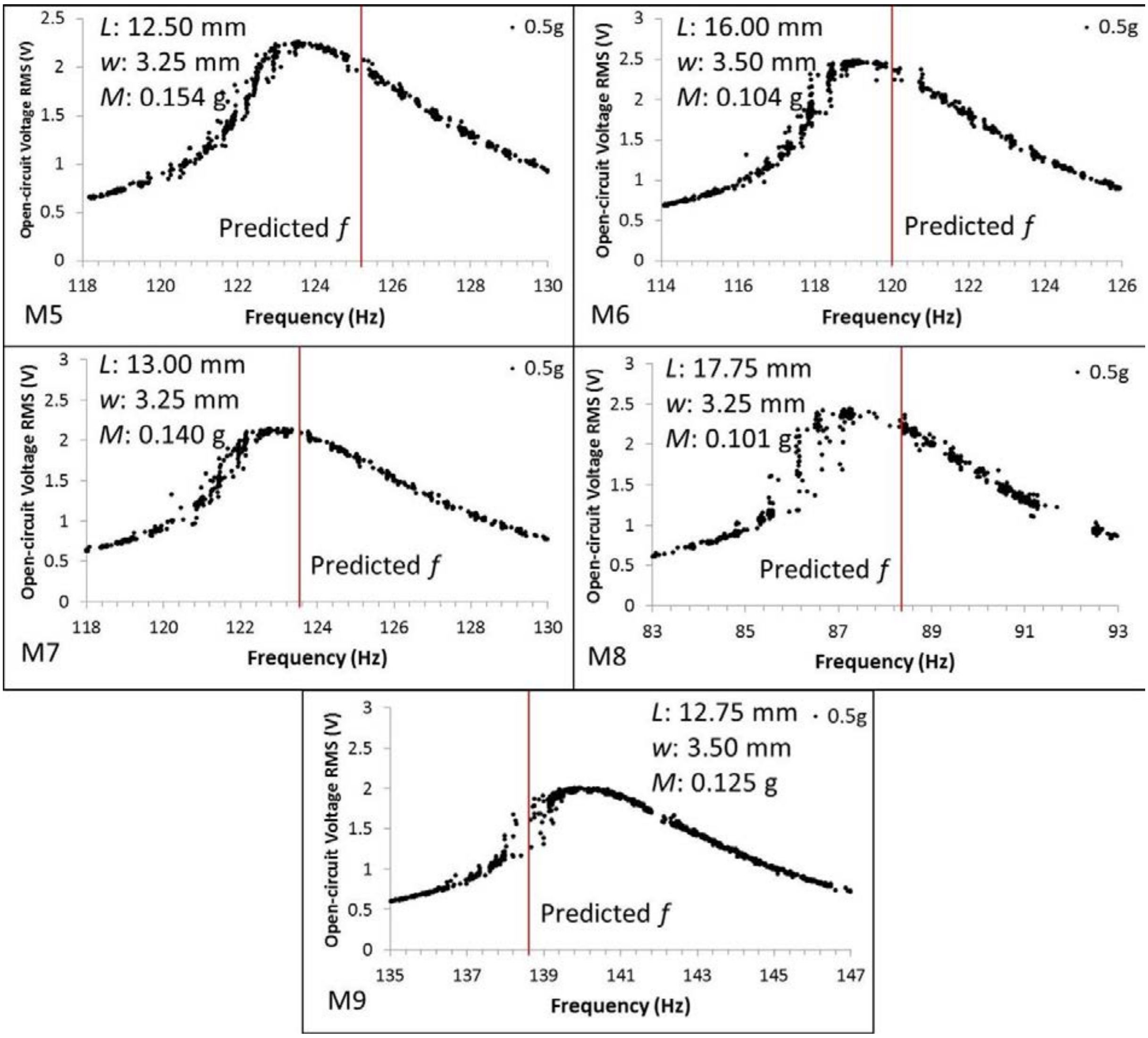

Figure 8-23. Dependence of RMS open-circuit voltage on input frequency for cantilevers (samples M5-M9) with marked predicted resonant frequencies (L – free-standing length, w – cantilever width, M – tip mass).

However, although the predicted frequencies did not precisely and perfectly match the peaks of the open-circuit voltage, this modelling method was still reliable enough for designing energy harvester arrays, as the outputs at the predicted resonant frequencies were at least 80 % of the peak values. Considering the relatively wide bandwidth of the proposed individual harvester (> 5 %), the tolerance of using such modelling method to properly design harvester arrays was acceptable.

A further implementation of this modelling method is shown in Figure 8-24, where the effect of tip mass and cantilever length have been explored. A cantilever width in the range of 3.0-3.5 mm was proved appropriate to both ensure better output performance and avoid ceramic cracks after sintering. Therefore, the modelling in Figure 8-24 was taken with the width of 3.25 mm, and no further modelling on the effect of bimorph width was undertaken. Based on Figure 8-24, energy harvester arrays could then be designed by selecting appropriate length and tip mass combinations to fit the required frequencies.

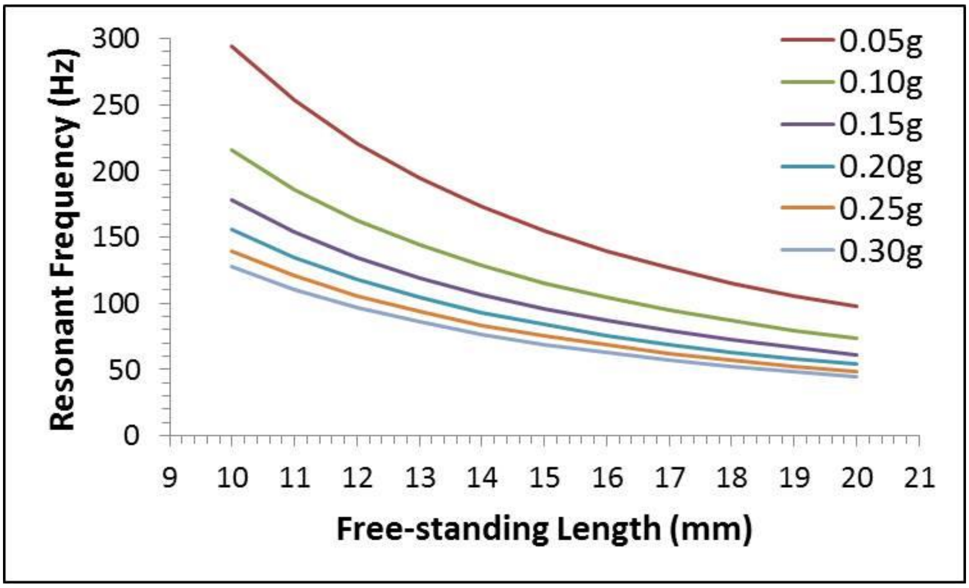

Figure 8-24. Dependence of theoretical resonant frequency on free-standing length for the individual harvesters of 3.25 mm width and 198 μm thickness (19-76-17-67-19 μm from top layer to bottom layer) with different tip masses.

8.4.2 Harvester Array Integration and Vibration Test

Two sets of harvester arrays were designed, fabricated, integrated and tested, of which the information of dimensions, tip masses and designed frequencies was summarised in Table 8-10. Array A1 was designed for a triple-peak response with split resonant frequencies, which suited the environment where several main vibrations co-exist. Array A2 targeted on a wide bandwidth response, where three peaks partially overlapped each other at the frequencies of half maximum outputs, which could fit the circumstance containing a single main frequency but where noises around the main frequency also exist. The two piezoelectric layers of each single element (A1-1 to A1-3, A2-1 to A2-3) were poled in parallel while connected in series.

Table 8-10. Summary of the dimensions, tip masses and designed frequencies of the harvester arrays.

Array ID	**Single-element Harvester ID**	**Free-standing Length (mm)**	**Width (mm)**	**Tip Mass (g)**	**Designed Frequency (Hz)**
A1	A1-1	15.65	3.25	0.10	108
	A1-2	15.15	3.25	0.08	125
	A1-3	13.10	3.25	0.10	142
A2	A2-1	12.45	3.25	0.15	128
	A2-2	12.05	3.25	0.15	134
	A2-3	13.25	3.25	0.10	140

Figure 8-25 shows the picture of integrated array A1. Figure 8-26 shows the harmonic vibration response of arrays A1 and A2, where the positions of half maximum and designed resonant frequencies are also marked. For both arrays, the resonant frequencies with 0.5g acceleration fitted the original design very well. However, the resonant frequencies slightly increased with the decrease of acceleration, resulting in larger errors when comparing the designed resonant frequencies to the corresponding measured frequencies at peak positions with 0.1g and 0.3g acceleration. Considering the FWHM with 0.5g acceleration as a criterion, array A1 could work effectively (open-circuit voltage above 1.5 V) in the frequency ranges of 106-112 Hz, 124-130 Hz and 140-146 Hz, whilst array A2 possessed a bandwidth of about 14 % where the open-circuit voltage remained above 1.4 V compared to 5-6 % for the individual harvesters.

Such outcomes proved the feasibility of the proposed harvesters for development of wideband devices.

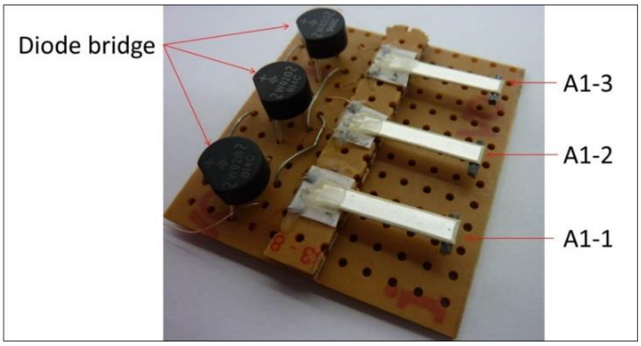

Figure 8-25. Picture of array A1.

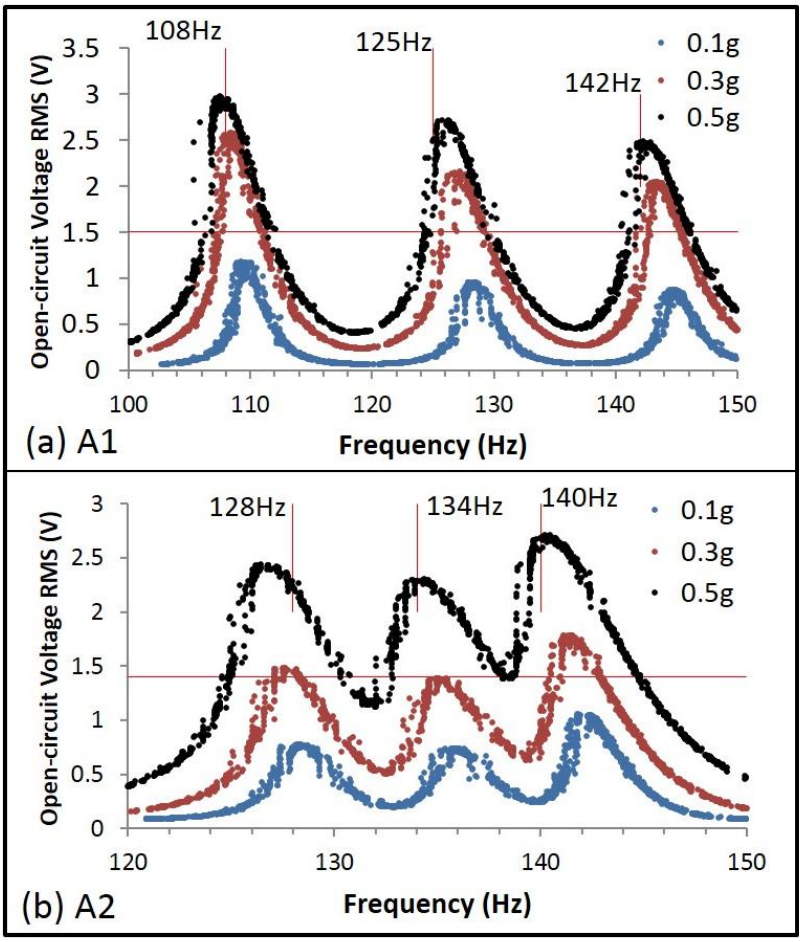

Figure 8-26. Dependence of RMS open-circuit voltage on frequency for arrays A1 and A2 vibrating with different accelerations (marked with half maximum and designed resonant frequencies).

8.5 Other Energy Harvesters Based on Free-standing Structure

In order to further discover the feasibility and compatibility of the proposed configuration (free-standing thick-film bimorph), two individual harvesters (H-3 and H-5) were integrated with a computer fan (070010A, Intel, UK), in order to harvest wind energy (air flow). The internal permanent magnets of the fan were removed in order to reduce the start wind speed limit (i.e. to make the fan free-spinning in wind). The removed magnets were cut into small patches (approximately 5×3×2 mm^3) and attached to the edges of the blades with super glue. Also, another type of permanent magnet (Neodymium-Iron, Swift Levick Magnet Ltd., UK) was ground into flakes, and small pieces (about 0.03g) were attached on the tip mass of each individual harvester so that, repulsive magnet forces would be induced between the magnets on the blades and on the harvester tips. Similar to the harvester arrays, the two individual harvesters were fixed on a piece of test circuit board (about 5×1 cm^2) and connected to two diode bridge rectifiers. Finally, the circuit board was mounted on the frame of the fan, keeping the distance between the magnets on the tips and on the blades at approximately 2 mm. Figure 8-27 shows the schematics and pictures of the integrated device, which was intended to collect wind energy and transfer it into electricity (named as wind harvester).

When being tested, the wind harvester was connected to the vibration test system presented in Chapter 6, however only the data acquisition and computer program were utilised to monitor and record data, while the driving component was replaced by an electric fan (HT-800E, Honeywell, USA) which provided air flow (energy source) to the harvester. By adjusting the distance between the fan and the harvester, the direction of the air flow as well as the switch position that controlled the wind speed, the optimum output was discovered.

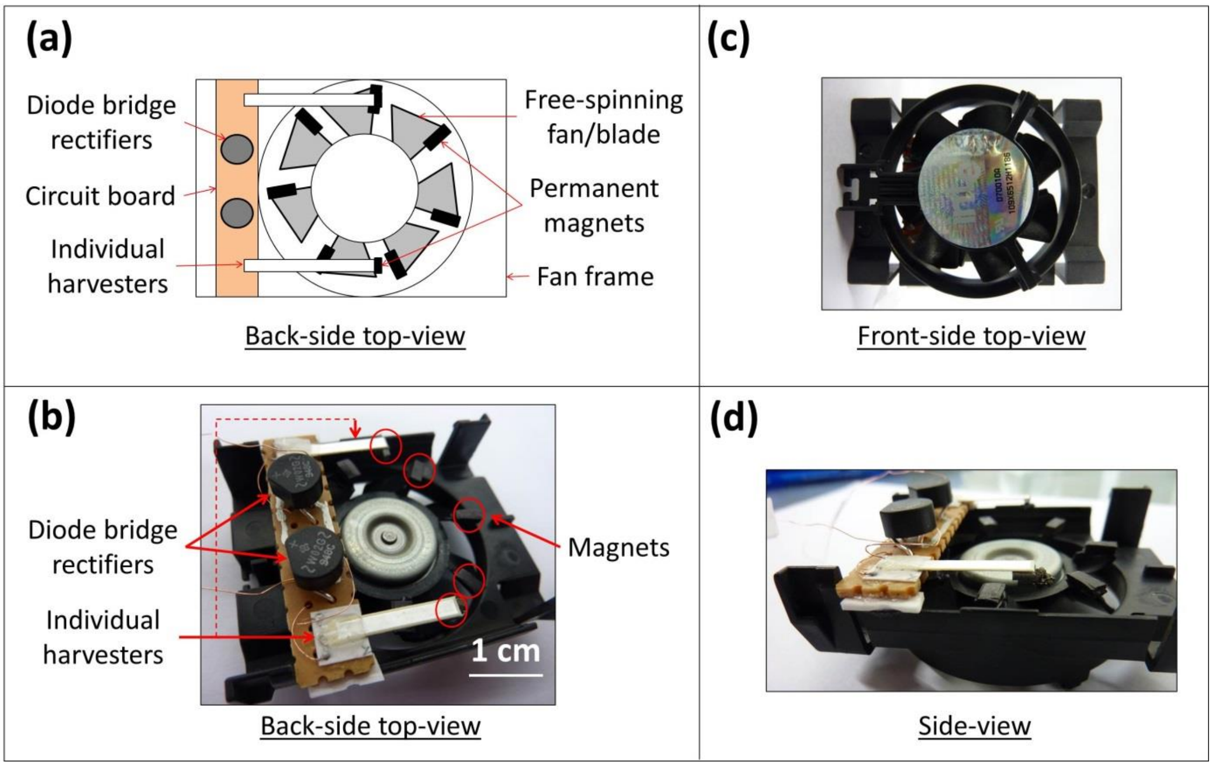

Figure 8-27. (a) Schematic and (b), (c) and (d) pictures of the integrated wind energy harvester.

Figure 8-28 shows the instantaneous open-circuit voltage of the harvester and the charging behaviour of a 1000 μF capacitor connected to the harvester. An average open-circuit voltage of about 3.4 V was generated according to Figure 8-28 (a). This is comparable with the optimised output voltage (1.0 V and 2.4 V) with best matched resistive loads and wind speed of two of the reported designs based on contacting type piezoelectric wind harvesters[13] (presented in Figure 4-12). In Figure 8-28 (b) a stable charging rate of 30-50 mV/min was obtained in 4 consecutive tests, which is comparable with the charging rates obtained on harvester H-3 under harmonic vibration (Figure 8-19). Further optimisations of such a design can be expected with dynamically improved fan, enhanced magnetic coupling, low-power management circuitry, as well as with optimised the individual energy harvesting elements (free-standing thick-film cantilevers). This showed that the proposed free-standing piezoelectric thick-film structure was not only able to harvest vibration energy, but also compatible with harvesting energy from other sources, such as wind energy, with the appropriate supporting configurations.

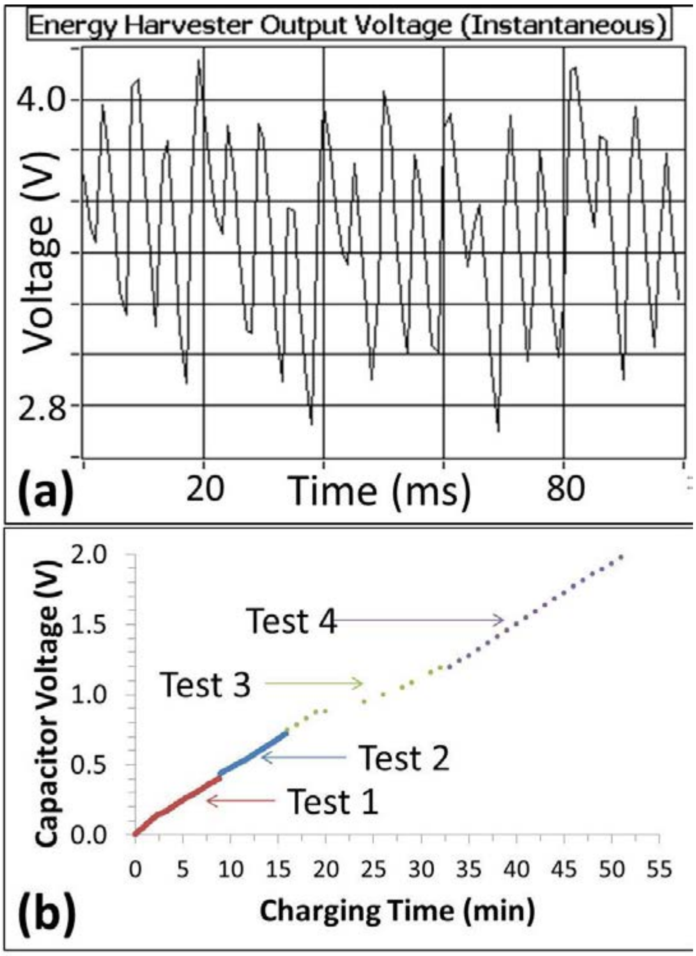

Figure 8-28. (a) Dependence of instantaneous open-circuit voltage on real time (b) dependence of capacitor voltage on charging time for the wind harvester tested on the optimum air flow condition.

References

1 Kok, S.-L., White, N. M. and Harris, N. R. Fabrication and characterization of free-standing thick-film piezoelectric cantilevers for energy harvesting. *Measurement Science and Technology* **20**, 124010 (2009).

2 Roundy, S., Leland, E. S., Baker, J. *et al.* Improving power output for vibration-based energy scavengers. *IEEE Pervasive Computing* **4**, 28-36 (2005).

3 Cho, J., Anderson, M., Richards, R., Bahr, D. and Richards, C. Optimization of electromechanical coupling for a thin-film PZT membrane: II. Experiment. *Journal of Micromechanics and Microengineering* **15**, 1804-1809 (2005).

4 Bai, Y., Meggs, C. and Button, T. W. Investigation of Using Free-standing Thick-film Piezoelectric Energy Harvesters to Develop Wideband Devices. *International Journal of Structural Stability and Dynamics* **14**, 1440016 (2014).

5 Abdelkefi, A., Najar, F., Nayfeh, A. H. and Ben Ayed, S. An energy harvester using piezoelectric cantilever beams undergoing coupled bending-torsion vibrations. *Smart Materials & Structures* **20**, 115007 (2011).

6 Szarka, G. D., Stark, B. H. and Burrow, S. G. Review of Power Conditioning for Kinetic Energy Harvesting Systems. *IEEE Transactions on Power Electron.* **27**, 803-815 (2012).

7 Kim, H. S., Kim, J. H. and Kim, J. A Review of Piezoelectric Energy Harvesting Based on Vibration. *International Journal of Precision Engineering and Manufacturing* **12**, 1129-1141 (2011).

8 Sodano, H. A., Inman, D. J. and Park, G. Generation and storage of electricity from power harvesting devices. *Journal of Intelligent Material Systems and Structures* **16**, 67-75 (2005).

9 en.wikipedia.org/wiki/Silver [online access] 17/12/2014.

10 www.trstechnologies.com [online access] 16/04/2014.

11 Walter, V., Delobelle, P., Le Moal, P., Joseph, E. and Collet, M. A piezo-mechanical characterization of PZT thick films screen-printed on alumina substrate. *Sensors and Actuators A-Physical* **96**, 157-166 (2002).

12 Park, J. H., Kwon, T. Y., Yoon, D. S., Kim, H. and Kim, T. S. Fabrication of microcantilever sensors actuated by piezoelectric Pb(Zr0.52Ti0.48)O-3 thick films and determination of their electromechanical characteristics. *Advanced Functional Materials* **15**, 2021-2028 (2005).

13 Myers, R., Vickers, M., Kim, H. & Priya, S. Small scale windmill. *Applied Physics Letters* **90**, 054106 (2007).

CHAPTER 9. CONCLUSIONS AND FUTURE WORK

9.1 Conclusions

In Chapter 5 a number of aims and objectives for the project were set out. It now remains to summarise to what extent these have been achieved.

Bulk ceramic samples made from traditional ‘soft’ PZT and two other lead-based piezoelectric compositions (3 mol% and 5 mol% La-doped PZnN-PZT) have been fabricated and characterised. The calcined ceramic powders exhibit perovskite structures as expected (tetragonal for the PZT, tetragonal and rhombohedral for the two types of La-doped PZnN-PZT) and particle sizes suitable for ceramic fabrication (D_{50} ranging from 1 μm to 3 μm). The bulk ceramic samples have achieved >90 % theoretical densities and exhibited 15-17 % linear shrinkage, with 1-3 μm grain sizes. The perovskite phases in the powders have been maintained in the bulk sintered ceramics. Also, ferroelectric-paraelectric phase transitions (Curie temperatures) have been found in the range of 325-425 °C (for the PZT) and 350-400 °C (for the two types of La-doped PZnN-PZT), which is consistent with other reports. Optimum dielectric and piezoelectric properties are summarised in Table 9-1 for the PZT samples sintered at 1200 °C and the 3 mol% and 5 mol% PZnN-PZT samples sintered at 1230-1250 °C. The data for the PZT samples are consistent with those in the literature, and the 5 mol% La-doped PZnN-PZT samples have shown similar dielectric and piezoelectric properties to the PZT. However, it has been suggested that with larger g_{33} but smaller $d_{33}{\cdot}g_{33}$ values, the 3 mol% La-doped PZnN-PZT composition should be more suitable for vibrational energy harvester applicaions being able to generate higher open-circuit voltage but with a lower energy density than PZT and 5 mol% La-doped PZnN-PZT. In addition, the 3 mol% La-doped PZnN-PZT ceramics have shown a slower aging rate compared to their PZT and 5 mol% La-doped PZnN-PZT counterparts.

Bulk ceramic samples made from a lead-free composition, $(Ba_{0.85}Ca_{0.15})(Zr_{0.1}Ti_{0.9})O_3$, have also been fabricated and characterised. With particle size of about 4.6 µm (D_{50}), the calcined ceramic powder had a two-phase perovskite structure. The phases have been identified as tetragonal and orthorhombic, confirming recently published phase diagram studies, rather than tetragonal and rhombohedral phases reported previously. These phases are retained in the sintered ceramics. Three phase transitions have been observed with increasing temperature, which are a rhombohedral-orthorhombic transition at about -5 °C, an orthorhombic-tetragonal transition at about 23 °C, and a tetragonal-cubic transition at about 88 °C (the Curie temperature). This is also consistent with recent literature and with what is essentially a doped $BaTiO_3$ composition. The sintered ceramics have >85 % theoretical densities, exhibit 12-14 % linear shrinkage, and have grain sizes in the range of 20-30 µm. Although the grain size is similar to that of pure $BaTiO_3$ ceramics, it is considered rather large compared to the PZT. Optimum dielectric and piezoelectric properties are shown in Table 10-1 for samples sintered at 1490 °C. However, the main drawback with this composition is the poor temperature stability due to the much lower Curie temperature compared to PZT and some other lead-free compositions. The poling regime has been shown to play a critical role in optimising functional properties as well as decreasing ageing rates. In general, the 50BCZT composition has exhibited comparable potential energy harvesting capability to PZT, especially for applications near room temperature.

Both the lead-based and lead-free compositions have been combined with borosilicate glass for liquid-phase low-temperature sintering. With 1 wt% glass addition, the lead-based compositions sintered at 900-950 °C and the lead-free composition sintered at 1200 °C have achieved approximately 70-80 % of the density values compared to their respective high-temperature sintered ceramics, and with similar phase structures to the corresponding ceramic powders. The dielectric and piezoelectric properties have been reduced compared to their high temperature sintered ceramic counterparts, and these are also shown in Table 9-1 for glass additions of 1 wt%. Increasing glass content further improves the sintered density, but the dielectric and piezoelectric properties are dramatically deteriorated. Although these low-temperature sintered samples have not exhibited the full properties of their high-temperature sintered counterparts, they have been considered sensible as the samples have not been able to be sintered at all at such low temperatures and exhibited no piezoelectric properties without the glass addition. Of the four investigated compositions, the 5 mol% La-doped PZnN-PZT composition has exhibited the largest overall reduction in properties as a result of low temperature sintering.

The PZT and 3 mol% La-doped PZnN-PZT with 1 wt% glass additions have been fabricated to printable inks. Single-layer free-standing piezoelectric thick-films have been fabricated via low temperature sintering and characterised. They have achieved approximately 70-90% of the densities of their high-temperature sintered bulk counterparts, and with the same perovskite phase structures and similar grain sizes. Both the PZT and 3 mol% La-doped PZnN-PZT thick-films exhibited larger d_{33}, d_{31}, g_{33}, g_{31} and k_{31} but smaller ε_r and Q_M compared to those in relevant literature as shown in Figure 9-2 for the PZT and 3 mol% La-doped PZnN-PZT samples sintered at 900 °C. Compared to each other, the 3 mol% La-doped PZnN-PZT thick-films used for vibrational energy harvesting are expected to generate higher open-circuit voltage and off-resonant output power than the PZT thick-films.

Multi-layer free-standing piezoelectric thick-films (unimorph and bimorph cantilevers) co-sintered with silver electrodes have been fabricated using the same process and tested as vibrational energy harvesters. It has been found empirically that only by maintaining a difference of 3 % to 6 % in the overall shrinkage of the silver (larger shrinkage) and the piezoelectric elements can a flat, free-standing thick-film cantilever, free from residual stress be obtained. Under harmonic vibrations, the 3 mol% La-doped PZnN-PZT unimorphs without tip proof masses generated larger open-circuit output voltage and output power density than the PZT unimorphs, matching with resistive loads at their individual resonant frequencies with different accelerations. The optimum average output power densities of the 3 mol% La-doped PZnN-PZT harvesters have been 900 % (0.1g), 68 % (0.5g), 73 % (1.0g) and 173 % (1.5g) better than those of the respective PZT harvesters. When compared to the relevant reported data, the advantages have even approached to 25 % (0.1g), 92 % (0.5g) and 121 % (1.0g). The 3 mol% La-doped PZnN-PZT bimorphs poled in series but connected in parallel and without tip proof mass have been able to double the output power density of the unimorphs with half the resistive load. The optimum average output power density of the bimorphs without any structural or electrical optimisation has been approximately 147±7 $\mu W/cm^3$, vibrating at resonant frequencies of 610-625 Hz with 1.5g acceleration. A structure incorporating a shorter bottom electrode has not had any apparent effect on the overall open-circuit voltage, but does reduce the overall measured output power with resistive loads. The theoretical relations between harvester performance and material properties have also been confirmed and validated. For the bimorph energy harvesters with tip proof masses and with series connection, an optimum average open-circuit output voltage of approximately 2.8 V has been achieved at 127 Hz with 1.0g acceleration. And for those with parallel connection, an optimum average output power of about 9 μW has been obtained at 129 Hz with 1.0g acceleration and 470 kΩ resistive load. The maximum peak to peak tip displacements of the bimorphs with tip masses have reached 1200 μm. All of the above data have been 5-10 times higher than those of the bimorphs without tip masses. Also, a novel configuration with asymmetrical tip mass attachment has shown nonlinear behaviour and the potential to widen bandwidth.

Resonant frequencies of the individual energy harvesters have been analysed and modelled. The errors caused by predicted and measured resonant frequencies have been validated < 1.5 %.

Table 9-1. Summary of the optimum dielectric and piezoelectric properties of the high-temperature and low-temperature sintered bulk samples.

Composition	**Sintering Temp. (°C)**	ε_r	$tan\delta$	d_{33} **(pC/N)**	g_{33} **(Vm/N)**	$d_{33}\cdot g_{33}$ **(×10^{-12} m^2/N)**	k_p	Q_M
PZT	1200	2300	0.024	500	0.025	12.5	0.51	42
	900-950	690		95-120	0.020	4.5-4.9		44-48
PZnN-P3LZT	1230-1250	1100	0.026	300	0.031	9.3	0.49	75
	900-950	286-352		80	0.267-0.031	2.1-2.4		29-48
PZnN-P5LZT	1230-1250	2900	0.024	590	0.023	13.6	0.60	40
	900-905	348-464		80	0.020-0.025	1.6-1.9		41-43
BCZT	1490	4700	0.015	630	0.015	9.5	0.56	90
	1200	1175-1410		176-220	0.017	3.1-5.3		96-114

Table 9-2. Summary of the optimum dielectric and piezoelectric properties of the thick-films sintered at 900 °C.

Composition	ε_r	d_{33} **(pC/N)**	d_{31} **(pC/N)**	g_{33} **(Vm/N)**	g_{31} **(Vm/N)**	k_{31}	Q_M
PZT	383	168	97	0.049	0.029	0.20	32
PZnN-P3LZT	328	177	102	0.061	0.035	0.026	19

Based on such a modelling process, individual harvesters and wideband harvester arrays with specific resonant frequencies have been designed, fabricated and tested. The individual harvesters with series connection have been able to charge a 1000 μF capacitor with an average charging rate of 30 mV/min at resonant frequencies with 0.5g acceleration. The wideband harvester arrays have exhibited a bandwidth of about 14 % across the designed resonant frequencies, which is much wider than that of the individual harvesters and advantageous compared to those in relevant literatures. A harvester prototype incorporating the individual harvesters, a free-spinning fan and permanent magnets for the application of harvesting wind energy has also been fabricated and tested. It has shown a possibility of using piezoelectric energy harvesters to harvest wind energy, with an average open-circuit output voltage of about 3.4 V and a charging rate of 30-50 mV/min when charging a 1000 μF capacitor under optimum wind conditions.

9.2 Future Work

More compositional optimisations need to be done in order to enhance the Curie temperature as well as the temperature stability of the 0.5BZT-0.5BCT composition. This would promote such lead-free materials to substitute traditional PZT in a wider range of applications. The issue could be solved by introducing compositions with much higher Curie temperatures, e.g. $BiFeO_3$, thus compensating for the low Curie temperature of 0.5BZT-0.5BCT. However, according to previous experience, this modification would probably result in inferior dielectric/piezoelectric properties. Therefore, how to balance the property and the temperature stability would be a new issue to be investigated. Trying to create nano-domain microstructures may be helpful to some degree.

As the sintering temperature of the 0.5BZT-0.5BCT composition has not been desirable for co-sintering with silver electrodes, two suggestions could be considered in order to further fabricate free-standing thick-film energy harvesters with such lead-free compositions. Firstly, other types of electrode materials could be used to replace silver, e.g. gold, platinum, etc. This may be the quickest method to solve the issue. However, the manufacturing cost would dramatically increase in such a method. Alternatively, an effort to select another sintering aid or develop nano-particles could be made, in order to further reduce the sintering temperature that could match the use of silver. According to the author's experience, Li_2O could aid sintering better than the commercial borosilicate glass, however the lowest sintering temperature was still much higher than 950 °C. Thus a combination of two or more sintering aids could be considered. However, as the introduction of more sintering aid may deteriorate the piezoelectric properties further, the development of nano-particles seems more promising, where no sintering aid would be needed.

Although the harvesters have been proved functional to harvest vibration energy, the absolute output power was not enough to directly power any sensor node, in spite of the reasonable open-circuit voltage and output power density. Therefore, either energy generation ability or energy conversion efficiency (or both) needs to be improved. Energy generation ability could benefit from multi-morph structures and/or higher relevant material properties. In particular, multi-morph structures could be achieved by applying a more automatic deposition process, such as screen printing and tape casting, which may reduce the fabrication complexity as well as ensure high production quality. And higher material properties would rely on qualities of the films, which is in fact a joint issue of the compositional optimisation and low-temperature sintering investigation presented above. Use of high-quality interdigitated electrodes may also be helpful in realising different design concepts. Energy conversion efficiency is a more complex factor, which would be affected by material properties, mechanical configurations and electric circuitry. This may need a collaborative investigation by researchers from different backgrounds. Also, the durability of the harvesters needs to be understood through tests with various environmental conditions (e.g. temperature, vibration type/level) and time scales.

In addition, more accurate mathematic models with a broader applicability could be developed, in order to precisely predict not only working frequencies but also outputs of the proposed energy harvesters.

Lastly, as the proposed harvesters have shown a good compatibility, other possibilities could be explored in order to harvest fluidic, thermal, or magnetic energy, etc., of which the principles have been presented in Chapter 4.

APPENDIX I. ACTUAL AMOUNT OF RAW POWDERS ADDED FOR INITIAL SYNTHESES

1. Lead-based Compositions

Raw Materials (Unit: g)	PZnN-P3LZT	PZnN-P5LZT
PbO	68.9583	68.5895
ZnO	2.0434	2.0325
Nb_2O_5	6.6469	6.6114
La_2O_3	1.1099	1.8400
ZrO_2	15.2649	14.6311
TiO_2	8.0884	8.4027

2. Lead-free Composition

Raw Materials (Unit: g)	$BaZrO_3$	50BCZT
$BaCO_3$	16.1480	28.4705
ZrO_2	10.0000	N/A
$BaZrO_3$	N/A	5.3086
$CaCO_3$	N/A	2.8879
TiO_2	N/A	13.7023

APPENDIX II. COMPUTER PROGRAM WRITTEN IN LABVIEW FOR VIBRATION TEST OF THE ENERGY HARVESTERS

1. Flow Chart of Program

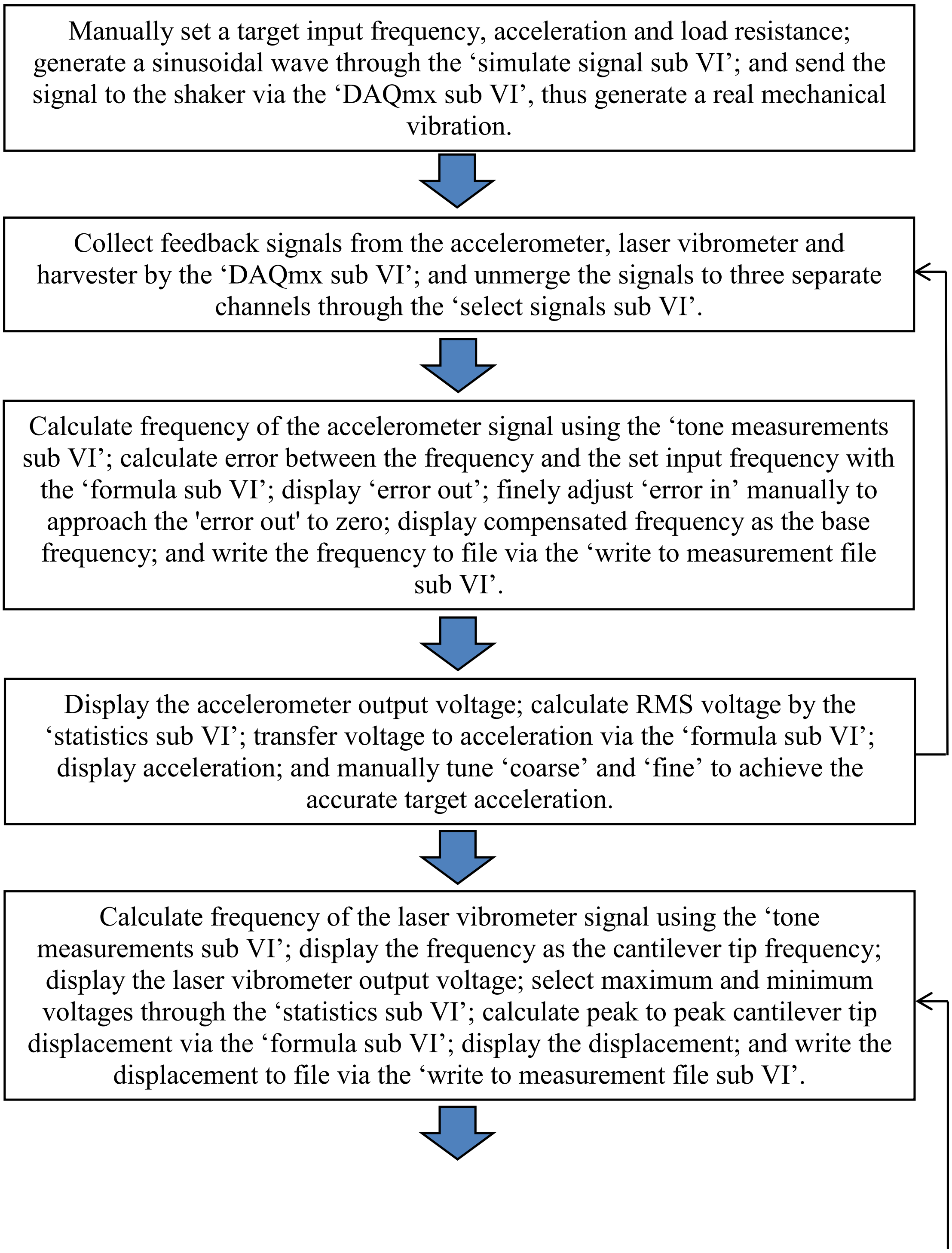

Manually set a target input frequency, acceleration and load resistance; generate a sinusoidal wave through the ‘simulate signal sub VI’; and send the signal to the shaker via the ‘DAQmx sub VI’, thus generate a real mechanical vibration.

Collect feedback signals from the accelerometer, laser vibrometer and harvester by the ‘DAQmx sub VI’; and unmerge the signals to three separate channels through the ‘select signals sub VI’.

Calculate frequency of the accelerometer signal using the ‘tone measurements sub VI’; calculate error between the frequency and the set input frequency with the ‘formula sub VI’; display ‘error out’; finely adjust ‘error in’ manually to approach the 'error out' to zero; display compensated frequency as the base frequency; and write the frequency to file via the ‘write to measurement file sub VI’.

Display the accelerometer output voltage; calculate RMS voltage by the ‘statistics sub VI’; transfer voltage to acceleration via the ‘formula sub VI’; display acceleration; and manually tune ‘coarse’ and ‘fine’ to achieve the accurate target acceleration.

Calculate frequency of the laser vibrometer signal using the ‘tone measurements sub VI’; display the frequency as the cantilever tip frequency; display the laser vibrometer output voltage; select maximum and minimum voltages through the ‘statistics sub VI’; calculate peak to peak cantilever tip displacement via the ‘formula sub VI’; display the displacement; and write the displacement to file via the ‘write to measurement file sub VI’.

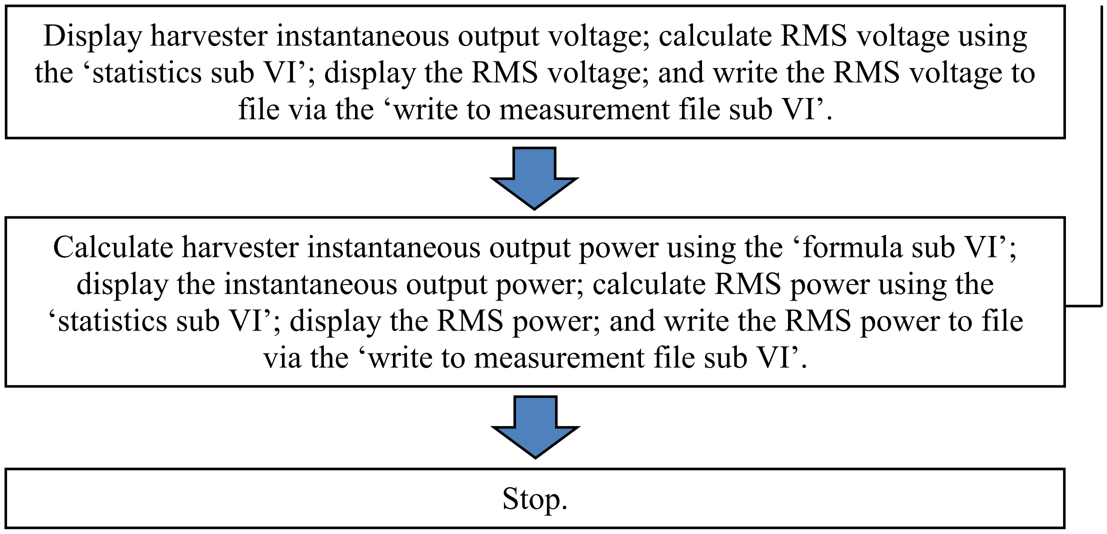

Display harvester instantaneous output voltage; calculate RMS voltage using the ‘statistics sub VI’; display the RMS voltage; and write the RMS voltage to file via the ‘write to measurement file sub VI’.

Calculate harvester instantaneous output power using the ‘formula sub VI’; display the instantaneous output power; calculate RMS power using the ‘statistics sub VI’; display the RMS power; and write the RMS power to file via the ‘write to measurement file sub VI’.

Stop.

NB: all of the sub VIs used were integrated in the software.

2. Front Panel of Main Program

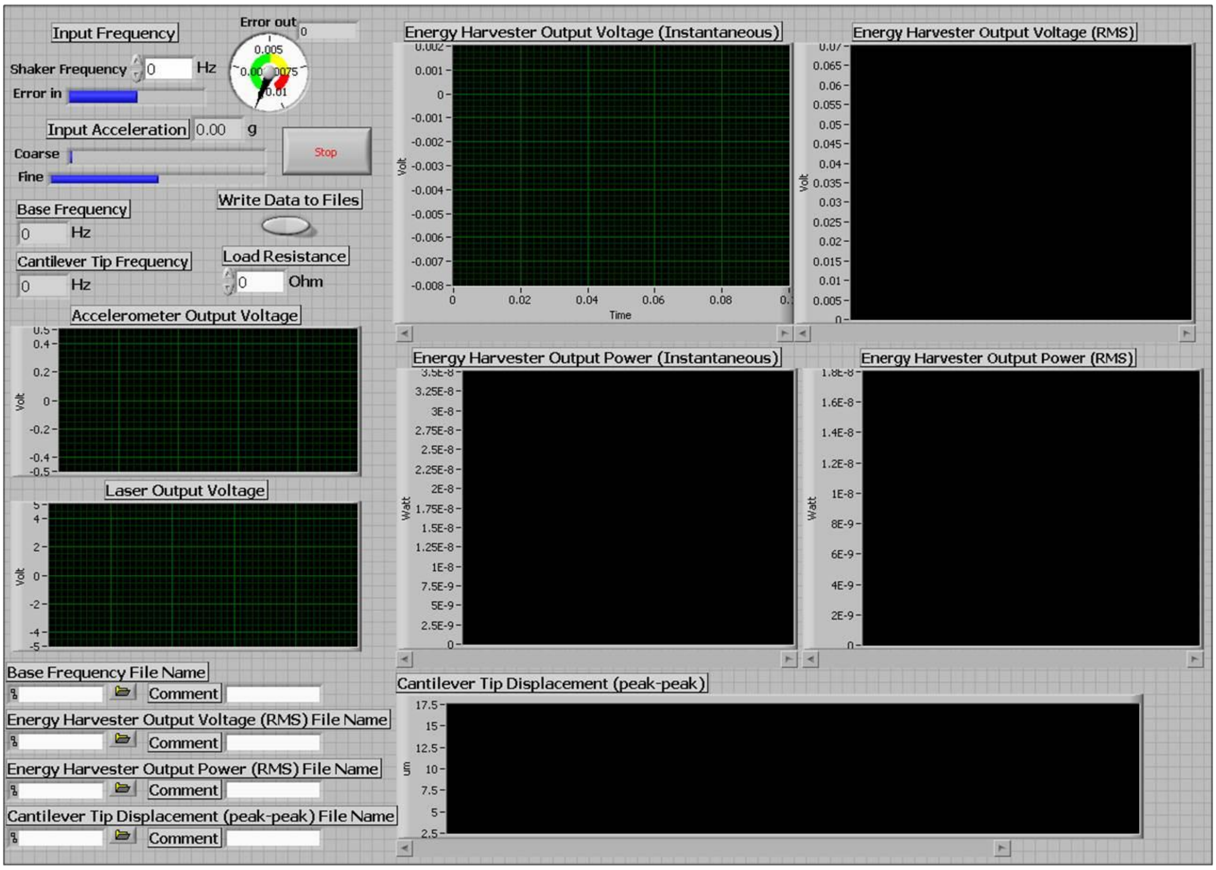

3. Block Diagram of Main Program

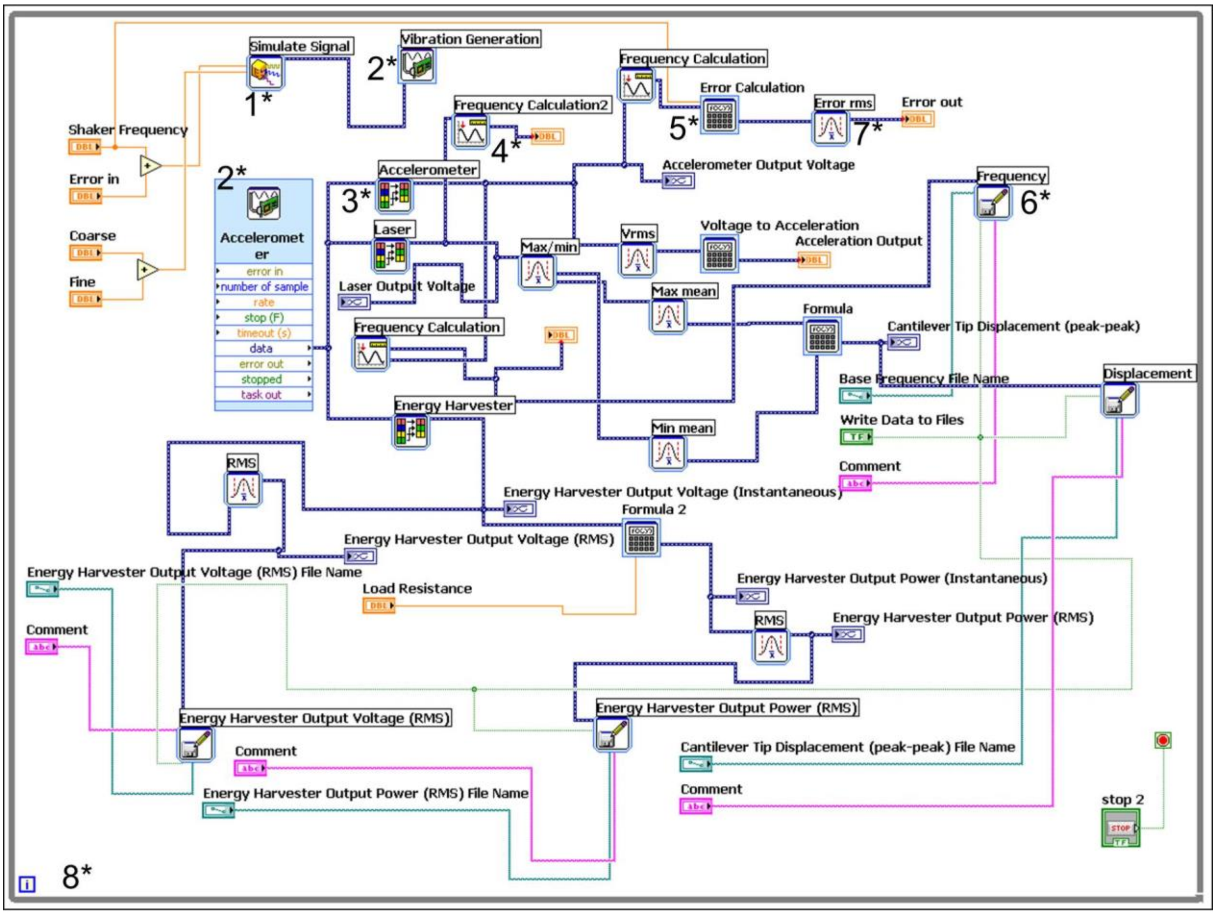

1*: simulate signal sub VI;

2*: DAQmx sub VI;

3*: select signals sub VI;

4*: tone measurements sub VI;

5*: formula sub VI;

6*: statistics sub VI;

7*: write to measurement file sub VI;

8*: while loop.

4. Equations Used in Formula Sub VIs

Error calculation:

$$\text{error} = \frac{\text{set frequency} - \text{accelerometer frequency}}{\text{set frequency}}$$

Acceleration calculation:

$$\text{Acceleration} = \frac{\text{RMS accelerometer output voltage} \times 1000}{98}\ (g), g \approx 9.8\ m/s^2$$

Peak-peak displacement calculation:

$$\text{Displacement} = (\text{maximum } - \text{minimum laser output voltage}) \times 100\ (\mu m)$$

Instantaneous output power calculation:

$$\text{Power} = \frac{\text{harvester instantaneous output voltage}^2}{\text{load resistance}}\ (W)$$

PUBLISHED PAPERS

International Journal of Structural Stability and Dynamics
Vol. 14, No. 8 (2014) 1440016 (12 pages)

DOI: 10.1142/S0219455414400161

Investigation of Using Free-Standing Thick-Film Piezoelectric Energy Harvesters to Develop Wideband Devices

Yang Bai[*,‡], Carl Meggs[*,§] and Tim W. Button[*,†,¶]

[*]*School of Metallurgy and Materials, University of Birmingham*
Birmingham, B15 2TT, United Kingdom

[†]*Central European Institute of Technology*
Brno, 616 00, Czech Republic
[‡]*YXB087@bham.ac.uk*
[§]*c.meggs@bham.ac.uk*
[¶]*t.w.button@bham.ac.uk*

Received 18 December 2013
Accepted 2 May 2014
Published 2 July 2014

This paper is concerned with the wideband behavior of single-frequency and multi-frequency free-standing thick-film piezoelectric energy harvesters. The energy harvesting devices have been fabricated and brief fabrication information is provided. The individual harvesters have been combined with either symmetric or asymmetric tip masses, with some being connected together to form a harvester array. Testing has been undertaken using harmonic vibrations with a wide range of frequencies and accelerations, and also using a random machinery vibration, and data have been recorded in terms of un-rectified and rectified open-circuit voltage, output power with matched resistive loads, peak-to-peak tip displacement, and even charging rates of capacitors. As a general result, the individual harvesters with asymmetric tip masses have vibrated nonlinearly below and in the vicinity of the resonant frequencies. An individual harvester vibrating at the resonant frequency with 0.5 g acceleration has been able to charge a 1000 μF capacitor to 1 V within 12 min and to 1.5 V within 30 min. Also, the harvester array has exhibited a wideband response, where an open-circuit voltage of above 0.8 V has been provided within a certain range of frequencies. Finally, the harvester array has successfully charged a capacitor on a vibrating test sieve shaker, proving the feasibility of the proposed device in real applications.

Keywords: Piezoelectric thick-film; array; wideband; nonlinear; charging capacitor; machinery vibration.

[‡] Corresponding author.

Fabrication and Investigation of Free-standing Piezoelectric Thick-film Cantilevers for Energy Harvesting Applications

Yang Bai[1], *Carl Meggs*[1], *Tim W Button*[1,2]
1 School of Metallurgy and Materials, University of Birmingham, Edgbaston, Birmingham, UK
Corresponding author: Tim W Button, e-mail address: t.w.button@bham.ac.uk
2 Central European Institute of Technology, Brno, Czech Republic

Abstract:

Free-standing thick-film cantilevers with a silver/piezoelectric multi-layer bimorph structure for use as vibration energy harvesters are presented. The use of silver electrodes has decreased the material cost of each harvester compared to Au, Pt or Ag/Pd, and a self-synthesized new lead-based piezoelectric composition has been applied, in order to compensate for the poorer properties of traditional soft PZT thick-films than those of their bulk ceramic counterparts. Also, the redundant supporting layers and substrates have been removed, reducing the total volume and enabling the realization of the simplest structure. Output power densities of the harvesters have been tested subsequently so that the advantages have been practically proved. Finally the modeling and further applications based on the structure have been proposed.

Key words: free-standing, thick-film, energy harvesting, silver electrode, PZN-PZT

DOI: http://dx.doi.org/10.2314/IWPMA_02

J. Am. Ceram. Soc., **97** [8] 2479–2483 (2014)
DOI: 10.1111/jace.12949

Journal

Temperature-Stable Relative Permittivity from −70°C to 500°C in $(Ba_{0.8}Ca_{0.2})TiO_3$–$Bi(Mg_{0.5}Ti_{0.5})O_3$–$NaNbO_3$ Ceramics

Aurang Zeb,[‡] Yang Bai,[§] Tim Button,[§] and Steven J. Milne[‡,†]

[‡]Institute for Materials Research, University of Leeds, Leeds LS2 9JT, United Kingdom

[§]School of Metallurgy and Materials, University of Birmingham, Birmingham B15 2TT, United Kingdom

Temperature-stable relaxor dielectrics have been developed in the solid solution system: $0.45Ba_{0.8}Ca_{0.2}TiO_3$–$(0.55 - x)Bi(Mg_{0.5}Ti_{0.5})O_3$–$xNaNbO_3$. Ceramics of composition $x = 0$ have a relative permittivity $\varepsilon_r = 950 \pm 15\%$ over a wide temperature range from +70°C to 600°C. Modification with $NaNbO_3$ at $x = 0.2$ decreases the lower limiting temperature to −70°C, but also decreases relative permittivity such that $\varepsilon_r \sim 600 \pm 15\%$ over the temperature range −70°C to 500°C. For composition $x = 0.3$, the low-temperature dispersion in loss tangent, tan δ, (at 1 kHz) shifts to lower temperature, giving tan δ values ≤0.02 across the temperature range −60°C to 300°C in combination with $\varepsilon_r \sim 550 \pm 15\%$. Values of dc resistivity for all samples are of the order of 10^{10} Ω m at 250°C and 10^7 Ω m at 400°C.

W. Jo—contributing editor

Manuscript No. 34454. Received January 22, 2014; revised March 12, 2014; approved March 14, 2014.

[†] Author to whom correspondence should be addressed. e-mail: s.j.milne@leeds.ac.uk

10.1109/ULTSYM.2014.0221

Lead-Free Piezoelectric Materials and Composites for High Frequency Medical Ultrasound Transducer Applications

Y. Jiang, T. Thongchai, Y. Bai, C.Meggs,T. W. Button
University of Birmingham
Edgbaston, Birmingham, UK
T.W.BUTTON@bham.ac.uk

A. Matousek, P. Tofel, H. Hughes, T. W. Button
CEITEC – Central European Institute of Technology
Czech Republic
Hana.Hughes@ceitec.vutbr.cz

Abstract*—Lead-free ceramics based on the (1-x)Ba($Zr_{0.2}Ti_{0.8}$)O_3-x($Ba_{0.7}Ca_{0.3}$)TiO_3 (BZT-BCT) system have been reported to exhibit piezoelectric properties comparable to lead zirconate titanate ceramics, and are thus being considered as replacement materials for some applications. In this work, the possibility of fabricating BZT-BCT based 1-3 piezocomposites for high frequency ultrasound imaging has been explored. An investigation of the interdependence of synthesis, processing and sintering conditions on the physical, structural, microstructural and functional properties of piezoelectric compositions in the BZT-BCT system has been carried out. Ceramic powders with a composition of 0.5BZT-0.5BCT and a particle size of 1 μm were chosen for the fabrication of the ceramic segments which were subsequently sintered at 1425°C. A novel randomised pattern that has recently demonstrated its advantages in suppressing undesirable spurious resonances was adopted for the lead-free composites and a micro-moulding technique based on gel casting ceramic processing has been used for the fabrication of the composites. A 0.5BZT-0.5BCT based randomised composite operating at ~30 MHz with an electromechanical coupling factor of 0.63 has been achieved.

***Keywords*—(BaCa)(ZrTi)O_3 ceramics; piezoelectric; lead-free; processing; Piezoelectric composite; High frequency transducer; Gel-casting**

CONFERENCE ORAL AND POSTER PRESENTATIONS

1. Ferroelectrics UK 2013, 17-18 January 2013, Sheffield, UK

   Oral presentation: Energy Harvesting Using Piezoelectric Materials

2. Energy Harvesting 2013, 25 March 2013, London, UK

   Poster: Free-standing Piezoelectric Thick-film Energy Harvester with Enhanced Output Power Density

3. Invited Talk, 03 June 2013, CEITEC, Brno, Czech Republic

   Oral presentation: Piezoelectric Energy Harvesting

4. 10th International Workshop on Piezoelectric Materials and Applications in Actuators & 8th Annual Energy Harvesting Workshop, 14-18 July 2013, Hannover, Germany

   Oral presentation: Free-standing Piezoelectric Thick-film Energy Harvester

5. MEGS IV Annual Conference, 12-13 September 2013, Loughborough, UK

   Poster: Piezoelectric Energy Harvesting: Promising Market & Bright Future

6. MEGS Christmas Conference, 12 December 2013, Birmingham, UK

   Oral presentation: Energy Harvesting Using Piezoelectric Materials

7. Workshop of Nonlinear and Multi-scale Dynamics of Smart Materials in Energy Harvesting, 17-18 February 2014, Lublin, Poland

   Oral presentation: Free-standing Piezoelectric Thick-films for Wideband Energy Harvesting Devices (presented by other author)

8. Energy Harvesting 2014, 12 March 2014, London, UK

   Poster: Charging Behaviour of Vibration and Wind Energy Harvesters Based on Free-standing Piezoelectric Thick-films

9. International Workshop on Relaxor Ferroelectrics, 12-16 October 2014, Stirin, Czech Republic

   Poster: Evaluation of BCZT Lead-free Piezoelectric Ceramics Using Different Measurement Techniques

Free-standing Piezoelectric Thick-film Energy Harvester with Enhanced Output Power Density

Yang Bai [1], Carl Meggs [1], Tim W Button [1,2]

[1] School of Metallurgy and Materials, University of Birmingham, UK [2] Central European Institute of Technology, Brno, Czech Republic

Background: Free-standing Configuration

The use of free-standing piezoelectric thick-film cantilevers as vibration energy harvesters was first reported by White et al. [1] and Kok et al. [2]. This configuration has advantages over more traditional structures in piezoelectric energy harvesters, including reduced cost, smaller dimensions, simplified fabrication and easier integration with wireless sensor networks [1]. However, there have been few publications investigating and discussing this configuration since the first reports, which may be because piezoelectric ceramics were thought to be too fragile to form a film-based free-standing structure [2][3].

Problems

In practice, the drawbacks of a free-standing piezoelectric thick-film multi-layer cantilever may include:

- De-lamination after co-sintering caused by mismatched shrinkage rates of different layers (piezoelectric, electrode and substrate).
- Dramatically reduced piezoelectric properties of piezoelectric layers inherent in thick-film processes with low sintering temperatures.

Work Objectives

- Resolve the de-lamination problem by optimising the thick film ink formulations and thus matching the overall shrinkage rates during the drying and sintering processes.
- Utilise an optimised piezoelectric composition with higher g_{31}, d_{31}·g_{31} and k_{31} instead of traditional soft PZT in order to compensate for the poorer piezoelectric performance of thick-film materials.
- Measure the real transverse properties of single-layer thick-films and test the energy conversion abilities of the cantilevers.

Experiments/Research Methods

Inks Used for Cantilever Fabrication

Ink Name	Powder	Glass [a] (wt%)	Vehicle [b] (wt%)
PZT Ink	Commercial 'soft' PZT (TRS 610C)	1	20
PZN-PZT Ink	3 mol% La + PZN-PZT (self-synthesized)		
Silver Ink	Silver Flake	N/A	30
Carbon Ink	Carbon		70

[a] Borosilicate Glass; Powder = 100 wt% [b] Blythe; Powder+Glass+Vehicle = 100 wt%

Process: Doctor Blading

Single Piezoelectric Layer

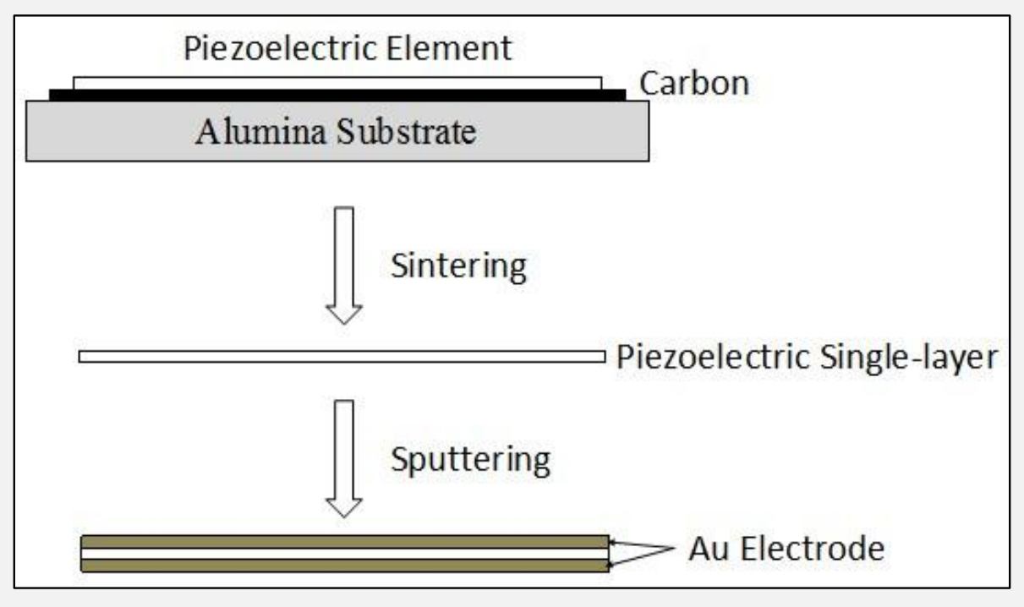

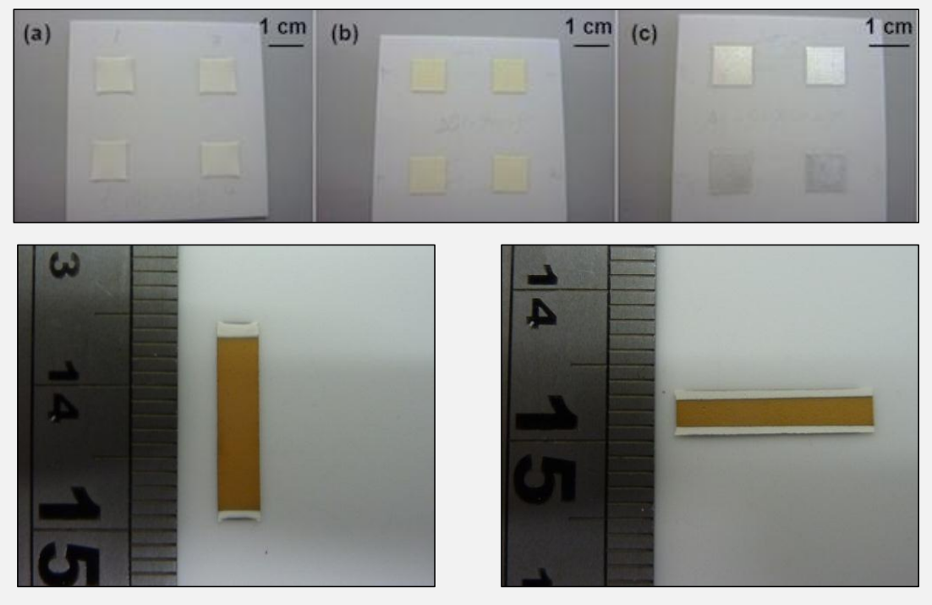

For Shrinkage Rate Measurements

For Piezoelectric Property Measurements

Unimorph Cantilever

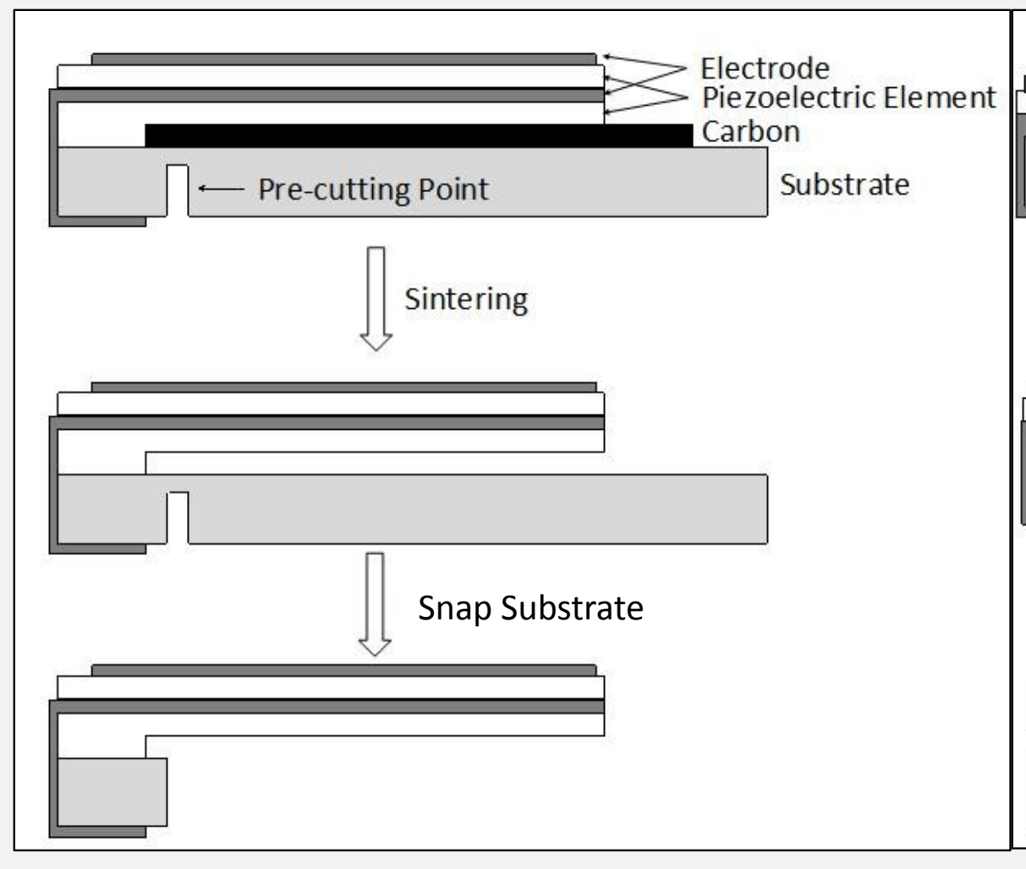

Bimorph Cantilever

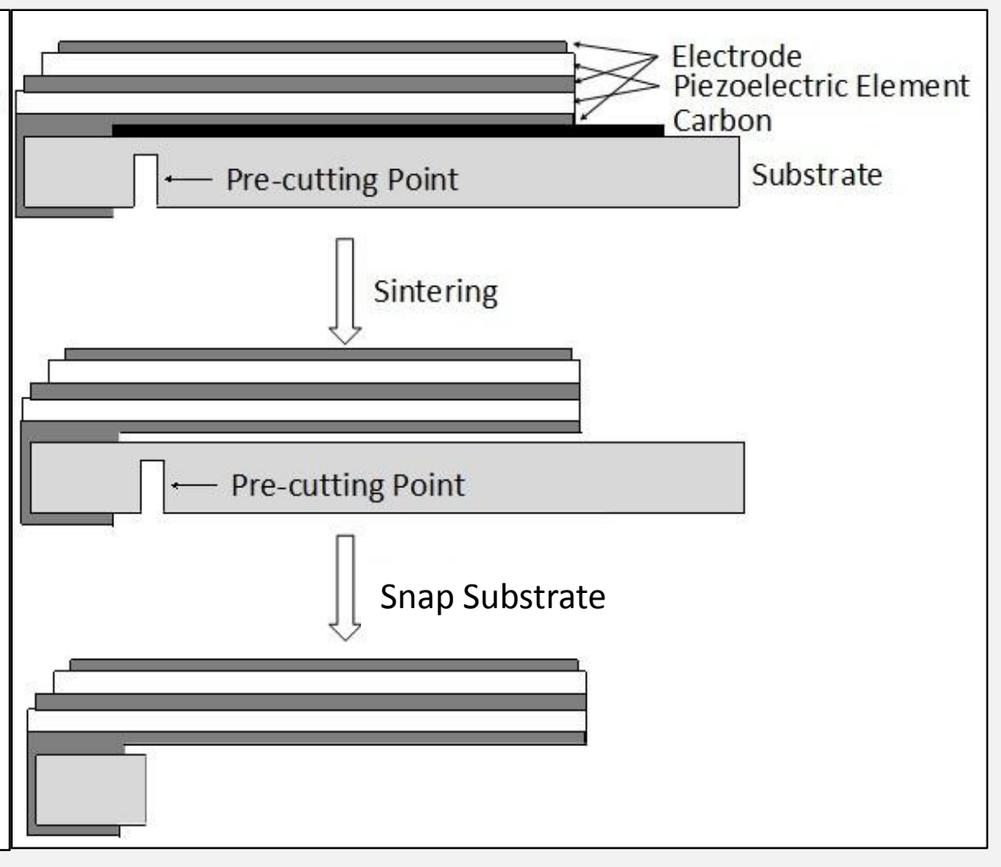

For Energy Conversion Tests

Characterisation

- The shrinkage rates (η) were calculated from equation $\eta=\frac{A_0-A_1}{A_0}\times 100\%$, where A_0 is the surface area before sintering while A_1 is the surface area after sintering.
- Piezoelectric properties were measured with an Impedance Analyser.
- Energy conversion of the multi-layer cantilevers was tested as shown below.

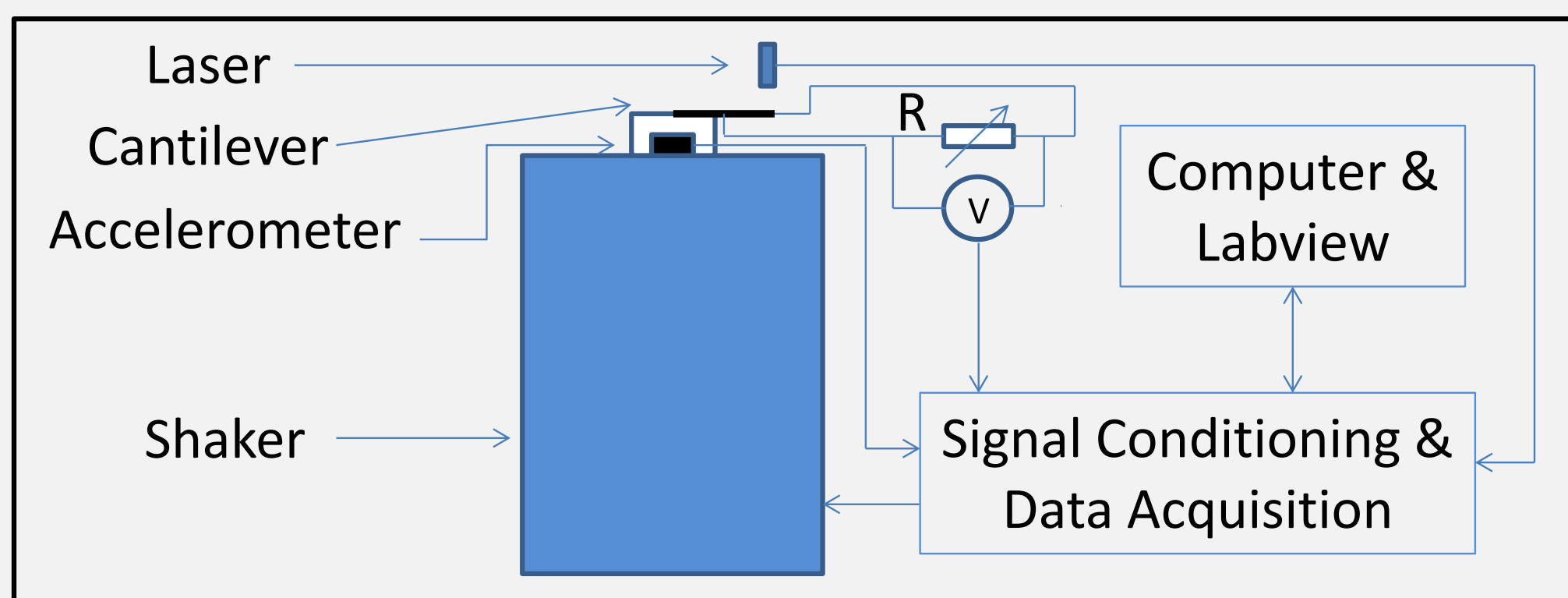

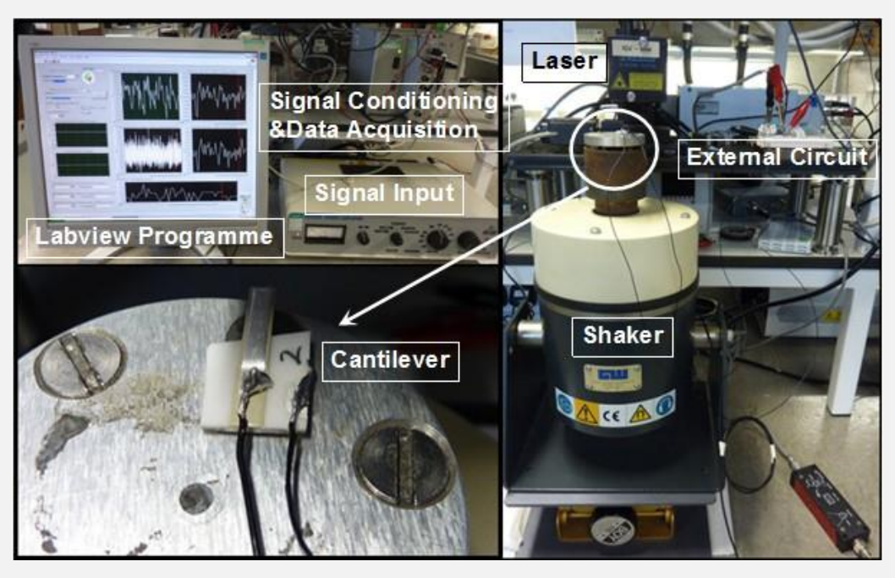

Output Power (P) =V^2/R Power Density=P_{RMS}/Cantilever Volume

Results

Shrinkage Rates

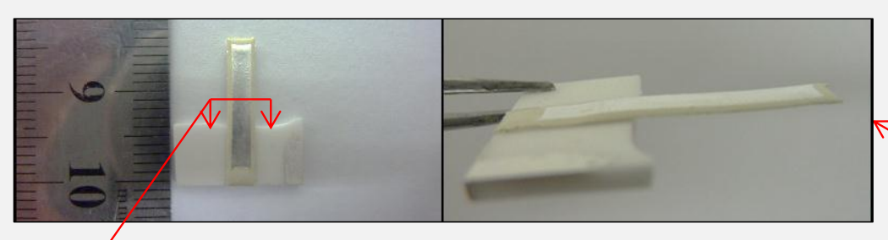

Figure 1.
Good unimorph sample

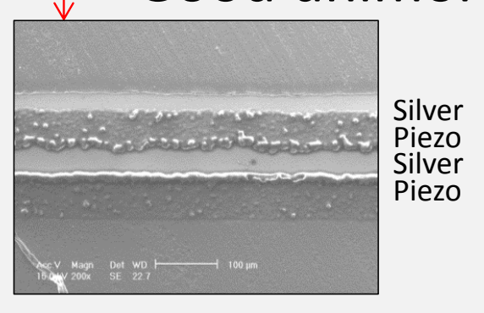

Figure 2.
Cross-section
SEM image

Figure 3.
De-lamination

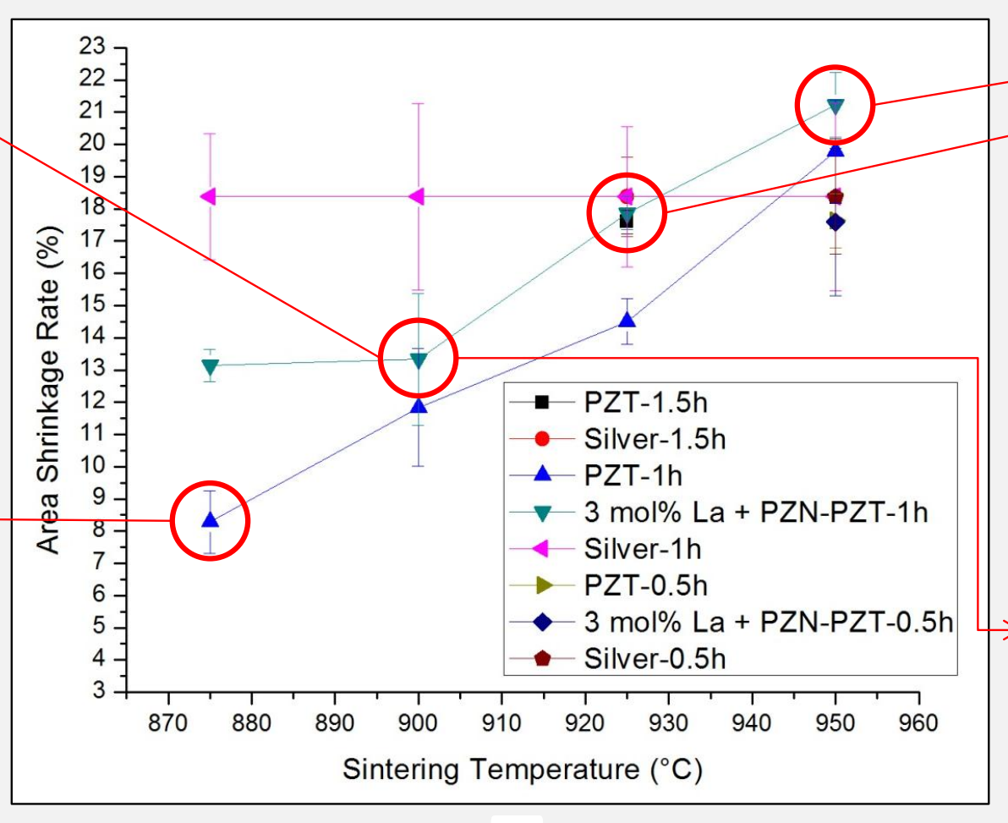

Figure 4.
Droop effect

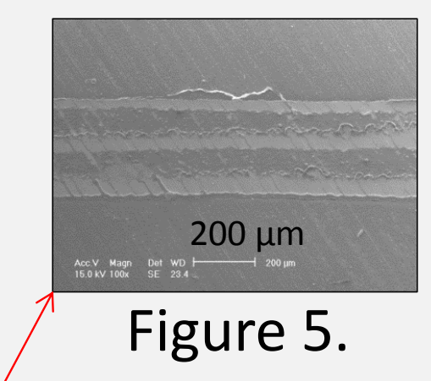

Figure 5.
Cross-section
SEM image

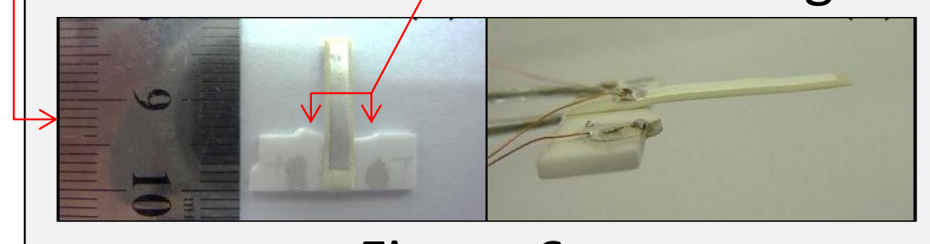

Figure 6.
Good bimorph sample

- When the shrinkage of the piezoelectric layer was much less than shrinkage of the silver layer, de-lamination was observed (see figure 3).
- When the shrinkage of the piezoelectric layer was equal to or more than that of the silver layer, the cantilever deformed and contacted the substrate (see figure 4).
- When the shrinkage rate of the piezoelectric layer was approximately 5-6% smaller than that of the silver layer, flat cantilevers, free from residual stresses and without de-lamination or droop, were successfully fabricated (see figure 1 and 6).
- The SEM images (figure 2 and 5) show the cross-section of the cantilevers. Good interfaces were observed.

Piezoelectric Properties

	PZT [c]	3 mol% La + PZN-PZT [d]
Piezoelectric charge coefficient d_{31} (pC/N)	-97±3	-102±12
Piezoelectric voltage coefficient g_{31} (mV·m/N)	-28.5±0.9	-32.5±4.1
Transverse electromechanical coupling coefficient k_{31} (dimensionless)	-0.20±0.01	-0.26±0.01

[c] Sintered at 900 ˚C for 2 hours [d] Sintered at 900 ˚C for 1 hour

Energy Conversion [e]

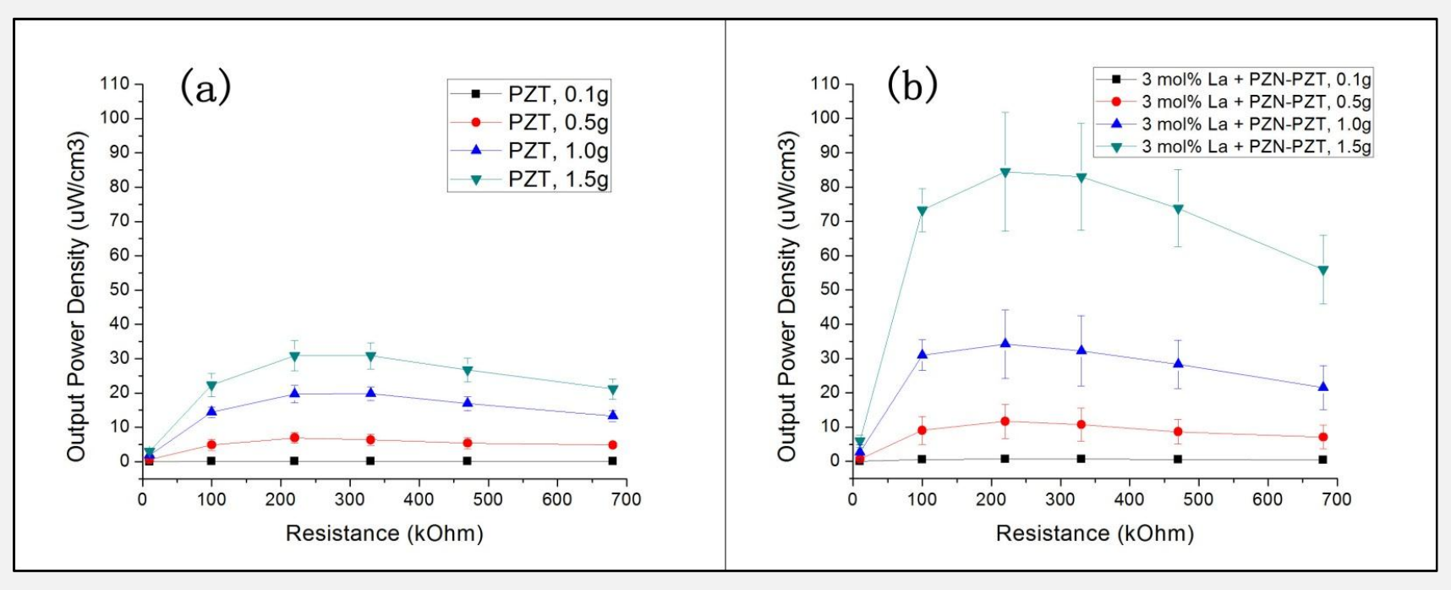

Figure 7. The dependence of the output power density on resistive load for the unimorph thick-film free-standing cantilevers.

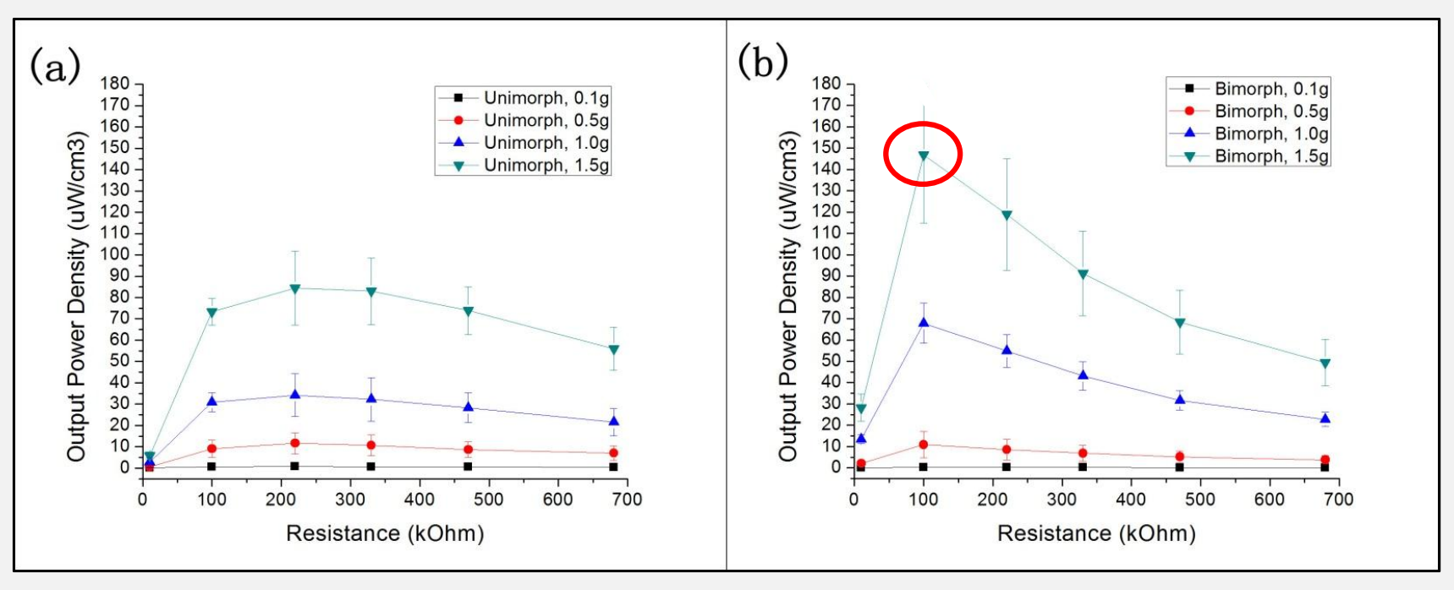

Figure 8. The dependence of the output power density on resistive load for the 3 mol% La + PZN-PZT cantilevers

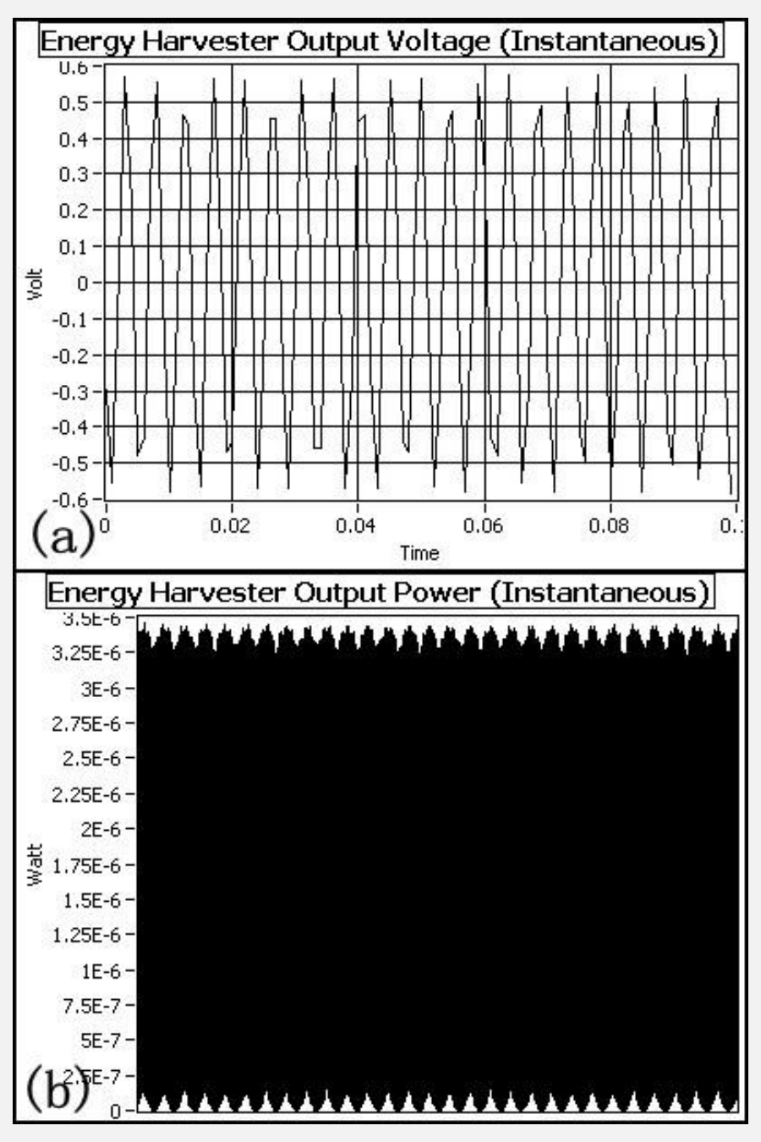

Figure 9. The instantaneous (a) voltage (b) power of a bimorph sample vibrating at 440 Hz, 1.5*g* with 100 kΩ resistive load.

[e] The data were obtained when the cantilevers were vibrating at their own natural resonant frequencies.

- Unimorph cantilevers of 3 mol% La + PZN-PZT showed performance improvements of up to 173% at 1.5*g* (*g*≈9.8m/s^2) compared to commercial PZT (see figure 7).
- Improvements were 68% at 0.5*g*, 73% at 1.0*g* and 173% at 1.5*g*, respectively. When compared to reference [2], the improvements reached 92% at 0.5g and 121% at 1.0*g*, respectively.
- The output power density of the bimorph with optimum resistive load was about twice that of the unimorph at 1*g* and 1.5*g* (see figure 8). At lower values of acceleration (0.1*g* and 0.5*g*) the output power density of the bimorph was lower than the unimorph. This may be because the bimorph was thicker than the unimorph so that it was less sensitive to the vibration at lower accelerations.
- The bimorph seemed more sensitive to the value of resistive load (see figure 8).
- A maximum output power density of 146.8 μW/cm^3 was obtained when the 3 mol% La + PZN-PZT bimorph was vibrating at 440 Hz, 1.5*g* with the resistive load of 100 kΩ (see figure 8(b)).
- Figure 9 shows an example of the instantaneous voltage and power of the resistive load. As this work concentrates on composition optimisation and process development, the cantilevers used for testing were not optimised in terms of structural or electrical properties. It is anticipated that increased output power densities will be obtained when a traditional oscillation magnifier (proof mass and/or spring) or a high efficiency circuit (booster/AC-DC converter) is introduced.

Conclusions

1. Free-standing piezoelectric thick-film cantilevers without de-lamination effect have been fabricated.
2. The advantages of an optimised composition over the traditional PZT material has been experimentally confirmed for the application of vibration energy harvesting.

References

[1] White N W, Harris N R, Kok S L and Tudor M J (2008) 2nd *Electronics System-integration Technology Conference (Greenwich, UK, September)* pp. 589-592

[2] Kok S L, White N M and Harris N R (2009) *Measurement Science and Technology* **20** 124010

[3] Anton S R and Sodano H A (2007) *Smart Materials & Structures* **16**(3) R1-R21

Contacts Yang Bai: YXB087@bham.ac.uk; Carl Meggs: c.meggs@bham.ac.uk; Prof. Tim W Button: t.w.button@bham.ac.uk

Energy Harvesting
An EPSRC Funded Network

Midlands Energy
Graduate School

UNIVERSITY OF
BIRMINGHAM

Loughborough
University

The University of
Nottingham
UNITED KINGDOM · CHINA · MALAYSIA

Piezoelectric Energy Harvesting

Promising Market & Bright Future

Yang Bai[1], Tim W Button[1,2]

[1] Metallurgy & Materials,
University of Birmingham,
Birmingham, United Kingdom

[2] Central European Institute
of Technology,
Brno, Czech Republic

For several decades, the renewable energy research has involved macro-scale ambient resources (e.g. out-door solar, strong fluidic - wind) in order to generate kW-MW power for industrial or domestic use. However, as portable/microelectronic devices consume much less energy due to innovation in electronic hardware and processing, harvesting micro-scale ambient energy (μW-W) for such devices, and designing them to be self-recharged or self-powered, necessitate the development of novel energy harvesters suitable for micro-dimensions, where the conventional technology is likely to be less efficient or face severe practical problems.

Concept

Low-frequency/Small-amplitude Vibration (building, machine)

Small Temperature Gradient (<10 °C)

Weak Fluid (breeze, droplet)

Supporting Structure

Piezoelectric Energy Harvester (Free-standing Cantilever)

Deformation/Bending

Electric Potential/Voltage

Signal Conditioning/Energy Storage

Circuitry/End User

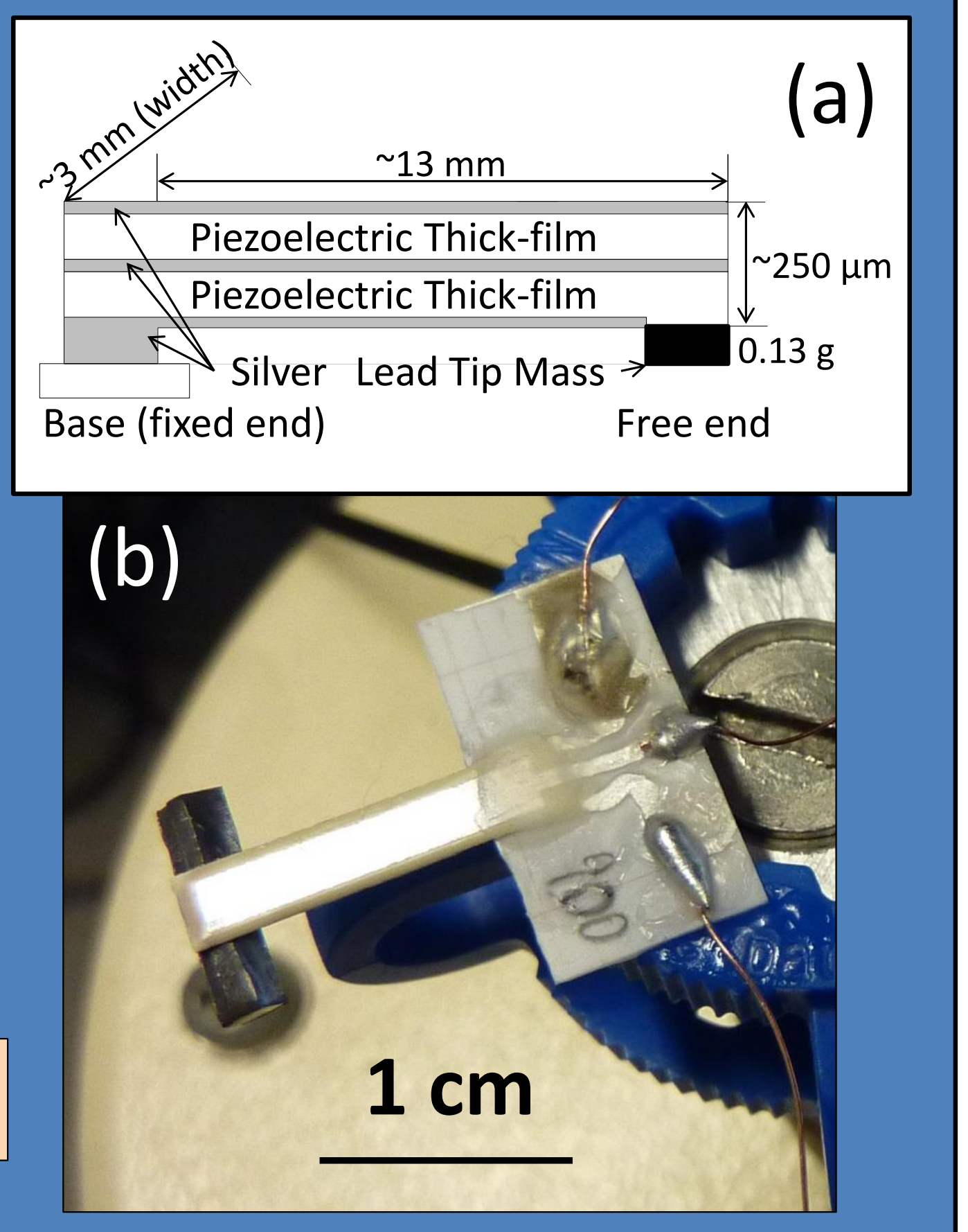

Figure 1. A novel piezoelectric energy harvester (free-standing thick-films): (a) schematic of the construction; (b) the fabricated harvester.

Market Size

Energy Harvesting Devices*

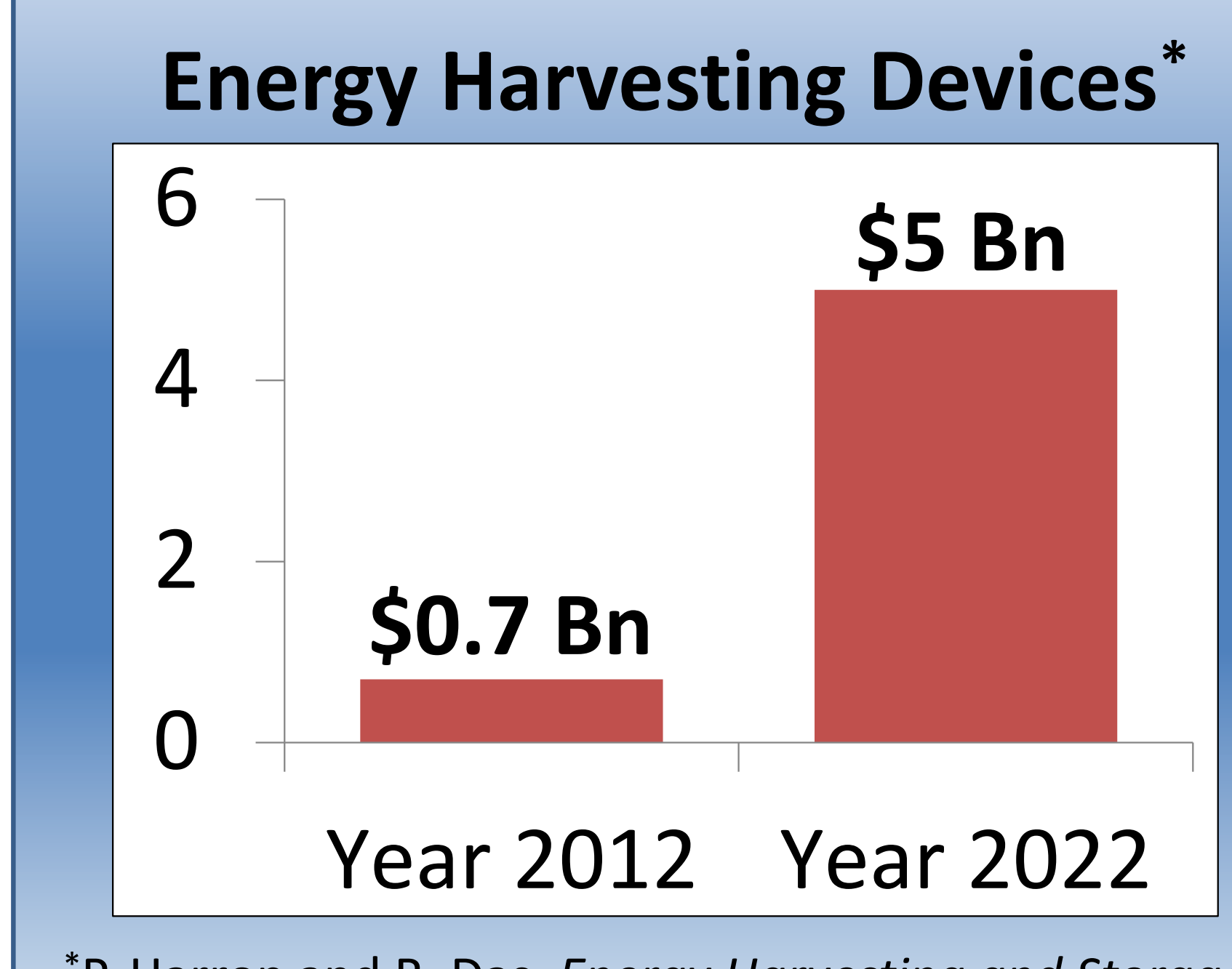

Piezoelectric Harvesters**

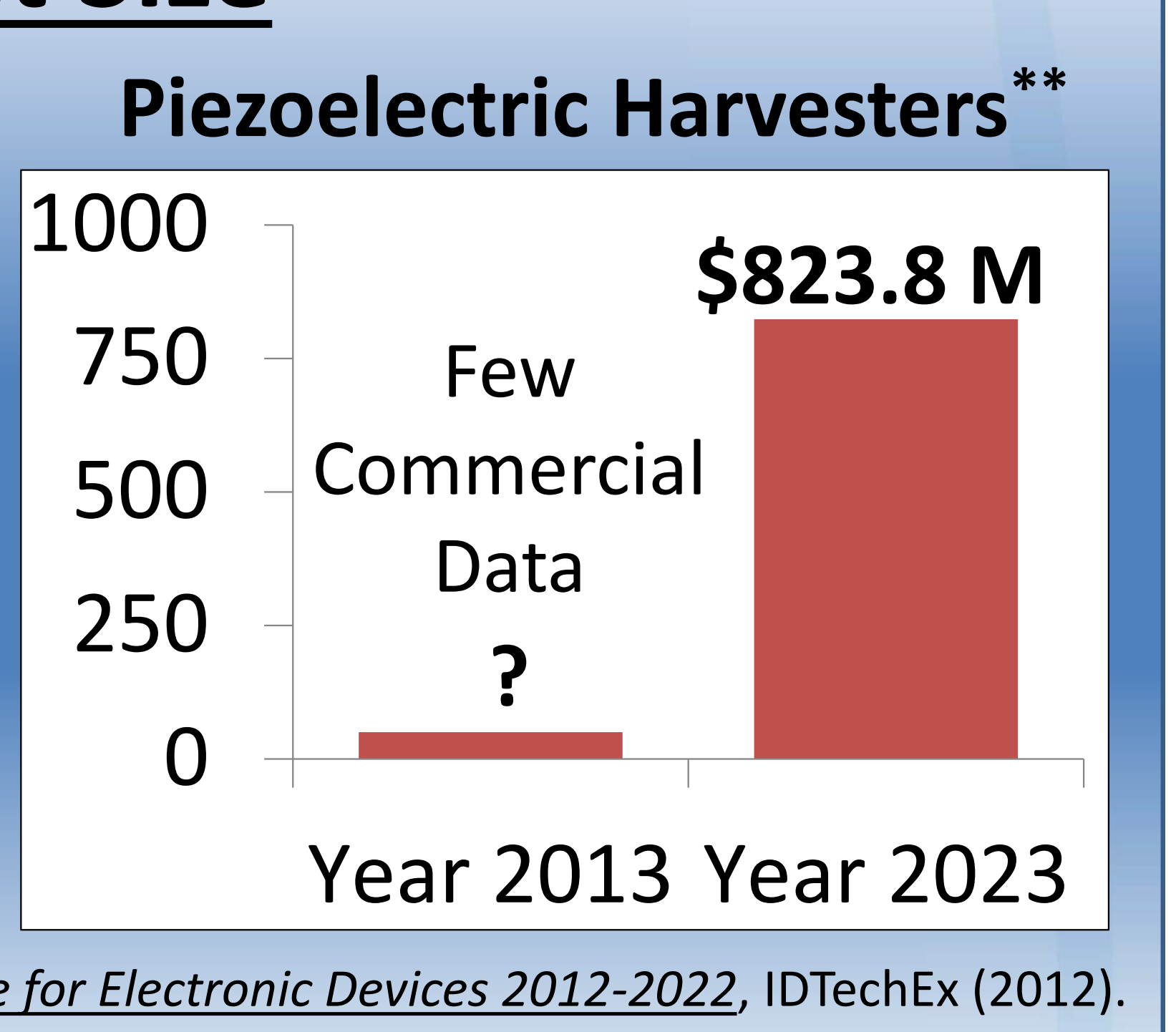

*P. Harrop and R. Das, *Energy Harvesting and Storage for Electronic Devices 2012-2022*, IDTechEx (2012).
**H. Igbenehi and R. Das, *Piezoelectric Energy Harvesting 2013-2023*, IDTechEx (2012).

Research Achievements

- Two lead-based piezoelectric compositions have been investigated on energy harvesting related parameters.
- A batch of novel piezoelectric energy harvesters (shown in figure 1.) made with one of the investigated compositions has been fabricated, with about 2.5V average voltage and 10 μW average power harvested under harmonic vibration.
- A lead-free (green and clean) piezoelectric composition has been proved suitable for energy harvesting.

Applications

Consumer Electronics **Remote Control** **Aerospace**

Structural Health Monitoring Sensors (buildings, bridges, railways)

Other Micro-electromechanical Systems (MEMS)
Wireless Sensor Networks (WSNs)

Challenges & Tasks

- Keep improving the output and reliability - under real environment test conditions.
- Develop matched external circuitry.
- Innovative applications – enlarging the market.
- Build up standards – giving users confidence.

Piezoelectrics For Micro-scale Energy Storage

Energy Source	Conventional Technology	Problems In Micro-scale	Piezoelectric Solution
Vibration	Piezoelectric Conversion	High Working Frequency; Integration	Thick-films/Thin-films
Wind	Wind Turbine	Low Efficiency; Threshold Wind Speed	Thick-film Cantilevers + Free-spinning Fan + Magnets
Thermal Energy	Thermoelectric Harvester	Ultra-low Output with Small Temp. Gradient	Piezo-cantilever + Hard Magnet (hot side) + Soft Magnet (cold side)
Solar Energy	Photovoltaic Panel	Small Surface Area; Low efficiency	No Direct Solution

E-mail Addresses: YXB087@bham.ac.uk (Y. Bai); t.w.button@bham.ac.uk (T. W. Button)

Charging Behaviour of Vibration And Wind Energy Harvesters Based On Free-standing Piezoelectric Thick-films

Yang Bai[1], Car Meggs[1], Tim W Button[1,2]
[1] Metallurgy & Materials, University of Birmingham, Birmingham, United Kingdom
[2] Central European Institute of Technology, Brno, Czech Republic

Introduction

Having experienced more than 20 years' research, Piezoelectric Energy Harvesting has shown to be a promising technology, and is predicted to approach commercialisation in several years. In order to evaluate the feasibility and explore potential applications, this poster presents the charging behaviour of vibration and wind energy harvesters based on integrated free-standing thick-film piezoelectric cantilevers, in which individual elements have been investigated and developed by the authors at earlier stages of the project.

Vibration Harvester - Individual

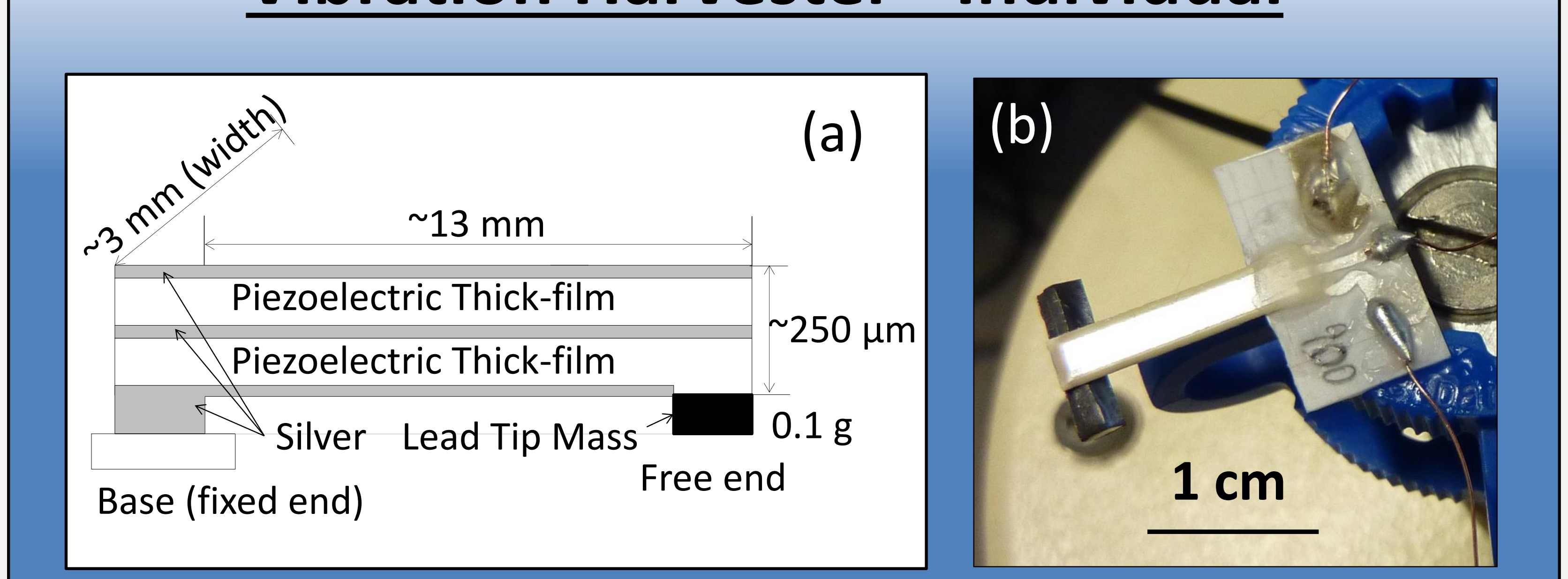

Figure 1. Proposed individual energy harvester with free-standing thick-film structure: (a) schematic of the construction; (b) the fabricated harvester.

Vibration Harvester - Array

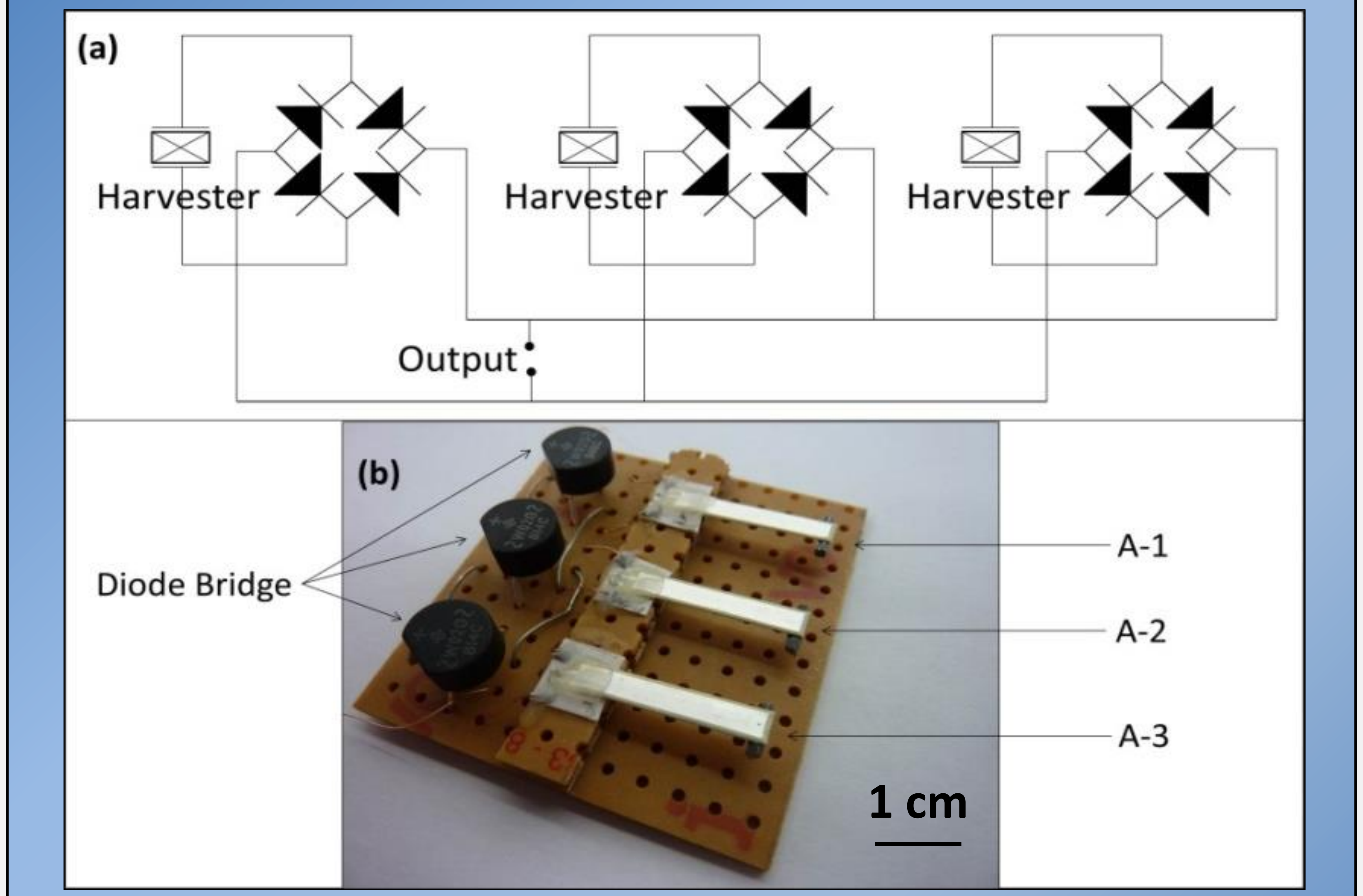

Figure 2. (a) The schematic of the connection method (b) the picture of an array.

Table 1. Summary of the dimensions, tip masses and frequencies of the array.

Single-element Harvester No.	Free-standing Length (mm)	Width (mm)	Layer Thicknesses (µm) (top Ag/P_T/Ag/P_B/bottom Ag)	Tip Mass (g)	Designed Frequency (Hz)
A-1	16.00	3.50	18.6/76.0/17.0/67.3/19.0	0.095	110
A-2	16.10	3.50		0.106	104
A-3	16.00	3.50		0.074	123

Wind Harvester Based on Piezoelectrics

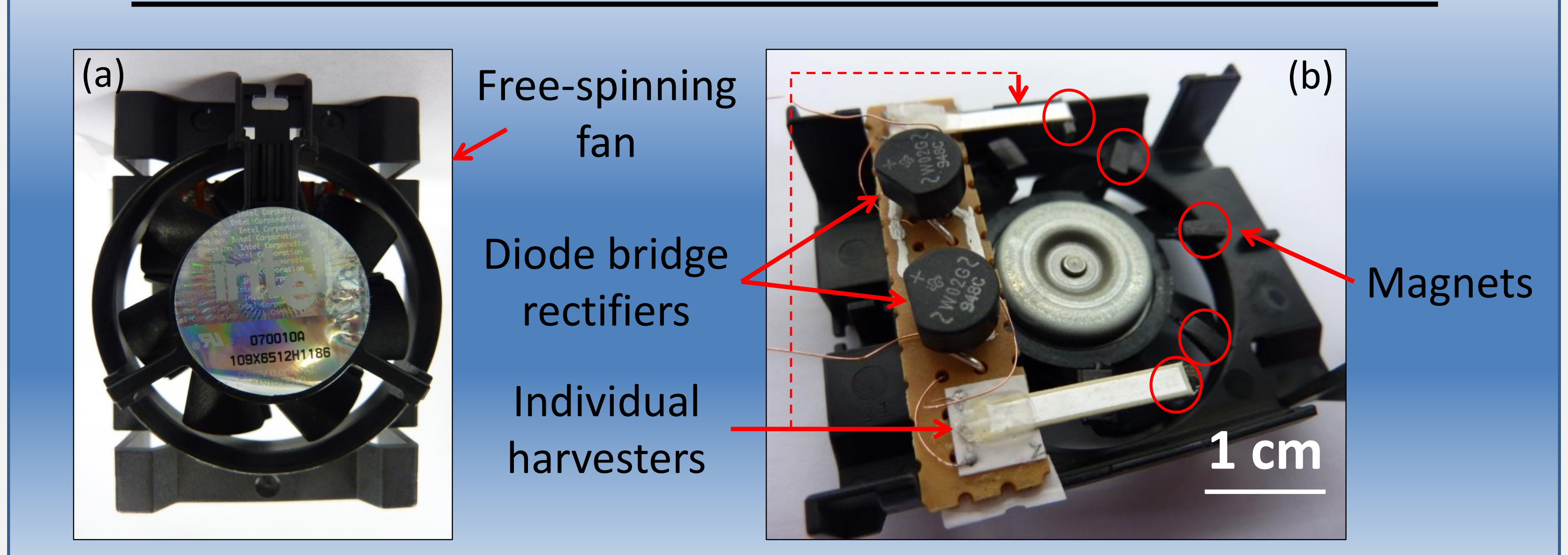

Figure 3. Pictures of wind harvester incorporating piezoelectrics: (a) front-side; (b) back-side

Charging 1000 µF Capacitor - Individual

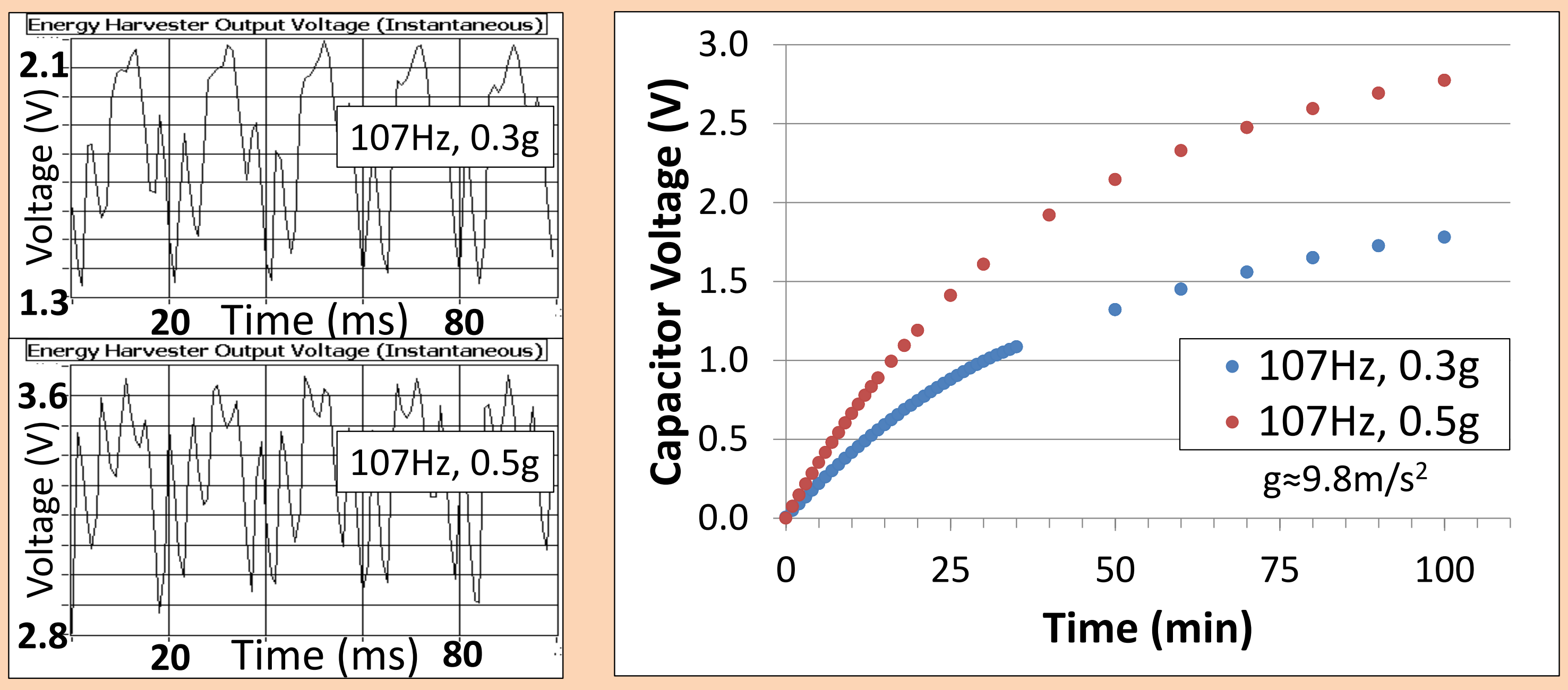

Figure 4. Instantaneous output voltage and charging response of an individual harvester.

Charging 1000 µF Capacitor - Array

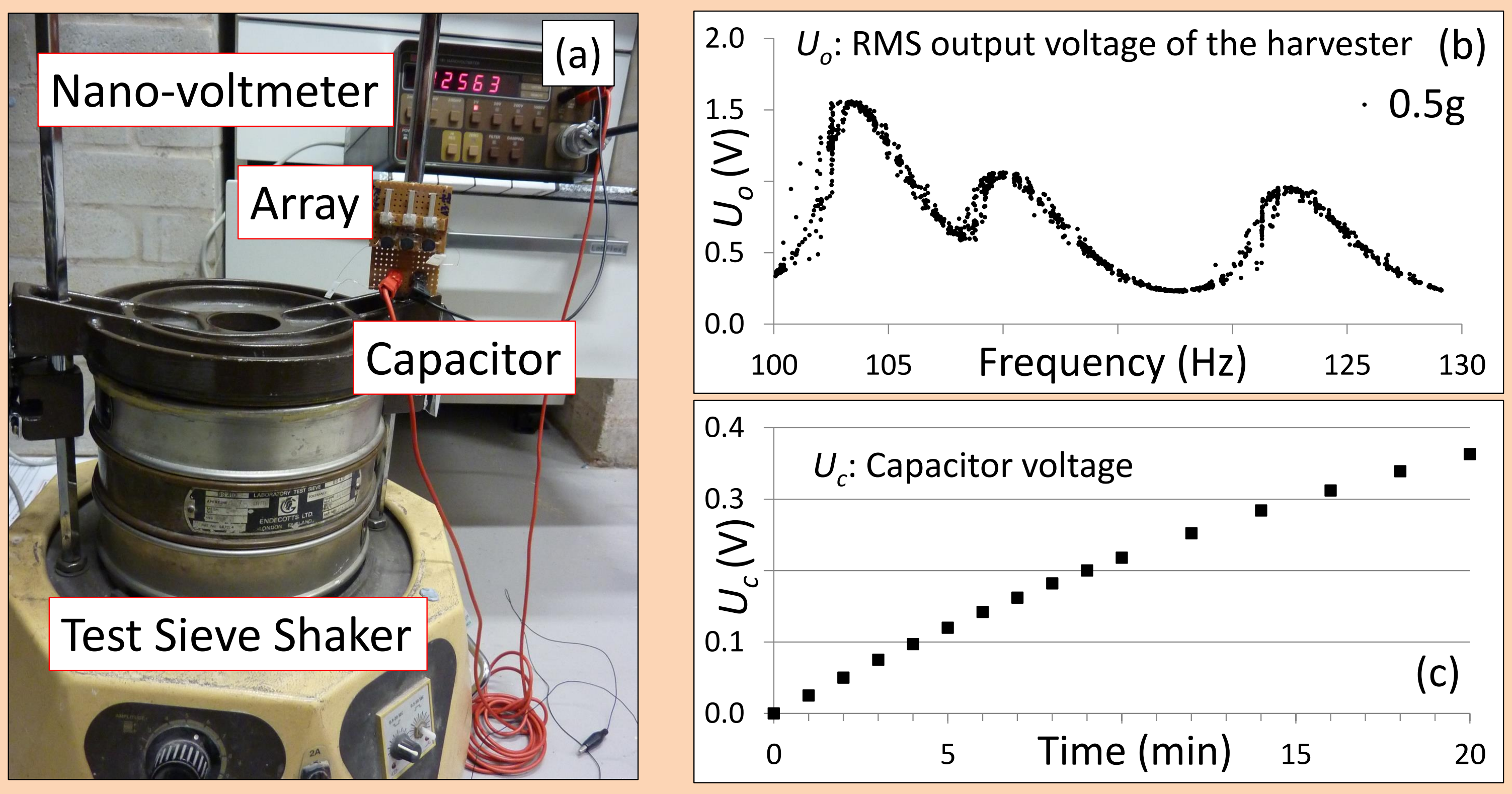

Figure 5. (a) Test configuration, (b) harmonic output and (c) charging response of an array mounted on a sieve shaker.

Charging 1000 µF Capacitor - Wind

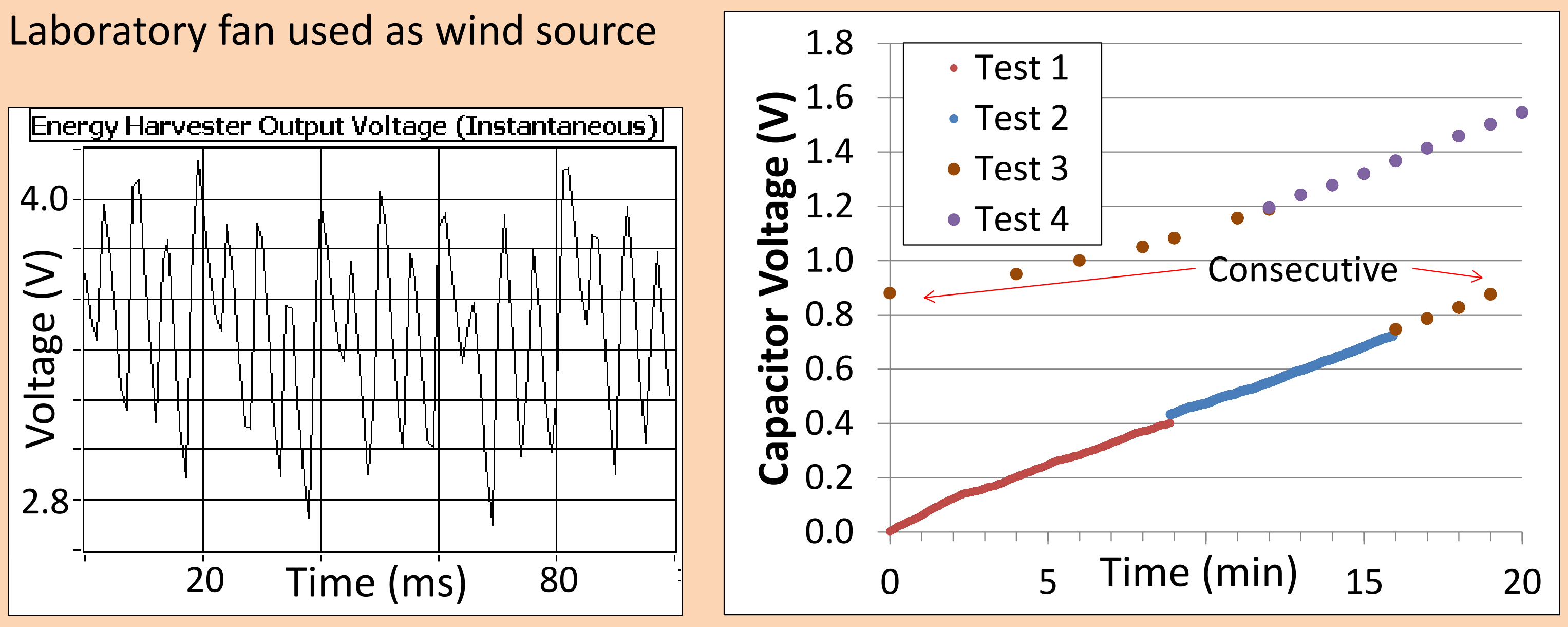

Figure 6. Instantaneous output voltage and charging response of a wind harvester in a series of four consecutive tests.

Summary

- Vibration harvesters have been able to charge a 1000 µF capacitor, under both harmonic and machinery vibration.
- Proposed structure has also been proved feasible to incorporate to a wind system, showing comparable output voltage and charging rate to those of the vibration systems.

Contacts: YXB087@bham.ac.uk (Y. Bai); c.meggs@bham.ac.uk (C.Meggs); t.w.button@bham.ac.uk (T. W. Button)

Evaluation of BCZT Lead-free Piezoelectric Ceramics Using Different Measurement Techniques

P. Tofel[1a], A. Matousek[1], H. Hughes[1], J. Bennett[3], A. J. Bell[3], Y. Bai[1,2] and T. W. Button[1,2]

[1]*CEITEC – Central European Institute of Technology, Technicka 3058/10, 61600 Brno, Czech Republic*
[2]*School of Metallurgy and Materials, University of Birmingham, Birmingham, B15 2TT, United Kingdom*
[3]*Institute for Materials Research, University of Leeds, Leeds, LS2 9JT, United Kingdom*

Introduction

This work is concerned with the measurement of the dielectric and piezoelectric parameters of $(BaCa)(ZrTi)O_3$ (BCZT) ceramic materials, which are being widely investigated as potential lead-free replacements for lead zirconate titanate (PZT). Measurements of the dielectric and piezoelectric properties of the sintered materials have been made by a range of techniques at three institutions. Sets of sintered samples included a range of BCZT compositions and samples sintered under different conditions (temperature and heating/cooling rates).

Experimental

- Bulk disc ceramic samples with compositions of 1/9, 3/7 and 5/5 $Ba(Zr_{0.2}Ti_{0.8})O_3/(Ba_{0.7}Ca_{0.3})TiO_3$ (BZT/BCT) (see Figure 1) were prepared by solid-state reaction, where sintering was carried out at 1400-1500 °C for 4 hours.
- Poling was taken at 3 kV/mm for 10 minutes in silicone oil at room temperature.

Table 1. Parameters measured by different equipment

	University of Birmingham, UK	**University of Leeds, UK**	**CEITEC, CZ**
d_{33}	Berlincourt d_{33}-meter (YE2730A, Sinocera, China)	Berlincourt d_{33}-meter	Laser Interferometer (Aixacct, Germany)
ε_r	Impedance Analyser (4294A, Agilent, USA)	Impedance Analyser (4294A, Agilent, USA)	N/A
Displacement loop	N/A	Radiant (Precision, Technologies Ing., USA)	Laser Interferometer (Aixacct, Germany)

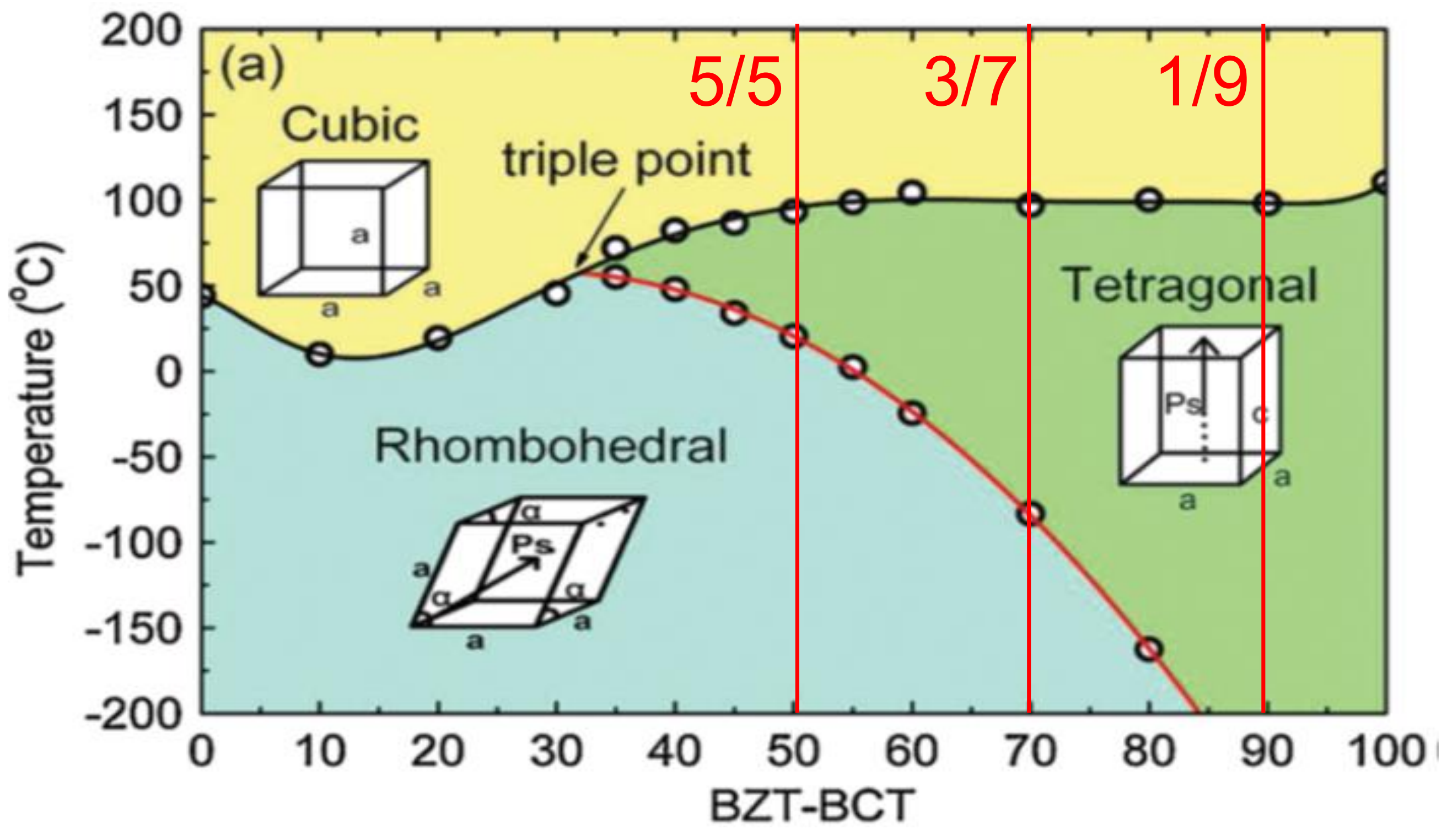

Liu, W. F. and Ren, X. B. Large, *Physical Review Letters* **103** 257602 (2009)

Figure 1. Phase diagram of BZT-BCT solid solution.

Results

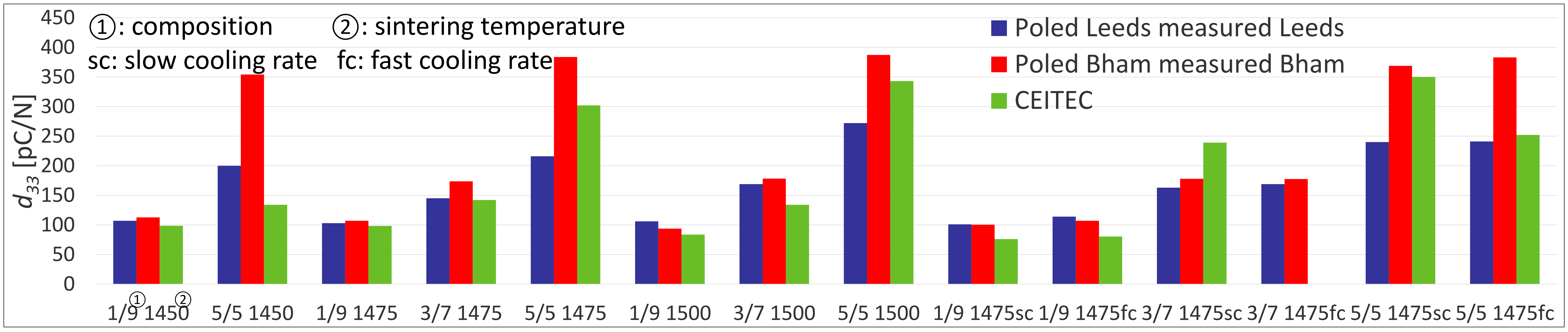

Figure 2. Piezoelectric coefficients of different samples measured in different institutes.

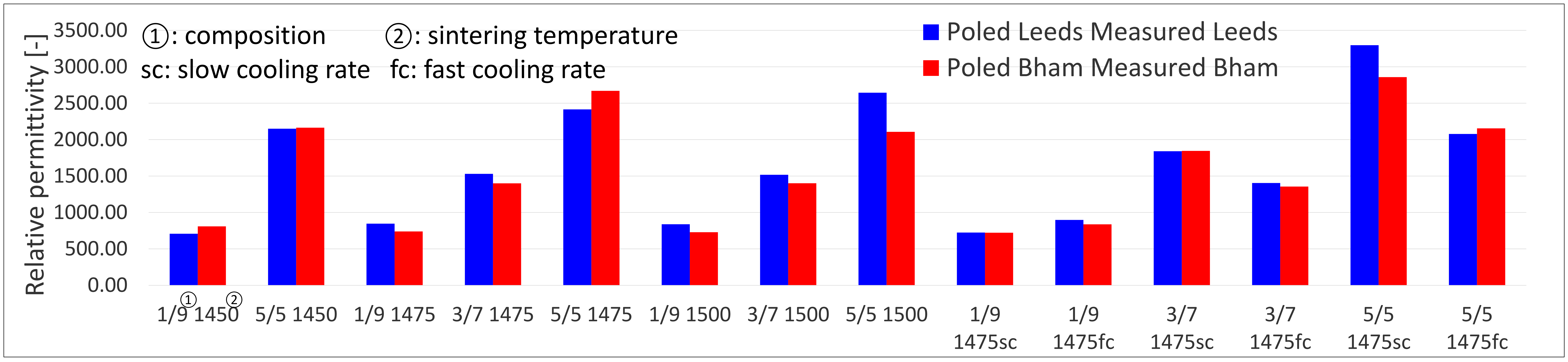

Figure 3. Dielectric constants of different samples measured in different institutes.

Figure 4. Dependence of displacement on voltage for a 3/7 BCZT sample sintered at 1475 °C measured in different institutes.

Conclusions

- BCZT lead-free piezoceramic samples (14 specimens) with different compositions have been measured by different techniques.
- Results of dielectric constants and piezoelectric coefficients obtained from different techniques have been compared.
- Generally, very good agreement between the different techniques has been found, and the results are in agreement with the phase diagram.
- The largest differences between results of piezoelectric coefficients measured by different techniques have been observed on the 5/5 composition.
- The measured properties of the 5/5 composition are very sensitive to processing and poling conditions.

Acknowledgments

- CEITEC - Central European Institute of Technology" **(CZ.1.05/1.1.00/02.0068)** from European Regional Development Fund.
- SoMoPro II programme. The research leading to these results has acquired a financial grant from the People Programme (Marie Curie action) of the Seventh Framework Programme of EU according to the REA Grant Agreement **No. 291788**. The research is further co-financed by the South-Moravian Region.
- Czech Science Foundation under the grant number **P108/13-09967S**

contact person

Tofel Pavel
tofel@feec.vutbr.cz
gsm.: +420 54114 3224

www.ceitec.vutbr.cz